



## OpenAIR@RGU

### The Open Access Institutional Repository at Robert Gordon University

<http://openair.rgu.ac.uk>

#### Citation Details

**Citation for the version of the work held in 'OpenAIR@RGU':**

OLUYEMI, G. F., 2007. Intelligent grain size profiling using neural network and application to sanding potential prediction in real time. Available from *OpenAIR@RGU*. [online]. Available from: <http://openair.rgu.ac.uk>

#### Copyright

Items in 'OpenAIR@RGU', Robert Gordon University Open Access Institutional Repository, are protected by copyright and intellectual property law. If you believe that any material held in 'OpenAIR@RGU' infringes copyright, please contact [openair-help@rgu.ac.uk](mailto:openair-help@rgu.ac.uk) with details. The item will be removed from the repository while the claim is investigated.

---

INTELLIGENT GRAIN SIZE PROFILING USING NEURAL NETWORK  
AND APPLICATION TO SANDING POTENTIAL PREDICTION  
IN REAL TIME

GBENGA FOLORUNSO **OLUYEMI**



## **IMAGING SERVICES NORTH**

Boston Spa, Wetherby

West Yorkshire, LS23 7BQ

[www.bl.uk](http://www.bl.uk)

**BEST COPY AVAILABLE.**

**VARIABLE PRINT QUALITY**

---

INTELLIGENT GRAIN SIZE PROFILING USING NEURAL NETWORK  
AND APPLICATION TO SANDING POTENTIAL PREDICTION  
IN REAL TIME

GBENGA FOLORUNSO **OLUYEMI**

A thesis submitted in partial fulfilment of the  
requirements of  
The Robert Gordon University  
for the degree of Doctor of Philosophy

November 2007

## **Dedication**

This work is dedicated to the glory of God, the almighty; and to the memory of my late father, Mr Johnson Folorunso Oluyemi, who encouraged me to seek knowledge. The work is also dedicated to my beautiful and loving wife, Folasade; and my wonderful boys, Favour and Blessing.

## Acknowledgment

“For I know the thoughts that I think toward you, saith the Lord, thoughts of peace, and not of evil, to give you an expected end (Jeremiah. 29:11).” First, I give all glory to God Almighty, the author and finisher of my faith for He has lived up to His promise to give me an expected end: the successful completion of this programme of studies. He has taken me through the long and tortuous journey of the programme and at the end granted me success. I owe Him lots of thanks.

My profound gratitude goes to my supervisory team in persons of Prof. Babs Oyeneyin and Dr. Chris Macleod. God has really used them to give me vital technical and moral supports throughout the period of this research programme. These supports have been a source of inspiration to me, without which completion of this research would not have been possible. I also extend words of gratitude to my uncle, Prof J. A. Oluyemi, for the fatherly roles he has played in my life; my brothers, Mr Tunji Oluyemi and Mr Segun Oluyemi, for their support and encouragement; my mum, my father and mother in-laws (Mr and Mrs Faro), for their moral and prayer supports; Mr and Mrs Taiwo Oladele, for their encouragement and prayers; and my friends and colleagues, Godwin Nwagbuna, Gideon Darmayam, Donald Igbuegwu, Abdulrahman Mohammed, Babatunde Moriwawon, Dr. Kim Wonk-seo, Dr. Mohammed Amish, Busayo Abraham, Wasiu Adekitan, Soji Omotoso, Idowu Akinbode, and many others, whom I cannot mention due to space constraint, for being of great help to me in one way or the other during the course of these research studies.

This acknowledgement will not be complete without thanking my beautiful wife, Folasade, for her support, encouragement and understanding and for holding fort for me on the home front while this research lasted; and my wonderful sons, Favour and Blessing for enduring my incessant never-ending unavailability in times they had need of my presence.

Thank you all!

## Abstract

Production of hydrocarbon from both consolidated and unconsolidated clastic reservoir rocks poses a risk of sand production especially if a well articulated programme of sand management strategy is not put in place to deal with the problem at the onset of field development. A well articulated programme of sand management would include sand production potential prediction in real time if it is going to be effective at all in achieving the goal of dealing with likely sand problem.

Sanding potential prediction in real time is considered an element of sand management strategy that involves the evaluation of risk of sand failure/production and the prediction of the likely sand rate and volume to facilitate optimum design of both downhole and surface equipment especially as related to sand control. Sanding potential prediction is therefore very crucial to reducing costs of field developments to make hitherto unattractive development environments profitable. This undoubtedly will impact positively the present drive to increase worldwide production of hydrocarbon. Specifically, real time sanding potential prediction enables timely reservoir management decisions relating to the choice, design and installation of sand control methods. It is also an important input to sand monitoring and topside management.

The current sanding potential prediction models in the industry are found to lack the robustness to predict sanding potential in real time. They also are unable to provide the functionality to track the grain size distributions of the sand producing formation and that of the produced sand. This functionality can be useful in the application of grain size distribution to sanding potential prediction. The scope of this work therefore covers the development of coupled models for grain size distribution and sanding potential predictions in real time.

A previous work has introduced the use of a commercial neural network technique for grain size distribution prediction. This work has built upon this by using a purposefully coded neural network in conjunction with statistical techniques to develop a model for grain size distribution

prediction in both horizontal and vertical directions and extending the application to failure analysis and prediction of strength and sanding potential in formation rocks. The theoretical basis for this work consists in the cross relationships between formation petrophysical properties and grain size distribution parameters on one hand and between grain size distribution parameters and formation strength parameters on the other hand. Hoek and Brown failure criterion, through an analytical treatment, serves as the platform for the development of the failure model, which is coupled to the grain size distribution and Unconfined Compressive Strength (UCS) models.

The results obtained in this work have further demonstrated the application of neural network to grain size distribution prediction. They also demonstrate that grain size distribution information can be used in monitoring changes in formation strength and by extension, the formation movement within the failure envelope space especially during production from a reservoir formation.

---

# Table of contents

Dedication	i
Acknowledgement	ii
Abstract	iii
Table of contents	v
List of figures	xi
List of tables	xv
Nomenclature	xvii
<b>Chapter 1 Introduction</b>	<b>1</b>
1.1 Background	1
1.1.1 Research Objectives	5
1.2 Research Methodology/Approach	5
1.3 Contributions to knowledge	7
1.4 Thesis Layout/Arrangement.	9
<b>Chapter 2 Sand production and management concept</b>	<b>11</b>
2.1 Sand production: a definition	11
2.2 Sand management	12
2.2.1 Sand prediction	16
2.2.2 Sand control	20
2.2.2.1 Gravel packs sand control completion	23
2.2.2.2 Stand-Alone screens completion	24
2.2.2.3 Expandable Sand Screen (ESS) completion	27
2.2.2.4 Screenless completions	28
2.2.3 Sand monitoring	30
2.2.4 Topside management/handling	33
2.3 Influence of sanding potential on field operations	35
2.3.1 Influence on drilling	35
2.3.2 Influence on well completion	35
2.3.3 Influence on oil production strategy	36
2.3.4 Influence on production facilities	36
2.4 Summary	36
<b>Chapter 3 Rock strength and textural/grain parameters correlation</b>	<b>38</b>
3.1 Basic failure theory	38
3.2 Conventional sanding potential prediction (SPP) techniques/models	39
3.2.1 Plastic (failed) extension model (PZE)	40
3.2.2 Shear failure model (BP's model)	41

3.2.3 Coates and Denoo model	42
3.2.4 Equivalent Critical plastic strain model	45
3.2.5 Linear poro-elastic and brittle plasticity model	46
3.2.6 Neural network based approach	48
3.3 A new failure concept: quantitative effect of textural/grain parameters on rock Strength	49
3.3.1 Grain and textural parameters and their relationship with strength	50
3.3.1.1 Grain size vs. rock strength	50
3.3.1.2 Grain sorting vs. rock strength	54
3.3.1.3 Grain Shape vs. strength	56
3.3.1.4 Grain packing vs. strength	57
3.4 Grain size profiling and Measurement techniques	57
3.4.1 Sieve analysis	58
3.4.2 Statistical presentation of sieve data	61
3.4.2.1 Mean	62
3.4.2.2 Median grain size	62
3.4.2.3 The Mode	63
3.4.2.4 Sorting	63
3.4.2.5 Skewness	63
3.4.2.6 Kurtosis	65
3.4.3 Direct Measurement	65
3.4.4 Laser diffraction method	66
3.4.5 Digital video core images	66
3.4.6 Empirical Models	67
3.4.6 Neural Network Technique	70
3.5 Summary	71
<b>Chapter 4 Geomechanical evaluation of rock</b>	<b>72</b>
4.1 Elastic properties of rocks	72
4.1.1 Young Modulus	73
4.1.2 Poisson ratio	74
4.1.3 Bulk Modulus	75
4.1.4 Shear Modulus	76
4.2 Rock strength evaluation	77
4.2.1 Unconfined Compressive Strength (UCS)	78
4.2.2 Cohesive strength	83
4.2.3 Tensile strength	84
4.2.4 Thick Walled Cylinder (TWC) strength	85
4.3 Reservoir rock stresses and their estimation	87
4.3.1 Theory of force and stress	87

4.3.2 State of Stress around a wellbore	89
4.3.3 Estimation of in-situ stresses	92
4.3.3.1 Vertical stress estimation	92
4.3.3.2 Minimum and maximum horizontal stresses estimation	94
4.4 Failure Criteria	96
4.4.1 Mohr Coulomb failure criteria	97
4.4.2 Hoek-Brown failure criterion	98
4.4.3 Drucker-Prager failure criterion	99
4.5 Failure Mechanism	100
4.5.1 Shear failure mechanism	100
4.5.2 Tensile failure	101
4.6 Summary	101
<b>Chapter 5 Neural network: Theory and application</b>	<b>103</b>
5.1 Background	103
5.2 Operations in Neural Network	104
5.2.1 Signal processing in Artificial Neural Network	104
5.2.2 Mathematical operation of a neural network	105
5.3 Justification for the wider use of neural network as a data mining method	105
5.4 Activation functions	106
5.4.1 Linear function	107
5.4.2 Step function	107
5.4.3 Sigmoid function	108
5.4.4 Hyperbolic tangent function	109
5.4.5 Gaussian function	110
5.5 Neural Network Training	111
5.5.1 Supervised training	111
5.5.2 Unsupervised training	111
5.5.3 Reinforcement training	112
5.6 Application of neural networks in the oil and gas industry	112
5.7 Data preparation for Neural Network Modelling	114
5.7.1 Data transformation and normalisation	114
5.7.2 Input and output data Normalisation	115
5.7.3 Input and output data de-normalisation	116
5.8 Summary	117
<b>Chapter 6 Grain size distribution modelling</b>	<b>118</b>
6.1 Relationship between grain size and well log data	118
6.1.2 Data distribution	119
6.1.3 Data transformation	119

6.1.4 Plots of Natural log of $d_{50}$ against various transformed log parameters	128
6.1.5 Principal Component Analysis (PCA)	133
6.1.6 Regression analysis	135
6.2 Modelling grain size distribution using statistical techniques	140
6.2.1 Variable controlling grain size distribution	140
6.2.2 Interrelationship among variables	141
6.2.3 Multiple Regression Analysis	145
6.3 Modelling grain size distribution using analytical technique	146
6.3.1 Rationale for the analytical model	146
6.3.1.1 Analytical model development	147
6.4 The dimensional analysis Model	150
6.5 Modelling grain size distribution using combined neural networks and statistical techniques	153
6.5.1 First neural network implementation	153
6.5.1.1 Input and output data selection	154
6.5.1.2 Data Normalisation and de-normalisation	155
6.5.1.3 Neural network coding	155
6.5.1.4 The Network training and validation	156
6.5.2 Network optimisation	156
6.5.2.1 Effect of learning rate on network	157
6.5.2.2 Effect of number of hidden layers on network performance	158
6.5.2.3 Effect of number of neurons in the hidden layers	158
6.5.3 Optimised network	159
6.5.4 Neural network testing	161
6.5.5 Neural network prediction of orientational median grain size	163
6.5.5.1 Application of permeability anisotropy	163
6.5.6 Determination of other percentile sizes	165
6.5.6.1 Equation relating percentile sizes with standard deviation	166
6.5.6.2 Equations for estimating the standard deviation	168
6.5.6.3 Orientational grain size distribution prediction	173
6.6 Validation of NN/analytical grain size distribution model	174
6.7 Summary	177
<b>Chapter 7 UCS modelling</b>	<b>178</b>
7.1 Existing UCS models review and ranking	178
7.1.1 Parameters exercising control on rock strength	182
7.1.1.1 Mechanical property parameters	183
7.1.1.2 Failure-inducing parameters	183
7.1.1.3 Petrophysical parameters	183
7.1.2 Ranking Criteria and Procedure	184
7.1.3 Results of Ranking	184

7.1.4 Further evaluation of some existing models	185
7.2 UCS modelling using dimensional analysis	187
7.2.1 Variable controlling rock strength	187
7.2.2 Application of Buckingham Pi Theorem	189
7.2.3 Validation of Dimensional Analysis model for UCS	190
7.3 Neural network modelling	191
7.3.1 Input and output data selection	191
7.3.2 Building the network	192
7.3.3 Network training	193
7.3.4 Network cross-validation	194
7.3.5 Sensitivity analysis studies	195
7.3.5.1 Effect of learning rate on network	195
7.3.5.2 Effect of number of hidden layer	197
7.3.5.3 Effect of number of neurons in the hidden layer	198
7.3.6 Final network implementation	200
7.3.7 Neural network model testing	200
7-4 Validation of neural network model for predicting UCS	202
7.5 Summary	203
<b>Chapter 8 Real time sanding potential prediction</b>	<b>205</b>
8.1 Onset of sanding model	205
8.1.1 Hoek and Brown (1988) estimates of model parameters	209
8.1.2 Preliminary analysis and testing of model	210
8.2 Coupling CDD model with time	214
8.2.1 Case studies: example calculations	219
8.3 Effect of water breakthrough on sand failure	221
8.3.1 Theoretical background	221
8.3.2 Field evidence supporting the roles of water in sand production	223
8.3.3 Experimental evidence supporting the roles of water in sand production	224
8.3.4 Modelling the effect of water breakthrough on sanding potential	225
8.3.4.1 Validation of effect of water breakthrough	229
8.4 Effects of completion types on CDD	232
8.4.1 Perforated completion	232
8.4.2 Open-Hole Completion	235
8.4.3 Gravel Pack Completion	236
8.5 Further validation of Critical Drawdown (CDD) model	241
8.6 Real time sand volume and rate quantification	244
8.6.1 Equation for yield flow rate and fluid velocity	245
8.6.1.1 Sensitivity of yield flow rate to permeability and viscosity	247
8.6.1.2 Validation of yield flow rate	248
8.6.2 Estimation of detached/produced sand volume	250

8.6.3 Sand volume and rate prediction models	252
8.6.3.1 Sand volume prediction model	252
8.6.3.1 Rate of sand production model	255
8.7 Sand volume and rate model testing	256
8.8 Summary	258
<b>Chapter 9 Field analysis package</b>	<b>259</b>
9.1 Critical Drawdown (CDD) package	259
9.1.1 The Input module	259
9.1.2 The gravel pack completion results module (GP_Comp)	262
9.1.3 The perforation completion results module (Perf_Comp)	263
9.1.4 Using the CDD package	264
9.2 Grain size distribution package	265
9.2.1 Input module	265
9.2.2 Standard deviation module	266
9.2.3 GSD chart module	267
9.2.4 The GSD results module	268
9.2.5 Using the GSD package	269
<b>Chapter 10 Conclusions</b>	<b>270</b>
10.1 Conclusion	270
<b>Chapter 11 Review and recommendations for further studies</b>	<b>272</b>
11.1 Review of work	272
11.2 Recommendations for further work	273
<b>Reference</b>	<b>276</b>
<b>Appendices</b>	<b>295</b>
Appendix A-1 Derivation of tangential stress at $\theta_a = 0^\circ$ and $\theta_a = 90^\circ$	296
Appendix B-1 Grain size for wells C4, C6 and C7	297
Appendix B-2 Grain size for wells C5 and C8	298
Appendix B-3 Grain size for well C10	299
Appendix B-4 Well logs - well C4	300
Appendix B-5 Well logs - well C6	301
Appendix B-6 Well logs - well C7	302
Appendix B-7 Well logs - well C5	303
Appendix B-8 Well logs - well C8	304
Appendix B-9 Well logs - well C10	305
Appendix C-1 Existing UCS models ranking spreadsheet	306

---

## List of figures

Figure 1-1 Concept of change in petrophysical and textural parameters as grain size Distribution changes	4
Figure 2-1 Sand Management flowchart	15
Figure 2-2 A schematic of gravel pack completion	24
Figure 2-3 A wire wrapped screen	25
Figure 2-4 A Pre-packed screen	26
Figure 2-5 A premium screen	26
Figure 2-6 Example of expandable sand screen (ESS)	28
Figure 2-7 ClampOn™ acoustic sand detector	32
Figure 2-8 Positioning of extrusive acoustic system	32
Figure.2-9 A typical processed output of acoustic sand detector showing reducing sand production	33
Figure 2-10 A typical processed output of acoustic sand detector showing increasing sand production	33
Figure 3-1 Correlation between UCS and $d_{50}$	52
Figure 3-2 Correlation between UCS and Sorting	56
Figure 3-3 Various packing arrangements	57
Figure 3-4 Sieve data presentation using histogram	60
Figure 3-5 Sieve data presentation using frequency curve	61
Figure 3-6 Sieve data presentation using arithmetic cumulative curve	61
Figure 3-7 Skewed distributions	64
Figure 3-8 Comparison of the performance of Bergs and Krumbein and Monk equations	70
Figure 4-1 A schematic showing transverse and axial strains	75
Figure 4-2 A typical load versus displacement curve from laboratory UCS determination	83
Figure 4-3 (a) an open ended TWC (b) stress loading in TWC	85
Figure 4-4 a schematic of TWC strength test set up	86
Figure 4-5. The stresses acting on an infinitesimal block within the earth	89
Figure 4-6. The hoop stress around a borehole	92
Figure 4-7 Typical pressure/time record of fracturing	96
Figure 4-8 Mohr-Coulomb failure model	98
Figure 5-1 A neural network schematic	104
Figure 5-2 Mapping function in neural network	105
Figure 5-3 Linear activation function	107
Figure 5-4 Step activation function	108
Figure 5-5 Sigmoid activation function	109
Figure 5-6 Hyperbolic tangent activation function	110
Figure 5-7 Gaussian activation function	110
Figure 5-8 A normal distribution model	115
Figure 6-1 Histogram of gamma ray with normal curve for well C10	126

Figure 6-2 Histogram of squared gamma ray with normal curve for well C10	126
Figure 6-3 Histogram of square root of gamma ray with normal curve for well C10	127
Figure 6-4 Histogram of gamma ray with normal curve for well C10	127
Figure 6-5 Histogram of log of gamma ray with normal curve for well C10	128
Figure 6-6 Scatter plots of natural log of Gamma Ray and natural log of $d_{50}$ for wells C10, C5, C6 and C7	129
Figure 6-7 Scatter plots of natural log of Resistivity and natural log of $d_{50}$ for wells C10, C5, C8 and C7	130
Figure 6-8 Scatter plots of square of Density and natural log of $d_{50}$ for wells C10, C5, C6 and C7	131
Figure 6-9 Scatter plots of square of Sonic and natural log of $d_{50}$ for wells C7 and C8	131
Figure 6-10 Scatter plots Neutron and natural log of $d_{50}$ for wells C5, C7, C6 and C8	132
Figure 6-11 Scree plot of the principal component analysis	134
Figure 6-12 Three-log regression model output compared with measured output	136
Figure 6-13 Four-log regression model output compared with measured output	137
Figure 6-14 Five-log regression model output compared with measured output	138
Figure 6-15 Normal P-P plot of standardized residual $d_{50}$ (natural log) for the 3-log regression model	139
Figure 6-16 Normal P-P plot of standardized residual $d_{50}$ (natural log) for the 4-log regression model	139
Figure 6-17 Normal P-P plot of standardized residual $d_{50}$ (natural log) for the 5-log regression model	140
Figure 6-18 Comparison of the statistical regression model with measured data	146
Figure 6-19 Comparison of analytical model predictions with measured data	150
Figure 6-20 Predictions from the dimensional analysis model	153
Figure 6-21 Topology of the NN used for the first implementation	154
Figure 6-22 NN error versus epoch for the initial training implementation	156
Figure 6-23 Effect of learning rate on NN performance	157
Figure 6-24 Effect of number of hidden layers on NN performance	158
Figure 6-25 Effect of number of neurons in the hidden layer on NN performance	159
Figure 6-26 Topology of NN for the final implementation	160
Figure 6-27 Error versus epoch for the final training implementation	161
Figure 6-28 Comparison of NN predictions with measured data	162
Figure 6-29 Directional median grain size predicted from neural network	165
Figure 6-30 A typical normal probability curve for a range $-4 < t > 4$	167
Figure 6-31 Comparison of standard deviation or sorting predicted using transposed Bergs model with measured data	171
Figure 6-32 Comparison of standard deviation or sorting predicted using transposed Krumbein and Monk model with the measured data	172
Figure 6-33 Example of directional grain size distribution at 1805ft	173
Figure 6-34 Example of directional grain size distribution at 1905ft	174

---

Figure 6-35 Validation of grain size distribution model on well CK-2, sand sequence I-20 at depth 4112ft	175
Figure 6-36 Validation of grain size distribution model on well CK-1A, sand sequence I-25 at depth 3962.33	175
Figure 6-37 Validation of grain size distribution model on well CK-3, sand sequence I-10 at depth 4196.5ft	176
Figure 6-38 Validation of grain size distribution model on well CK-2, sand sequence I-20 at depth 4112ft	176
Figure 7-1 Histogram of Model ranking	185
Figure 7-2 Further evaluation of Sarda et al Model	186
Figure 7-3 Further evaluation of Gavito Model	186
Figure 7.4 Comparison of the dimensional analysis model predictions with measured UCS	191
Figure 7-5. Network error vs. epoch during training	194
Figure 7-6. Network error vs. epoch during validation	194
Figure 7-7 Effect of learning rate on network during training	196
Figure 7-8 Effect of learning rate on network during validation	196
Figure 7-9 Network training using varying no of hidden layers	197
Figure 7-10 Network validation using varying no of hidden layers	198
Figure 7-11 Comparison of network training error for NN with varying no of neurons in the hidden layer	199
Figure 7-12 Comparison of network validation error for NN with varying no of neurons in the hidden layer	199
Figure 7-13 Neural network testing for UCS prediction	201
Figure 7-14 Measured versus predicted UCS from the NN	201
Figure 7-15 Validation of UCS NN model on laboratory data obtained from a Middle East field	203
Figure 8-1 Comparison of CDD model with Abass et al CDD model using a North Sea field data (Field A)	211
Figure 8-2 Correlation coefficients of predicted versus measured CDD for the current model and Abass et al model (Field A)	212
Figure 8-3 Comparison of CDD model with Abass et al CDD model using a North Sea field data (Field B)	213
Figure 8-4 Correlation coefficients of predicted versus measured CDD for the current model and Abass et al model (Field B)	213
Figure 8-5 A linear fit into Hettema et al (2006) data	216
Figure 8-6 CDDc versus depletion at 4675ft	217
Figure 8-7 CDDc versus depletion at 6412ft	217
Figure 8-8 CDDc versus depletion at 4675ft	218
Figure 8-9 CDDc versus depletion at 17000ft	218
Figure 8-10 Case study 1: Change in CDD with time	219

---

---

Figure 8-11 Case study 2: Change in CDD with time	220
Figure 8-12 Comparison of sand production during and before water breakthrough for several North Sea field wells	224
Figure 8-13 Effect of water saturation on oil relative permeability, water relative permeability and fractional flow of water for cases 1, 2 and 3	231
Figure 8-14 effect of water breakthrough on capillary pressure	231
Figure 8-15 Perforation completion schematic	233
Figure 8-16 Effect of perforation length and area on pressure drop	235
Figure 8-17 A cross section of gravel pack completion	239
Figure 8-18 Pressure drop versus area of screen slot openings	240
Figure 8-19 CDD/Depletion vs. time for sand sequence I_25 in well CAK-A8	243
Figure 8-20 CDD/Depletion vs. time for sand sequence II_20 in well CAK-B1	243
Figure 8-21 CDD/Depletion vs. time for sand sequence II_30 in well CAK-B2	244
Figure 8-22 Sensitivity of yield flow rate to permeability	247
Figure 8-23 Sensitivity of yield flow rate to viscosity of flowing fluid	248
Figure 8-24 Comparison of change in yield flow rate at varying critical drawdown CDD	249
Figure 8-25 Plot of sand production versus time (North Sea data)	252
Figure 8-26 Plot of sand production versus time (Niger Delta data)	253
Figure 8-27 Plot of sand production versus time (Gulf of Mexico)	253
Figure 8-28 Plot of sand production versus time (experimental data)	254
Figure 8-29 sand volume and rate predictions from well I	257
Figure 8-30 model sand volume and rate prediction from well II	257
Figure 9-1 Screen shot of CDD input module	262
Figure 9-2 Screen shot of gravel pack completion results module	263
Figure 9-3 Screen shot of perforation completion results module	264
Figure 9-4 Screen shot of GSD input module	266
Figure 9-5 Screen shot of GSD S_deviation module	267
Figure 9-6 Screen shot of GSD chart module	268
Figure 9-7 Screen shot of GSD table module	268

---

## List of tables

Table 2-1 Classification of sand prediction techniques and philosophies	19
Table 2-2 Some sand control and prevention methods and their shortcomings	22
Table 3-1 Various grain size scales	53
Table 3-2 Folk (1974) qualitative descriptions for ranges of values returned by the sorting formulae	55
Table 3-3 Skewness interpretation	64
Table 3-4 Kurtosis interpretation	65
Table 4-1 Static and dynamic elastic properties	77
Table 6-1 Gamma Ray log data transformation - well C10	120
Table 6-2 Resistivity log data transformation - well C10	121
Table 6-3 Neutron log data transformation - well C10	122
Table 6-4 Density log data transformation - well C10	123
Table 6-5 Sonic log data transformation-well C7	124
Table 6-6 Median grain size transformation - well C10	125
Table 6-7 Data transformation optimum functions	126
Table 6.8 Linear correlation coefficients of plots of well log data versus median Grain size	133
Table 6-9 Eigenvalues of the principal component analysis	135
Table 6-10 Summary table for three-log regression analysis	136
Table 6-11 Summary table for four-log regression analysis	137
Table 6-12 Summary table for five-log regression analysis	138
Table 6-13 Parameters exercising control on grain size distribution	140
Table 6-14 The statistical parameters used to assess interrelationship between four variables	142
Table 6-15 The statistical parameters used to assess interrelationship between three variables when porosity is removed	143
Table 6-16 The statistical parameters used to assess interrelationship between variables when packing is removed	143
Table 6-17 The statistical parameters used to assess interrelationship between variables when specific surface area is removed	144
Table 6-18 The statistical parameters used to assess interrelationship between Variable when pore size distributions is removed	144
Table 6-19 Correlation coefficients and p-value for linear correlation evaluation	145
Table 6-20 Summaries of the initial neural network topology	154
Table 6-21 Summaries of the final neural network topology	160
Table 6-22 Error analysis for neural network model	163
Table 6-23 Equations for 1,2,98 and 99 percentiles	168

---

Table 6-24 Error analysis for Bergs equation	171
Table 6-25 Error analysis for Krumbein & Monk equation	172
Table 7-1 Models for UCS prediction	180
Table 7-2 Variables impacting rock formation strength (UCS)	182
Table 7-3 Calculations in UCS model validation	187
Table 7-4 Affiliation of input parameters	192
Table 7-5 Summaries of the neural network topology for UCS modelling	193
Table 7-6 Summaries of the final neural network topology for UCS modelling	200
Table 8-1 Hoek and Brown (1988) estimates of m and s	210
Table 8-2 Results of analysis and testing of preliminary CDDi model with data from Field A	212
Table.8-3 Results of analysis and testing of preliminary CDDi model with data From Field B	214
Table 8-4 Case study 1 well data	220
Table 8-5 Case study 2 well data	221
Table 8-6 Reservoir/well data: case 1	230
Table 8-7 Reservoir/well data: case 2	230
Table 8-8 Reservoir/well data: case 3	230
Table 8-9 Average inner roughness of commercial pipe	240
Table 8-10 Well Data for CDD model validation	242
Table 8-11 Predicted CDD versus measured CDD for a Middle East field	242
Table 8-12 Reservoir data; predicted and measured yield flow rate for a North Sea field	249
Table 8-13 North Sea well data	256
Table 9-1 Input parameters' symbol in CDD package	261
Table 9-2 Input parameters' symbols in GSD package	265

# Nomenclature

The symbol used in this thesis and their definitions are given below:

<b>Symbol</b>	<b>Description</b>
A	Poroelastic constant
a, b, c, d, e, f, g	Tokle et al regression constants
$a_0, a_1$	Constants of Equivalent Plastic strain model
$a_p$	Slichter packing parameter
$A_p$	Flow area of perforation tunnel
$A_{pore}$	Area of pore
$A_g$	Flow area of gravel pack
$A_s$	Area of screen slot opening
B	Formation volume factor
$C_o, UCS, \sigma_{ucs}$	Unconfined Compressive Strength
CBHFP	Critical Bottom Hole Flowing Pressure
$C_b$	Bulk compressibility
CAL	Caliper log
CDD	Critical Drawdown pressure
$C_1$	Cohesion
$C_r$	Rock matrix compressibility
$C_p$	Pore volume compressibility
$C_{pf}$	Final pore volume compressibility
$C_{pi}$	Initial pore volume compressibility
d	Grain size
$d_{25}$	25 <sup>th</sup> percentile
$d_m$	geometric mean grain diameter
$d_{75}$	75 <sup>th</sup> percentile
DT	Sonic Log
$d_{50}$	50 <sup>th</sup> percentile
D	Data point to be normalised
$D_{max}$	Maximum data point within the data set to be normalised
$D_{min}$	Minimum data point within the data set to be normalised
$d_{pore}$	Diameter of pore

---

$d_g$	gravel median size
$d_o$	Density of screen slot opening
$d_s$	Screen diameter
E	Young modulus
ELOT	Extended leak off test
$F_{peak}$	Peak load
$F_c$	Cohesive bond force
$f_w$	Fractional flow of water
G	Shear modulus
GR	Gamma ray log
$G_i$	Constant
GSD	Grain Size Distribution
h	reservoir thickness
I	Normalised value of the data point of interest
ID	Inner diameter
$I_{max}$	Highest end member of the range for a particular transfer
$I_{min}$	Lowest end member of the range for a particular transfer Function
$J_1$	First stress invariance
$J_2$	Octahedral shearing stress
k	parameters related to cohesion
$K_b$	Bulk modulus
$K_T$	Kurtosis
$k_{rw}$	Relative water permeability
$k_{ro}$	Relative oil permeability
$K_{rd}$	Ratio of roughness to diameter
$L_i$	First invariant of stress tensor
LOT	Leak off test
$L_g$	Length/thickness of gravel pack
$L_p$	length of perforation
M	Mean
m, s	Hoek constant
N	Peak strength parameters related to angle of internal friction
$N_r$	Residual strength parameters related to angle of internal friction
NPHI	Neutron log
OD	Outer diameter

---

---

$P_i(t)$	Constant pore pressure around well (at time t)
$P(\infty, t)$	Far field (reservoir) pore pressure (at time t)
$P_r$	Reservoir pressure
P	Pore Pressure
$P_{mud}$	Mud column pressure
$P_p$	Pore pressure
phi	Equivalent grain size in phi unit
$\Delta P$	Change in pressure
$P_b$	Breakdown pressure
$P_{ri}$	Initial reservoir pressure
$P_{rc}$	Current reservoir pressure
$P_{gc}$	Total pressure drop in gravel pack completion
$p_f$	Reservoir far field pressure
$\Delta P_c$	Capillary pressure
$\Delta P_{OH}$	Pressure drop in open hole completion
$\Delta P_s$	Pressure drop through screen slot opening
$\Delta P_g$	Pressure drop through gravel pack completion
$\Delta P_B$	Pressure drop through a section of perforation
$q$	Flow rate
$q_y$	Yield flow rate
$q_T$	Total fluid rate from reservoir
$r_p$	Plastic radius
$r_{cp}$	Radius of cavity
$r_w$	Wellbore radius
$r_o$	Radius of outer boundary
$r_e$	Radius of elastic boundary
RHOB	Density log
$R_s$	Rate of sand production
$r_g$	Radius of grain particle
$r_e$	reservoir drainage radius
$R_e$	Renold Number
ROK	Rock
$S_o$	Peak strength parameters related to cohesion

---

---

$S_{ro}$	Residual strength parameters related cohesion
SK	Skewness
$S_A$	Grain surface area
$s_o$	Oil saturation
SPF	Shots per foot
$s_w$	water saturation
(t)	Time
TWC	Thick Walled Cylinder strength
T	Trask sorting coefficient
$t_s$	Shear transit time
t	Time
$t_c$	Compressional transit time
$v_r$	Velocity of propagation of ultrasonic pulse
$\Delta V$	Change in volume
$V_o$	Initial volume
$V_{cp}$	Critical particle velocity
$V_p$	Pore volume
$V_{pi}$	Initial pore volume
$V_s$	Volume of sand production
$V_{pf}$	Final pore volume
YFR	Yield Flow Rate

**Greek symbol****description**

$\alpha$	Biot constant
$\beta$	High velocity coefficient
$\beta_1$	Constant of linearity
$\epsilon_e$	Effective strain
$\epsilon_{11}^p, \epsilon_{22}^p, \epsilon_{33}^p$	Directional plastic stain
$\epsilon_e^p$	Effective or equivalent plastic strain
$\epsilon_{\alpha}^p$	Tangential plastic strain
$d\epsilon$	Change in strain
$\epsilon_y$	Strain in y direction
$\epsilon_x$	Strain in x direction

---

$\varepsilon$	Elastic strain
$\varepsilon_v$	Volumetric strain
$\varepsilon_s$	Screen slot openings
$\theta$	Angle of internal friction
$\theta_a$	Well Azimuth
$\theta_c$	Contact angle
$\lambda_n$	Factor for non-uniform particle size effects
$\mu_e$	Radial displacement in elastic zone
$\nu$	Poisson ratio
$\rho_b$	Bulk density
$\rho_g$	Density of grain particle
$\rho_{\log}$	Density read off bulk density log
$\rho_f$	Fluid density
$\sigma'_h$	Effective minimum horizontal stress
$\sigma_1$	Maximum stress
$\sigma_3$	Minimum stress
$\sigma_x, \sigma_y, \sigma_z$	Principal stresses
$\sigma_{OB}$	Overburden stress
$\sigma_{z_{eff}}$	Effective overburden stress
$\sigma_{\theta_{eff}}$	Effective tangential stress
$\sigma_{r_{eff}}$	Effective radial stress
$\sigma_{11}, \sigma_{22}, \sigma_{33}$	Directional stress
$\sigma_\theta$	Tangential stress
$\sigma_r$	Radial stress
$\sigma_{rc}$	Total radial stress at elastic-plastic boundary
$\sigma_{ri}$	Total radial stress at cavity surface
$\sigma_{ro}$	Total radial stress at outer boundary
$\sigma_{gs}$	Folk graphic standard deviation
$\sigma_\phi$	Standard deviation or sorting

---

---

$d\sigma$	Change in stress
$\sigma_o$	Constant
$\sigma_T$	Tensile strength
$\sigma_H$	Maximum horizontal stress
$\sigma_h$	Minimum horizontal stress
$\sigma_v$	Vertical stress
$\sigma_f$	Normal stress at failure
$\sigma_n$	Normal stress
$\sigma_{\text{int}}$	Interfacial tension
$\sigma_{\text{var}}$	Variance
$\tau$	Shear stress
$\tau_{xz}$	stress in xz direction
$\tau_{xy}$	stress in xy direction
$\tau_{zx}$	stress in zx direction
$\tau_{zy}$	stress in zy direction
$\tau_{yz}$	stress in yz direction
$\tau_{yx}$	stress in yx direction
$\tau_o$	Cohesive strength
$\tau_{r\theta}$	Tangential radial stress
$\tau_f$	Shear stress at failure
$\phi_{84}$	phi 84
$\phi_{16}$	Phi 16
$\phi_{95}$	Phi 95
$\phi_5$	phi 5
$\phi_{50}$	phi 50
$\phi$	Porosity
$\phi_f$	Final porosity
$\phi_i$	Initial porosity
$\phi_g$	Gravel porosity

---

$\omega$	Parameters related to the internal friction angle
$\varpi$	Parameter that controls steepness of sigmoid function

# CHAPTER ONE

## Introduction

### 1.1 Background

More than 70% of the world oil and gas are domiciled in unconsolidated clastic reservoir rocks with a high risk of sand production<sup>1</sup>. Even though oil and gas production from well consolidated clastic rocks does not pose as much sand production risk, they are however also prone to failure if a well articulated sand management strategy is not in place to deal with the problem at the onset of field development.

Besides, the circumstances of oil and gas exploration and production, which have led to reduced oil production; and the astronomical global demand for fossil-based energy, occasioned by the increased energy demand from developing and developed economies, have created an imbalance in demand and supply situation. This has consequently forced the industry to move exploration and production operations into harsh and hitherto unattractive environments such as deep offshore, subsea and high pressure and high temperature (HPHT) fields and marginal fields to increase oil production to at least match the astronomically growing demand. New enhanced recovery technologies are also being developed to get more hydrocarbon from already matured reservoirs. The typical characteristics of these fields and reservoirs include high depletion rate, high rock instability and high degree of non-consolidation. These characteristics, no doubt, favour production of sand, which undoubtedly has serious safety and cost implications. Operations in sand prone fields will therefore require deployment of cheap but yet versatile technologies to arrest problems that may arise from sand production and make their operations profitable.

Sand prediction is an element of sand management strategy that involves the evaluation of risk of sand failure/production and the prediction of the likely sand rate and volume to facilitate optimum design of both downhole

---

and surface equipment especially as related to sand control. The most important and critical parameter that has been used to evaluate the risk of sand failure in the industry is mechanical strength<sup>2,3,4</sup>; this is mostly characterised by the angle of internal friction, shear strength and Unconfined Compressive Strength (UCS). Laboratory tests on cores and use of mechanical properties logs are the two most "versatile" techniques available to the industry to acquire information about mechanical strength for the purpose of geomechanical characterisation. However, laboratory test is currently not popular because of scarcity of cores – the test material. This is as a result of dwindling interest in core acquisition due to prohibitive costs and high risk factor with regard to the present field development environment. Mechanical properties log technique which is readily available, easy and probably cheap has also got its own shortcomings, which render it unreliable; among its shortcomings are inapplicability in some fields due to non-consolidation and high clay content and uncertainty that usually surrounds its results.

The two techniques outlined above are the basis for the many sand prediction models currently being used in the oil and gas industry for sand production prediction. Since the underlying processes and information input to these models have been proved to be fraught with errors, it is only logical to expect unreliable results from them.

The most critical setback however of the current sand prediction models in the industry is that they are static i.e. can only predict sanding potential for the initial field development prior to drilling; they also cannot predict the corresponding sand production volume as a function of time. However, sanding potential predictions made prior to drilling a well cannot be said to be valid during or after drilling and during production operations. It is therefore appropriate to evolve a dynamic method, which is capable of real time sand prediction at any time - from pre-drilling to abandonment – during the life of a field. Real time prediction holds a lot of promises for the oil and gas industry. Ability to predict if, when and how much sand will be produced is very crucial to optimum design of both surface and downhole equipment and facilities.

---

Apart from the foregoing issues, sanding in this present work is also considered a life cycle problem, which changes with time throughout the entire life of a field due to constraints imposed, by operational, drilling production and stimulation factors such as production rate, bean-up pattern, water/gas injection, water breakthrough, fracturing for stimulation etc. This change can be tracked during the field life through a real time programme of data acquisition of formation textural and petrophysical parameters. The reservoir rock formation strength is the most important factor which determines the movement of the rock formation within the failure envelope space, and hence its sand production potential. Strength of formation rock is known to strongly correlate with textural and petrophysical parameters such as porosity, packing, sorting and grain size. The schematic in figure 1-1 illustrates the concept of change in some of these parameters with time. Sorting and grain size in particular characterise the grain size distribution of a formation, which is expected to change during production, especially in sand producers. The change in grain size distribution together with depletion may cause corresponding change in the strength profile of the formation rock. It is therefore possible to relate the initial undisturbed rock strength and subsequent strength profile due to production with the grain size distribution profile. Not only is this relationship utilisable for real time prediction of sanding potential, it also creates the ability to measure grain size distribution of the produced sand. This then makes it possible to compare the formation grain size distribution with that of the produced sand with a view to making scientific inferences about the origin of the sand.

The importance of real time sanding prediction is underlined by changes in reservoir pressure due to depletion and water/gas breakthrough, both of which affect formation rock strength and the potential for sand production. Real time sanding prediction results are therefore very crucial to making decisions regarding the type and design of sand control method or installation to be used and the timing of the sand control application. For example it could be used to decide whether to gravel pack a certain pay section of the reservoir or not and to select an optimum gravel size in

case there is a need for gravel packing. Sand prediction therefore enables timely decision on the sand control methods or techniques; this of course has an economic dimension as premature installation of sand control increases early investment and reduces unnecessarily the well productivity. The results of sand prediction are also important inputs in sand production monitoring and topside management.

As a result of the complex cross-relationship between grain size distribution, other textural parameters and formation strength, neural networks have been used to resolve the relationship. Oyenehin and Faga (1999)<sup>5</sup> have reported the use of a commercial neural network for grain size distribution prediction directly from log parameters; they opted for neural network on the basis of its ability to resolve the complex relationship between these parameters. The present work builds upon Oyenehin and Faga (1999)<sup>5</sup> work by using a special C++-coded neural network for predicting grain size distribution in both horizontal and vertical orientation and extending the application to the prediction of strength and sanding potential.

This research is therefore aimed at developing an entirely new robust method of sand prediction, which utilises the perfect relationship between grain size distribution and rock strength.

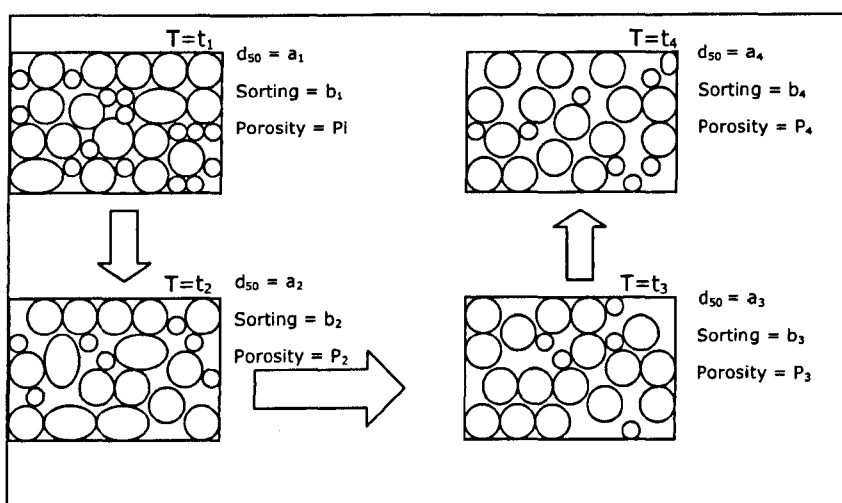


Figure 1-1 Concept of change in petrophysical and textural parameters as grain size distribution changes

### **1.1.1 Research Objectives**

As earlier emphasised, the aim of this research is to develop a real -time model which is capable of predicting grain size profiles and potentials for sand production in a well or reservoir right from spudding through all developmental operations of drilling, completion and production to abandonment. The objectives include the following:

- Development of a customised neural network system for clastic reservoir grain size profiling.
- Development of a model for predicting sand production volume and rate
- Identification of appropriate conventional log suites as well as production log suites which can be used to develop real time grain size profiles of typical reservoir sands.
- Establishment of the relationship between changes in grain size profiles and failure envelope of typical reservoir sands in real time.
- Development of failure criteria and failure envelope for typical reservoir sand failure analysis.
- Development of appropriate professional analysis package cum interface system for field application.
- Showing and demonstrating that a coded neural network will perform better in predicting sanding potential than a commercial neural network.

## **1.2 Research Methodology/Approach**

This section gives an overview of initial approach, theories and procedures employed in these studies. Theories and procedures employed in the studies include the general empirical and theoretical relationship/correlation between petrophysical parameters and strength parameters.

---

Petrophysical, textural and compositional and strength information of any field or reservoir formation are known to be embedded in logs and drilling data. An array of pre-drilling, drilling and production data of a typical well/field is gathered. Pre-drilling data are data from exploratory or appraisal drilling in the target field or reservoir/rock formation; drilling data include LWD tools like sonic, density, gamma, resistivity and neutron; while production data are those from PLT tools. These logs are essentially used for the derivation of petrophysical, textural and geomechanical parameters, which are in turn used for the estimation of strength parameters via a neural network model and prediction of grain-size profiles of reservoir rocks using the correlations that exist between them.

The general basis for this is the plethora of empirical, analytical and theoretical models, which suggest cross correlations between textural petrophysical and geomechanical properties of clastic reservoir rocks.

Construction of continuous grain size and strength profiles across a formation is possible from these logs and this has the potential to facilitate the establishment of a relationship/correlation between changes in grain-size profiles and strength parameters. This relationship is then used to determine both quantitatively and qualitatively how changes in grain size profiles impact rock strength. Development of failure criteria and failure envelope of reservoir sands prior to drilling, during drilling and during production, and perhaps during other various developmental operations on the field/well, which may impact the strength of the reservoir rocks, is also made possible. The linkage between failure envelope and/or strength of a typical reservoir rock and grain size distribution is then used at any stage of field operation from spudding to abandonment to predict failure and thus sanding in reservoir formation. At the onset of continuous sand production during production operation, it is expected that the grain size profiles of the reservoir formation will continuously change and so will the strength profile. Sand production monitoring during production operation is therefore considered critical to the evaluation of changes in grain size profiles across the reservoir formation. Sand production monitoring tools currently available are

therefore identified and employed. These tools are used to constantly evaluate the changes in grain-size profiles as a function of the produced sands and their impact on the strength of the residual sands.

In developing models for both Unconfined Compressive Strength (UCS) and Grain Size Distribution, many modelling techniques (analytical and dimensional analysis) were adopted and compared with Neural Network. However in the development of Critical Drawdown (CDD) failure model for sanding potential prediction, an existing failure criterion was adopted, and simple yet elaborate mathematical and analytical solutions of the adopted failure criterion carried out.

Appropriate neural network type and architecture are identified, trained with appropriate integrated data from this sequence of studies and consequently utilised for real-time sanding potential prediction. In neural network modelling, data inputs to the networks were processed by transformation via various mathematical functions to make their distribution normal. The processed input data into the network and the output from the network were also normalised using various formulae; this was to ensure that they fall within a range of 0 – 1 recognised by the sigmoid transfer function of the Neural Network.

The models reported in this work - grain size distribution (GSD) model, strength (UCS) model and the critical drawdown (CDD) model - have been tested and validated within the limits of available experimental and field data. The testing and validation have shown promising results.

### **1.3 Contributions to knowledge**

In this section the original contribution these research studies have made to the body of knowledge in the specialist areas of neural network modelling, grain size distribution studies and sand prediction are discussed.

Neural network is a data-mining tool, which has been used extensively in the oil and gas engineering as well as in other branches of engineering to

---

solve complex engineering and design problems. However its use, especially with respect to grain size distribution prediction, has been limited to commercially packaged ones (e.g. Oyenehin and Faga 1999<sup>5</sup>), whose shortcomings have been detailed in these studies. These studies have, as a result of this, identified specially coded neural network as a way of dealing with the problem posed by the commercial neural network. Consequently a neural network is coded in C++ for the neural network modelling aspect of this work.

In predicting grain size distribution of a reservoir rock in real time the precursor of this work used a number of log parameters such as Sonic log interval transit time, Gamma ray log hydrogen counts and density log bulk density, as inputs to a multi output multilayer neural network, representing a complex topology. These studies have been able to identify the problems inherent in complex neural network topology and have therefore come up with a new novel NN approach, which integrates statistical and neural network methods to predict grain size distribution in real time. In addition, the studies have made prediction of orientational grain size distribution in x- and y-plane possible.

Before now, real time integrated sand prediction – prediction of onset of failure, movement of sand and sand volume/rate - has not been possible. In these studies integrated models for accomplishing these prediction tasks have been developed.

In addition, the relationship between grain size distribution and unconfined compressive strength (UCS) has been utilised to predict change in reservoir rock strength and then extended to the prediction of sanding potential in real time. The utilisation of this unique relationship is original to this work, as it has not been used before in any work.

In summary, this work has made the following contributions to knowledge:

- Application of specially coded neural network in grain size and strength modelling
- Integration of neural network and statistical methods for modelling
- Integrated real time sand production prediction

- 
- Grain size distribution prediction in both vertical and horizontal orientation
  - Application of grain size distribution in strength and sand production prediction

## **1.4 Thesis Layout/Arrangement.**

In this section, a general overview of the layout of the thesis, wherein the underlying theories and results of these research studies are detailed, is given. The aim of this is to give a first hand picture of the ideas being put forward in each chapter and a general summary of the whole thesis.

The entire thesis is generally divided into three broad sections: chapters, appendices and references. There are eleven chapters overall.

Chapter one is a general introduction of the engineering problems the research is out to solve, how the problems have been solved or difficult to solve in the past and the approach or methodologies that these studies have fashioned out to solve these problems. It also details the research aim and objectives as well as the achievements of the research studies in relation to these aim and objectives. Chapter two introduces the concept of sand production and management and gives a deep insight into all aspects of sand management with particular emphasis on sand prediction. It also touches briefly on the influence of sanding potential on field operations. Chapter three gives a logical insight into the underlying theories and concepts driving the ultimate aim of this research studies. This chapter also reviews all the existing methods of analysing grain size distribution of a typical reservoir rock.

Chapter four gives a general overview of the geomechanical characteristics and failure evaluation of a typical reservoir rock. Chapter five provides the underlying theories of neural network, justifying the preference for it over other data mining methods. It also discusses the diverse applications of neural network and the procedure for data preparation for this work. In chapter six, results of grain size distribution

modelling using different modelling techniques and their comparative analysis are presented. Also presented in this chapter are the results of the model validation.

Chapter seven presents the results of ranking of existing models for predicting Unconfined Compressive Strength (UCS). It also gives the results of comparative studies of neural network and dimensional analysis techniques for UCS modelling and the subsequent neural network model. In addition, it also presents the results of the neural network based UCS model validation. Chapter eight presents the developed sanding potential and sand volume prediction models including their validation. It also presents the models development and development approach; the effects of certain operational parameters on the failure envelope and hence sanding tendencies are also discussed. Chapter nine presents two different excel-based field analysis packages - Grain Size Distribution (GSD) predictor and Critical Drawdown (CDD) predictor. These are based on the various models developed in this work. In chapter ten, the conclusions of the research studies are presented whilst in chapter eleven the review of the entire work and recommendations for further studies are presented.

## Chapter 2

### Sand production and management concepts

This chapter reviews the concepts of sand production and management. It particularly focuses on an extensive discussion of what constitutes sand management with particular attention to sanding potential in the light of new approaches and concepts that have been introduced in the recent years. It attempts to give a detailed analysis of the current most widely used sand production definitions and to present a more acceptable definition which takes into account all processes that usually lead to sand production. Also reviewed are the conventional methods of sand control including downhole screen and screenless completions. The influence of sanding potential on field operational activities such as drilling, well completions, oil production and production facility design is also discussed.

#### 2.1 Sand production: a definition

Sand production has come to be defined in many different ways by different workers and industry experts. These varying definitions essentially reflect the varying approaches that have been utilised in the industry to manage and mitigate sand production.

Some workers have erroneously defined sand production as the failure of sand either in tension or compression without having regard to whether the hydrodynamic force of the flowing fluid in the reservoir or in the production strings is enough to detach the failed sands from the sandface. Yet another common definition of sand production is given by Fjaer E. et al. (2006)<sup>6</sup> as the production of small or large amounts of solids together with the reservoir fluid. This definition also does not take into account the need for the sand to fail before they are produced to the surface; it is therefore also considered incomplete.

---

Recent consensus in the industry has recognised the need for a complete all-inclusive definition of sand production to allow for a common well-defined strategy in dealing with the risks of sand production. In line with this, sand production in this work is defined as the shear or tensile failure of reservoir rocks, the detachment of the failed regions from the sandface by the hydrodynamic force of the flowing reservoir fluid and the subsequent suspension and transport of the sand to the surface via the production line.

Sand production from the reservoir is always an undesirable phenomenon because of its many undesirable problems some of which are stated here:

- Reduction of production rate<sup>7</sup>
- Corrosion of pipelines and other facilities<sup>6 & 7</sup>
- Instability of the wellbore and the production cavities<sup>1</sup>
- Casing collapse
- Erosion of production strings and flow lines
- Environmental issues relating to sand handling at rig sites
- Cost issues relating to huge sand disposal

However, the sand management paradigm for heavy oil<sup>8 & 9</sup> and asphalt production, as well as low PI wells<sup>10 & 11</sup> have proved that sand production may be beneficial especially in terms of production rate enhancement<sup>8</sup>.

## 2.2 Sand management

Sand management is a broader term used to describe the strategies usually employed in the industry to deal with sand issues. These strategies may include, but not limited to the following<sup>12</sup>:

- Models to predict sand production tendencies
- Field techniques to prevent formation failure

- 
- Downhole equipment to prevent failed formation materials from entering the well bore
  - Best practices for installing completion to maximize productivity
  - Monitoring techniques to determine when sand is produced
  - Surface equipment for handling produced sand
  - Workover equipment for perforating remedial operations

Inherent rock characteristics, operational and economic factors often dictate which strategy will be used among these.

Tronvoll et al. (2001)<sup>9</sup> defined sand management as an operating concept where traditional sand control means are not normally applied and production is managed through monitoring and control of well pressures, fluid rates and sand influx. This definition presupposes that only sand prediction is the only operational activity carried out in sand management; and that sand prediction and sand management are the same. This is however not true given the operational strategies in current use in the industry to manage sand issues as published by some earlier and later workers<sup>8, 12-13</sup>. Mathis, S. P. (2003)<sup>12</sup> gave one of the most complete, widely accepted, all-embracing definitions of sand management; he defined sand management as all technologies, processes, and completion techniques that are meant to address the issue of producing fluids from weak formations.

Sand management is the industry response to the need for effective proactive management of production from weak as well as consolidated clastic reservoir. The ultimate aim of any sand management strategy is production optimisation and cost reduction. Sand management strategies may be grouped under four broad headings viz:

- Sand prediction
- Sand control
- Topside management
- Sand monitoring

These broad groupings will be discussed in detail in the following sections. Figure 2-1 is the sand management flowchart showing the links between its various aspects.

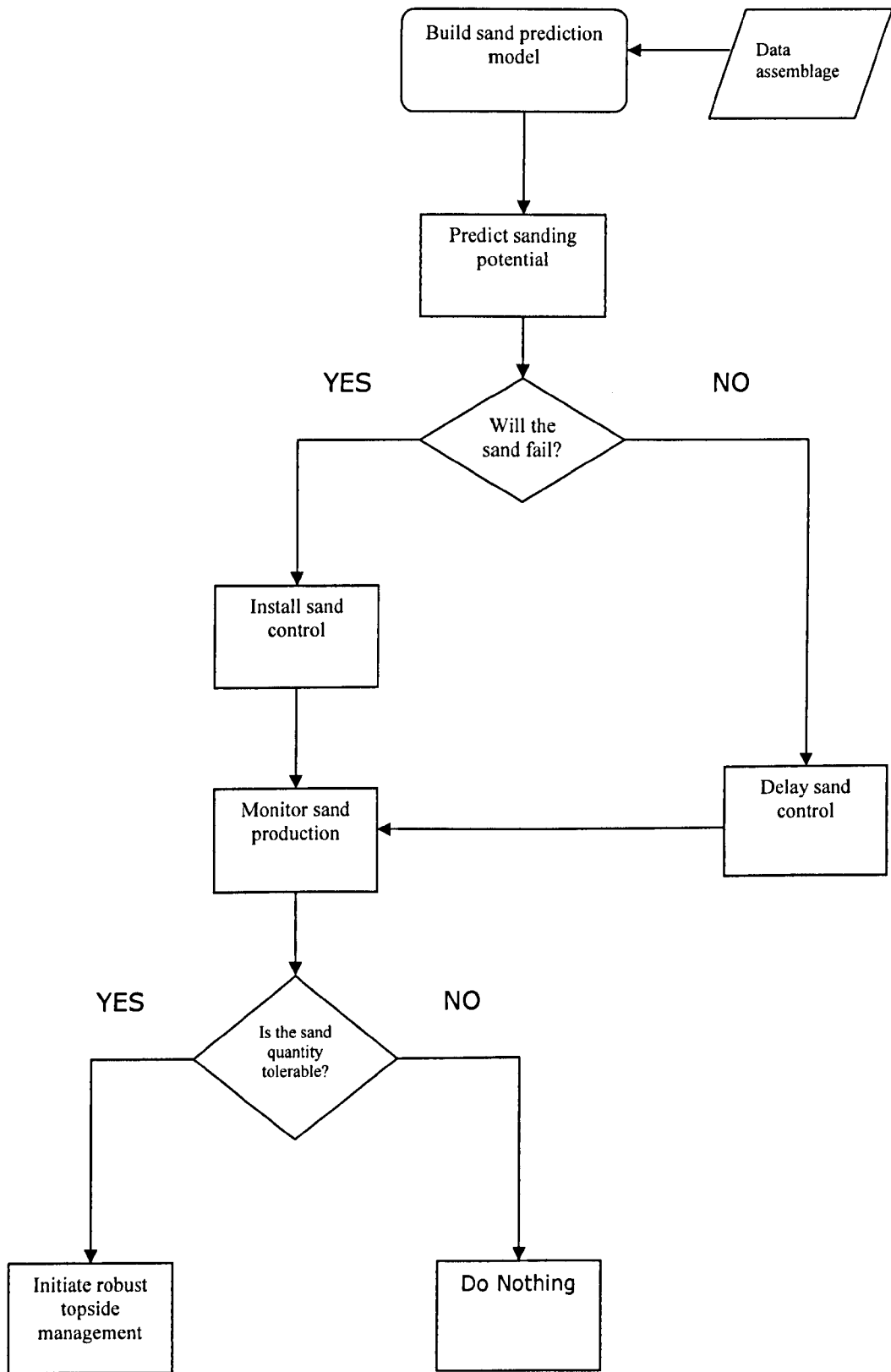


Fig. 2-1 Sand Management flowchart

---

### 2.2.1 Sand prediction

Sand prediction is the first in the series of activities in sand management and is the key to effective overall sand management. It is often aimed at quantifying the risks of sand failure. Recent advances in sand prediction studies have identified the added advantage of coupling the failure prediction to time for real time prediction<sup>14 & 15</sup>.

Conventional sand prediction techniques in the petroleum industry today are based on field observation and experience, laboratory sand production experiments and theoretical or numerical modelling<sup>16</sup>. Only recently neural network based technique evolved through the work of Kanj and Abousleima<sup>17</sup>.

Techniques based on field observation and experience usually attempt to establish a correlation using multi-variable linear regression between the data collected from a sand producing well and operational and field parameters relating to formation, completion and production e.g. strength, flow rate, drawdown etc. These correlations are usually established with a small selection from the vast assemblage of parameters that could possibly affect sand production. Some of them use one parameter, some two and some many, for example Stein and Hilchie (1972)<sup>18</sup> and Stein et al. (1974)<sup>19</sup> correlated sand production from the reservoir with production rate, neglecting the effects of other parameters that affect sand production.

Operational parameters (for example bean-up pattern, flow rate and drawdown) affecting sand production are known to be many and to vary from field to field. Using just a small selection of these parameters and extrapolating the results from one field to another may give inaccurate sand production prediction.

Techniques based on laboratory sand production experiments involve observation and simulation of sand production in controlled laboratory environments. These experiments have suggested that sand production in unconsolidated sandstone is caused by the flow rate and capillary forces<sup>20</sup> while in friable-consolidated sandstone, by boundary stress<sup>21</sup>.

---

Laboratory sand production experiments are usually performed on cores. The great setback of this technique is the fact that most wells are not cored, meaning that cores are not always available. Even when they are available, they may be affected adversely during retrieval, transportation and processing by a number of factors e.g. core damage, stress relief etc. All these add to the degree of uncertainty surrounding the results of laboratory sand production. Extrapolating these results to field conditions may also represent a source of error.

Techniques based on theoretical modelling suggest compressive failure, tensile failure and erosion as mechanisms responsible for sand production<sup>22-27</sup>. Theoretical modelling also suggests that compressive failure can be triggered by both far-field stresses (depletion) and drawdown pressure; and tensile failure, exclusively by drawdown. Erosion is believed to occur when the drag forces exerted on a particle at the sand face exceed its apparent cohesion. However, theoretical modelling requires a mathematical approach to failure mechanisms<sup>16</sup> and relies heavily on log-derived geomechanical parameters.

A plethora of theoretical model for sand prediction exists in the oil and gas industry. Drucker-Prager model proposed by Atheunis et al (1976)<sup>23</sup> was based on the intact rock compressive strength, drawdown and in-situ stress. A model developed by Bratli and Risnes (1979)<sup>28</sup> and Risnes and Bratli (1981)<sup>27</sup> was based on the comparison of flow-induced pressure gradient with the residual strength of disaggregated material surrounding the borehole and perforation. Morita et al (1989)<sup>26</sup> proposed a conceptual model of sand production prediction based on the compressive (shear) failure, induced by a combination of in-situ stresses and drawdown, and by tensile failure induced by the near-cavity pore pressure. Van den Hoek et al. (2000)<sup>29</sup> proposed a theoretical model, which based failure of sands on the size of cavity rather than the effect of in-situ stresses, drawdown and pore pressure.

However the uncertainty in the formation strength from log-derived parameter affects the reliability of theoretical modelling. Estimating formation strength from the mechanical properties log may be inapplicable in some fields due to non-consolidation and high clay content<sup>30</sup>. Often

times these models are not validated with field sand production data, their results, in these circumstances, can best be described as qualitative.

Neural network based sand prediction was first reported by Kanj and Abousleiman (1999)<sup>17</sup>. Parameters that were thought to affect production of sand in a gas well were presented to a feedforward backpropagation network (BPN) and a generalized regression neural network (GRNN) to predict important sanding indication parameters (SIP) for the gas wells of Northern Adriatic Basin. It was concluded that neural network proved capable of predicting sanding potentials with an unprecedented level of accuracy.

However the presentation of many input parameters to the network is capable of increasing the network complexity due to increased network size<sup>14</sup>. This may have a negative performance impact on the ability of the network to predict sanding potential accurately. In addition, one of the input data to the network - formation cohesive strength - can only be obtained using Mohr circles. Generation of Mohr circles is heavily dependent on core acquisition; this therefore does not allow for real time sanding potential prediction.

Table 2-1 is the summary of the classification of all sand prediction techniques, their driving philosophies or principles and the workers who have either put them forward or have used them. The underlying principles and application of a select few under each technique category are discussed further in section 2.3

<b>Table 2-1 Classification of sand prediction techniques and philosophies</b>		
<b>Prediction techniques</b>	<b>Philosophy/Principles</b>	<b>References</b>
Field observation	Correlation between sand production well data and field/operational parameters is established	Stein and Hilchie (1972) <sup>18</sup> Stein et al. (1974) <sup>19</sup>
Laboratory sand production experiments	Sand production experiments are carried out under controlled conditions in the laboratory.	Vriezen et al (1975) <sup>21</sup> ; Hall & Harrisberger (1970) <sup>20</sup>
Theoretical modelling	Mathematical formulations of sand failure mechanisms are required. These formulations have been made based on some intrinsic strength properties of wellbore and surrounding rocks.	Antheunis et al. (1976) <sup>23</sup> ; Coates & Denoo (1981) <sup>24</sup> ; Morita et al. (1989) <sup>26</sup> ; Geertsma (1985) <sup>25</sup> ; Risnes & Bratli (1981) <sup>27</sup> ; Van den Hoek et al. (2000) <sup>29</sup>
Neural Network	BPNN & GRNN were used to predict important sanding indication parameters (SIP) for gas wells of the Northern Adriatic Basin.	Kanj and Abousleiman (1999) <sup>17</sup>

## 2.2.2 Sand control

Sand control is considered second in the series of sand management activities. It constitutes all the technologies, processes, procedures methods or installations by which sand coming through or with the potential to come through with the produced fluid from a failed or dilated sand reservoir are either contained or stabilised through consolidation within the reservoir or prevented from migrating into the wellbore or near-wellbore area. Restriction of production on the basis of the knowledge of expected failure time or maximum fluid production rate that can cause failed sand fluidization can also be classified as a sand control method. The overall goal of sand control is exclusion of failed sand likely to be produced with the reservoir fluids.

Sand control techniques are many, but they are generally grouped into four broad categories<sup>30</sup> based on their governing principles, application procedures and characteristic features. The four categories are:

1. Mechanical Methods
2. Chemical consolidation methods
3. Combination methods
4. Production Restriction methods

Sand control techniques under the first three categories usually provide some means of mechanical support for the reservoir formation helping to prevent formation movement during stress loading whilst the last one is purely operational in nature<sup>30</sup>. Cole and Ross (1998)<sup>30</sup> recommended that selection of any sand control methods should be based on the knowledge of four key parameters: economics, historical success, applicability and length of service. However the mechanical methods are the most widely used sand exclusion method.

Mechanical methods are diverse and consist of mechanical devices installed downhole with the sole purpose of preventing the produced sand from entering the wellbore with the produced reservoir fluid.

Of great importance to sand control is the concept of sand prevention. Sand prevention involves deployment of some completion strategies for example selective perforation in formation with a risk of sand production with a view to conserving the formation strength and preventing sand production.

Table 2-2<sup>9</sup> shows some of the most widely used mechanical sand control and prevention methods and their shortcomings. A few of them will be discussed in brief in the following sections.

However many of the sand control and prevention methods have their own downside, the most important of which is introduction of skin into the formation and the consequent production reduction. The cause of the skin or damage has been recognised<sup>31</sup>, especially for gravel pack sand control completion, to be the effects of pressure loss due to non-darcy or turbulent flow around the wellbore and the inherent skin due to the gravel placement.

**Table 2-2 Some sand control and prevention methods and their shortcomings (After Tronvoll, J et al (2001)<sup>9</sup>)**

No	Control and prevention methods	Shortcomings
1	Screens, slotted liners, special filters	<ul style="list-style-type: none"> <li>• Lack of zonal isolation</li> <li>• High placement and workover costs</li> <li>• Plugging and screens collapse</li> <li>• Screen erosion</li> </ul>
2	Inside casing gravel packing	<ul style="list-style-type: none"> <li>• PI reduction</li> <li>• Placement and workover difficulty</li> <li>• High cost of installation</li> <li>• Positive skin development</li> </ul>
3	Open hole gravel packing	<ul style="list-style-type: none"> <li>• PI reduction</li> <li>• Complexity of operation</li> <li>• Necessity for extensive under-reaming in most cases</li> <li>• Costs of installation</li> </ul>
4	Propped fracturing, including Frac pack stress pack, and use of resin coated sand	<ul style="list-style-type: none"> <li>• Risks of tip screen out during installation</li> <li>• Directional control and tortuosity issues (in inclined wells)</li> <li>• Fracture containment control</li> <li>• Proppant flow-back on production</li> </ul>
5	Selective perforating	<ul style="list-style-type: none"> <li>• Problematic in relatively homogeneous formation</li> <li>• Need for formation strength data</li> </ul>
6	Chemical Consolidation	<ul style="list-style-type: none"> <li>• Some permeability reduction</li> <li>• Placement and reliability issues</li> <li>• Short intervals only</li> </ul>
7	Oriented perforating	<ul style="list-style-type: none"> <li>• Necessity for full stress mapping</li> <li>• Theoretical analysis required</li> <li>• Perforation tool orientation</li> <li>• Little field validation available</li> </ul>

---

### 2.2.2.1 Gravel packs sand control completion

Gravel pack completion is a mechanical sand exclusion method and is the most common of all sand exclusion methods. It entails placing a screen in the well across the face of the producing zone. High permeability gravel pack sand is then used to fill the annulus between the screen and the sand face. The sand pack is usually circulated into the screen-sandface annulus in a carrier fluid.

Selection of the pack sand is very crucial to the success of gravel pack completion in preventing formation sand from entering the wellbore. Cole & Ross (1998)<sup>30</sup> recommended that the sand size should be quality-controlled by sieving so that a proper formation sand-to-pack sand size ratio can be maintained and absolute formation permeability near wellbore is not reduced. Various pack sand-formation sand size ratios have been suggested. Earlier workers<sup>32-34</sup> suggested a size ratio of 4 - 10 times  $d_{10}$  of the formation size. However, Britt (2000)<sup>35</sup> reported that this sizing ratio resulted in the failure of many gravel packs. A new gravel size criterion was consequently developed by Saucier, R. J. (1974)<sup>36</sup>. The criterion recommended pack sand sizes of 5 - 6 times  $d_{50}$  of formation sand. A recent work<sup>37</sup> suggests that this criterion performs better in well sorted sands.

The general limitation of the pack sand size sizing criteria is that they do not consider the effect of sorting in pack sand selection. Oyeneyin et al (1992)<sup>38</sup> have shown that sorting of both the pack sand and the formation sand could influence the performance of gravel pack completion.

Failure to integrate formation sorting effects into the sizing formulae for sand packs may result in fine contamination<sup>39</sup> within the pack sand, blocking screen openings, and causing formation damage and additional pressure loss in the system. The consequence of this is of course reduced productivity. However despite the shortcomings of all the gravel pack design criteria, Saucier criteria has been used for the design of more than 90% of the gravel packs operation in the oil and gas industry. The

criterion is however often adjusted especially for poorly sorted sand. A schematic of gravel pack completion is shown in figure. 2-2.

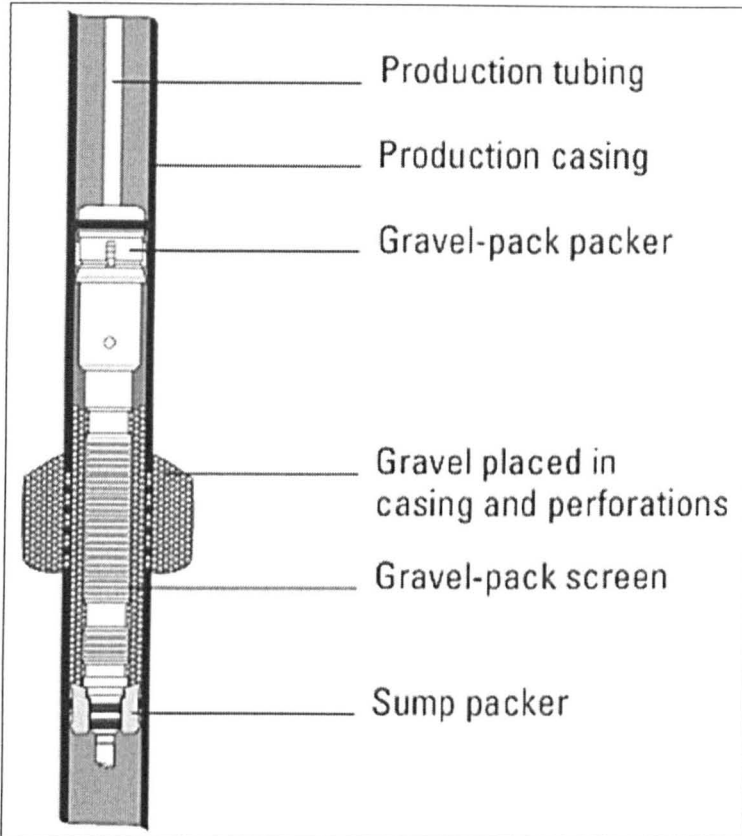


**Figure 2-2 A schematic of gravel pack completion (courtesy of Schlumberger)**

#### **2.2.2.2 Stand-Alone screens completion**

This is a screen alone completion without pack sand in the screen-formation sand annulus. There are many varieties of stand alone screens; most important ones are the pre-packed screens, wire-wrapped screens and premium screens.

Screen alone completion as a sand control method has been successfully used for well-sorted, large grained formation, which poses a less risk of

finer mobilisation and movement. Selection of a stand-alone screen for a formation, which contains a range of particle size distribution, or not well sorted, will require consideration of the amount and size of formation material that can be tolerated in the production flow streams as well as the flow capacity necessary for the well to be commercially successful<sup>40</sup>. Even when this is considered, detailed risk analysis relating to fines mobilisation and movement and deposition needs to be conducted to avoid possible plugging of screen openings. Figures 2-3 to 2-5 shows the common types of stand-alone screens used in the oil and gas industry.

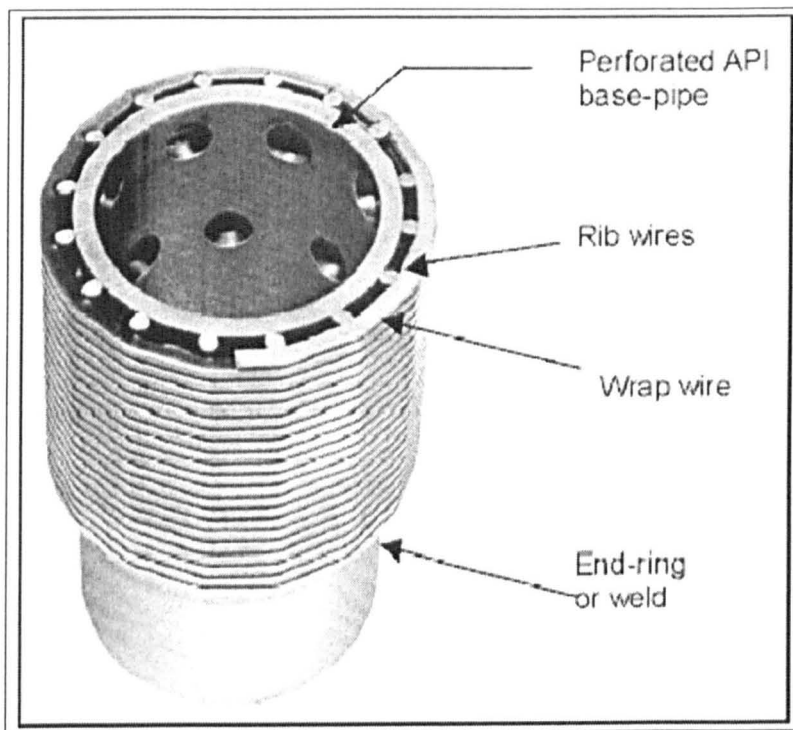


**Figure 2-3 A wire wrapped screen**

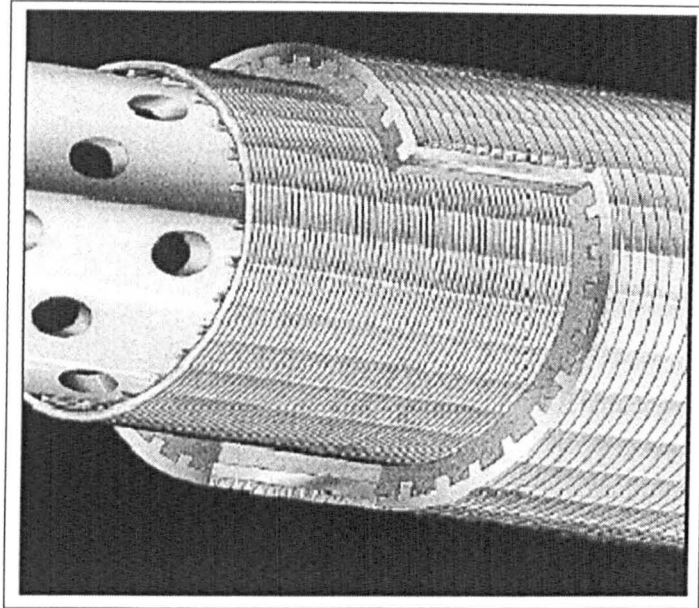


**Fig 2-4 A Pre-packed screen**

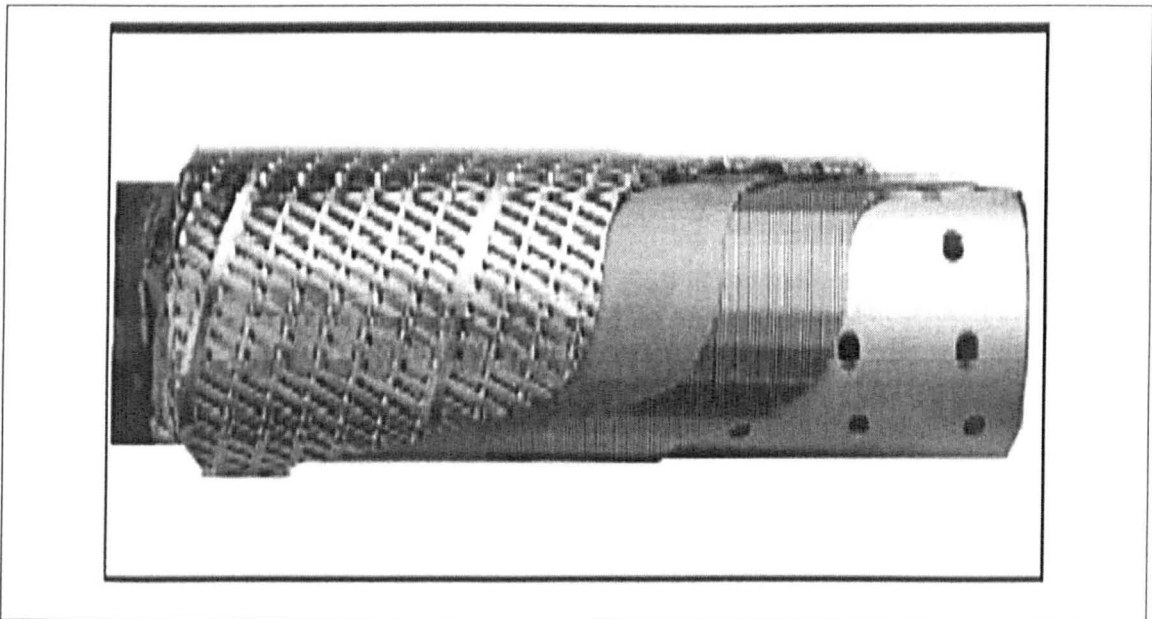


**Figure 2-5 A premium screen**

---

### 2.2.2.3 Expandable Sand Screen (ESS) completion

Expandable sand screen is a relatively recent sand control method compared to other proven, well established methods such as gravel packs and screen completion; it was introduced just a little over half a decade ago<sup>41</sup>, and is now gaining wider acceptance than any other known sand control methods<sup>42-43</sup>.

Expandable sand screen consists of multiple overlapping rectangular sheets of metal-weave filters attached to an expandable base pipe and encased within a protective metal shroud. During expansion of the system, the base pipe and the protective shroud's slots open to expose a flow area through the metal-weave filters, which accommodate the expansion by sliding away from each other while maintaining a tight overlap at all time<sup>44</sup>.

Lau et al (2004)<sup>44</sup> and Weekse et al (2002)<sup>45</sup> gave the following probable reasons for the wider acceptance of ESS:

- It offers a large inflow area that minimises screen plugging and erosion
- It is operationally simple to install
- It offers a larger internal diameter than most sand control screens thus facilitating tubular installation for zonal isolation
- In openhole applications, it eliminates the annulus between the screen and the sandface, thereby stabilising the sandface and minimising sand movement, thus reducing the risk of sand failure and sand erosion caused by sand production.
- It offers high production rate and low pressure drawdown compared to other screen system.

Published data from many of the world petroleum provinces have confirmed these advantages and shown that ESS is indeed better in terms of production performance, low skin and long term reliability<sup>45-48</sup>. Figure 2-6 shows a typical ESS.

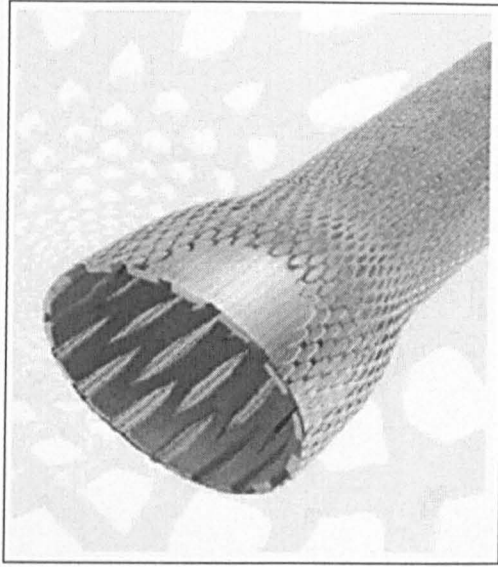


**Figure 2-6 Example of expandable sand screen (ESS)**

#### **2.2.2.4 Screenless completions**

Screenless completions are an alternative sand control method to conventional sand control techniques. They are a sand control technique that prevents production of sand and solids without the use of downhole screens. They therefore include such sand control methods as hydraulic fracturing, chemical consolidation and selective and oriented perforation completions.

Hydraulic fracturing entails the fracturing of the entire perforated interval of a formation and the stabilisation of the fractures with proppant flow back control additives<sup>12</sup>.

Selective perforation involves perforation of the well interval based on the interval rock strength. In order to assess the strength of the interval rock, a rock strength log e.g. sonic log may be used<sup>12</sup>. Based on the strength assessment, the strong intervals of the reservoir formation are perforated. The expectation from this is that production from the weak intervals, which may result in failure and subsequent sand production will be

---

achieved by vertical flow within the formation<sup>12</sup>, thereby limiting production from this interval. Limiting production from the weak interval is expected to lead to reduced sand production or its outright elimination.

Oriented perforation on the other hand is based on the clear knowledge and understanding of the distribution and orientation of field insitu stresses. The knowledge of the orientation of insitu stresses is very important as the drilling of a borehole through a formation has the potential to disturb the insitu stress field creating a higher stress concentration that may cause failure (break out) in the direction of minimum horizontal stress<sup>49</sup>. Generally, the orientation of the minimum and maximum horizontal stresses is usually considered for efficient oriented perforation completion strategy for sand control. The design of orientation perforation is such that the perforations are oriented in the direction of minimum horizontal stress<sup>12, 49</sup>.

Chemical consolidation is a screenless sand control method that involves consolidating the reservoir formation by injecting a consolidating fluid. A conventional consolidating fluid may comprise a resin, a curing agent, a catalyst and an oil wetting agent<sup>50</sup>, which are usually injected in different stages of the consolidation process. The injected fluid causes consolidation of the formation to a rigid state and reduction in the concentration of formation particulates<sup>50</sup>. One big disadvantage of chemical consolidation however, as indicated in Table 2-2, is the potential of the resin fluid to damage the permeability near well bore. Additional programmes of perforations can however help to bypass this damage and connect the near wellbore with the permeability deep into the reservoir.

The majority of screenless completions are usually used to complete wells in high strength formation rock and provide numerous advantages over the conventional sand control methods<sup>51</sup>. For example, hydraulic fracturing reduces crossflow caused as a result of pressure differential between two zones of a reservoir in wellbore; it also creates a negative skin near wellbore.

### 2.2.3 Sand Monitoring

Sand monitoring involves all activities, processes and technologies aimed at detecting sand production and quantifying the amount of sand produced. Sand monitoring is very critical to the performance evaluation and calibration of the sanding potential prediction models. Predicted onset of sand production and volume of sand can be compared with the results of sand monitoring devices or technologies for this purpose. The only problem though is that many of these monitoring devices or technologies are not reliable due to certain limitations which are discussed in the following paragraphs. Sand monitoring is particularly important for safety on production platforms as produced sand is very erosive and may erode chokes, pipeworks and valves.

Many methods exist for detecting and monitoring produced sand. Such methods include

- Intrusive and non-intrusive electronic sand detector
- Flowline fluid sampling
- Sand traps

However the most widely used methods/equipment are the electronic detectors and fluid sampling; fig. 2-7 shows a typical electronic sand detector. The two methods are often used to complement each other for effective sand monitoring especially in critical field environments such as subsea, deepwater and offshore fields where even low level of sand production may not be tolerated due to safety reasons<sup>52</sup>.

Intrusive and extrusive sand detectors have become very popular in the last few years. They have been deployed in all types of field developments to monitor produced sand and other solid particles that may come through with the flow stream.

Intrusive detectors are so called because they are installed inside the pipeline or flowline. The system consists of a metal probe positioned within the flow stream for transmitting acoustic signals triggered by sand

---

---

impinging on the metal probe to a sensor and signal processing circuit which produces a discrete signals related to the impact of each of the particles striking the probe. Non-intrusive detectors are usually installed outside downstream of pipe bends; a typical installation is shown in figure 2-8. They also consist of acoustic sensors which receive and process ultrasonic signal generated by sand particles forced out of the flow passing the bend, hitting the inside of the pipe.

The signals from both intrusive and extrusive sand detectors are usually converted to produced sand volume and sand rate by some mathematical manipulation. Figure 2-9 and 2-10 shows typical sand production trends and rates from a sand monitoring operation.

The performance of both sand detector types can be affected adversely by flow velocity and sand production level or sand concentration in the flow stream<sup>52</sup> leading to a situation where sand in the flow stream is not detected. Another major setback of the electronic sand detectors is related to their location; proximity to chokes or manifolds can significantly impact signal-noise ratio, leading to unreliable results.

Flowline sampling involves taking samples of the fluid periodically and analysing such fluid for sand presence. This, as stated earlier, is used to complement sand detector systems and is basically for identification and characterisation of produced solids<sup>52</sup>. The different types of available sampling techniques were given by Nisbet & Dria (2003)<sup>52</sup> as:

1. Full production stream sampling
2. Deposit sampling
3. Slip Stream sampling



**Fig 2-7 ClampOn™ acoustic sand detector (ClampOn, 1999<sup>53</sup>)**

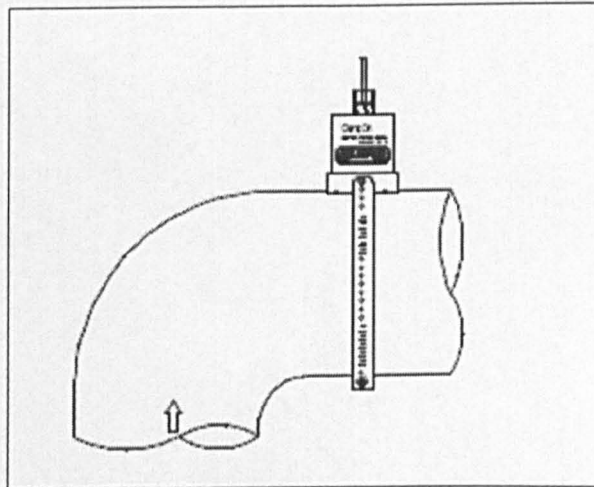


**Fig 2-8 Positioning of extrusive acoustic system (ClampOn (1999)<sup>53</sup>).**

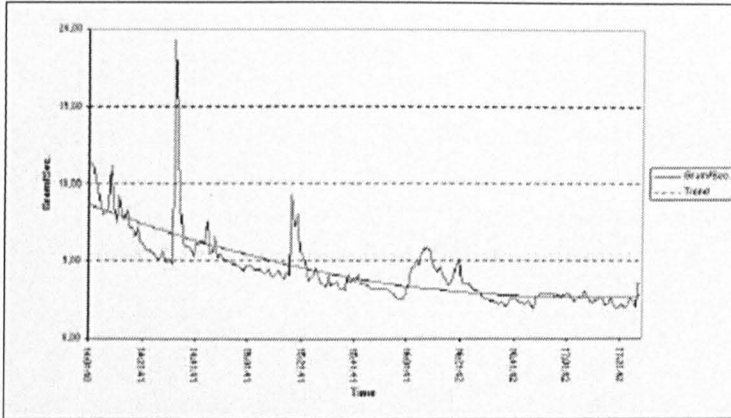


**Fig.2-9 A typical processed output of acoustic sand detector showing reducing sand production (ClampOn (1999)<sup>53</sup>)**

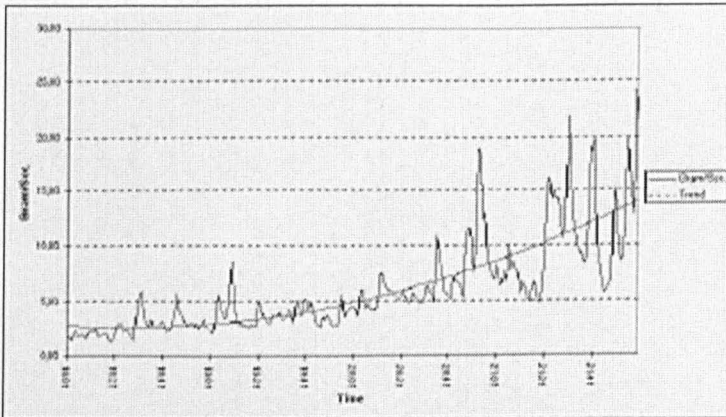


**Fig 2-10 A typical processed output of acoustic sand detector showing increasing sand production (ClampOn (1999)<sup>53</sup>)**

### 2.2.4 Topside management/handling

Topside sand management constitutes all approaches and technologies, and integration of these, for handling produced sand at the surface which eventually results in safe disposal of the sand in an environmentally

---

friendly manner. Managing sand at the surface will therefore follow this sequence of activities: separation of sand from the produced fluid, collection and preparation for environmental friendliness and safe disposal of the sand.

Critical to effective topside management are the accurate prediction of failure and onset of sand production, volume and rate of sand production, and evaluation of erosion risks of equipment and facilities. Accurate and reliable prediction of onset of sand production can help optimise the overall sand management strategy of any field development. This may be in terms of being able to make projections on when to include surface sand handling facilities in the overall design of the topside. Sand volume, rate and erosion risks of sand production can be a veritable tool in material selection, capacity or size design and selection of metallurgy for the design of sand handling facilities.

The main concern with sand production is often the erosion risk; this is because of the major technical and economic constraints surrounding it, which may lead to serious safety problem<sup>4</sup> especially in offshore and subsea field developments.

Produced sand coming from the subsurface will usually pass the wellhead, after which it passes through the surface lines, or for subsea wells, through the sea line to deposit in the separator, which must be cleaned and flushed from time to time according to the expected average sand rate<sup>4</sup>. However the need to clean and flush the separator from time to time has perhaps been removed by the recent development, introduction and field applications of a mechanical system which can remove sand from the separator and vessels on-line<sup>54</sup>.

Of all the activities that topside sand management entails, sand disposal is very critical. In the years past, sand was easily disposed to disposal sites on land, or dumped onto the seafloor, for offshore and subsea field operations. New international environmental laws on sand disposal subscribed to by many oil producing countries have however made this practice unethical.

## **2.3 Influence of sanding potential on field operations**

### **2.3 1 Influence on drilling**

Sand formations are classified as consolidated, poorly consolidated and unconsolidated based on their elastic properties, mechanical strength and cementation materials<sup>49</sup>.

It is therefore very important that a thorough geomechanical and geochemical evaluation of the formation is carried out as part of sanding potential evaluation prior to drilling to establish the category to which the rock belongs for proper planning of drilling programmes. Evidently, sanding potential prediction exerts a great deal of influence on the selection of drilling methods, drilling bits, drilling fluid and drilling fluid composition.

### **2.3.2 Influence on well completion**

The type of completion in a formation is greatly influenced by the sanding potential of the rock. Abass et al (2003)<sup>49</sup> recommended the evaluation of possible breakout failure in a well during drilling. They further suggested two possible lines of actions to deal with the scenario for efficient completion strategy

- If a breakout zone is distinguished, a 180-degree phasing oriented perforation in the direction of the maximum horizontal stress is recommended.
- If a breakout is not distinguished, and the UCS is less than 1000psi, a 180-degree phasing may be considered in any direction.

Also many sand control completions such as oriented perforation, selective perforation, frac-pack etc are usually planned and applied on the basis of sanding potential evaluation of the rock

### **2.3.3 Influence on oil production strategy**

Sand potential prediction has been used as an important tool in fashioning out a production strategy for any field development. Production strategy is often fashioned in a way that a formation that has been evaluated in terms of sanding potential is not moved across the established failure envelope by stress loading during production.

Once the sanding potential of a formation has been evaluated and the potential to produce sand established, the usual practice in the industry is to reduce the pulling rate on the rock to the optimum level that will help maintain the formation within the safe region of the failure envelope. Any attempt to go beyond the failure boundary may lead to the formation failure and hence sand production. However the benefits of this option have to be weighed against other possible sand management options for best results.

### **2.3.4 Influence on production facilities**

Sanding potential prediction in the early stage of field development planning has become an essential tool for selecting material and designing both downhole and surface facilities. In designing production facilities, consideration is often given to the amount of sand, erosion rate of sand and transport rate of sand. These factors often determine how severe the erosive capability of sand could be; and this often helps the design engineer select material and design optimum size capacity especially for surface facilities.

## **2.4 Summary**

In this chapter, an attempt has been made to present a holistic view of broader sand management concept, which incorporates sand prediction, control, monitoring, and topside management in comparison to the current sand control concept, being used in the industry, which tends to concentrate exclusively on sand exclusion. In particular, the importance of sand prediction as the first in the series of sand management process has been highlighted. Attempts have also been made to establish a link between sanding potential prediction and field development philosophy.

## **Chapter 3**

# **Rock strength and textural/grain parameters correlation**

This chapter presents the basic failure theory and reviews the underlying principles, theories and limitations of the conventional techniques being used in the oil and gas industry for sanding potential prediction. The broad categories of these techniques and general discussion about their application have been presented in chapter 2. The chapter thereafter introduces a new concept of rock failure, which this present work is aiming to advance. It also reviews the grain and textural properties of rocks, which are fundamental to the understanding of the concept of grain size distribution and establish how each of these textural properties affects the Unconfined Compressive Strength (UCS) of rock. Furthermore it reviews the grain size profiling and profiling techniques and technologies available in the oil and gas industry to carry out grain size profiling. These reviews are intended to showcase the textural parameters, which are critical in strength characterisation of clastic rocks. They are also intended to point out the technology gap in profiling techniques that needs to be filled. This is with a view to designing appropriate grain size profiling technologies with the potential for application in the conceptual technology this work is aiming to advance.

In order to achieve the aforementioned tasks, field and published data have been used to examine and consequently establish the possible correlations between these textural/grain parameters and Unconfined Compressive Strength (UCS).

### **3.1 Basic failure theory**

Petroleum rock formations are in a constant state of stress from the weight of layers of overlying rocks. This stress is referred to as the

overburden stress,  $\sigma_{OB}$ . However this stress is counterbalanced by the stress or pressure generated from the pores of the rock formations by the pore filling fluids, called pore or reservoir pressure, thereby reducing the net overburden pressure acting on the formation<sup>3</sup>. The relationship between the overburden and pore pressure is given in equation 3-1.

$$\sigma_{eff} = \sigma_{OB} - P_p \quad 3-1$$

Where  $\sigma_{eff}$  is effective pressure;  $\sigma_{OB}$ , the overburden pressure and  $P_p$  is pore pressure

The effectiveness of the pore pressure in counterbalancing the overburden stress is a very important factor in the failure of the rock. In the early life of formation rock when it has not experienced production or has only experienced little production, the pore pressure is able to effectively counterbalance the overburden pressure and gives stability to the rock. However as the reservoir experiences more and more production and becomes more mature, the pore pressure depletes correspondingly in a drastic manner. This depletion in pore pressure affects negatively the ability of the rock to counterbalance the effects of the overburden pressure, which eventually may lead to an increase in the net (effective) overburden pressure acting on the rock. Usually this phenomenon represents the onset of failure of formation rocks.

### **3.2 Conventional sanding potential prediction (SPP) techniques/models**

In chapter two (section 2.2.1) of this thesis, broad categories of sanding potential prediction are discussed. In this section, the underlying principles, applications and some of the limitations of some of the most popular sanding prediction models across all the categories mentioned in the chapter (chapter two) are discussed.

### 3.2.1 Plastic (failed) extension model (PZE)<sup>44, 55-56</sup>

This model is based on a yield zone approach that accounts for shear failure triggering sand failure, the existence of a plastic (failed) zone around the perforations, and the effective stress state near the well. The calibration parameter used to define the critical conditions for sand production is the ratio of the plastic zone radius to the wellbore/perforation radius ( $r_p/r_w$ ). The model is represented thus:

$$\left[ \frac{r_p}{r_w} \right]^{q-1} = \frac{q-1}{q+1} \frac{1}{C_o} \left\{ 2\sigma'_h(t) - (2-\gamma)[P_i(t) - p(\infty, t)] + \frac{2C_o}{q-1} \right\} \quad 3-2$$

Where:

$r_p$  = radius of plastic zone, ft

$r_w$  = radius of wellbore or perforation, ft

$$q = \tan^2 \left( \frac{\Pi}{4} + \frac{\theta}{2} \right), \text{ in radian} \quad 3-3$$

$\sigma'_h$  = effective minimum horizontal stress (at time t), psi

$$\gamma = \frac{1-2\nu}{1-\nu} \quad 3-4$$

$\nu$  = Poisson ratio

$\theta$  = angle of internal friction (degree)

$P_i(t)$  = Constant pore pressure around well (at time t), psi

$p(\infty, t)$  = far field (reservoir) pore pressure (at time t), psi

$C_o$  = Unconfined Compressive Strength, psi

---

Input parameters for the model include UCS ( $C_o$ ), frictional angle,  $\theta$ , Poisson ratio ( $\nu$ ), in-situ stress state – horizontal stresses, ( $\sigma_h(t)$ ), well drawdown and planned depletion level –  $P_i(t)$  and  $p(\infty, t)$ .

Though the model was originally based on vertical gas wells with open hole completions, modelling of horizontal wells and other completion styles can be accommodated via modification of the critical sanding parameter ( $r_p/r_w$ ) ratio – either from direct calibration or from a knowledge database obtained from other fields.

### 3.2.2 Shear failure model (BP's model)<sup>57-59</sup>

This is a stress-based model of shear failure around a perforation or an open hole wellbore. The essential of the models are summarised as<sup>59</sup>:

- Prediction of shear failure around a perforation or an open hole
- Prediction of the onset of sand production in cased and perforated; and open hole completions using a combination of empirical and analytical relationships
- The essential inputs to the model are Thick-Walled Cylinder (TWC) tests obtained from cores tested in the laboratory, and Unconfined Compressive Strength (UCS) predicted from logs (gamma ray, density and dipole sonic)
- The TWC collapse strength corresponds to the point of significant sanding (equivalent to development of many shear bands that eventually coalesce)
- Analysis is performed at the weakest point of the UCS log. The UCS log is calibrated to the measured TWC.
- Sand production is assumed to occur once the maximum value of the effective tangential stress around the perforation exceeds the apparent UCS (i.e. the perforation fails at the same cavity loading as occurs in the TWC test). No consideration is given to sand drag forces.

- The model can account for different orientations of the well or perforations.

The model is mathematically represented thus:

$$CBHFP \leq \frac{3\sigma_1 - \sigma_3 - \sigma_{ucs}}{2 - A} - P_r \frac{A}{2 - A} \quad 3-5$$

CBHFP = critical bottom hole flowing pressure

$P_r$  = current average reservoir pressure

$\sigma_1$  &  $\sigma_3$  = the total principal major and minor stresses

A = poro-elastic constant (it is a function of Poisson ratio & formation compressibility).

$\sigma_{ucs}$  is the Unconfined Compressive Strength and is given as  $\sigma_{ucs} = 3.1 * TWC$

The factor 3.1 includes the scale transformation from TWC laboratory sample (OD:ID = 3) to field (OD:ID = infinity)

### 3.2.3 Coates and Denoo model<sup>24</sup>

This model, based on Mohr coulomb theory, is also a shear failure model specifically developed for borehole stability analysis during drilling and sand prediction during production.

In formulating the model, three principal stresses, x, y and z acting on a block of material deep down the earth, are first written in terms of overburden stress, pore pressure and Poisson ratio apparently for ease of computation. It is sometimes difficult to estimate x and y stresses from conventional means such as leak off test, extended leak off test, hydraulic fracturing etc. though z stress can always be estimated by integrating bulk density log. The equations for their computation are written below:

$$\sigma_x = \frac{\nu}{1-\nu} \sigma_{ob} + \alpha P_p \left( 1 - \frac{\nu}{1-\nu} \right) \quad 3-6$$

$$\sigma_y = \frac{\nu}{1-\nu} \sigma_{ob} + \alpha P_p \left( 1 - \frac{\nu}{1-\nu} \right) \quad 3-7$$

$$\sigma_z = \sigma_{ob} \quad 3-8$$

$\nu$  is Poisson ratio;  $\sigma_{ob}$  is overburden pressure;  $\alpha$  is Biot poroelastic constant; and  $P_p$  is pore pressure.

The three stresses are then written as radial coordinates for ease of analysis during drilling, and transformed to radial systems of overburden, tangential and radial stresses (equation 3-9 to 3-11). This transformation is similar to Kirsch's stress transformation.

$$\sigma_z = \sigma_{ob} + 2\nu(\sigma_1 - \sigma_2) \quad 3-9$$

$$\sigma_\theta = 3\sigma_1 - \sigma_2 - P_{mud} \quad 3-10$$

$$\sigma_r = P_{mud} \quad 3-11$$

The radial coordinate equations are then expressed as effective stresses by subtracting the pore pressure component from them to get the stresses that produce deformation in the rock. The equations are presented below:

$$\sigma_{z_{eff}} = \sigma_{ob} + 2\nu(\sigma_1 - \sigma_2) - \alpha P_p \quad 3-12$$

$$\sigma_{\theta_{eff}} = 3\sigma_1 - \sigma_2 - P_{mud} - \alpha P_p \quad 3-13$$

$$\sigma_{r_{eff}} = P_{mud} - \alpha P_p \quad 3-14$$

For a penetrating fluid, a factor was added to all the three equations to account for the gradual change between the mud column pressure and pore pressure. The factors (equation 3-15) and the equations (3-16 to 3-18) are presented below:

$$\frac{a(1-2\nu)}{(1-\nu)(P_p - P_{mud})} \quad 3-15$$

$$\sigma_{z_{eff}} = \sigma_{ob} + 2\nu(\sigma_1 - \sigma_2) - \alpha P_p + \frac{a(1-2\nu)}{(1-\nu)(P_p - P_{mud})} \quad 3-16$$

$$\sigma_{\theta_{eff}} = 3\sigma_1 - \sigma_2 - P_{mud} - \alpha P_p + \frac{a(1-2\nu)}{(1-\nu)(P_p - P_{mud})} \quad 3-17$$

$$\sigma_{r_{eff}} = P_{mud} - \alpha P_p + \frac{a(1-2\nu)}{(1-\nu)(P_p - P_{mud})} \quad 3-18$$

The two sets of equations (equations 3-17 & 3-18) can be used to solve for a stress level in the vicinity of the well bore during drilling and production.

Mohr circles can be drawn for various combinations of radial and tangential stress to determine whether or not a rock will fail during drilling and production. Analysis of the interplay between the radial and tangential stresses can give a clue to the failure potential in rocks and hence sanding potential especially during drilling. A rock formation is usually assumed to

have failed and to possess a risk of sand production when the effective tangential stress is far higher than the effective radial stress<sup>24</sup>.

Coates and Denoo (1981)<sup>24</sup> demonstrate the use of this model for estimating the mud weight during drilling that will not lead to sand failure and by extension, sand production; though no details of comparison of the obtained results with the actual sand production data were given. One obvious limitation of the model however is that it does not consider the effect of fluid drag on sand production and equates sand failure with sand production.

### 3.2.4 Equivalent Critical plastic strain model<sup>60</sup>

This model is implemented and developed using finite element numerical method; it is based on the equivalent critical plastic strain and developed by fully coupling a comprehensive geomechanic model to three-phase reservoir model. The equivalent critical plastic strain level is considered to signify the onset or initiation of hole collapse and sand production. The onset of plastic yielding, sand production and wellbore collapse are defined based on a combined criterion in which stress concentration and strain are calculated and compared to critical strength and strain.

Onset of wellbore instability or sand production is defined when the following criterion for effective or equivalent plastic strain,  $\epsilon_e^p$ , is satisfied:

$$\epsilon_e^p = a_o + a_1 J_1 = \sqrt{\frac{2}{3} [(\epsilon_{11}^p)^2 + (\epsilon_{22}^p)^2 + (\epsilon_{33}^p)^2]} \quad 3-19$$

$\epsilon_{11}^p$ ,  $\epsilon_{33}^p$ , and  $\epsilon_{22}^p$  are directional plastic strains

$a_o = 0.02$  and  $a_1 = 0.008$  have been suggested for sand production, provided the compression is taken to be positive<sup>61</sup>

$$J_1 = \sigma_{11} + \sigma_{22} + \sigma_{33} \quad (J_1 \text{ is the first stress invariance}) \quad 3-20$$

### 3.2.5 Linear poro-elastic and brittle plasticity model<sup>62</sup>

This model is an improvement on the earlier one by Wang, Z. et al. (1991)<sup>63</sup>. It is based on linear poro-elasticity and brittle plasticity with a critical equivalent plastic strain on cavity surface as the sanding criterion. Inclusion of the effect of residual strength in the plastic zone surrounding cavity is the major improvement on this model. The inclusion is based on the assumption that rock is linearly poro-elastic prior to the peak strength and become brittle plastic after the peak strength is exceeded, and with the stress exceeding the peak strength, the strength of the rock reduces to its residual strength.

Equations for Mohr Coulomb criterion in terms of peak and residual strength are written respectively:

$$\sigma_{\theta} - N^2 \sigma_r + (N^2 - 1)P - 2S_o N = 0 \quad (\text{for peak strength}) \quad 3-21$$

where  $\sigma_{\theta}$  is tangential stress;  $\sigma_r$  is radial stress;  $N = \tan(45 + \theta/2)$  and  $S_o$  are peak strength parameters related to angle of internal friction and cohesion respectively;  $\theta$  is internal friction angle; and  $P$  is pore pressure

$$\sigma_{\theta} - N_r^2 \sigma_r + (N_r^2 - 1)P - 2S_{r_o} N_r^2 = 0 \quad (\text{for residual strength}) \quad 3-22$$

where  $N_r$  and  $S_{r_o}$  are residual strength parameters related to angle of internal friction and cohesion respectively.

Equations are then derived for the radial, tangential and axial stresses for both plastic zone of the cavity in terms of residual strength parameters and for the elastic zones of the cavity in terms of elastic constants.

Equations are similarly obtained for radial displacements in both plastic and elastic zones.

The tangential plastic strain on the cavity surface is calculated from:

$$\varepsilon_{\theta}^p = \frac{1}{4N_r^2 G} \left\{ (1-\nu)(1-N_r^4) \left( \sigma_{ri} + \frac{2S_{r0}N_r}{N_r^2-1} \right) - 2N_r^2 [(1-\nu)(1-N_r^2) - (1-\nu)\beta] \sigma_{ri} + cr_{cp}^{-(N_r^2+1)} \right\} \quad 3-23$$

where

G is Lamé constant

$\beta$  is the turbulence coefficient

$\nu$  is Poisson ratio

$r_{cp}$  is the radius of cavity

And c is the integrating constant and can be computed from:

$$c = r_c^{N_r^2} \left\{ u_e 4N_r^2 G - A_1 r^{N_r^2} \int_{R_p}^{r_c} P r^{-N_r^2} dr - (A_1 + A_2) r^{-N_r^2} * \int_{R_p}^{r_c} P r^{N_r^2} dr + \left[ A_3 \left( \frac{r_c}{r_p} \right)^{N_r^2} + A_4 \right] r_c \right\} \quad 3-24$$

where  $u_e$  is the radial displacement in the elastic zone and  $r_c$  is radius of elastic plastic boundary. Equations for estimating  $u_e$ ,  $A_1$ ,  $A_2$ ,  $A_3$  and  $A_4$  are respectively given as:

$$u_e = \frac{\alpha}{\lambda + 2G} \frac{1}{r} \int_{r_c}^r P_r dr + \frac{\sigma_{r_c}}{2(\lambda + G)} r + \frac{r_o}{r_o^2 - r_c^2} x \left[ \sigma_{r0} - \sigma_{r_c} - \frac{1-2\nu}{1-\nu} \frac{\alpha}{r_o^2} \int_{r_c}^r P_r dr \right] \left[ \frac{r}{2(\lambda + G)} + \frac{r_c^2}{2Gr} \right] \quad 3-25$$

$$A_1 = [N_r^4 + 1 - \nu (N_r^2 + 1)^2] [1 - N_r^2] \quad 3-26$$

$$A_2 = 2N_r^2 [N_r^2 (N_r^2 - 1) - \nu (N_r^4 - 1) + (N_r^2 + 1)(1 - 2\nu)\alpha] \quad 3-27$$

$$A_1 = \left[ N_r^4 + 1 - \nu (N_r^2 + 1) \right] \left[ \sigma_{ri} + \frac{2S_{ro}N_r}{N_r^2 - 1} \right] \quad 3-28$$

$$A_4 = \frac{4S_{ro}N_r^3(1-2\nu)}{1-N_r^2} \quad 3-29$$

$\sigma_{ri}$  is the total radial stress at cavity surface

$r_o$  is the radius of outer boundary

$r_c$  is the radius of elastic-plastic boundary

$\sigma_{ro}$  is total radial stress at outer boundary

$\sigma_{rc}$  is the total radial stress at elastic-plastic boundary

The equivalent plastic strain at the cavity surface is then given as a function of the tangential plastic strain at the cavity surface as:

$$\varepsilon_e^p = \sqrt{\frac{2}{3}(N_r^4 + 1)} \varepsilon_{\theta}^p \quad 3-30$$

The strain level at which the equivalent plastic strain equals the tangential plastic strain function is considered to correspond to the initiation of sand production.

### 3.2.6 Neural network based approach<sup>17</sup>

Neural network based sand prediction involves the use of all parameters thought to influence failure and sand production in a rock formation as inputs into either a generic or purpose built neural network model in order to predict sand production or potential for sand production.

The work of Kanj and Abousleiman (1997)<sup>17</sup> is perhaps the only published work on the use of neural network for predicting sanding potential of a reservoir rock.

All the parameters believed by the authors to contribute to or affect sanding potential of the gas reservoir rock on which the studies was based, such as total vertical depth, transit time, formation cohesive strength, gas and water flow rates, drawdown, original static reservoir pressure, effective overburden vertical stress, interval length and perforation density were presented to a neural network. These data were sourced from 23 sand producer and 8 sand-free wells. Anyone of the following four options was the expected output from the network:

- A Boolean classification of the well; output was 1 for a sand producer and 0 for a sand-free well.
- A forecast of the period in the life (or life span) of the well before sanding started (or the well was shutdown)
- An assessment of the sanding potential number
- A prediction of the total drawdown (or critical total drawdown) of the well.

### **3.3 A new failure concept: quantitative effect of textural/grain parameters on rock strength**

The conventional failure/sand prediction methods do not account for the effect of textural/grain parameters on the failure tendencies of a typical reservoir rock. In failure analysis and prediction for sand management purposes in the last twenty years, attention has focussed on several geomechanical parameters such as Poisson ratio, Young modulus, Bulk modulus etc.; and a few petrophysical parameters such as porosity and cementation exponent. Even though a lot has been published in the literature on the qualitative evaluation of possible effects of textural/grain parameters on rock strength, virtually nothing has been done in the area

of quantitative evaluation of these effects and in their application to real time sanding potential prediction.

When a reservoir rock has failed and the failed rock has become fluidized by the hydrodynamic force of the flowing fluid, leading to sand production, the reservoir sand framework is expected to re-adjust to reach a new equilibrium. As this phenomenon takes place, many of the rock textural parameters or features such as median grain size, sorting, grain shape, grain orientation, etc. may also change.

In this work, the correlation between textural/grain parameters has been quantitatively evaluated in a neural network model to predict rock strength and this has been extended to real time evaluation of sanding potential in a clastic reservoir rock. This, in turn, is expected to impact the rock strength.

### **3.3.1 Grain and textural parameters and their relationship with strength**

#### **3.3.1.1 Grain size vs. rock strength**

Many definitions of grain size have been given in literatures. For example Prikryl (2001)<sup>2</sup> defined grain size as the diameter of the circle of an equivalent area occupied by a grain analysed using computer image analysis. The various literature definitions of grain size were however summarised in one succinct definition by Faga (2000)<sup>64</sup> as the diameter of a sphere having the same specific property such as surface area, volume, and resistance to motion as the grain particle.

In formation evaluation and sedimentological characterisation of sedimentary rocks, of which clastic sandstone is one, grain size has been the most widely used textural parameter for their description. Grain size in this context refers to the physical dimensions of particles or grains of rocks. It is the most fundamental property of sedimentary rocks affecting their entrainment, transport and deposition<sup>65</sup>. Grain size is also one of the

textural parameters used largely in gauging sediment textural maturity. At the source or provenance, the grain sizes are generally big; as they go through the maturation process, they become smaller and smaller.

Grain size of a typical sedimentary rock may range from very small particles to large boulders. Numerous grade scales, created by assigning arbitrary subdivisions on a natural continuum, exists for defining the grain size in sediments and sedimentary rocks such as Udden (1914)<sup>66</sup>, Wentworth (1922)<sup>67</sup> and US Bureau of Soils scales, but the most widely used are perhaps Udden and Wentworth scales, perhaps because they present more subdivisions of the major classes than other scales in use. The Udden-Wentworth scale was however modified by Krumbein (1934)<sup>68</sup> using a logarithmic function to account for larger grain sizes. This modified scale is usually referred to as phi scale; the formula for obtaining equivalent grain size in phi unit is given as

$$\phi = -\log_2 d \quad 3-31$$

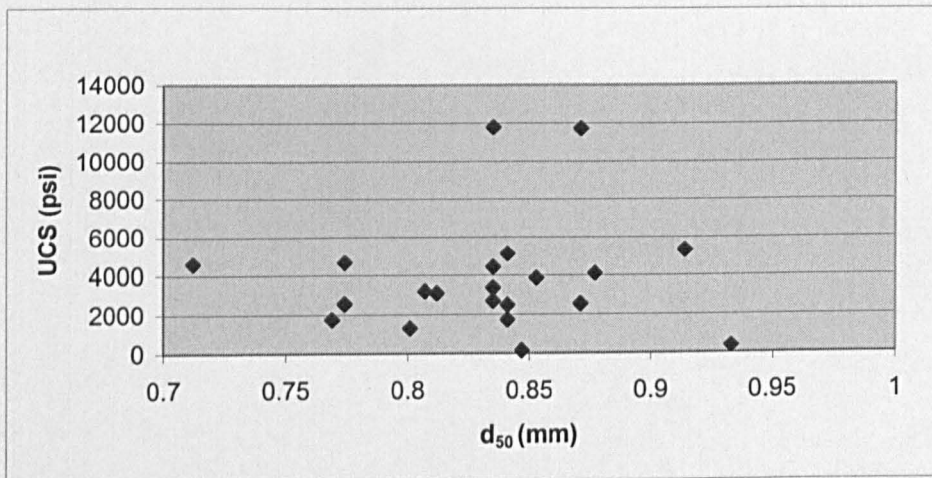
Where phi is the equivalent grain size in phi unit and d is the grain size in mm.

Table 3-1 shows some of the grade scales used for defining grain size.

The effect of grain size on rock strength is a widely debated subject; yet it is not well understood. Researchers have diverse opinions on the kind of relationship between grain size and rock strength. Hugman and Friedman (1979)<sup>69</sup> showed that ultimate strength of rock is inversely proportional to the mean grain size in carbonates rocks such as limestones and dolomites. Olsson (1974)<sup>70</sup> reported that the stress difference at failure is linearly proportional to the inverse square root of the mean grain size in marbles. Prikryl (2001)<sup>2</sup> also reported a non-linear negative correlation between UCS and the average grain size of the rock minerals. This may however not be applicable to clastic rocks considering that they have a structural framework totally different from that in carbonate and metamorphic rocks. This notion is buttressed by the results obtained by

Palchik (1999)<sup>71</sup> in his studies on the effect of grain size on the strength of clastic rock. The results showed a weak correlation between UCS and the inverse of square root of mean grain size. This perhaps shows that it is not only mean grain size, which influences the strength of clastic rocks. This particular notion is buttressed by the scatter plot of UCS against  $d_{50}$  using a North-Sea field data (figure 3-1); the plot shows no defined correlation between UCS and  $d_{50}$ .

However, there seems to be a consensus of opinion on the role grain size plays in impacting rock strength<sup>2,69-71</sup>. It is generally believed that grain size controls the inter-grain boundary size, which impacts the strength of rock.



**Fig. 3-1 Correlation between UCS and  $d_{50}$**

**Table 3-1 Various grain size scales**

diameter (millimetres)	Hopkins (1899)		Udden (1914)		Wentworth (1922)		U. S. Bureau of Soils	diameter (millimetres)
2048					boulders			2048
1024					boulders			1024
512			boulders	vc				512
256				c	cobbles			256
128				f				128
64				vf				64
32			gravel	vc	pebbles			32
16				c				16
8				f				8
4				vf	granules			4
2	gravel						gravel	2
1			sand	vc	sand	vc	sand	1
1/2				c		c		c
1/4	sand			f	m	m		1/4
1/8	m			vf	f	f		1/8
1/16	0.1			vc	vf	vf		1/16
1/32	0.032		silt	c			0.05	1/32
1/64	0.01			f	silt			1/64
1/128	silt			vf				1/128
1/256	0.0032		day	vc			0.005	1/256
1/512	f			c				1/512
1/1024	0.001			f	day			1/1024
1/2048	day			vf				1/2048

### 3.3.1.2 Grain sorting vs. rock strength

Sorting refers to the range of grain sizes in a rock. Selley (1982)<sup>72</sup> defined it as the degree of scatter or tendency for all grains in a sediment to be all of one class of grain size. Sorting and grain size are the two most important textural parameters of clastic rocks<sup>73</sup> and they are both used to parametise the grain distribution in these rocks.

A number of formulae derived from statistical analysis exist for estimating sorting. Trask sorting coefficient can be estimated using:

$$T = \left( \frac{d_{25}}{d_{75}} \right)^{\frac{1}{2}} \quad 3-32$$

$d_{25}$  and  $d_{75}$  are the 25<sup>th</sup> and 75<sup>th</sup> percentile sizes respectively and are measured in millimetre<sup>74</sup>. This formula accounts for the sorting of the central 50% of the grain distribution; the sorting in either tails of the distribution is not accounted for. Faga (2000)<sup>64</sup> discouraged the use of this formula on account of this. Folk (1974)<sup>74</sup> all inclusive graphic standard deviation formula for calculating sorting accounts for 90% of the distribution and is expressed as:

$$\sigma_{gs} = \frac{\phi_{84} - \phi_{16}}{4} + \frac{\phi_{95} - \phi_5}{6.6} \quad 3-33$$

Folk (1974)<sup>74</sup> gave the corresponding qualitative descriptions of the values returned by these formulae; these are shown in Table 3-2

**Table 3-2 Folk (1974)<sup>74</sup> qualitative descriptions for ranges of values returned by the sorting formulae**

Qualitative description	Range of values
Very well sorted	< 0.35
Well sorted	0.35 - 0.50
Moderately well sorted	0.50 - 0.71
Moderately sorted	0.71 - 1.00
Poorly sorted	1.00 - 2.00
Very poorly sorted	2.00 - 4.00
Extremely poorly sorted	> 4.00

Grain sorting is determined by deposition and may affect sediment bulk and elastic properties in a non linear and non-unique way. Laboratory measurements, theoretical models, and field data indicate that in sediments and sedimentary rocks, the deterioration of grain sorting results in a more efficient packing<sup>73</sup>, reducing porosity. This may be as result of finer particles filling up the spaces created in-between larger particles, resulting in a tighter packing, and subsequently in strength improvement. Increasingly poor sorting may also lead to strength deterioration if the particles filling the spaces in-between the large particles are fines, which are known to be non-load carrying, compared to large particle sizes, which are load-carrying. Most recent works<sup>75-76</sup> have also shown strong correlation between sorting and the strength of rock. These results are in agreement with the scatter plot of a North-Sea data (Fig 3-2), which shows a correlation, best approximated by a power function. This perhaps explains even further why results of correlation between only grain size and UCS from previous work<sup>71</sup> have been inconsistent.

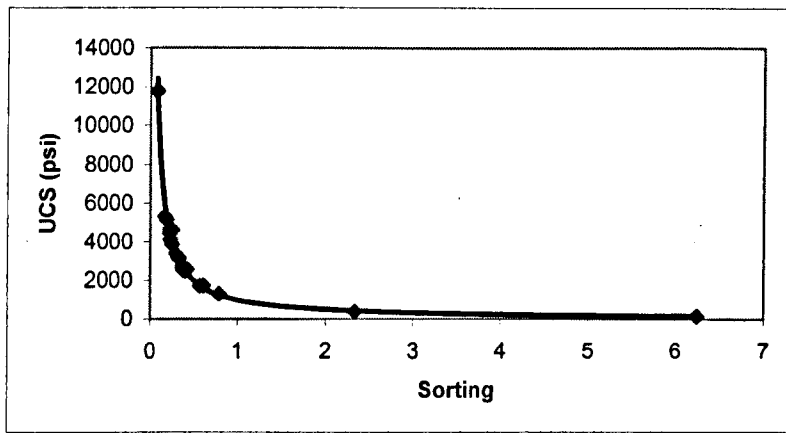


**Fig. 3-2 Correlation between UCS and Sorting**

### 3.3.1.3 Grain Shape vs. strength

Grain shape can be characterised by two dimensionless ratios of sphericity and roundness. Sphericity is the measure of approximation of a sphere by a sand grain, and it is defined as the diameter of the largest inscribed sphere relative to the diameter of the smallest circumscribed sphere. Roundness is a measure of the degree to which the angular edges and corners of grains have been smoothed by sedimentary processes, and it is defined as the average radius of curvature of surface features relative to the radius of the maximum sphere that can be inscribed in the grain. Shape and texture are fundamental characteristics of sand grains which have long been used by sedimentologists to provide information about grain provenance, transport distance and pathways, post depositional weathering<sup>65</sup> and textural maturity.

A number of techniques are available for estimating the shape of particle; one is visual inspection and comparison with charts<sup>77-78</sup>, another is digital image analysis including Fourier analysis and fractal analysis<sup>79-83</sup>.

Grain shape may also exercise a lot of control on the reservoir quality of clastic rocks as it is one of the very important parameters that control packing, which in turn controls porosity. Porosity of course has been shown to correlate very well with rock strength<sup>84-85</sup>.

### 3.3.1.4 Grain packing vs. strength

Packing is the arrangement of the individual grains in a clastic rock. Packing may be a product of depositional or diagenetic process in sediment. As has been established in the previous section, packing exercises a lot of control on the flow properties of clastic rocks and therefore contributes to the quality of such rocks' reservoir properties. With contribution from other rock properties such as grain shape, grain size, sorting, grain orientation, cementation and bedding, grain packing affects permeability and porosity of clastic rocks<sup>64</sup>. Figure 3-3 shows a variety of packing arrangement.

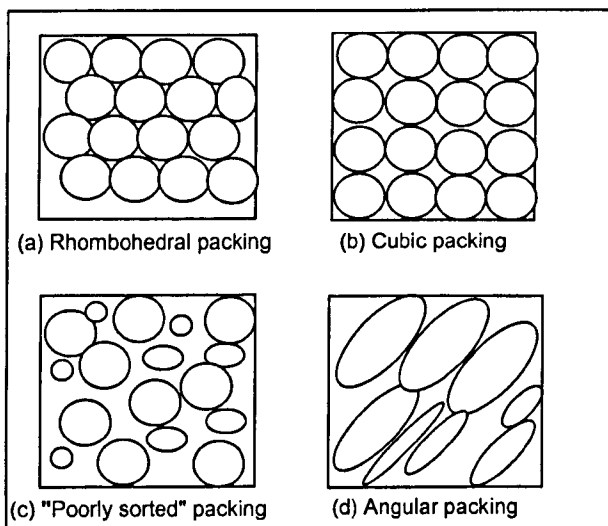


**Fig 3-3 Various packing arrangements**

## 3.4 Grain size profiling and Measurement techniques

Grain size profiling represents the logging of grain size and other textural parameters such as sorting, shape, roundness etc, for a particular reservoir, well, or field depth by depth or with time. Grain size profiles provide a better means of evaluating or assessing sediment depositional

patterns and depositional history, and for delineation of depositional environment for field development. They have also been used as a basis for gravel pack design as pointed out in chapter two. They can also be useful in the selection of loss control materials for drilling in highly porous and highly permeable formation.

The methods/techniques available for measuring and constructing grain size profiles in real time are very crucial to the successful application of the concept of change in grain size distribution to real time sanding potential prediction. Methods used for measuring grain size distribution are diverse and are normally chosen depending on whether the rock is consolidated or indurated<sup>64</sup>, the expected grain size range and the accuracy level desired. The shortcomings of many of the current grain size distribution revolve around the following:

- They are not capable of real time continuous grain size distribution prediction; they can only predict at discreet points.
- They are heavily dependent on cores, which are presently not often available due to high acquisition cost.
- Representation of grain size distribution with a simple correlation between grain size and some other petrophysical and textural parameters.
- Representation of grain size distribution with only median grain size; however two parameters (median grain size and sorting) best characterise grain size distribution

### **3.4.1 Sieve analysis**

Of the numerous methods available for measuring grain size distribution of clastic rocks, whether consolidated or unconsolidated, sieve analysis is the most widely used and is perhaps the oldest.

Sieve analysis is very tedious and time consuming; its wider application may be a result of being the most tested and the cheapest of all the

techniques<sup>64</sup>. Another reason that perhaps contributes to its wider application is the functionality to be used for a wide range of particle sizes ranging from as low as 36µm to 8mm, a range representing fines and gravel end members. The range of particle size found in the oil and gas industry is usually within this range.

Sieve analysis generally involves the following steps:

1. Collect Sample
2. Disaggregate sample, if it is consolidated, into individual grains
3. Stack sieves onto each other, and make sure the most appropriate range of mesh sizes compatible with the expected grain size distribution of sample is used.
4. Measure a pre-determined weight from the sample into the uppermost sieve; make sure that the weighed portion is representative of the sample.
5. Cover up the uppermost sieve and set the stack of sieves on a mechanical shaker. Mechanical shakers are usually timed to work between 15 to 20 minutes depending on the quantity of sample and the amount of fines it contains
6. After 20 minutes, remove the stack of sieves and collect the sand samples retained in each sieve.
7. Weigh the sand retained in each sieve and convert them to the percentage of the total weight
8. Plot the cumulative weight percentage on the abscissa and the corresponding grain size represented by the corresponding mesh sizes on the ordinate on either an arithmetic or probability scale.

Histogram and frequency curve can also be used to present sieve analysis data graphically but they are not commonly used. Figures 3-4 to 3-6 show examples of common graphical presentations of sieve analysis data. The resultant curve or ogive is referred to as grain size distribution curve.

The above procedures describe dry sieving and are usually used for sand sample that contains little or no fine particles such as mud or fine silts.

For sand samples that contain appreciable amount of fine particles, wet sieving is usually used.

Wet sieving involves placing the sample, after weighing, in a 200 mesh sieve and washing the sample under gentle running water. When the sample has been rid of all or nearly all the fines, the washing is stopped. The sample is then poured onto a clean surface and either oven-dried or air-dried. The dry sieving procedures can then be utilised to determine the grain size distribution of the remaining sample fraction. The weight loss, which is equivalent to the weight of the fines washed off can be recorded with what is retained in the pan.

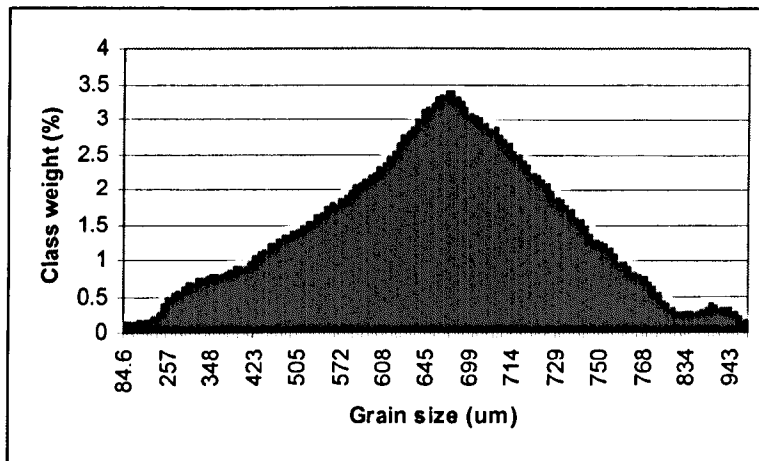


**Figure 3-4 Sieve data presentation using histogram**

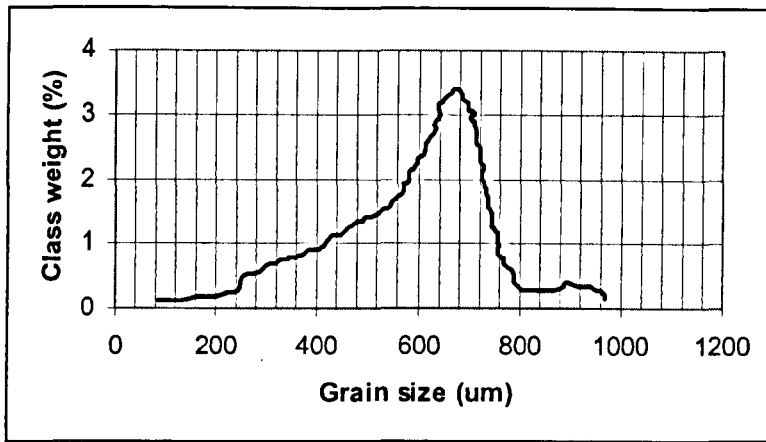


**Figure 3-5 Sieve data presentation using frequency curve**

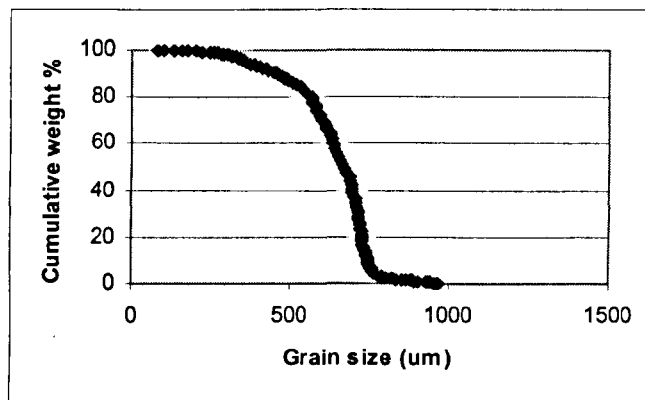


**Figure 3-6 Sieve data presentation using arithmetic cumulative curve**

### 3.4.2 Statistical presentation of sieve data

In using statistical parameters to describe grain size distribution, an assumption of normal distribution is often made. However some sediments or rocks may exhibit distributions that are not normal.

Sieve data from sieve analysis have to be presented in one of the graphical methods described in section 3.4.1. The cumulative arithmetic or probability curve is however the only graphical display method that allows the computation of the statistical measure of grain size distribution using various statistical formulae. The cumulative probability curve is

more reliable than the cumulative arithmetic curve where there is a need for the extrapolation of the grain size curve to the range not covered by the distribution curve due perhaps to limited data. However, the cumulative arithmetic curve is more widely used. This may be due to the fact that it readily gives a clue to the grain size parameters especially sorting with just ordinary visual inspection.

The statistical parameters in common use for grain size distribution description are grouped into:

- Those that measure central tendency
- Those that measure symmetry or preferential spread to one side of the average
- Those that measure the degree of concentration of the grains relative to the average

These parameters are discussed in more details in sections 3.4.2.1 to 3.4.2.6

### 3.4.2.1 Mean

This is used as a statistical measure of central tendency. The mean is usually affected by the skewness of the sieve data; it thus gives a better reflection of the grain size especially for distributions that are not normal.

Folk (1974)<sup>74</sup> gave the most acceptable formula for computing the mean from the arithmetic cumulative curve.

$$M = \frac{\phi_{16} + \phi_{50} + \phi_{84}}{3} \quad 3-34$$

### 3.4.2.2 Median grain size

This is the most commonly used statistical measure of central tendency. It corresponds to the 50<sup>th</sup> percentile or  $d_{50}$  of the distribution curve and

divides the distribution into two. In a normal distribution, it divides the curve into two equal parts, but in a highly skewed distribution where the sieve data concentrates within a particular size range, it may not give a true reflection of the grain size

### **3.4.2.3 The Mode**

This is the grain size in the cumulative distribution curve, which occurs most frequently. The mode is also not affected by the grain size in the other part of the distribution. It also therefore does not give a true reflection of the grain size

### **3.4.2.4 Sorting**

This parameter measures the spread of the sieve data around the centre on the cumulative curve. Many of the formulae proposed for the computation of sorting are not reliable as they give the sorting in the middle of the curve<sup>64</sup> (see section 3.3.1.2). The most reliable and the most widely used formula (equation 3-3) together with the qualitative evaluation scheme by Folk<sup>74</sup> (Table 3-2) has been given in section 3.3.1.2.

### **3.4.2.5 Skewness**

This is a statistical parameter that measures the degree of asymmetry of a cumulative curve. A normally distributed curve has a skewness of 0. A distribution skewed with its tail to the right is described as a positively or fine skewed distribution; while a skewed distribution having its tail to the left is described as a negatively or coarse skewed distribution (figure 3-7). The more the skewness value departs from 0, the greater the degree of

asymmetry. Table 3-1 by Folk (1974)<sup>74</sup> gives both the qualitative and quantitative description of skewness.

The formula by Folk (1974)<sup>74</sup> is the most widely used for computing skewness.

$$SK = \frac{\phi_{16} + \phi_{84} - 2\phi_{50}}{2(\phi_{84} - \phi_{16})} + \frac{\phi_5 + \phi_{95} - 2\phi_{50}}{2(\phi_{95} - \phi_5)} \quad 3-35$$

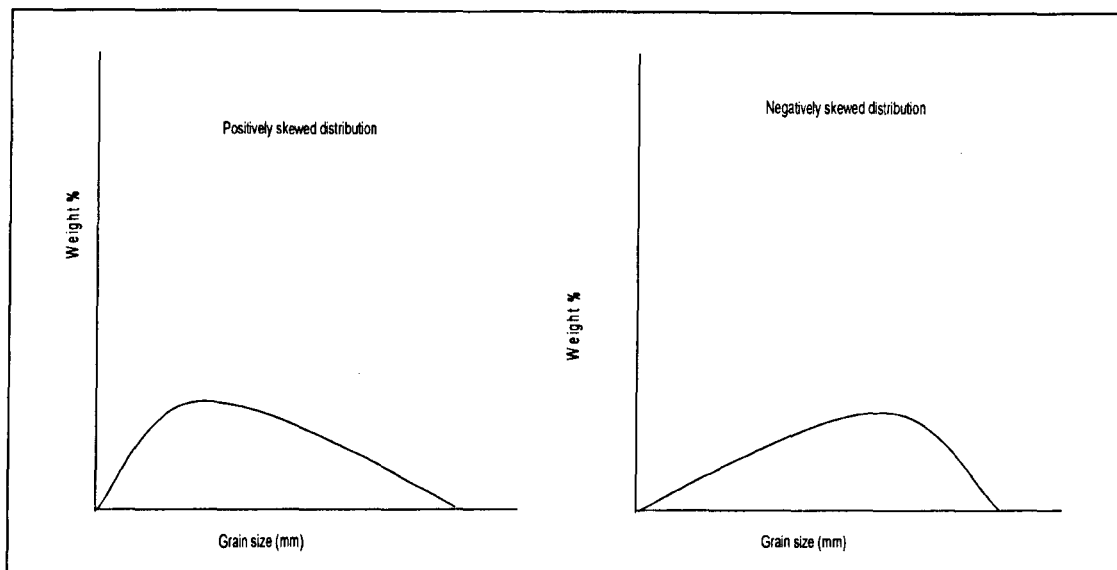


**Figure 3-7 Skewed distributions**

<b>Table 3-3 Skewness interpretation</b>	
Very negatively skewed	-1.0 - -0.3
Negatively skewed	-0.3 - -0.1
Nearly symmetrical	-0.1 - +0.3
Positively skewed	+0.1 - +0.3
Very positively skewed	+0.3 - +1.0

### 3.4.2.6 Kurtosis

This measures the degree of peakedness or departure from the normal distribution. Kurtosis was defined by Folk (1974)<sup>74</sup> as the ratio of the sorting in the tail of the curve and the sorting in the central portion; the formula for calculating this is given in equation 3-36. If the central portion is better sorted than the tail portion, curve is described as excessively peaked or leptokurtic; if the tail is better sorted than the central portion, the curve is described as flat peaked and platykurtic. Table 3-1 shows the Folk's qualitative interpretation of kurtosis.

$$K_T = \frac{\phi_{95} - \phi_5}{2.44(\phi_{75} - \phi_{25})} \quad 3-36$$

Very platykurtic	< 0.67
platykurtic	0.67 – 0.90
Mesokurtic	0.90 – 1.11
Leptokurtic	1.11 – 1.50
Very leptokurtic	1.50 – 3.00
Extremely leptokurtic	> 3.00

### 3.4.3. Direct Measurement

Direct measurement of grain size involves manual counting and visual inspection of grain particle to determine grain size distribution. This method is used only for larger sized particles such as gravels and cobbles which are not indurated or cemented together. It is however not commonly used as it is very slow and takes time. Above all, it does not support real time applications.

---

### 3.4.4 Laser diffraction method

Laser diffraction grain size analysis is particularly useful for the analysis of sand fraction of sub-micron sizes. It has therefore been used extensively for the analysis of rock samples, which contain large proportion of fines such as mica flakes<sup>86</sup> and carbonate<sup>87</sup>.

The technique is based on the principle of light beam scattering by small particles<sup>88</sup>. During measurement, particles are passed through a focussed laser beam. These particles scatter the light at an angle that is inversely proportional to their size. The angular intensity of the scattered beam is then measured by a series of photosensitive detectors. The map of scattering intensity versus angle is the primary source of information used to calculate the particle size<sup>89</sup>. The Scattering of particles is accurately predicted using either Fraunhofer's or Mie's theory depending on the particle size wavelength<sup>88</sup>. Examples of common laser diffraction based equipment for grain size distribution analysis in market are Malvern Mastersizer 2000 and Beckman-Coulter LS 230<sup>90</sup>

Apart from the obvious shortcomings of the laser diffraction as a method of grain size distribution analysis such as heavy dependence on core availability and unsuitability for use in real time grain size distribution analysis, a sparing presence of fine mica in a sand sample may cause significant alteration of grain size distribution characteristics due to likely overestimation of the fine mica portion.

### 3.4.5 Digital video core images<sup>91</sup>

This method was a novel method of grain size distribution and petrophysical properties prediction in 1998 when it was first reported. It was an extension of the earlier core photography method, which had been used for decades for the purpose of grain size distribution analysis. In core photography, photographs of core are usually printed on papers with a few core lengths.

In contrast, digital video core image technique involves taking core digital images continuously along a slabbed core. A special software converts the core images automatically to a seamless, continuous core image of the complete length of the core interval. The video core images are then processed digitally with a modified Gray Level Co-concurrence Matrix (GLCM) textural feature to obtain light/shadow patterns and textural spectral of the rock. The textural spectra are then calibrated with the measured petrophysical parameters by use of multivariate partial least regression to derive a model. Similar video core images from a completely different area are then used to estimate properties of the core material.

Even though the results presented by Oyno et al (1998)<sup>91</sup> looked promising, it is obvious that the method only measures median grain size; median grain size alone does not characterise a size distribution. Besides, it does not support real time application as it also depends heavily on core availability.

### 3.4.6 Empirical Models

Empirical models have been used for ages to estimate grain size through simple correlations with other textural and petrophysical parameters. Many of these models are however developed specifically for permeability estimation.

Slichter (1899)<sup>92</sup> presented an equation (eqn. 3-37) relating permeability with grain size and packing parameter.

$$k = 10.2 \frac{d}{a_p} \quad 3-37$$

Where  $d$  is grain size (mm) and  $a_p$  is the packing parameter

Perhaps realising that packing is difficult to measure; Slichter<sup>92</sup> developed a simple relation (eqn. 3-38) between packing and porosity for easy computation of packing

$$a_p = 0.97\phi^{3.3} \quad 3-38$$

Where  $\phi$  is porosity

This equation can only estimate grain size; also, Slichter<sup>92</sup> did not specify whether the grain size in the equation is the mean or median grain size. This information is vital for decision on the appropriateness or otherwise of the model for application to log-normal grain size distribution.

Building upon Slichter's work, Kozeny (1927)<sup>93</sup> developed an empirical equation, later modified by Carman (1937)<sup>94</sup>. This equation is today generally called Kozeny-Carman equation, and it correlates permeability with porosity and grain surface area.

$$k = \frac{\phi^3}{5S_A(1-\phi)^2} \quad 3-39$$

$S_A$  is the grain surface in  $\text{mm}^{-1}$  area and  $\phi$  is porosity in fraction.

Krumbein and Monk (1942)<sup>95</sup>, in a bid to improve upon Kozeny and Carman efforts, developed an empirical model using very well sorted sediment samples ranging from -0.75 to 1.25 phi in mean grain size and standard deviation ranging from 0.04 to 0.08phi. The model relates permeability with geometric mean grain diameter and standard deviation or sorting.

$$k = 760d_m^2 e^{-1.3\sigma_s} \quad 3-40$$

$d_m$  is the geometric mean diameter in mm,  $\sigma_\phi$  is the standard deviation or sorting; permeability  $k$ , is in Darcy unit.

This model may not perform well when used for sand with sand sizes and sorting outside the ranges used by Krumbein and Monk (1942)<sup>95</sup> for their experiment.

The observed shortcomings of the early models were to lead to the development of another permeability model by Bergs<sup>96</sup> in 1970. The model (equation. 3-41) relates permeability of sand to the median grain size, porosity and a term he called phi percentile deviation of sand grain size, which equals ( $\phi_{84.1} - \phi_{16.5}$ ). This equation was reported to perform well when used for 30% – 40% porosity sand<sup>97</sup>. Oluyemi et al (2006)<sup>14</sup> have also noted the negative impact of porosity effect on the performance of the model when transposed and used for the estimation of standard deviation and sorting. The result shown in figure 3-8 is the comparison of Bergs and Krumbein and Monk performance on a set of experimental data generated using 20/40 sand. The result further justifies Oluyemi et al's<sup>14</sup> conclusions.

$$k = 5.1 * 10^{-6} * \phi^{5.1} * d_m^2 * e^{-1.385\sigma_\phi} \quad 3-41$$

$\phi$  is porosity in percent,  $d_m$  is median grain size in mm; and  $k$  is the milliDarcy unit

Generally, empirical permeability models need to be transposed if they must be used to estimate the grain size. Transposing empirical equations which are often derived by fitting of appropriate models into experimental or field data may not be mathematically expedient and may constitute potential source of error.

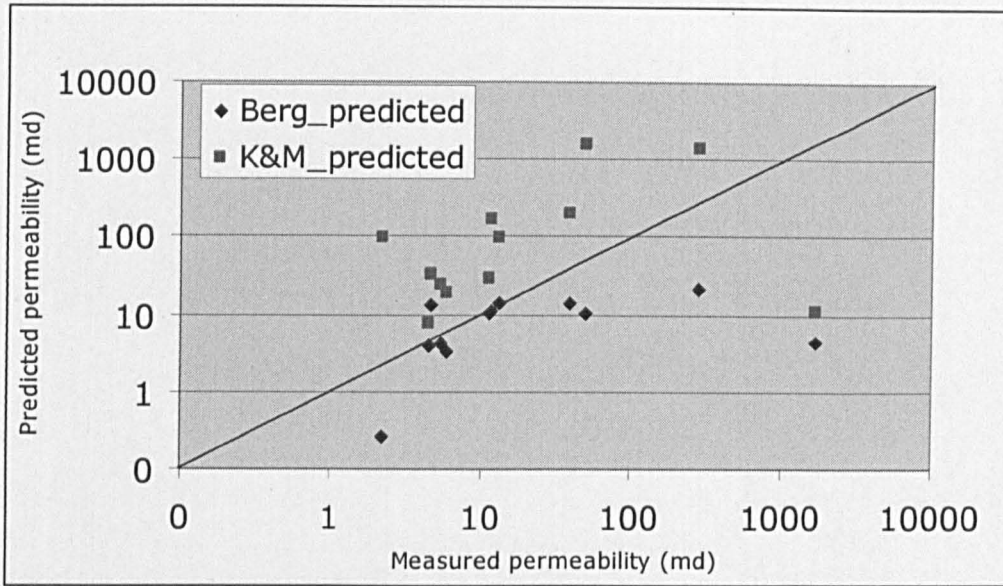


**Figure 3-8 Comparison of the performance of Bergs and Krumbein and Monk equations.**

### 3.4.6 Neural Network Technique

Neural network based grain size distribution is a relatively new technique. It was first introduced by Oyenehin and Faga (1999)<sup>5</sup> to blaze the trail in real time prediction of grain size distribution for gravel packing design optimisation.

Their methodology involved presentation of a variety of wireline logs and corresponding core data of seven percentile sizes, as input and output pair, to a commercial feed-forward back-propagation neural network to develop a neural network model for continuous real time grain size distribution prediction. The theoretical basis for using logs consists in the measurement of certain formation physical properties by the log parameters; for example bulk density of formation from density logs. These properties are often translated to the petrophysical and textural properties. However, the commercial neural network used as the platform for the model development is known to be very slow and non-flexible; it also has fixed training algorithms and its inner working is difficult to understand. Also the presentation of seven percentile sizes to the network

as the target outputs is potentially capable of increasing the network size and hence its inner complexity. This may make learning very slow and prediction error margin very high.

### **3.5 Summary**

In this chapter, the various sand prediction models and techniques being used in the oil and gas industry have been discussed in terms of their underlying principles, theories and extent of use in the oil and gas industry. Also discussed are some of the limitations of these current models or techniques, which may make their predictions fraught with unacceptable error level and unreliable.

The common methods of grain size distribution analysis are discussed; the link between grain size distribution and sand failure and production has also been established and attributed to change in grain size distribution parameters such as sorting, median grain size, packing and grain shape when a formation begins to produce sand.

In summary, this chapter has shown that change in grain size distribution parameters may effect a change in the formation strength, which may in turn lead to failure and sand production.

---

## Chapter 4

# Geomechanical evaluation of rock

In this chapter, the static and dynamic elastic properties of rocks and the relationship between the two are reviewed. In-depth understanding of these properties is considered helpful in understanding basic geomechanical control on the strength of reservoir rocks. The chapter also covers the review of the different parameters used in the oil and gas industry for the evaluation of rock strength; these are discussed in the light of their current level of application, with greater emphasis placed on the unconfined compressive strength (UCS). In situ strength evaluation of reservoir rock also needs to consider the extrinsic factors around the rock environment, which impact its strength; most important of these extrinsic factors are the in situ stresses acting on the rocks. These are also discussed and the methods or techniques available for their estimation reviewed. In addition the three most widely applied failure criteria for rock failure analysis and the current sanding prediction models in the oil and gas industry are also discussed.

### 4.1 Elastic properties of rocks

The elastic properties of reservoir rocks are usually classified as static and dynamic. The static elastic rock properties are determined using standard laboratory tests on cores of reservoir rocks<sup>98-99</sup>; the dynamic rock properties are measured either in the laboratory, using acoustic sonic and ultra sonic wave velocities on reservoir rock core; or in situ, using well log techniques under a hydrostatic pressure that lies between the pressure of the mud column and the reservoir pore pressure<sup>100-101</sup>. However the in situ measurement cannot be directly obtained; but is generally acquired indirectly through sonic and bulk density well logs interpretation.

In addition, because the dynamic elastic properties cannot be measured directly, certain equations have been developed to estimate them<sup>100-101</sup>.

These equations are based on the assumption that the reservoir rock is perfectly linear elastic, homogeneous, and isotropic<sup>3</sup>. This assumption is perhaps responsible for the differences that are usually observed between the static and dynamic values of rock elastic properties. In the laboratory measurement of elastic properties however, it is the static properties that are normally measured<sup>99</sup>

Though laboratory measurement allows for direct estimation of elastic properties, it is fraught with a lot of shortcomings which may increase the uncertainties surrounding its results. The most important of these are the core alteration<sup>98</sup>, inability to simulate effectively the in situ stresses acting on the reservoir rock in place and also to account effectively for the reservoir fluid effect. In the same vein, the increased differential stresses in the vicinity of a well and the possible invasion of the formation during drilling<sup>99</sup> may affect the results of elastic properties measurement from well logs.

Elastic properties of rocks are basically four; they are (a) Young Modulus, (b) Shear Modulus, (c) Bulk Modulus and (d) Poisson ratio.

### 4.1.1 Young Modulus

Young modulus is a measure of a rock ability to resist deformation. In other words, it measures the rock's stiffness. It is defined as the ratio of the rate of change of stress with strain; the mathematical expression for this is given in equation 4-1.

$$E = \frac{d\sigma}{d\varepsilon} \quad 4-1$$

$d\sigma$  is the change in stress and  $d\varepsilon$  is the change in strain.

The static value of Young Modulus can be determined experimentally in the laboratory from the slope of the purely elastic portion of stress-strain

plot generated in a tensile test conducted on the sample of a rock, where the strain is a linear function of applied stress.

Dynamic values of Young modulus have become important as a result of the current need for real time geomechanical evaluation of rock. Many methods are available to estimate this<sup>3</sup>. Hosking (1955)<sup>101</sup> related the dynamic value of Young modulus with the velocity of propagation in rock of ultrasonic pulse,  $v_r$ .

$$E = \frac{\rho_b v_r^2}{12g} \quad 4-2$$

$g$  is acceleration due to gravity,  $\rho_b$  is bulk density.

Dynamic Young modulus has also been correlated with the Shear modulus and Poisson ratio (see table 4-1). Shear modulus and Poisson ratio are estimated from sonic and density logs using the formula given in Table 4-1. Specifically, the compressional and shear waves' interval transit times are interpreted from sonic log to estimate Poisson ratio using the appropriate formula (Table 4-1); similarly, the bulk density of the host medium (the formation rock) is interpreted from the bulk density log. The data for these parameters can then be fed into the appropriate formula (Table 4-1) to compute dynamic Young modulus.

### 4.1.2 Poisson ratio

Poisson ratio measures the ratio of transverse or lateral strain to axial strain. When a material is under compression or tension parallel to one of its axis, the material will experience a change in length and diameter. This change in length and diameter is a measure of strain undergone by the material. The direction of the applied stress will determine the strain classification.

Supposing the direction of applied stress in Figure 4-1 is along x axis, the Poisson ratio can be written as:

$$\nu = \frac{\varepsilon_y}{\varepsilon_x} \quad 4-3$$

Where  $\varepsilon_y$  is the transverse strain;  $\varepsilon_x$  is the axial strain.

As pointed out earlier, and shown in Table 4-1, Poisson ratio can be computed from sonic log or determined through static test in the laboratory.

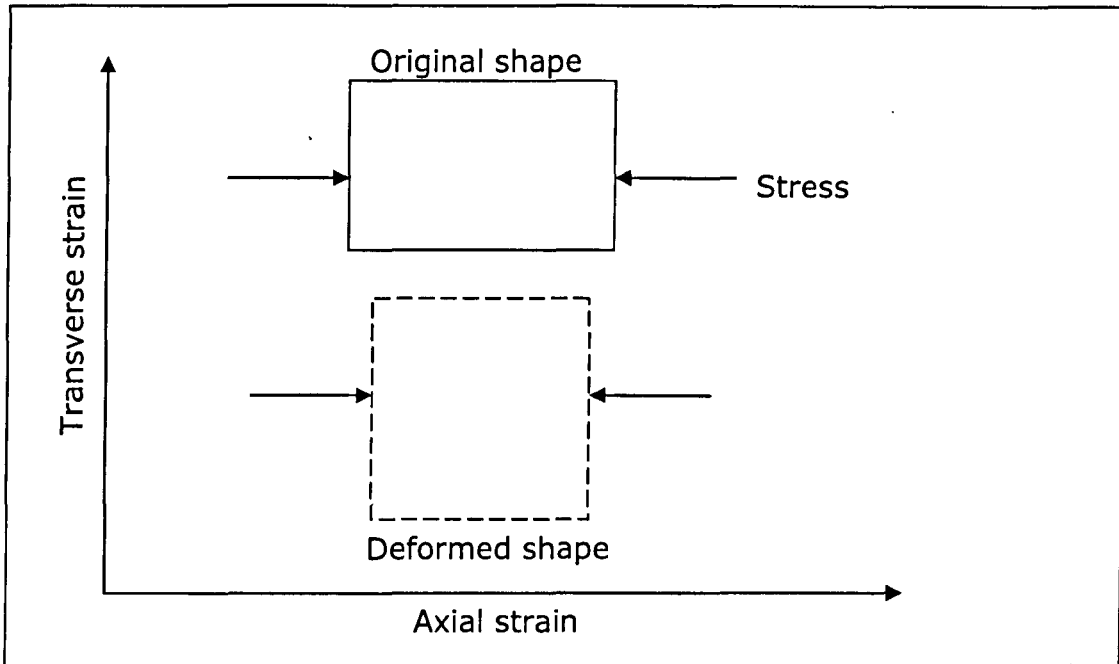


**Figure 4-1 a schematic showing transverse and axial strains**

### 4.1.3 Bulk Modulus

Bulk modulus is also called a variety of other names such modulus of rigidity, incompressibility etc. It is called incompressibility because it is an inverse of compressibility (equation 4-5). It is the ratio of change in hydrostatic pressure (stress) to the corresponding volumetric strain<sup>3</sup>:

$$K_b = \frac{\Delta P}{\Delta V/V_0} \quad 4-4$$

$K_b$  is bulk modulus (psi),  $\Delta P$  is the change in stress or pressure,  $\Delta V$  is the change in volume and  $V_0$  is the initial volume.

$$K_b = \frac{1}{C_b} \quad 4-5$$

Where  $C_b$  is the bulk compressibility.

The equation for estimating the dynamic value of bulk modulus from sonic and density log is also given in table 4-1. As with other elastic properties, the bulk modulus can be estimated for a material in a laboratory static test.

#### 4.1.4 Shear Modulus

Shear modulus measures the resistance of a rock to change in shape; hence it is also called modulus of rigidity. The static value of shear modulus can be estimated from the laboratory shear experiment by using the mathematical expression:

$$G = \frac{\tau}{\gamma} \quad 4-6$$

Where  $\tau$  is the shear stress; and  $\gamma$  is the shear strain.

It can also be determined straight from other elastic constants such as Young Modulus and Poisson ratio by using the relation<sup>3</sup>:

$$G = \frac{E}{2(1+\nu)}$$

4-7

$E$  is Young modulus and  $\nu$  is Poisson ratio.

From equation 4-7, it is obvious that a rock undergoing a relatively small shear strain after being subjected to a relatively large shear stress will have a large shear modulus, and hence will be more rigid. The formula for estimating the dynamic value is also given in Table 4-1.

<b>Table 4-1<sup>3</sup>: static and dynamic elastic properties</b>		
Coefficient $a = 1.34 \times 10^{10}$ if $\rho_b$ is in g/cm <sup>3</sup> and $t$ is in $\mu\text{s}/\text{ft}$		
Elastic properties	Laboratory static formulae	Field dynamic formulae
Poisson ratio ( $\nu$ )	$\frac{\text{transverse strain}}{\text{axial strain}} = \frac{\varepsilon_T}{\varepsilon_a}$	$\frac{0.5 (t_s/t_c)^2 - 1}{(t_s/t_c)^2 - 1}$
Young's Modulus ( $E$ )	$\frac{\text{stress}}{\text{strain}} = \frac{\sigma}{\varepsilon}$	$2 \times \frac{\rho_b}{t_s^2} (1 + \nu) \times a$
Bulk Modulus ( $K_b$ )	$\frac{\text{hydrostatic pressure}}{\text{volumetric strain}} = \frac{\Delta P}{\varepsilon_v}$	$\rho_b \left( \frac{1}{t_c^2} - \frac{4}{3t_s^2} \right) \times a$
Shear Modulus ( $G$ )	$\frac{\text{applied stress}}{\text{Shear strain}} = \frac{\tau}{\gamma}$	$\frac{\rho_b}{t_s^2} \times a$
$t_c$ the compressional wave interval transit time $t_s$ is the shear wave interval transit time $\rho_b$ is the bulk density		

## 4.2 Rock strength evaluation

Evaluation of rock strength is a routine activity in the oil and gas industry. Virtually all field operations require input of rock strength evaluation

results. In drilling, evaluation of rock strength is vital to making decisions on wellbore stability issues during and after drilling and in casing design and placement; during production, information on rock strength can be a veritable tool in drawdown and production rate management; in sand control completions such as frac pack, selective perforation etc, rock strength evaluation is used in the selection of strong zones for perforation; also in stimulation operation for enhanced oil recovery, rock strength evaluation is important if the operation must be optimised.

In evaluating the strength of rock, many parameters including the elastic properties of rocks discussed in section 4-1 have been used. Parameters like Unconfined Compressive Strength (UCS), Thick Walled Cylinder (TWC) strength, angle of internal friction, point load strength, tensile strength etc are the common ones in use. However, UCS is the most widely used<sup>3,84,102-103</sup>.

Rock strength generally depends on the intrinsic factors related to the rock and extrinsic factors related to the rock environment. Intrinsic factors governing the strength of rock include porosity, grain size, sorting, mineralogy or lithology, cementation and cementation type<sup>84-85</sup>. The extrinsic factors include stress around the rock and the operational factors like drawdown, bean-up pattern, production rate, depletion profile, stimulation option, stress distribution and redistribution and completion strategy<sup>84</sup>. Many of these factors are however interconnected in terms of their effects on sand production potential of a formation.

Estimation of rock strength has been made possible by mechanical testing on rock, use of prediction models formulated mathematically, analytically or statistically and recently by neural network models.

### **4.2.1 Unconfined Compressive Strength (UCS)**

Unconfined compressive strength is the most widely used parameter for rock strength characterisation even in other fields of engineering. Typically UCS is estimated by conducting uniaxial or triaxial laboratory

test on core samples obtained from the depth of interest. The core sample is loaded between two steel platens of a pre-calibrated compressive loading machine, and a load is applied at a constant pre-determined rate. Load and displacement are recorded throughout the test, and for some time after peak failure has occurred (Figure 4-2), so that post peak deformation behaviour is recorded. The static UCS is usually calculated using equation 4-8

$$UCS = \frac{F_{peak}}{A} \quad 4-8$$

where  $F_{peak}$  = peak load; A = cross sectional area of core.

Other laboratory tests in use for the laboratory estimation of UCS are the micro indentation test<sup>102</sup>, Schmidt hammer test<sup>103</sup> and scratch test<sup>104-105</sup>. Micro-indentation test involves the use of special micro-indentation equipment. Loads of known values are increasingly applied on the rock core. The indentation depth on the core for every added load is monitored and recorded. The Hardness Number, a dimensionless parameter is then calculated from the load and indentation data using a formula specific to the model/brand of equipment used. For Schmidt hammer test, a Schmidt hammer rebound Hardness of a core material is determined with the use of a Rebound Hammer. A Rebound Hammer consists of a spring-loaded steel piston. This piston is released in a test so that it strikes a metal plunger, which is in contact with the rock surface being tested. The hammer measures the rebound value, which is then correlated with the UCS of the same material measured in laboratory uniaxial or triaxial test. In the case of a Scratch test, special equipment is also used. The surface of the rock is scratched at constant depth by a cutter travelling at a constant velocity. The force applied on the cutter is monitored and recorded. This force is usually used to derive UCS of the core.

These methods are however new and yet to gain industry confidence. Perhaps as a result of cost and difficulty surrounding core acquisition, laboratory based UCS estimation is also being gradually discouraged.

Apparently in a bid to solve the problems surrounding laboratory based estimation of UCS, a number of workers have developed models relating UCS with petrophysical and textural parameters using varieties of modelling techniques<sup>84-85, 106-109</sup>.

Sarda et al (1993)<sup>84</sup> utilised some published data in a statistical operation to develop a model relating UCS and porosity. The general form (equation 4-9) of an earlier model relating UCS with porosity, developed by Knudsen (1959)<sup>110</sup> for porous ceramic materials was used as a platform for the development of his model.

$$UCS = \sigma_0 e^{-\beta_c \phi} \quad 4-9$$

$\sigma_0$  and  $\beta_c$  are constants;  $\sigma_0$  is dependent on formation damage whilst the  $\beta$  is dependent on the orientation of the pores with respect to the loading direction.

Similarly Edlmann K. et al (1998)<sup>85</sup> used statistical least squares regression method to develop models for predicting UCS and other elastic moduli. The specific equation they derived for predicting UCS is given in equation 4-10.

$$UCS = -3.225\phi + 129.54 \quad 4-10$$

Where  $\phi$  is porosity.

This model suggests UCS is a linear function of porosity. Four important shortcomings are however associated with this and their other models for estimating other elastic parameters:

- They are dependent on only a few parameters and do not take into account other parameters which could possibly affect UCS.
- They were formulated based on the assumption of very simple relationships between UCS and these parameters.

- They were developed for specific fields or petroleum provinces and cannot be transferred to other fields or petroleum provinces.
- They have operating window outside of which they cannot be applied.

Tokle et al (1986)<sup>106</sup> used multiple regression analysis to develop a model for UCS estimation using direct log parameters. The direct log parameters they considered include natural gamma ray, acoustic travel time, bulk density, neutron porosity, calliper and rock number representing lithology. These parameters were made dimensionless and normalised to get their numerical values in the same range. The model developed is of the form:

$$UCS = aGR' + bDT' + cRHOB' + dNPHI' + eCAL' + fROK' + g \quad 4-11$$

GR = natural gamma

DT = Acoustic travel time

RHOB = bulk density

NPHI = neutron porosity

CAL = Calliper, inches

ROK = rock number from numerical lithology log

A, b, c, d, e, f, and g are regression constants.

However the relationship between UCS and these parameters is much more complex than the picture painted by this model. Simple regression analysis may not resolve this satisfactorily.

Artificial intelligence methods especially neural network have also recently found wider use in the prediction of UCS. Meulenkamp and Grima (1999)<sup>107</sup> presented five parameters including Equotip hardness reading, porosity, density, grain size and rock type to a back propagation neural network to predict UCS. They converted "Grain size" and "type of rock" from nominal to numerical values before presenting them alongside other parameters to the network. The numerical values used in the conversion

of "grain size" represent ranges of values and could not be said to be representative of actual grain size of the rock if they were actually analysed in the laboratory using sieve analysis. Besides the equotip hardness test data cannot be obtained in real time and the data were obtained from hard igneous rock making them unstable for making predictions for soft usually unconsolidated sedimentary rocks of petroleum reservoirs.

Singh et al (2001)<sup>108</sup> work was similar to Meulenkamp and Grima (1999)<sup>107</sup>. They presented rock type, mineral composition, grain size, area weighting, aspect ratio, form factor, and orientation of foliation planes to a feed-forward network to predict three strength attributes namely UCS, tensile strength and axial point load strength. Even though their NN model was more versatile and robust than that used by Meulenkamp and Grima (1999)<sup>107</sup>, it also suffers the same setbacks.

However most of the works done so far on UCS prediction using the neural network modelling technique have been based on some input parameters whose data can only be derived from core analysis, which may necessitates time consuming laboratory experiment. Besides, some of the information, being not measurable and in qualitative form, often have to be converted to numerical form to be used in the modelling work. The conversion of qualitative to quantitative or numerical information may not give a true representation of the actual data obtained by direct measurement.

Xue T., et al (2004)<sup>109</sup> reported the use of numerical methods for mechanical properties prediction. In their work, they assumed a rock mass to be a continuous object with no space, based on the continuity hypothesis of engineering. However, the numerical methodology they used still depended on the results of laboratory measurements of the common rock elastic properties to construct a rock mass model for the numerical implementation. This is an indication that numerical solution to mechanical properties estimation is not simple and may not be provide reliable results if used independently.

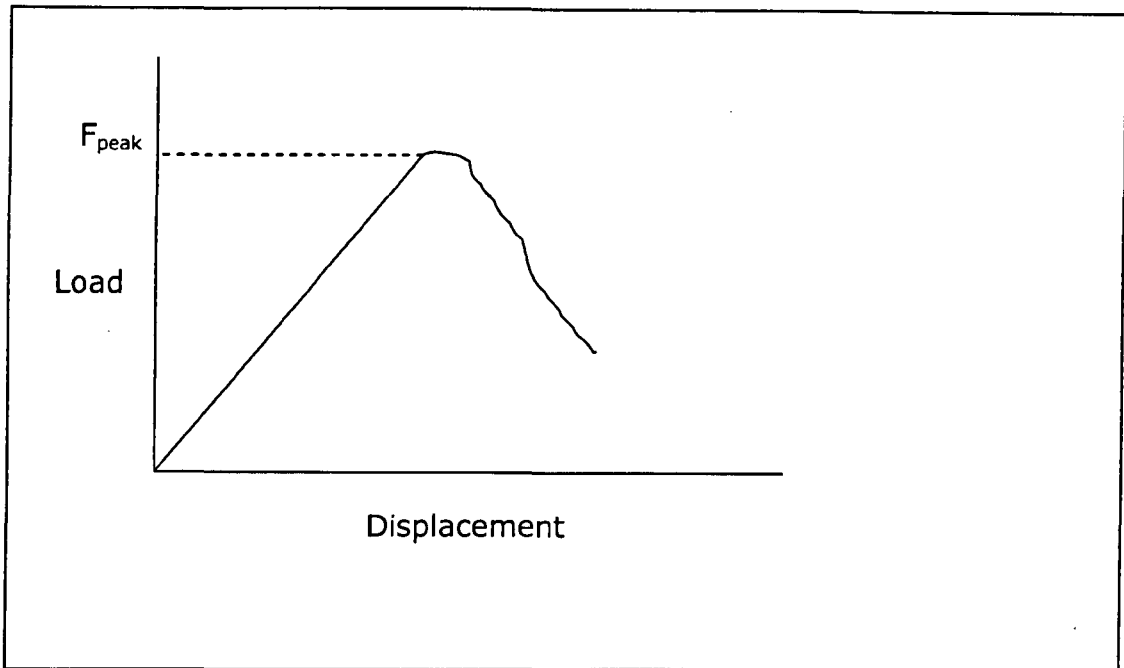


**Figure 4-2 A typical load versus displacement curve from laboratory UCS determination**

### 4.2.2 Cohesive strength

Cohesive strength is not commonly used in geomechanical evaluation of rocks for failure analysis and sanding potential evaluation. Perhaps this is due to the fact that it does not, in practice, represent the total stabilising strength of a rock formation but only a part of the stabilising strength.

Mohr-Coulomb shear failure criterion relates the shear strength of rock at failure to the cohesive strength in a linear approximation. A plot of shear strength at failure against the applied normal stress gives a linear equation (this equation is presented in section 4-4 (equation 4-35)). Cohesion represents the intercept of the linear model. When re-written in terms of the peak stress and confining stress in a triaxial compression, Mohr-Coulomb also relates cohesion with the Unconfined Compressive Strength<sup>111</sup>.

$$\sigma_{ucs} = \frac{2C \times \cos \theta}{1 - \sin \theta}$$

4-12

C is cohesion and  $\theta$  is angle of internal friction.

### 4.2.3 Tensile strength

Tensile strength is also not often used for failure analysis perhaps because its magnitude is lower than the equivalent unconfined compressive strength. In practice, the ratio of tensile strength to that of Unconfined Compressive Strength is of the order of 10 - 100<sup>112</sup>, with the average being 20.

The simplest tensile test to perform in order to determine tensile strength is the Brazilian test. However experience has shown that tensile strength in many rocks is lower than that determined from compressional yield data<sup>113</sup>.

Capes (1980)<sup>114</sup> and Schubert (1984)<sup>115</sup> related, based on statistical-geometrical considerations, the tensile strength,  $\sigma_T$  of a rock to the cohesive force  $F_c$ , of a single bond among the rock particles.

$$\sigma_T = \lambda_n \frac{1 - \phi}{\phi} \frac{F_c}{4r_g^2} \quad 4-13$$

$\lambda_n$  is a factor accounting for non-uniform particle size effects on total rock strength.  $\lambda_n = 6 \approx 8$  is suggested for particles with a narrow size distribution and  $\lambda_n = 1.9 \approx 14.5$  for packs with wider particle size distribution<sup>115</sup>.  $F_c$  is the cohesive bond force due to capillary pressure of water.  $r_g$  is the radius of grain particles.

Assuming perfectly spherical grains,  $r_g$  in equation 4-13 can be written in terms of median grain size,  $d_{50}$ , and substituted back to give equation 4-14

$$\sigma_T = \lambda_n \frac{1 - \phi}{\phi} \frac{F_c}{4d_{50}^2} \quad 4-14$$

#### 4.2.4 Thick Walled Cylinder (TWC) strength

Thick Walled Cylinder (TWC) strength is usually determined from the laboratory using Thick Walled Cylinder Test. TWCs are right circular cylinder approximately 3 inches in height and 1.5 inches in diameter<sup>116</sup>. When they are loaded with a test sample, a co-axial hole of 0.5inch diameter is drilled through the sample as shown in Figure 4-3<sup>117</sup>. The inner and outer radii of the TWC are represented as  $r_i$  and  $r_o$  respectively. The inner and outer surfaces are subjected to axial and radial stresses respectively, often in a Hoek cell (Figure 4-4<sup>118</sup>), both of which are usually increased together until the sample fails. The inner radius of the TWC exerts a lot of influence on the results of TWC test <sup>116</sup>.

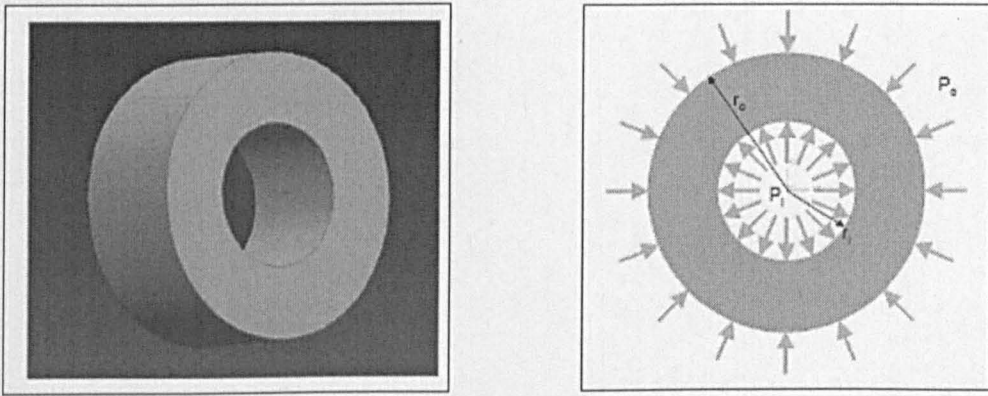
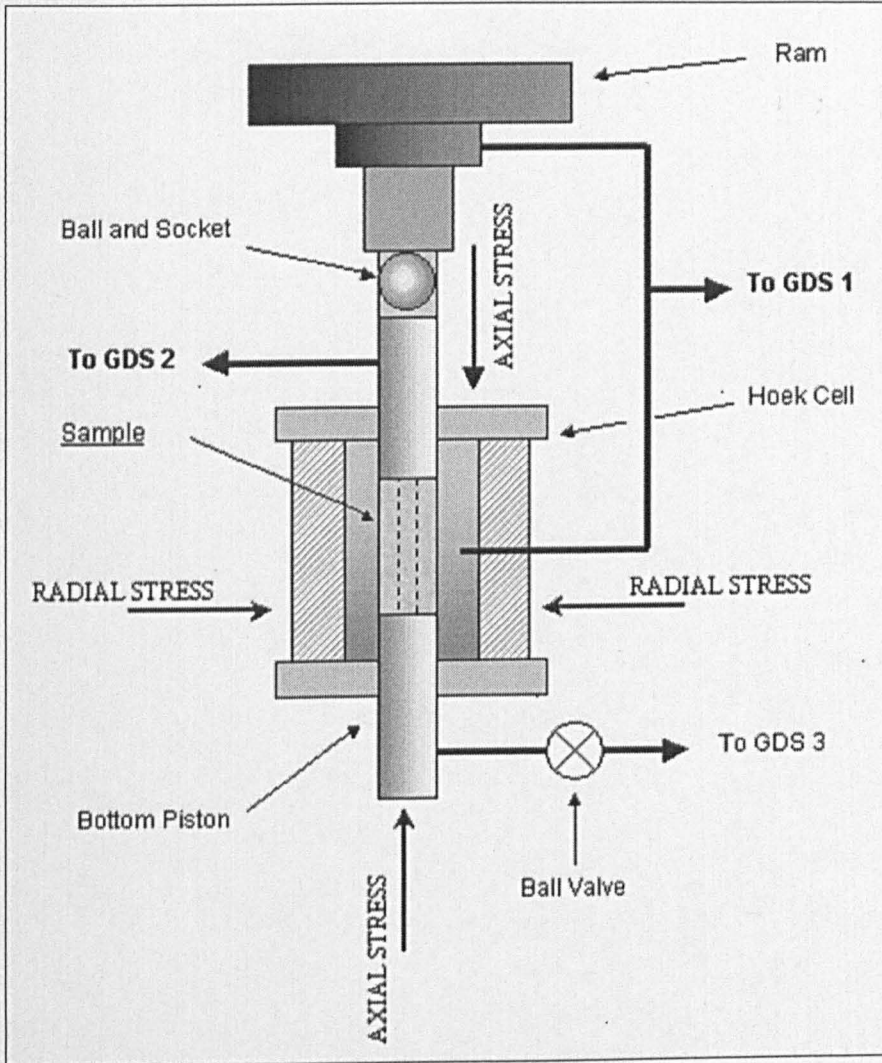


Figure 4-3<sup>117</sup> (a) an open ended TWC

(b) stress loading in TWC



GSD1 – Controls sleeves/confining pressure

GSD2 – Controls pore pressure

GSD3 – Bleeds through the borehole

**Figure 4-4 a schematic of TWC strength test set up<sup>118</sup>.**

## 4.3 Reservoir rock stresses and their estimation

### 4.3.1 Theory of force and stress

Reservoir rocks and the fluid they contain are constantly under the influence of gravitational and tectonic forces<sup>100</sup>. The gravitational forces are due to the burial depth or depth of occurrence; whilst the tectonic forces are due to tectonic activities such as salt diapirs localisation and earthquake. In order to remain in their original state of stress, the rocks and their fluid content resist these forces through inter-granular friction, inter-granular cement bonds and generation of pressure in their fluid components. This resistance is mobilised as the in situ stresses<sup>119</sup> and describes the rock stress state.

A relatively undisturbed rock mass is in a state of constant stress equilibrium and stability. The principal stresses acting on the rock during this period are the vertical stress,  $\sigma_v$ , which acts vertically downwards; the maximum horizontal stress,  $\sigma_H$ , and the minimum horizontal stress,  $\sigma_h$ , both of which act in the horizontal plane. Terzaghi (1936)<sup>120</sup> and Terzaghi (1943)<sup>121</sup> expressed the relationship between the total external stresses acting on the rock and the pore fluid resistance in equation 4-15

$$\sigma' = \sigma - \alpha P \quad 4-15$$

$\sigma'$  is the effective stress;  $\sigma$  is the total external stress;  $P$  is the reservoir pore/fluid pore pressure; and  $\alpha$  is the Biot's poro-elastic constant.

Han (2000)<sup>122</sup> described the effective stress,  $\sigma'$  as the part of the total external stress carried by the rock skeleton and the product of Biot's poro-elastic constant and pore/fluid pressure,  $\alpha P$ , as the part carried by the fluid in the porous medium. Biot's poro-elastic constant,  $\alpha$ , is a correction or scaling factor, which measures the effectiveness of the pore/fluid

pressure response to the total applied stress<sup>123</sup>. Its value, which depends on the pore geometry and the physical properties of the constituents of the solid system, varies between 0 and 1. The expression for its computation is given as:

$$\alpha = 1 - \frac{C_r}{C_b} \quad 4-16$$

$C_r$  is the rock matrix compressibility and  $C_b$ , the rock bulk compressibility.

The stresses acting on an infinitesimal block of material within the earth are represented with Cartesian coordinates X, Y, Z and shown in Figure 4-5. Nine different stress components of three normal or principal stresses and six shear stresses are defined by the figure. Of the three principal stresses, the vertical stress has the greatest magnitude, the magnitude of the minimum horizontal stress is considered to be the smallest while the magnitude of the maximum horizontal is considered to be intermediate between the two. The vertical stress can be determined by the integration of overburden weight from the density log while the two horizontal stresses are often determined from a variety of field operations such as leak off test, fracpack test, mini fracpack test and extended leak off test. The techniques for the stress estimation will be discussed in more detail in section 4.3.3. The two horizontal stresses are often assumed to be equal, the only exception being areas with tectonic activities and presence of geological features such as salt diapirs<sup>3</sup>.

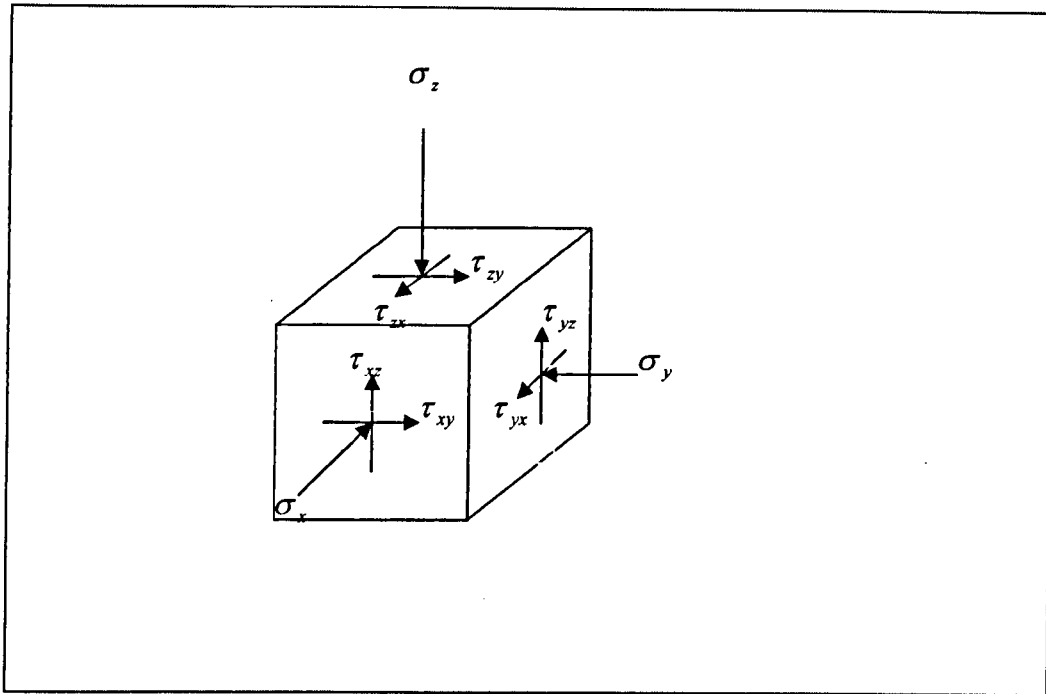


**Figure 4-5. The stresses acting on an infinitesimal block within the earth**

### 4.3.2 State of stress around a wellbore

The stress around a wellbore can be resolved into three principal stresses, axial stress,  $\sigma_z$ ; tangential stress,  $\sigma_\theta$ ; and radial stress,  $\sigma_r$ <sup>3, 124</sup>. These three components can be expressed in terms of or resolved into the principal stresses acting on a stable rock formation.

If a homogenous, isotropic, linearly elastic rock mass undergoing stress is assumed, a stress field expressed in polar coordinates as vertical or axial, tangential, radial and tangential shear stress derived by Kirsch<sup>124</sup> can be customised to include the effective minimum and maximum horizontal stress.

$$\sigma_z = \sigma_{zz} - 2\nu(\sigma_H - \sigma_h) \frac{r_w^2}{r^2} \cos 2\theta_a - 4\nu\tau \frac{r_w^2}{r^2} \sin 2\theta_a \quad 4-17$$

$$\sigma_{\theta} = \frac{1}{2}(\sigma_H + \sigma_h) \left(1 + \frac{r_w^2}{r^2}\right) - \frac{1}{2}(\sigma_H - \sigma_h) \left(1 + \frac{3r_w^4}{r^4}\right) \cos 2\theta_a - \frac{r_w^2}{r^2} p_w \quad 4-18$$

$$\sigma_r = \frac{1}{2}(\sigma_H + \sigma_h) \left(1 - \frac{r_w^2}{r^2}\right) + \frac{1}{2}(\sigma_H - \sigma_h) \left(1 - \frac{4r_w^4}{r^4} + \frac{3r_w^4}{r^4}\right) \cos 2\theta_a + \frac{r_w^2}{r^2} p_w \quad 4-19$$

$$\tau_{r\theta} = \left\{ \frac{1}{2}(\sigma_H - \sigma_h) \sin 2\theta_a + \tau \cos 2\theta_a \right\} \left(1 - 3\frac{r_w^4}{r^4} + 2\frac{r_w^2}{r^2}\right) \quad 4-20$$

Where  $\theta_a$  is the azimuth measured from the direction of the maximum horizontal stress.

$\sigma_{zz}$  = vertical stress

$\sigma_H$  = maximum horizontal stress

$\sigma_h$  = minimum horizontal stress

$\nu$  = Poisson ratio

$r_w$  = well radius

$r$  = infinite radius away from the well

$p_w$  = wellbore pressure

$\tau$  = shear stress

$\tau_{r\theta}$  = tangential radial stress

However, at the borehole wall where stress concentration is experienced,  $r$ , the radius extending beyond the borehole boundary at infinity, equals  $r_w$ , the radius of the borehole<sup>125</sup>; this is shown in Figure 4-6. The effect of the boundary condition can be applied to equations (4-17), (4-18), (4-19) and (4-20) to modify them. Applying the effect to equations (4-18) and (4-19) for the tangential and radial stresses respectively, being the most relevant in failure analysis, they reduce to:

$$\sigma_{\theta} = \sigma_H + \sigma_h - 2(\sigma_H - \sigma_h)\cos 2\theta_a - p_w \quad 4-21$$

$$\sigma_r = p_w \quad 4-22$$

Two cases can be considered for the tangential stress with regard to the maximum (where  $\theta_a = 0$ ) and minimum (where  $\theta_a = 90$ ) horizontal stresses, giving<sup>125</sup> (see appendix A-1 for derivation):

$$\sigma_{\theta=0} = 3\sigma_h - \sigma_H - p_w \quad 4-23$$

$$\sigma_{\theta=90} = 3\sigma_H - \sigma_h - p_w \quad 4-24$$

Equations (4-22), (4-23) and (4-24) can be written to reflect the effective variants of the stresses. Effective stresses are the net stresses acting around the wellbore; they are responsible for failure in petroleum rock mechanics. The magnitude of stress arising from pore pressure effect is subtracted from these equations to get the effective stress variants.

$$\sigma'_r = p_w - \alpha p_p \quad 4-25$$

$$\sigma'_{\theta=0} = 3\sigma_h - \sigma_H - p_w + \alpha p_p \quad 4-26$$

$$\sigma'_{\theta=90} = 3\sigma_H - \sigma_h - p_w + \alpha p_p \quad 4-27$$

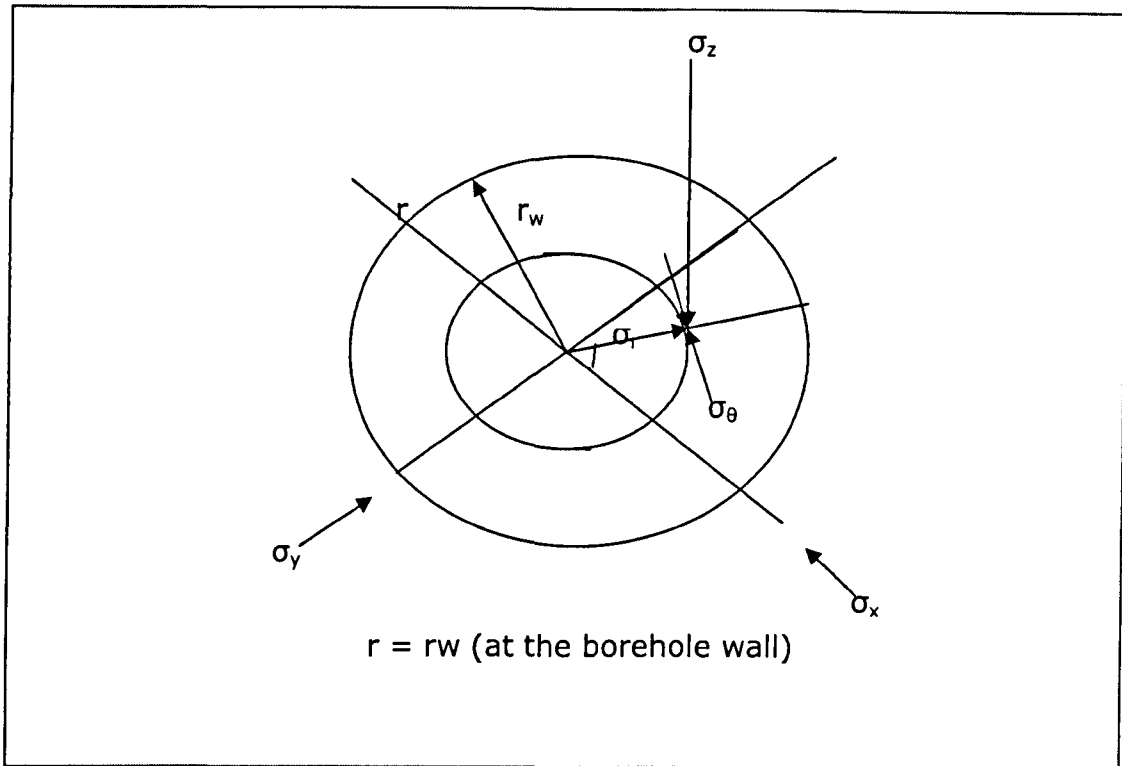


**Figure 4-6. The hoop stress around a borehole**

### 4.3.3 Estimation of in-situ stresses

Accurate estimation of in-situ stresses is very crucial to the optimisation of field operations. A variety of techniques exists for their estimation; these can be generally classified as (a) field techniques, (b) well log and (c) empirical correlations

#### 4.3.3.1 Vertical stress estimation

The vertical stress is often taken to be a function of the weight of overburden. It is therefore most often computed by the integration of density log. The general equation for its computation is written as<sup>3</sup>:

$$\sigma_v = \int_0^d \rho_b g d \quad 4-28$$

Where  $\rho_b$  is rock bulk density;  $g$  is acceleration due to gravity; and  $d$  is the reference depth.  $\rho_b$  can be estimated from the density log by using equation 4-29

$$\rho_b = \rho_g (1 - \phi) + \rho_{\log} \phi \quad 4-29$$

Where  $\rho_g$  is matrix density;  $\rho_{\log}$  is the density read off the density log at the reference depth; and  $\phi$  is porosity of the rock.

Density log is however not available throughout the length of a borehole especially in development wells. Also of critical importance is the quality of the density log; degradation of the borehole wall caused by mechanical failure of spalling, breakouts, etc. can cause impairment in density log quality<sup>100</sup>.

If density log is not available, field pressure gradient information can be used instead. Field pressure gradient is the change in pressure per unit depth; in using pressure gradient, it is assumed that the pressure increases linearly with depth. However this may not be true in abnormally pressured zones; and in areas where the rocks have experienced tectonic activities of uplift or subsidence<sup>100</sup>.

Empirical correlations have also been used in recent times to estimate the vertical stress. Most of these models relate vertical stress with the depth of occurrence of the rock. For example, McPhee, C A (2000)<sup>56</sup> proposed a correlation (equation 4-30) for Bongkot field, Gulf of Thailand. This model was a product of extensive density log integration and hydraulic fracturing studies.

$$\sigma_v = 1.64 + 3.4 \times 10^{-4} d^2 - 4.12 \times 10^{-8} d^2 \quad 4-30$$

Where  $d$  is the reference depth

Also Lowrey and Otessen (1995)<sup>126</sup> developed two separate models for estimating the vertical and minimum horizontal stresses for Niger Delta in Nigeria. The models are respectively presented in equations 4-31 and 4-32.

$$\sigma_v = 0.3741D^{1.0984} - 10.7 \quad 4-31$$

$$\sigma_h = 0.1779D^{1.1586} \quad 4-32$$

Where  $D$  is the total vertical depth in feet and  $\sigma_v$  is the vertical stress in (psi). The constants in the two equations are dependent on water depth.

Similar correlations have been developed for many of the world's prolific petroleum provinces for the estimation of vertical stress. These correlations are particularly useful where density log is unavailable or unreliable due to poor quality.

#### **4.3.3.2 Minimum and maximum horizontal stresses estimation**

A richer variety of techniques exists for estimating minimum and maximum horizontal stresses. The techniques span across the major classifications of general stress estimation techniques – field technique, empirical correlation and well log technique. Field techniques include well breakout analysis, macro-frac, mini-frac, hydraulic fracturing; Leak off test (LOT) and extended leaked off test (ELOT).

In borehole breakout analysis, it is always assumed that borehole will fail in the direction of the minimum horizontal stress<sup>127</sup>.

In macro fracture test, a hydraulic fracture is initiated within a short packed off interval by injecting about 1 m<sup>3</sup> of low viscosity fluids slowly through perforated casing or in open hole. A fracture is opened and closed

several times so that successive pressure declines can be monitored until a consistent closure pressure is obtained. This pressure is equated with the minimum principal stress<sup>128</sup>.

In mini fracture, a relatively high rate of viscous fluids in excess of 10 m<sup>3</sup> is ejected into the formation. The minimum horizontal stress is equated with the fracture closure pressure from the generated pressure/time plot.

Hydraulic fracturing technique involves massive fracturing of the rock. Fluids of relatively high viscosity are injected into the formation at a higher rate enough to fracture the formation rock. At the point of fracture initiation, the rock breaks down as it absorbs the injected fluid. The horizontal stress is then estimated from the fracture breakdown pressures recorded using Haimson and Fairhurst equation:

$$P_b = \sigma_T + 3\sigma_h - \sigma_H - P_p \quad 4-33$$

Where  $P_b$  is the breakdown pressure and  $\sigma_T$  is the tensile strength;

In leak off test, pressure on the drilling mud column is slowly raised until the pressure build up ceases to be linear<sup>129</sup>. At this point, a small volume of mud is believed to have begun to leak off into the formation. This pressure is the sum of the fracture breakdown pressure and the rock's tensile strength. This method should however be used with caution as near-surface rocks often exhibit high tensile strength and generate leak off pressures that are far higher than the stresses to which they are subjected<sup>129</sup>. Bell (2003)<sup>129</sup> suggested they be used only at depths greater than 300m.

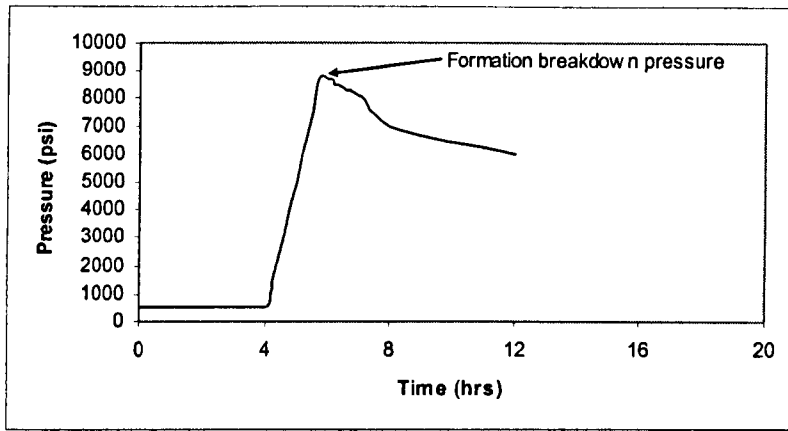


**Figure 4-7 Typical pressure/time record of fracturing**

A plethora of empirical correlations relating minimum and maximum horizontal stresses to depth have been developed for the world's petroleum provinces using leak off test and hydraulic fracturing data.

The log based model is the most commonly used in the oil and gas industry to estimate the minimum horizontal stress. The model (eq. 4-34) is simply a correlation between minimum or maximum horizontal stress, the vertical stress and Poisson ratio<sup>130</sup>.

$$\sigma_H = \sigma_h = \left[ \frac{\nu}{1-\nu} \right] \sigma_v \quad 4-34$$

## 4.4 Failure Criteria

The most discussed and most important failure criteria especially in the oil and gas industry are the Mohr-Coulomb criterion, Hoek-Brown criterion and the Drucker Prager criterion. These failure criteria are discussed in the following sections with the aim of drawing comparisons between them.

### 4.4.1 Mohr Coulomb failure criteria

Mohr Coulomb is the most widely applied failure criterion in the oil and gas industry, and elsewhere, for analysis of failure for the purpose of sanding potential prediction. It has, in fact, been used as the basis for more than 80% of the failure models being used in the industry. Many reasons have been given as to why it is more widely used than other failure criteria<sup>131</sup>. Han G. (2000)<sup>122</sup> attributed its wide application to its ability to capture and describe both frictional and cohesive strength factors in shear failure; and ease of application. Simplicity in understanding and use of the criterion; and description by a simple mathematical expression (equation 4-35) are also a factor often advanced in its favour.

$$\tau_f = \tau_o + \sigma_f \tan \theta \quad 4-35$$

$\tau_f$  is the shear stress at failure, and  $\sigma_f$ , the normal stress at failure;  $\tau_o$  and  $\theta$  are the shear or cohesive strength of rock and angle of internal friction respectively.

From equation 4-35, it is obvious that shear stress is a linear approximation of normal stress; this is depictive of a linear failure envelope. The general plot of normal versus shear stress, which defines the failure envelope for Mohr Coulomb criteria, is shown in figure 4-8.

Equation 4-35 is a linear approximation of the failure processes as shown in figure 4-8; and can be written in terms of the principal stresses and Unconfined Compressive Strength to evaluate compressive loading experiment in the laboratory.

$$\sigma_1 = \sigma_3 \tan \theta + \sigma_{ucs} \quad 4-36$$

Where  $\sigma_1$  is the maximum principal stress and  $\sigma_3$  the confining stress.

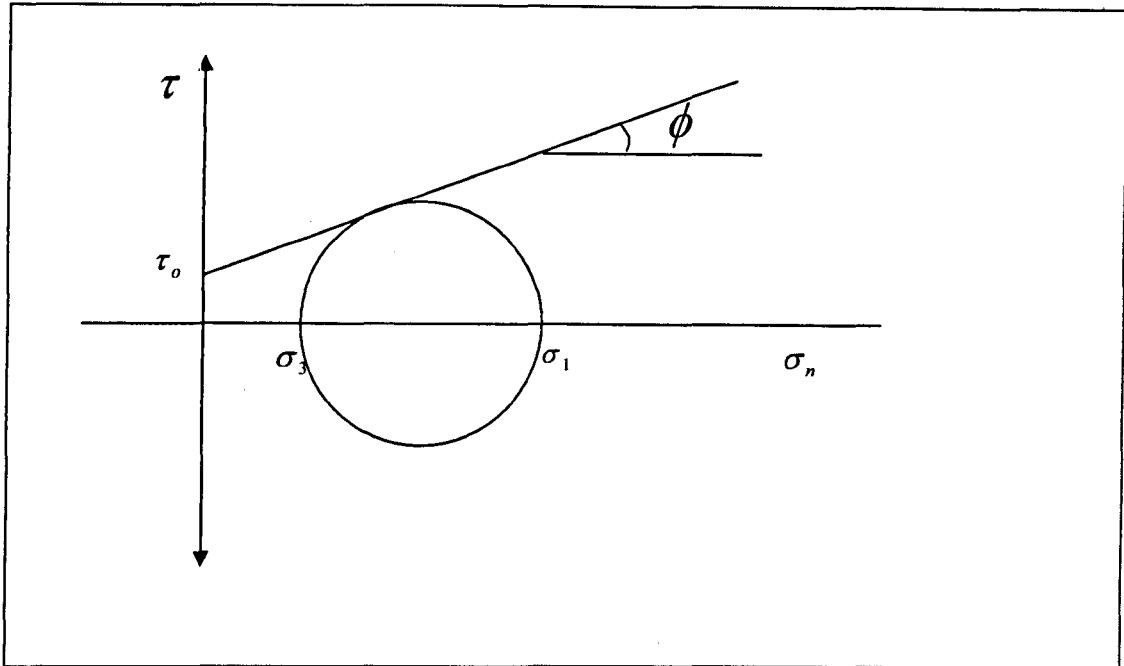


**Figure. 4-8. Mohr-Coulomb failure model**

#### 4.4.2 Hoek-Brown failure criterion

The linear approximation of failure behaviour of rocks by Mohr-Coulomb is considered an oversimplification of the failure process. Hoek-Brown criterion was therefore developed by Hoek and Brown (1980)<sup>132</sup> to address the problems relating to the linearity of the Mohr-Coulomb envelope and the influence of discontinuities on it.

The criterion was developed based on field, laboratory and theoretical considerations as well as experience. The criterion is applicable to both intact and failed rocks.

The equation describing the failure model is written as:

$$\sigma_1 = \sigma_3 + \sqrt{m\sigma_{ucs}\sigma_3 + s\sigma_{ucs}^2} \quad 4-37$$

m and s are constants that depend on rock strength and pre-loading failure of the rock fabrics;  $\sigma_1$  and  $\sigma_3$  are the maximum and minimum principal stresses respectively; whilst  $\sigma_{ucs}$  is the Unconfined Compressive Strength.

### 4.4.3 Drucker-Prager failure criterion

Drucker-Prager failure criterion is often called extended Von Mises criterion. It was formulated based on the assumption that the octahedral shearing stress reaches a critical value<sup>125</sup>. The expression describing the failure criterion is written as:

$$\omega l_i + \sqrt{J_2} - K = 0 \quad 4-38$$

$J_2$  is the octahedral shearing stress and  $l_i$  the first invariant of stress tensor; they are related to the effective principal stresses respectively by equations 4-39 and 4-40

$$J_2 = \frac{1}{6} \left[ (\sigma'_1 - \sigma'_2)^2 + (\sigma'_2 - \sigma'_3)^2 + (\sigma'_3 - \sigma'_1)^2 \right] \quad 4-39$$

$$l_i = \sigma'_1 + \sigma'_2 + \sigma'_3 \quad 4-40$$

Constants  $\omega$  and K are material parameters related to the Mohr-Coulomb angle of internal friction and cohesion respectively;  $\sigma_2$  is intermediate principal stress.

$$\omega = \frac{2 \sin \theta}{\sqrt{3} \times (3 - \sin \theta)} \quad 4-41$$

$$K = \frac{6C_1 \times \cos \theta}{\sqrt{3} \times (3 - \sin \theta)} \quad 4-42$$

Where  $C_1$  is cohesion

Equation (4-38) can be rearranged to assume the form:

$$\sqrt{J_2} = K - \omega I_1 \quad 4-43$$

A plot of  $\sqrt{J_2}$  on the ordinate against  $I_1$  on the abscissa will yield a straight line graph with  $\omega$  as the slope and  $K$  as the intercept.

## 4.5 Failure Mechanism

Two basic failure mechanisms are recognised in petroleum rock geomechanics<sup>133-134</sup>; they are (a) shear failure mechanism and (b) tensile failure mechanism. Fjaer et al. (2006)<sup>6</sup> however recognises that the two failure mechanisms will in practice work together and interact.

### 4.5.1 Shear failure mechanism

Shear failure mechanism is related to both drawdown and depletion of the reservoir over time. If during production, the drawdown is increased to the extent that it generates higher effective stresses around the well or perforation tunnel (for a perforated completion) than the strength of the formation can withstand, the rock may fail<sup>133</sup>. Similarly, increasing depletion can reduce the ability of the formation to counter the stress

---

around it, thereby increasing the effective stress around the formation; this also may lead to failure. Most failures in petroleum geomechanics are shear failure. Shear failure usually results in catastrophic amounts of sand<sup>6</sup>. This work therefore assumes that all failures are caused by shear mechanism and its results can only be applied to sanding problems caused by shear failure mechanism.

### **4.5.2 Tensile failure**

Tensile failure mechanism is primarily related to high fluid flow rate caused by high production rate<sup>6, 133</sup>. Tensile failure is therefore caused by high drawdown, which results in fluid high drag force on the formation grains. This type of failure does not result in large volume of sand production and it does self-stabilise with time. The self-stabilisation is brought about by the decrease in fluid gradient due to wellbore cavity growth<sup>6</sup>.

## **4.6 Summary**

In this chapter, all the important geomechanical parameters, which may be used to evaluate the strength of formation rock for application in sanding potential prediction, have been reviewed in terms of their importance and methods or techniques available to the oil and gas industry to estimate them. Specifically, this chapter has established that UCS is the most widely used of all the geomechanical parameters.

Also reviewed is the stress distribution in the vicinity of a well/formation, stress contribution to failure in rock and the various techniques and models for estimating the different kinds of stress. In addition, common failure criteria being used in the industry for failure evaluation and analysis are reviewed. The review has established that shear failure mechanism is the most common cause of rock failure encountered in the

field. As a result of this, all failures analysed in this work are assumed to be caused by shear failure mechanism.

## Chapter 5

### Neural network: Theory and application

In this chapter, the principal underlying theories of neural networks are discussed. Their application in the oil and gas industry is also discussed in more detail than was done in the previous chapters purposely to cover more areas and fields within the industry. The methods of data preparation for neural network modelling reported in chapters six and seven are also discussed.

#### 5.1 Background

Artificial Neural Networks are a system composed of many single processing elements operating in parallel, which can acquire, store and utilise experiential knowledge. They usually consist of a set of highly interconnected entities referred to as nodes or units as shown in Figure 5-1. The neurons are arranged and interconnected in the same fashion as the well-known biological neural systems are arranged and interconnected<sup>135-136</sup>. Just like the biological counterpart, the processing ability of an artificial neuron is stored in the inter-node or inter-unit connection weights, obtained by a process of adaptation to, or learning from a set of training patterns.

Artificial neural networks can either be implemented in hardware using electronic circuits or in algorithms using programming codes<sup>137</sup>.

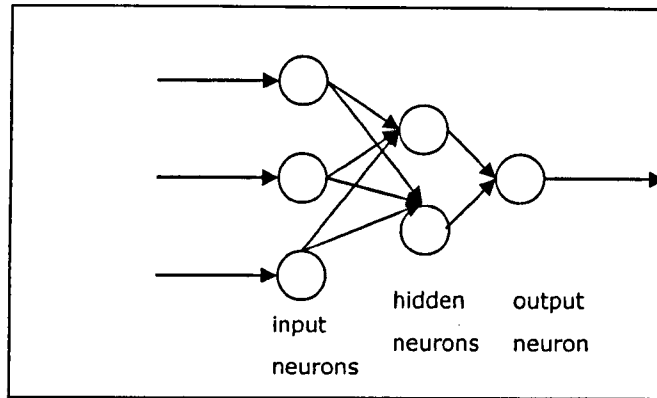


**Figure 5-1 A neural network schematic**

## 5.2 Operations in Neural Network

### 5.2.1 Signal processing in Artificial Neural Network

A typical Artificial Neural Network consists of three layers; each layer may consist of varying numbers of neurons, depending on the topology chosen. The first layer, where the signal is fed into the network, is called the input layer; the second layer, where most of the processing functions take place, is called the hidden layer; the third layer, where the output signal is obtained, is called the output layer (figure 5-2). The input layer neurons do not participate in the processing functions of the networks but only act as an interface for receiving signal from an external source.

Essentially, a set of inputs is fed into the network through the input neurons. Each input signal is then multiplied by the strength of the connection between these neurons and the immediate interconnected set of neurons (the hidden layer neurons); this connection strength is often called the connection weight. The results of this operation then become the inputs to the immediate interconnected set of neurons. This input is normalised in the hidden layer neuron by a squashing or activation function, the outcome of this squashing depends on the choice of function. This outcome represents the signal from the hidden layer neuron and is passed on as an input, after connection weight multiplication, to the next interconnected set of neurons, which may be the output neurons depending on the number of neural network layers.

## 5.2.2 Mathematical operation of a neural network

A neuron in an Artificial Neural Network system implements a non-linear mapping of input data from  $\mathfrak{R}^1 \Rightarrow |M, N|$  depending on the activation or squashing function<sup>135</sup>. For example, for a sigmoid activation,  $\mathfrak{R}^1 \Rightarrow |0, 1|$

Suppose a neuron receives a vector input signal  $X = (x_1, x_2, x_3 \dots x_n)$  with a corresponding weight vector,  $W = (w_1, w_2, w_3 \dots w_n)$  as shown in figure 5-2, the net input signal to the neuron is computed as the weighted sum of all the input signals and is given by<sup>135</sup>:

$$net = \sum_{i=1}^n x_i w_i \text{ (for a summation unit)} \quad 5-1$$

and

$$net = \prod_{i=1}^n x_i^{w_i} \text{ (for a product unit)} \quad 5-2$$

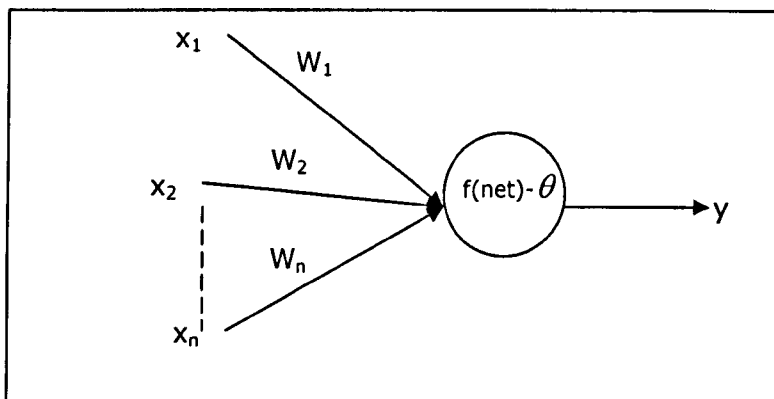


Figure 5-2 Mapping function in neural network<sup>135</sup>

## 5.3 Justification for the wider use of neural network as a data mining method

Neural network methods have been more widely applied to complex chemical, engineering, mathematical, scientific and social problems than other data mining methods in recent times. This is perhaps due to the

---

many advantages that neural networks have over the other data mining methods. Master T. (1993)<sup>136</sup> gave some of these advantages as:

- Neural networks possess robustness which enable them to detect fuzziness or large errors in data
- They can detect patterns in data which are so obscure as to be imperceptible to human researchers and other data mining methods
- They are adaptable to data which exhibits significant unpredictable non-linearity
- They have capability to detect noise in a data input. Other data mining techniques may not be able to handle this type of data

## 5.4 Activation functions

The ability of an artificial neural network to resolve complex non-linear engineering, scientific and social problems is largely dependent on the processing (hidden layer) unit activation functions. The activation function performs a mathematical operation to further process the net signal coming from the upstream neuron(s). The final output from the neural network after the processing of the net signal by the activation function is therefore a function of the activation level; this is given in a functional form as (equation 5-3);

$$\text{Out} = k_1(\text{net}) \qquad \qquad \qquad 5-3$$

Where  $k_1$  is the activation function and is constant

Many activation functions are available for use in neural network implementation. The choice will generally depend on the complexity of the data or problem to be solved.

### 5.4.1 Linear function

The linear activation function returns an output which has a linear relationship with the sum product of the weighted input. The mathematical function is given as<sup>135</sup>:

$$Out = \beta_1 (net)$$

5-4

Where  $\beta_1$  is a constant of linearity.

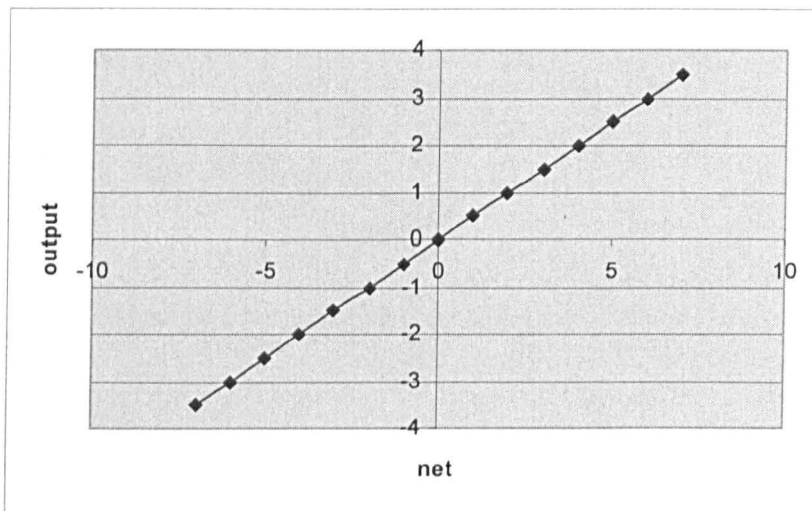


**Figure 5-3 Linear activation function**

### 5.4.2 Step function

The step activation function returns one of two scalar output values, depending on the value of a specified threshold (equation 5-5).

$$Out = \{0 \text{ if } net > 1; 1 \text{ if } net < 1\}$$

5-5

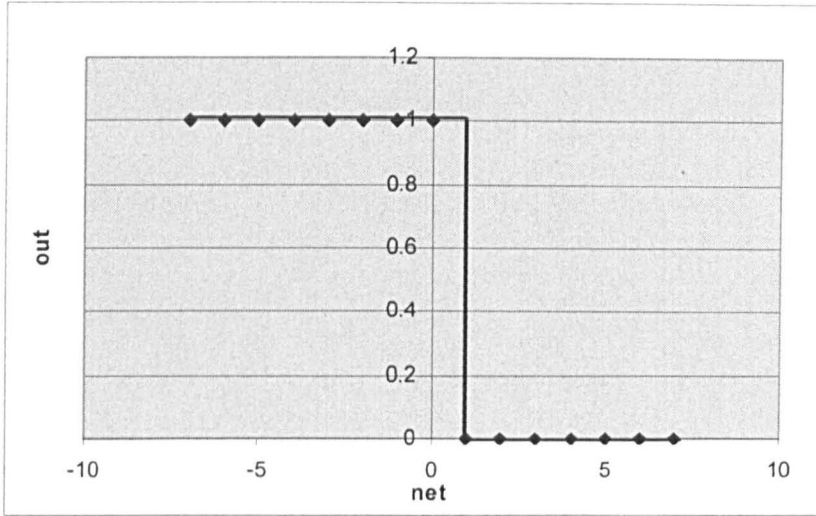


**Figure 5-4 Step activation function**

### 5.4.3 Sigmoid function

The sigmoid function returns an output which has an exponential relationship with the sum product of the net weighted output. The mathematical function is given as<sup>135</sup>:

$$Out = \frac{1}{1 + e^{-\varpi(net)}} \quad 5-6$$

Where  $\varpi$  is a parameter that controls the steepness of the function and it is generally equal to 1.

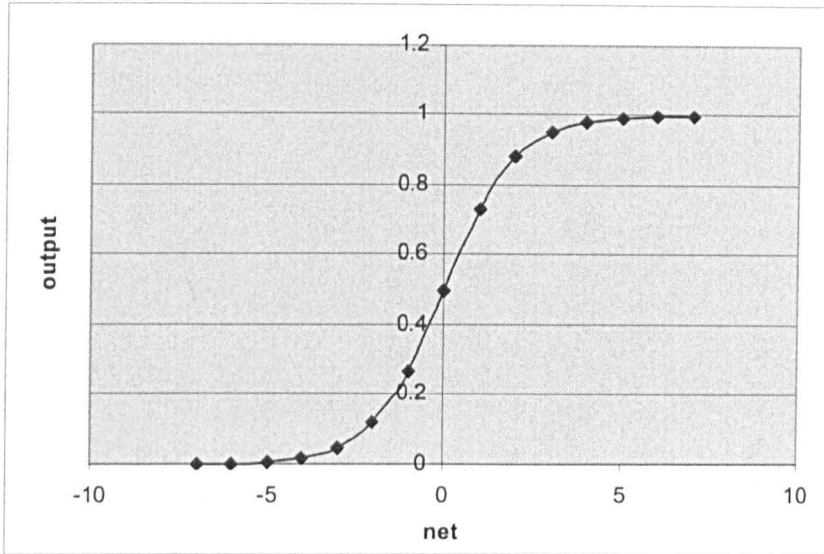


**Figure 5-5 Sigmoid activation function**

A neuron with sigmoid activation function will return output value within the range  $0 \leq out \leq 1$

#### 5.4.4 Hyperbolic tangent function

The hyperbolic tangent function normally returns output in the range between -1 and 1. The mathematical expression is given as<sup>135</sup>:

$$Out = \frac{e^{\varpi(net)} - e^{-\varpi(net)}}{e^{\varpi(net)} + e^{-\varpi(net)}} \quad 5-7$$

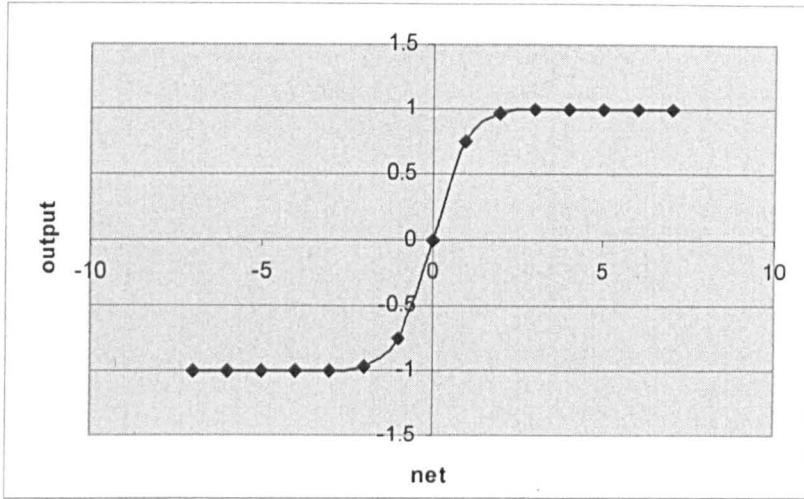


**Figure 5-6 Hyperbolic tangent activation function**

### 5.4.5 Gaussian function

The Gaussian function is described by a Gaussian distribution and is mathematically represented as<sup>135</sup>:

$$Out = e^{-(net)^2 / \sigma_{var}^2}$$

5-8

Where  $\sigma_{var}$  is variance

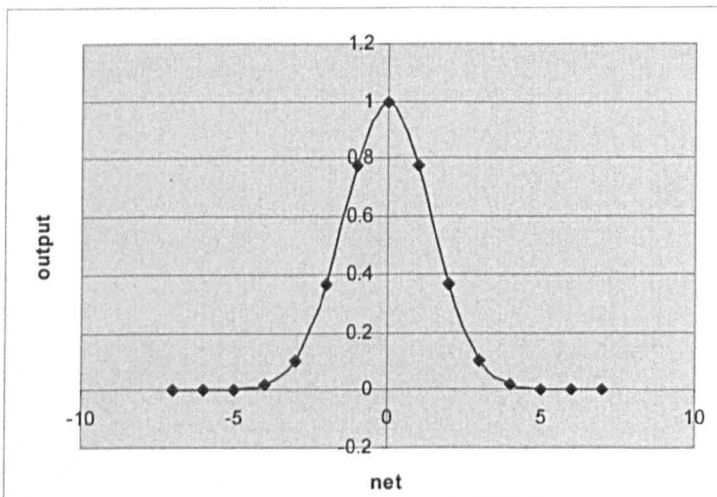


**Figure 5-7 Gaussian activation function**

## 5.5 Neural Network Training

The objective of training a neural network is generally to obtain a set of desired outputs from the network after the application of a set of inputs<sup>138</sup>.

Training therefore entails presentation of a set of inputs, computation of error and adjustment of the weights as a result of this, to obtain convergence. This process continues until a certain specified training condition has been met. The three basic types of learning in neural network are the supervised, unsupervised and reinforcement training<sup>135-136, 138</sup>

### 5.5.1 Supervised training

In supervised training, the neural network is presented with a set of input and desired output vectors called a training set. The aim of this type of training is to present the network with a standard so that the network can adjust its weights until it is able to replicate this standard within a reasonable error limit. This is the most common type of training in neural networks<sup>135</sup>.

### 5.5.2 Unsupervised training

In unsupervised training, there is no desired output vector or standard for the network to replicate; only input vectors are presented to the network. It is generally assumed that each input to the network arises from one of several classes, and the network's output is an identification of the class to which its input belongs. Training of the network entails letting the network discover salient features to group the inputs into classes that it finds distinct<sup>135, 136, 138</sup>

---

### 5.5.3 Reinforcement training

This is a hybrid of the supervised and unsupervised training. It is not as commonly used as the other two. In reinforcement training the desired outputs are not presented to the network but the network is allowed to know if it has replicated input signal well or otherwise<sup>135-136, 138</sup>.

## 5.6 Application of neural networks in the oil and gas industry

Neural networks have been used for wider applications in the oil and gas industry than was discussed in chapters two, three and four of this thesis. Even though artificial intelligence has found use in the oil and gas industry since its earlier days<sup>139</sup>, it was not until a few decades ago that neural network began to enjoy wide application in the industry. Ever since, neural network has been used for a variety of applications, ranging from simple characteristic property prediction of formation and formation fluids to advanced field and operation optimisation<sup>140-146</sup>. The following paragraphs are devoted to a brief discussion of some of the applications of neural network published in open literature.

Zhou and Wu (1993)<sup>140</sup> conducted a comparative study of conventional and neural network techniques for well log interpretation, using two different techniques under each broad category; the study was done using data from a Chinese field. The two conventional techniques used in the study were Model Based Inversion (MBI) and Principal Component Regression Algorithm (PCRAL); whilst for neural network application, a four-layer feed-forward neural network and a neural model of Principal Component Analysis and Linear Regression (PCALR) were considered. In the study, all the techniques were used to predict porosity. The Back-propagation training algorithm was used for the training of the feed-forward neural network. The conclusions from the study strongly suggest that the feed-forward neural network performed better than the other techniques.

Chawate et al (1994)<sup>141</sup> developed a process of automation of well log interpretation for application to classification of lithology. To achieve this, logs such as Gamma ray, Spontaneous Potential log, Neuron log, Spherically Focussed log (RSFL), Medium Phasor Induction log (IMPH) and Deep Phasor Induction log (IDPH), which correlate well with lithology, were presented to a Simulated Neural Network (SNN), using the Kohonen unsupervised training algorithm. The network was reported to have distinctly classified sandstone and shale and also identified fining of the lithology from sandstone to shale and coarsening from shale to sandstone. The capacity of conventional log interpretation to do this is minimal.

Mohaghegh et al (1995)<sup>142</sup>, through some deterministic studies, settled for a three layer neural network with 15 neurons in the hidden layer for the prediction of permeability of a heterogeneous reservoir in Granny Creek field in Clay and Roan Counties of West Virginia. A data set which included depth, gamma ray, bulk density, deep induction log responses, and zonal subdivision specification were presented to the network as training input set; and core data as the desired target. Their conclusion showed that estimation of permeability by using well-log data in a neural network model is feasible and that neural network performance in permeability prediction is indeed comparable to the core-based experimental method.

Soto et al (1997)<sup>143</sup> used the back-propagation training algorithm for a three layer network with 15 neurons in the two hidden layers to predict rock petrophysical properties of permeability and porosity of a heterogeneous reservoir in Cantagallo field in Colombia. They presented Gamma ray and Neutron porosity as the inputs to the network and core data of the two petrophysical properties as the target output. They reported, among other favourable results, excellent correlation coefficients of 0.9799 and 0.9967 for NN-predicted porosity and permeability respectively. The correlation coefficients obtained for porosity and permeability when they used conventional statistical analysis were 0.396 and 0.598 respectively.

Liu and Sacchi (2003)<sup>144</sup> used an unsupervised Support Vector Machine (SVM) to predict rock physical properties. They used seismic data as training input and compressional wave velocity as the desired output. The

SVM was then trained to develop a functional mapping between the input vector and the target output, which was later used to predict rock physical properties at locations where only seismic attributes are available. In many cases the study reported close agreement between the predicted and the known compressional velocities at the borehole locations.

Uden, Smith and Hubert (2003)<sup>145</sup> also trained a supervised artificial neural network with density, total porosity, longitudinal sonic wave velocity, transverse sonic wave velocity, clay volume and water saturation logs to predict different litho-facies in Norwegian Ormen Lange fields. The neural network was reported to have performed well.

## **5.7 Data preparation for Neural Network Modelling**

In this section the general techniques for all data preparations for the neural network modelling studies in these studies are discussed. Methods specific to each modelling study are discussed in the appropriate later chapters.

### **5.7.1 Data transformation and normalisation**

There is a need to transform both input and output data if the existence of outliers and non-normality is suspected in the data. The transformation is intended to bring the distribution of the data as close as possible to the normal distribution model shown in figure 5-8. Though a normal distribution is not particularly important to a neural network<sup>136</sup>, it is however important that the distribution be approximately symmetrical and is not heavily skewed. In fact the evidence so far obtained in this work shows that neural networks learn better and faster on transformed data. The transformation was achieved using several functions such as inverse, logarithm, square and square root in a "trial and observe" method, in which each of these functions was used on all the data sets in turn and

the skewness and kurtosis observed each time. The transformation function which brought the skewness and kurtosis of each data set closer to zero was then chosen as the best.

In cases where entries in a particular data set were either negative or less than 1, a constant was added throughout to bring their values above 1 in order to be able to perform transformation by logarithm and square root. This is informed by the need to apply the same treatment to all the data entries and to reduce error.

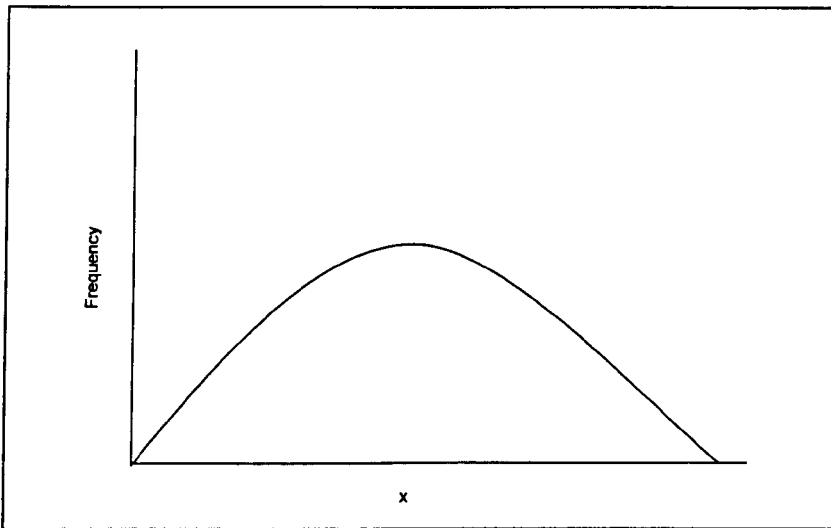


**Figure 5-8 A normal distribution model**

### **5.7.2 Input and output data Normalisation**

All data for the neural network modelling studies were normalised first to lie within a specified range; for example between 0 and 1 and -1 and 1. Normalisation is necessary because the transfer functions within the hidden and the output layers of the neural network are often only able to return values that lie within these ranges; this has been discussed in section 5- 4. The normalisation of the data to the range between 0 and 1 was meant for a sigmoid transfer function whilst the normalisation to the range between -1 and 1 was meant for tan transfer functions.

The normalisation of the data for both sigmoid and tan transfer functions was achieved using equation (5-9)<sup>147</sup>:

$$I = I_{\min} + [(I_{\max} - I_{\min}) \times (D - D_{\min})] / [D_{\max} - D_{\min}] \quad 5-9$$

Where:

I is the normalised value of the data point of interest

$I_{\min}$  is the lowest end member of the range for a particular transfer function

$I_{\max}$  is the highest end member of the range for a particular transfer function

$D_{\min}$  is the minimum data point within the data set to be normalised

$D_{\max}$  is the maximum data point within the data set to be normalised

D is the data point to be normalised

### 5.7.3 Input and output data de-normalisation

Data de-normalisation is the process of converting back the data to their original values. This is very important especially in the testing and validation stage of the neural network performance to avoid a situation where the errors between the measured and predicted data points are either completely or partially masked as a result of normalisation effect.

De-normalisation was achieved using the transposed form of equation (5-9).

$$D = D_{\min} + \frac{(D_{\max} - D_{\min}) * (I - I_{\min})}{I_{\max} - I_{\min}} \quad 5-10$$

## **5.8 Summary**

The general background theories and principles behind the operation and use of the neural network especially in the oil and gas industry have been discussed in this chapter. Neural network has also been compared with other popular and widely used data mining methods in the industry in terms of extent of use in the industry, versatility, and above all, ability to resolve complex non-linear data structure.

In summary, the choice of neural network for use in this work has been justified in this chapter.

## **Chapter 6**

### **Grain size distribution modelling**

In this chapter, the results of comparative studies on the application of statistical multivariate, analytical, dimensional analysis and neural network to grain size distribution modelling are presented. The procedures and processes of neural network modelling are however presented in more detail than the others. Based on the comparative studies and the need to integrate the modelling techniques neural network and statistical methods have been used to develop a model for predicting grain size distribution. Grain size distribution output results from these models are intended as input to the developed UCS models reported in chapter seven.

#### **6.1 Relationship between grain size and well log data:**

Multivariate and univariate statistical analysis have been used in petroleum engineering and related fields to predict or estimate important reservoir or field properties like porosity, permeability and grain size. These techniques were used in this study to make prediction of grain size distribution for the purpose of comparison with the neural network and others. Five different types of logs and grain size distribution data from core sieve analysis from six different wells (C4, C10, C5, C8, C6, C7) from a North Sea field were used for this study (see appendices B-4 –B-9 for the well logs and appendices B-1 – B-3 for all the grain size distribution data from sieve analysis). A commercial digitising software, TechDig™ was used to digitise all the well logs converting them to numerical data for useful analysis.

---

### 6.1.2 Data distribution

The statistical distributions of both the digitised log and grain size data were checked for normality by observing their histogram plots and calculating their skewness and kurtosis. Their skewness and kurtosis were found to be much greater than zero suggesting that the data are highly skewed and non-normally distributed (see Tables 6-1 to 6-6 for the results of the normality check). The results obtained here informed the data transformation reported in section 6.1.3.

### 6.1.3 Data transformation

The log well data and core grain size data were transformed to bring their distributions closer to the normal distribution using the methods and procedure already described in chapter 5. The transformation was achieved by using transformation functions such as inverse, logarithm, square and square root in a "trial and observe" method in which each of these functions was used on all the data sets in turn and the skewness and kurtosis observed each time. For Neutron data with negative values or values less than one (see Table 6-3), constant value of 1 or 2 was added throughout to allow transformation by logarithm and square root functions. The transformation function, which brought the skewness and kurtosis of each data set closer to zero, was then chosen as the best.

Tables 6-1 to 6-4 show the results of transformation of the Gamma ray, Resistivity, Neutron and Density log data from well C10, Table 6-5 shows the results of transformation of the Sonic log data from well C7 whilst Table 6-6 shows the results of transformation of the median grain size data from well C10. Table 6-7 shows the optimum functions that brought each set of log and grain size distribution data closer to the normal distribution model. Shown in Figures 6-1 to 6-5 are the histograms of gamma ray with normal curves for the different transformation functions used.

**Table 6-1 Gamma Ray log data transformation - well C10**

depth	g_ray	g_ray_sqrt	g_ra_sq	g_ray_inv	g_ray_nat_log	g_ray_log
9399.29	31.117	5.578	968.255	0.032	3.438	1.493
9419.98	30.847	5.554	951.531	0.032	3.429	1.489
9443.86	28.771	5.364	827.776	0.035	3.359	1.459
9459.79	25.035	5.003	626.731	0.040	3.220	1.399
9478.89	24.786	4.979	614.321	0.040	3.210	1.394
9494.81	22.814	4.776	520.456	0.044	3.127	1.358
9564.84	27.194	5.215	739.486	0.037	3.303	1.434
9582.33	37.552	6.128	1410.145	0.027	3.626	1.575
9603.03	31.989	5.656	1023.277	0.031	3.465	1.505
9636.47	22.730	4.768	516.671	0.044	3.124	1.357
9642.84	24.412	4.941	595.936	0.041	3.195	1.388
9668.30	24.080	4.907	579.832	0.042	3.181	1.382
9682.63	23.893	4.888	570.871	0.042	3.174	1.378
9704.91	25.367	5.037	643.469	0.039	3.233	1.404
9725.60	25.097	5.010	629.854	0.040	3.223	1.400
9739.92	28.439	5.333	808.777	0.035	3.348	1.454
9771.76	24.495	4.949	600.000	0.041	3.198	1.389
9802.00	25.865	5.086	668.993	0.039	3.253	1.413
9822.70	25.595	5.059	655.109	0.039	3.242	1.408
9841.80	25.346	5.034	642.420	0.039	3.233	1.404
9881.55	49.530	7.038	2453.171	0.020	3.903	1.695
9900.69	24.578	4.958	604.073	0.041	3.202	1.391
9926.16	24.246	4.924	587.859	0.041	3.188	1.385
9937.32	15.278	3.909	233.423	0.065	2.726	1.184
10018.50	35.393	5.949	1252.664	0.028	3.567	1.549
10036.00	26.342	5.132	693.922	0.038	3.271	1.421
10053.50	17.292	4.158	299.003	0.058	2.850	1.238
10091.70	15.029	3.877	225.874	0.067	2.710	1.177
10168.10	8.739	2.956	76.375	0.114	2.168	0.941
<b>skewness</b>	<b>0.740</b>	<b>-0.213</b>	<b>2.359</b>	<b>2.989</b>	<b>-1.197</b>	<b>-1.197</b>
<b>kurtosis</b>	<b>3.478</b>	<b>2.891</b>	<b>8.501</b>	<b>11.592</b>	<b>4.206</b>	<b>4.206</b>

**Table 6-2 Resistivity log data transformation - well C10**

depth	res	res_sqrt	res_sq	res_inv	res_nat_log	res_log
9393.51	9.271	3.045	85.956	0.108	2.227	0.967
9407.50	81.055	9.003	6569.978	0.012	4.395	1.909
9419.93	153.204	12.378	23471.466	0.007	5.032	2.185
9440.13	285.819	16.906	81692.501	0.003	5.655	2.456
9460.33	103.046	10.151	10618.478	0.010	4.635	2.013
9482.08	51.477	7.175	2649.902	0.019	3.941	1.712
9561.33	77.944	8.829	6075.329	0.013	4.356	1.892
9581.54	16.247	4.031	263.955	0.062	2.788	1.211
9603.29	8.116	2.849	65.871	0.123	2.094	0.909
9621.94	8.777	2.963	77.035	0.114	2.172	0.943
9632.82	35.819	5.985	1282.965	0.028	3.578	1.554
9662.34	21.989	4.689	483.525	0.045	3.091	1.342
9677.88	11.100	3.332	123.212	0.090	2.407	1.045
9698.08	20.708	4.551	428.838	0.048	3.031	1.316
9708.96	3.929	1.982	15.441	0.254	1.369	0.594
9721.39	10.318	3.212	106.463	0.097	2.334	1.014
9735.37	5.222	2.285	27.271	0.191	1.653	0.718
9750.91	2.117	1.455	4.483	0.472	0.750	0.326
9763.35	4.002	2.000	16.015	0.250	1.387	0.602
9783.55	3.467	1.862	12.020	0.288	1.243	0.540
9792.87	1.022	1.011	1.045	0.978	0.022	0.010
9814.63	1.100	1.049	1.210	0.909	0.095	0.041
9822.39	1.086	1.042	1.179	0.921	0.082	0.036
9836.38	1.060	1.030	1.125	0.943	0.059	0.025
9859.69	0.819	0.905	0.671	1.221	-0.200	-0.087
9876.78	0.991	0.995	0.982	1.009	-0.009	-0.004
9900.09	0.953	0.976	0.908	1.049	-0.048	-0.021
9920.29	0.825	0.909	0.681	1.211	-0.192	-0.083
9940.49	0.890	0.944	0.793	1.123	-0.116	-0.050
9993.33	2.185	1.478	4.773	0.458	0.781	0.339
10008.90	1.231	1.109	1.514	0.813	0.207	0.090
10022.90	0.965	0.983	0.932	1.036	-0.035	-0.015
10032.20	1.060	1.030	1.125	0.943	0.059	0.025
10038.40	0.941	0.970	0.885	1.063	-0.061	-0.027
10067.90	1.387	1.178	1.925	0.721	0.327	0.142
<b>skewness</b>	<b>3.073</b>	<b>1.737</b>	<b>4.681</b>	<b>0.788</b>	<b>0.384</b>	<b>0.384</b>
<b>kurtosis</b>	<b>10.659</b>	<b>2.865</b>	<b>23.176</b>	<b>-1.195</b>	<b>-0.988</b>	<b>-0.988</b>

**Table 6-3 Neutron log data transformation - well C10**

depth	neut	neut+2	neut_sqrt	neut_sq	neut_inv	neut_log
9394.93	-0.113	1.887	1.374	3.559	0.530	0.635
9416.69	-0.113	1.887	1.374	3.559	0.530	0.635
9439.99	-0.127	1.873	1.368	3.507	0.534	0.627
9457.09	-0.100	1.900	1.379	3.612	0.526	0.642
9477.29	-0.113	1.887	1.374	3.559	0.530	0.635
9497.60	0.429	2.429	1.558	5.899	0.412	0.887
9568.97	-0.127	1.873	1.368	3.507	0.534	0.627
9579.84	-0.127	1.873	1.368	3.507	0.534	0.627
9593.83	-0.113	1.887	1.374	3.559	0.530	0.635
9607.82	-0.100	1.900	1.379	3.612	0.526	0.642
9638.89	-0.169	1.831	1.353	3.352	0.546	0.605
9657.54	-0.155	1.845	1.358	3.404	0.542	0.612
9679.30	-0.127	1.873	1.368	3.507	0.534	0.627
9697.94	-0.141	1.859	1.363	3.455	0.538	0.620
9719.70	-0.127	1.873	1.368	3.507	0.534	0.627
9730.58	-0.113	1.887	1.374	3.559	0.530	0.635
9741.55	0.331	2.331	1.527	5.436	0.429	0.846
9778.84	0.318	2.318	1.522	5.371	0.431	0.841
9797.40	-0.113	1.887	1.374	3.559	0.530	0.635
9825.37	-0.113	1.887	1.374	3.559	0.530	0.635
9878.21	-0.086	1.914	1.384	3.665	0.522	0.649
9889.09	-0.072	1.928	1.389	3.718	0.519	0.657
9920.15	-0.127	1.873	1.368	3.507	0.534	0.627
9906.17	-0.127	1.873	1.368	3.507	0.534	0.627
9935.69	-0.141	1.859	1.363	3.455	0.538	0.620
<b>skewness</b>	<b>2.475</b>		<b>2.459</b>	<b>2.507</b>	<b>-2.409</b>	<b>2.443</b>
<b>kurtosis</b>	<b>4.809</b>		<b>4.727</b>	<b>4.982</b>	<b>4.495</b>	<b>4.648</b>

**Table 6-4 Density log data transformation - well C10**

depth	den	den_sqrt	den_sq	den_inv	den_nat_log	log_den
9395.06	1.407	1.186	1.979	0.711	0.341	0.148
9424.59	1.410	1.187	1.987	0.709	0.343	0.149
9441.68	1.411	1.188	1.991	0.709	0.344	0.150
9461.88	1.413	1.189	1.997	0.708	0.346	0.150
9482.08	1.415	1.190	2.002	0.707	0.347	0.151
9556.67	1.337	1.156	1.787	0.748	0.290	0.126
9567.55	1.350	1.162	1.823	0.741	0.300	0.130
9589.31	1.413	1.189	1.997	0.708	0.346	0.150
9639.03	1.418	1.191	2.010	0.705	0.349	0.152
9660.79	1.481	1.217	2.193	0.675	0.393	0.171
9679.43	1.470	1.213	2.162	0.680	0.386	0.167
9701.19	1.485	1.219	2.205	0.674	0.395	0.172
9726.05	1.475	1.214	2.175	0.678	0.389	0.169
9794.42	1.518	1.232	2.305	0.659	0.417	0.181
9800.64	1.482	1.217	2.197	0.675	0.393	0.171
9820.84	1.484	1.218	2.202	0.674	0.395	0.171
9878.34	1.514	1.230	2.292	0.661	0.415	0.180
9896.98	1.503	1.226	2.260	0.665	0.408	0.177
9917.18	1.518	1.232	2.303	0.659	0.417	0.181
skewness	-0.461	-0.461	-0.400	0.587	-0.523	-0.523
kurtosis	-0.689	7.585	-0.795	-0.441	-0.572	-0.572

**Table 6-5 Sonic log data transformation-well C7**

depth	sonic	sonic_sqrt	sonic_sq	sonic_inv	sonic_log
9468.29	101.118	10.056	10224.850	0.010	4.616
9482.33	95.815	9.789	9180.591	0.010	4.562
9492.63	95.639	9.780	9146.857	0.010	4.561
9559.14	91.971	9.590	8458.573	0.011	4.521
9589.14	96.520	9.824	9316.168	0.010	4.570
9598.51	96.360	9.816	9285.269	0.010	4.568
9612.55	91.057	9.542	8291.450	0.011	4.511
9620.98	92.179	9.601	8496.931	0.011	4.524
9630.36	94.550	9.724	8939.665	0.011	4.549
9639.72	91.858	9.584	8437.966	0.011	4.520
9650.96	91.666	9.574	8402.674	0.011	4.518
9662.20	90.208	9.498	8137.537	0.011	4.502
9671.57	90.048	9.489	8108.660	0.011	4.500
9700.52	56.645	7.526	3208.690	0.018	4.037
9732.38	61.163	7.821	3740.925	0.016	4.114
9764.29	79.603	8.922	6336.590	0.013	4.377
9785.81	67.844	8.237	4602.754	0.015	4.217
9791.44	71.544	8.458	5118.601	0.014	4.270
9807.35	64.944	8.059	4217.710	0.015	4.174
9834.51	61.948	7.871	3837.567	0.016	4.126
9856.10	74.236	8.616	5510.954	0.013	4.307
9873.94	89.119	9.440	7942.178	0.011	4.490
9886.10	81.317	9.018	6612.438	0.012	4.398
<b>skewness</b>	-0.769	-0.846	-0.620	1.089	-0.925
<b>kurtosis</b>	7.720	17.859	0.515	23.994	22.704

**Table 6-6 Median grain size transformation – well C10**

Depth (ft)	d <sub>50</sub>	d <sub>50_sqrt</sub>	d <sub>50_sq</sub>	d <sub>50_inv</sub>	d <sub>50_log</sub>
9403.90	375.000	19.365	140625.000	0.003	5.927
9417.00	440.000	20.976	193600.000	0.002	6.087
9430.60	350.000	18.708	122500.000	0.003	5.858
9439.30	420.000	20.494	176400.000	0.002	6.040
9444.40	310.000	17.607	96100.000	0.003	5.737
9450.70	360.000	18.974	129600.000	0.003	5.886
9456.50	350.000	18.708	122500.000	0.003	5.858
9558.10	230.000	15.166	52900.000	0.004	5.438
9564.10	250.000	15.811	62500.000	0.004	5.521
9573.10	410.000	20.248	168100.000	0.002	6.016
9583.70	355.000	18.841	126025.000	0.003	5.872
9588.40	90.000	9.487	8100.000	0.011	4.500
9597.70	163.000	12.767	26569.000	0.006	5.094
9605.50	186.000	13.638	34596.000	0.005	5.226
9622.00	520.000	22.804	270400.000	0.002	6.254
9640.00	400.000	20.000	160000.000	0.003	5.991
9661.80	90.000	9.487	8100.000	0.011	4.500
9694.10	400.000	20.000	160000.000	0.003	5.991
9700.80	360.000	18.974	129600.000	0.003	5.886
9728.00	53.000	7.280	2809.000	0.019	3.970
9747.00	275.000	16.583	75625.000	0.004	5.617
9760.20	66.000	8.124	4356.000	0.015	4.190
9761.30	59.000	7.681	3481.000	0.017	4.078
9769.10	420.000	20.494	176400.000	0.002	6.040
9805.60	530.000	23.022	280900.000	0.002	6.273
9834.70	60.000	7.746	3600.000	0.017	4.094
9847.30	255.000	15.969	65025.000	0.004	5.541
9857.60	200.000	14.142	40000.000	0.005	5.298
9889.40	390.000	19.748	152100.000	0.003	5.966
9896.30	210.000	14.491	44100.000	0.005	5.347
9906.50	430.000	20.736	184900.000	0.002	6.064
9927.60	115.000	10.724	13225.000	0.009	4.745
10020.50	400.000	20.000	160000.000	0.003	5.991
10034.80	113.000	10.630	12769.000	0.009	4.727
10043.90	230.000	15.166	52900.000	0.004	5.438
10054.30	380.000	19.494	144400.000	0.003	5.940
10057.20	270.000	16.432	72900.000	0.004	5.598
<b>skewness</b>	-0.254	-0.637	0.470	1.764	-1.030
<b>kurtosis</b>	-1.047	-0.778	-0.442	2.036	-0.127

Table 6-7 Data transformation optimum functions	
Well log and core data	Optimum transformation function
d <sub>50</sub>	Natural log
Gamma ray	Square root
Resistivity	Natural log
Density	Square
Neutron	Untransformed
Sonic	Square

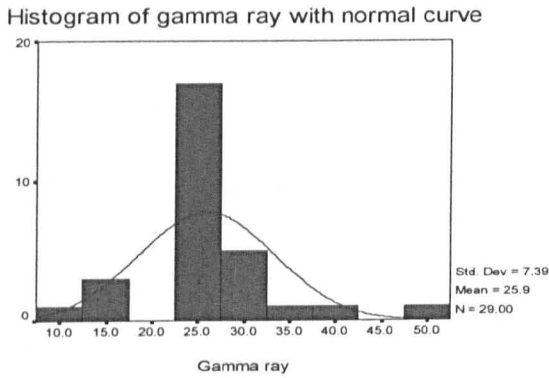


**Figure 6-1 Histogram of gamma ray with normal curve for well C10**

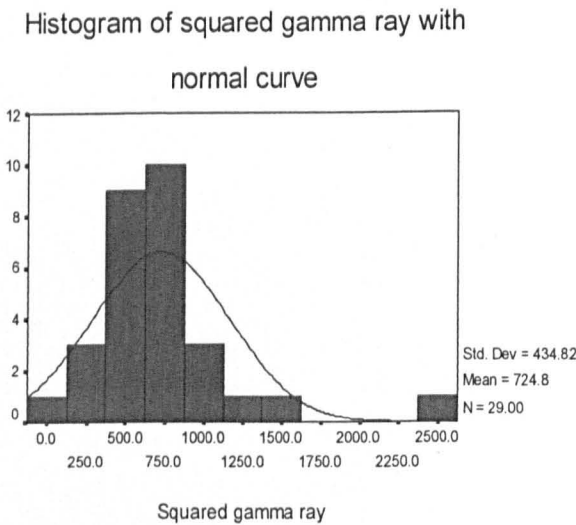


**Figure 6-2 Histogram of squared gamma ray with normal curve for well C10**

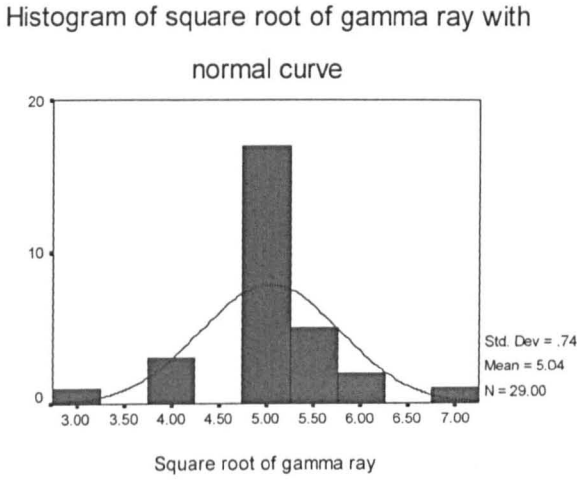


**Figure 6-3 Histogram of square root of gamma ray with normal curve for well C10**

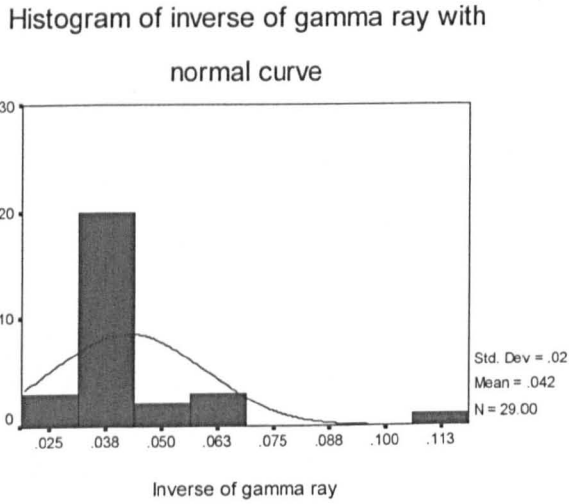


**Figure 6-4 Histogram of gamma ray with normal curve for well C10**

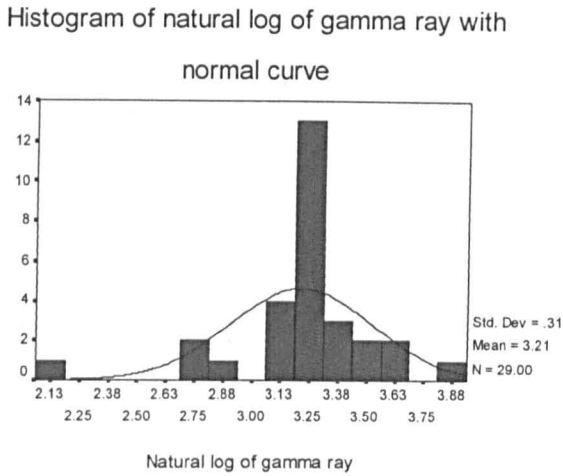


**Figure 6-5 Histogram of log of gamma ray with normal curve for well C10**

#### 6.1.4 Plots of Natural log of $d_{50}$ against various transformed log parameters

In order to understand better the complexities of the relationships between grain size distribution and the log parameters, scatter plots of the transformed  $d_{50}$  (natural log of  $d_{50}$ ) versus various transformed log variables from some of the wells were made (figures 6-6 – 6-10) and their linear correlation coefficients compared. The linear correlation coefficients of the plots are presented in table 6-8. The correlation coefficients for all the data sets were observed to be very low (near zero) for wells C10, C8, C6 and C5 suggesting near zero correlation between well log parameters and median grain size for these wells. Well C7 log parameters and median grain size data however show some level of correlation.

This preliminary studies suggest that simple statistical correlation analysis was not able to resolve the relationship between grain size and well log parameters in wells C10, C8, C6, C5 whilst it was able to bring out the link between some of the well log parameters and grain size in Well C7. This further confirms the complexity of the relationship between grain size distributions and well log parameters.

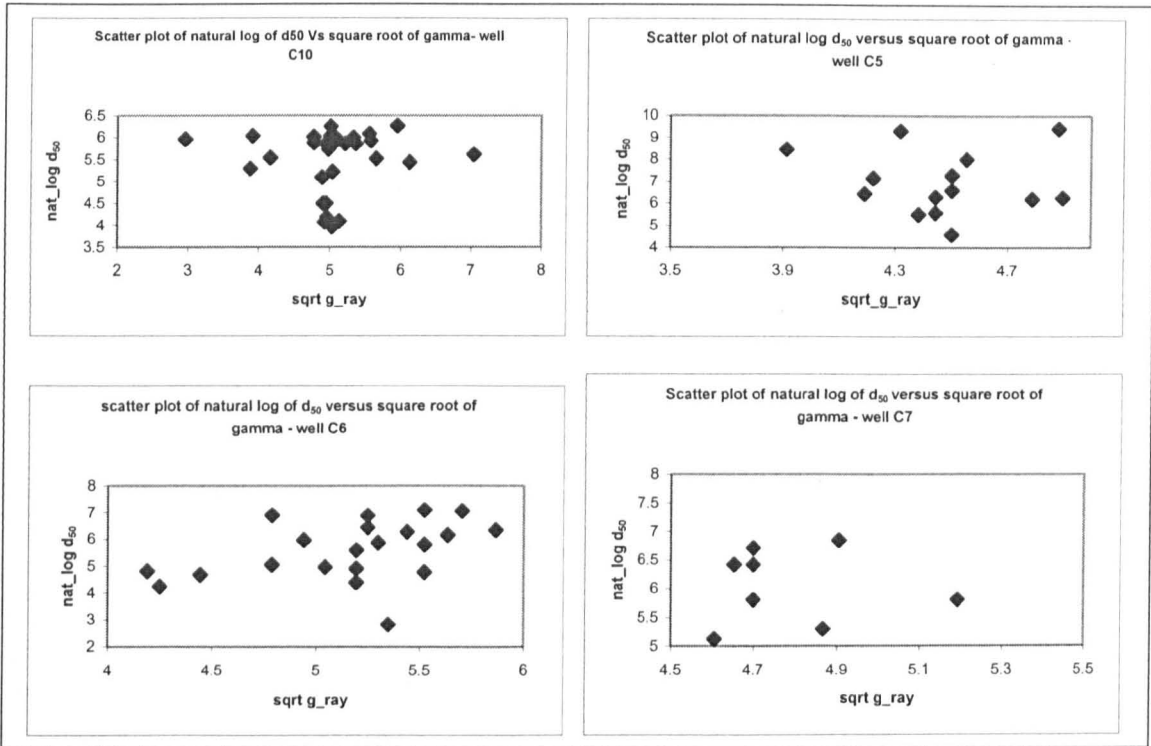


**Figure 6-6 Scatter plots of natural log of Gamma Ray and natural log of  $d_{50}$  for wells C10, C5, C6 and C7**

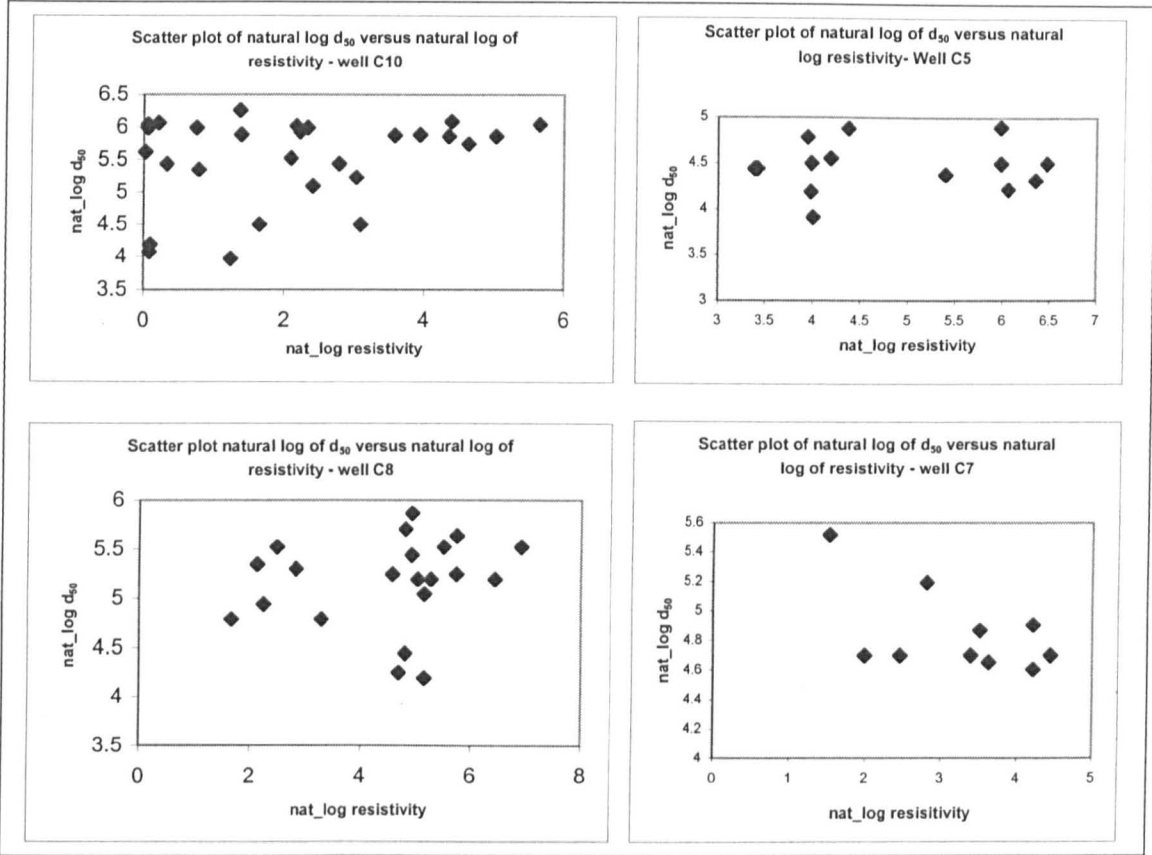


**Figure 6-7 Scatter plots of natural log of Resistivity and natural log of  $d_{50}$  for wells C10, C5, C8 and C7**

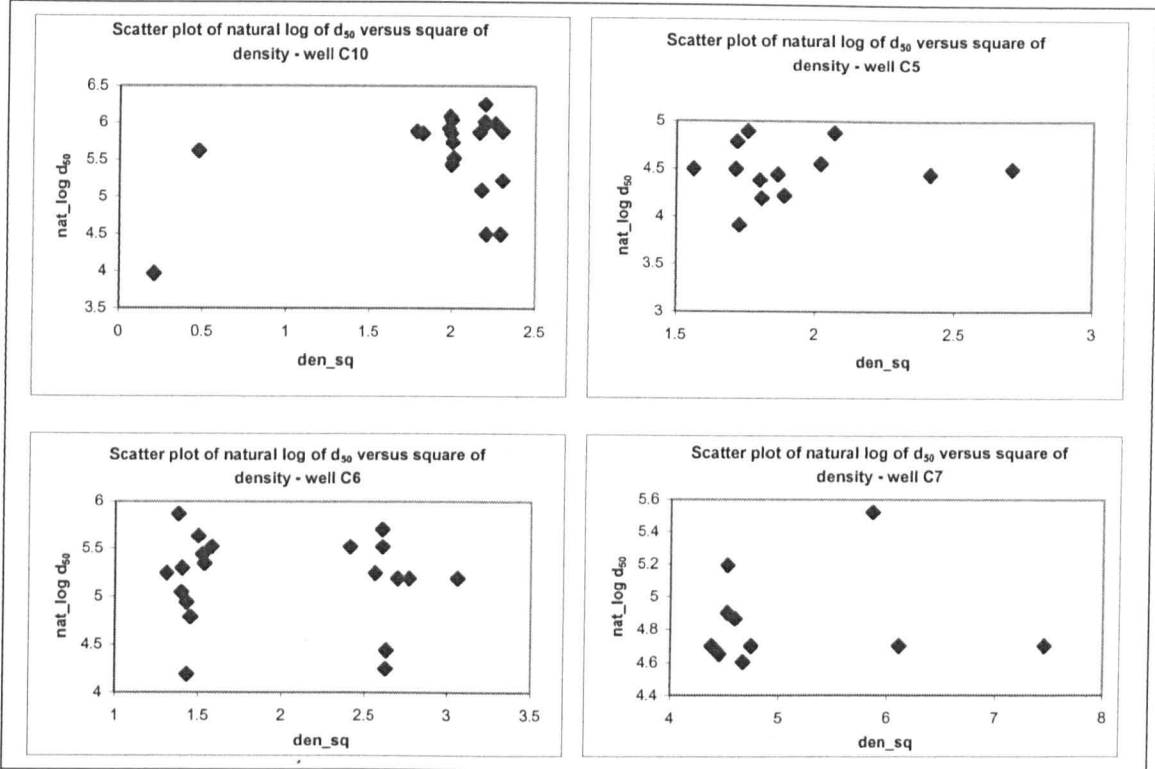


**Figure 6-8 Scatter plots of square of Density and natural log of d<sub>50</sub> for wells C10, C5, C6 and C7**

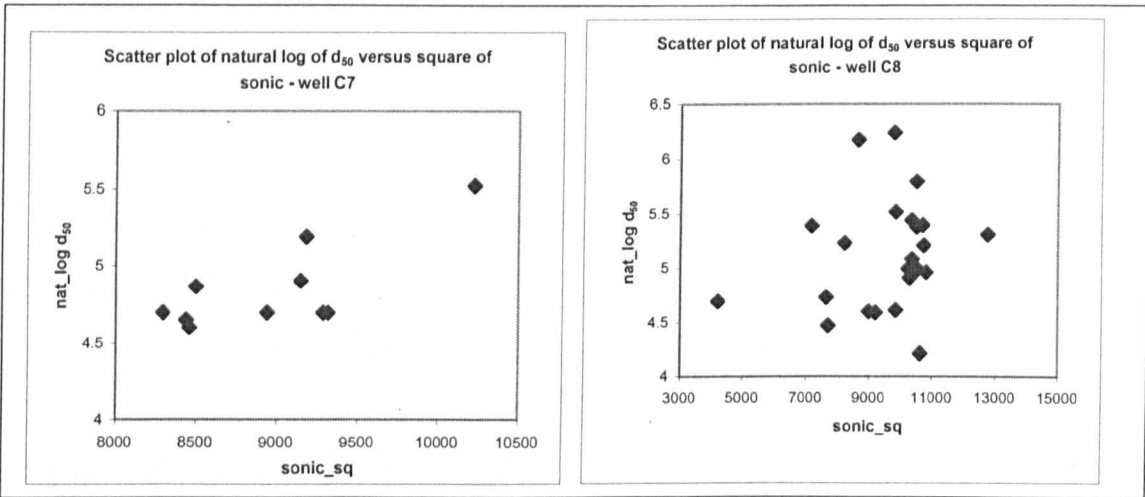


**Figure 6-9 Scatter plots of square of Sonic and natural log of d<sub>50</sub> for wells C7 and C8**

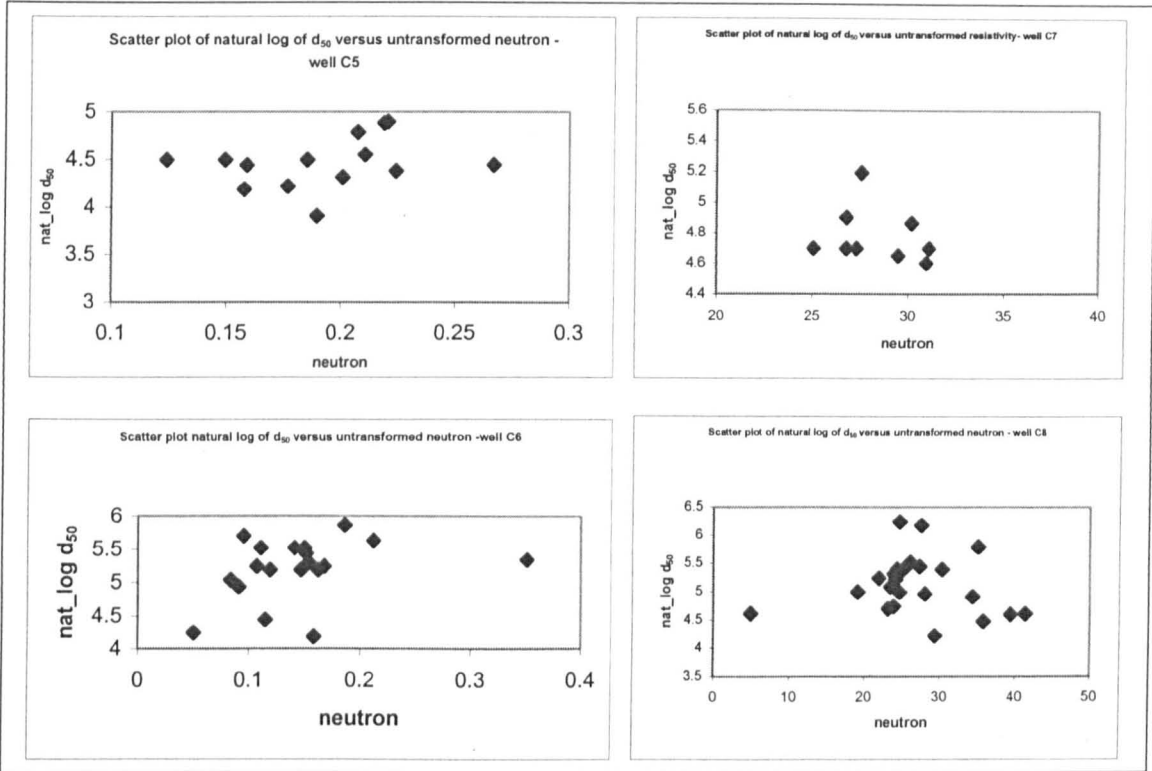


**Figure 6-10 Scatter plots Neutron and natural log of d<sub>50</sub> for wells C5, C7, C6 and C8**

**Table 6.8 Linear correlation coefficients of plots of well log data versus median grain size**

Plot	Well	Correlation Coefficient (R <sup>2</sup> )
Sqrt of Gamma Ray Vs Nat_log of d <sub>50</sub>	C10	0.001
	C5	0.007
	C6	0.165
	C7	0.220
Nat_log of Resistivity Vs Nat_log of d <sub>50</sub>	C10	0.079
	C5	0.003
	C8	0.003
	C7	0.313
Sq of Density Vs Nat_log of d <sub>50</sub>	C10	0.142
	C5	0.003
	C6	0.002
	C7	0.004
Sq of Sonic Vs Nat_log of d <sub>50</sub>	C7	0.565
	C8	0.036
Neutron Vs Nat_log of d <sub>50</sub>	C5	0.075
	C7	0.427
	C6	0.110
	C8	0.006

### 6.1.5 Principal Component Analysis (PCA)

Principal components analysis, a multivariate statistical technique, was used with a view to (1) removing redundant, highly correlated well logs, (2) reducing the number of well logs initially selected for this work and (3)

identifying a combination of well logs that better explain the pattern of observed correlations within data suites.

Figure 6-11 is a scree plot of the factor analysis components whilst Table 6-9 is a table of eigenvalues showing the total and individual contributions of the components to the total variability observed in data. The results show that the first four of the five components used in the analysis account for more than 93% of the variability in the data, with the last and fifth component accounting for just a little above 6% of the variability. The result suggests that the fifth component does not contribute much to the variability in the data and as such could be disregarded in further analysis.

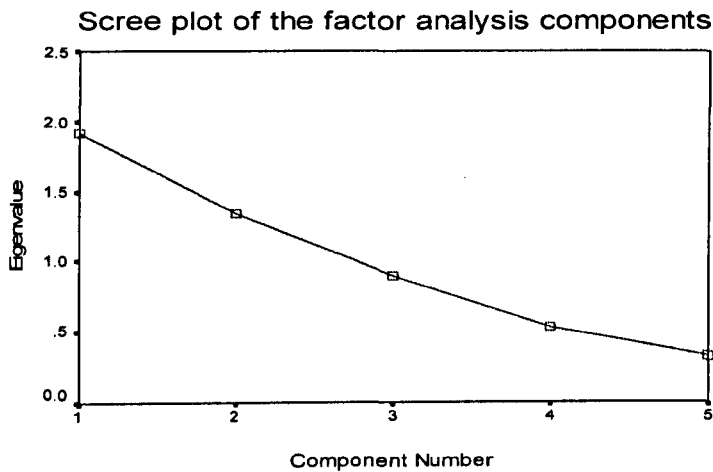


**Figure. 6-11. Scree plot of the Principal Component Analysis**

**Table 6-9 Eigenvalues of the Principal Component Analysis**

Table of eigenvalues						
Component	Initial Eigenvalues			Extraction Sums of Squared Loadings		
	Total	% of Variance	Cumulative %	Total	% of Variance	Cumulative %
1	1.925	38.495	38.495	1.925	38.495	38.495
2	1.337	26.749	65.244	1.337	26.749	65.244
3	.888	17.757	83.001	.888	17.757	83.001
4	.526	10.517	93.518	.526	10.517	93.518
5	.324	6.482	100.000	.324	6.482	100.000

Extraction Method: Principal Component Analysis.

### 6.1.6 Regression analysis

Based on the results of PCA, multiple linear regression analyses were performed using 3, 4 and 5 log components to further explore the nature of the relationship between log parameters and grain size. The 3-component regression analysis summary is shown in table 6-10 while the output from its resultant regression model is shown in figure 6-12. Similarly, the 4- and 5-component regression analyses' summaries are shown in tables 6-11 and 6-12 while the outputs from their resultant regression models are shown in figure 6-13 and 6-14.

Figures 6-15 to 6-17 are normal P-P plots of standardized residual  $d_{50}$  (natural log) for the three regression implementations. They show that the outputs from the three models are normally distributed.

Generally, the results obtained show that regression analysis was not able to resolve satisfactorily the non-linear complex relationships between the log parameters and the grain size distribution, justifying the need for neural network modelling.

**Table 6-10. Summary table for three-log regression analysis**

**Coefficients<sup>a</sup>**

Model	Unstandardized Coefficients		Standardized Coefficients	t	Sig.	95% Confidence Interval for B		Correlations			Collinearity Statistics	
	B	Std. Error	Beta			Lower Bound	Upper Bound	Zero-order	Partial	Part	Tolerance	VIF
1 (Constant)	4.075	.951		4.283	.000	2.076	6.074					
GRAY (sqrt)	.084	.117	.169	.711	.486	-.163	.330	.157	.165	.160	.890	1.124
RES (Ln)	.123	.107	.267	1.149	.266	-.102	.348	.254	.261	.258	.933	1.072
NEUT	.007	.017	.108	.441	.664	-.028	.043	-.017	.103	.099	.837	1.194

a. Dependent Variable: D50

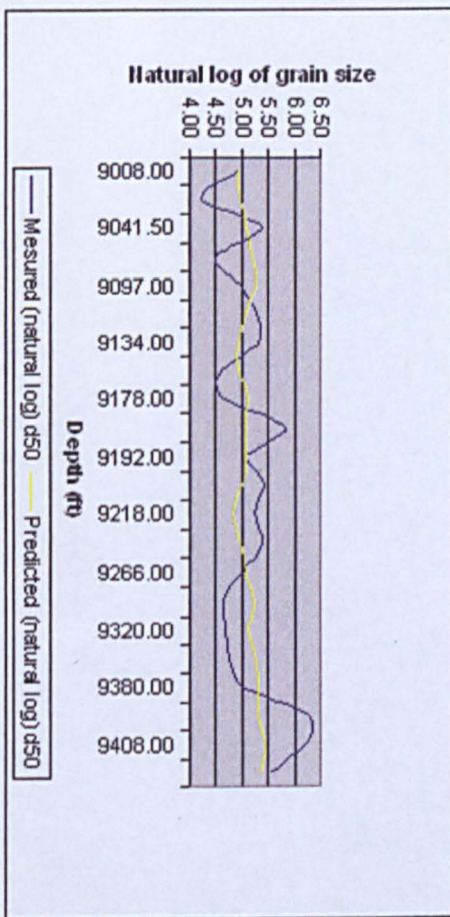


**Figure 6-12 Three-log regression model output compared with measured output.**

**Table 6-11. Summary table for four-log regression analysis**

**Coefficients**

Model	Unstandardized Coefficients		Standardized Coefficients	t	Sig.	95% Confidence Interval for B		Correlations			Collinearity Statistics	
	B	Std. Error	Beta			Lower Bound	Upper Bound	Zero-order	Partial	Part	Tolerance	VIF
1 (Constant)	2.515	3.932		.640	.531	-5.781	10.811					
GRAY (sqrt)	.070	.124	.143	.566	.579	-.192	.333	.157	.136	.130	.831	1.203
RES (Ln)	.118	.110	.257	1.07	.299	-.115	.351	.254	.252	.247	.923	1.084
NEUT	.010	.018	.147	.547	.592	-.029	.049	-.017	.131	.126	.735	1.361
DEN (sqd)	1.315	3.211	.110	.410	.687	-5.459	8.089	.148	.099	.094	.734	1.363

<sup>a</sup> Dependent Variable: D50

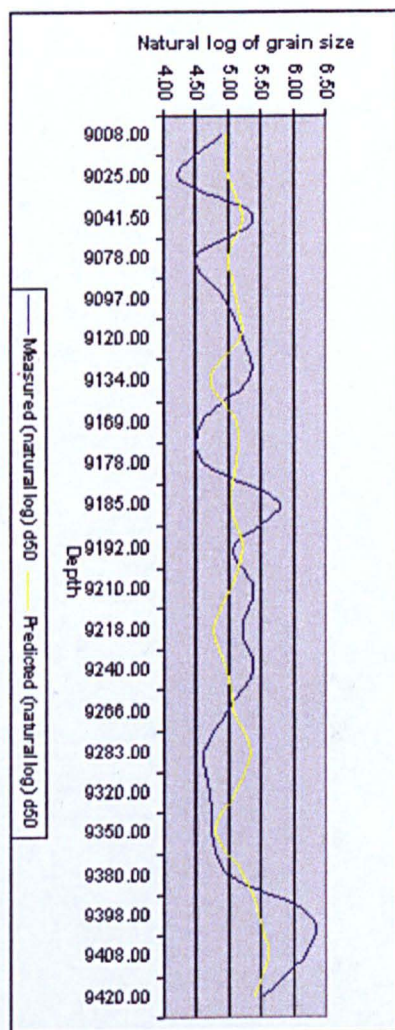


**Figure 6-13 Four-log regression model output compared with measured output.**

**Table 6-12. Summary table for five-log regression analysis**

Model		Coefficients													
		Unstandardized Coefficients		Standardized Coefficients	t	Sig.	95% Confidence Interval for B		Correlations			Collinearity Statistics			
		B	Std. Error	Beta			Lower Bound	Upper Bound	Zero-order	Partial	Part	Tolerance	VIF		
1	(Constant)	2.623	3.880		.676	.509	-5.603	10.849							
	GRAY (sqrt)	.141	.136	.285	1.037	.315	-.147	.429	.157	.251	.235	.679	1.473		
	RES (Ln)	.184	.122	.398	1.511	.150	-.074	.441	.254	.353	.343	.741	1.349		
	NEUT	.014	.018	.203	.754	.462	-.025	.053	-.017	.185	.171	.713	1.402		
	DEN (sqd)	-.139	3.387	-.012	-.041	.968	-7.320	7.042	.148	-.010	-.009	.642	1.559		
	SONIC (sqd)	.000	.000	.338	1.211	.243	.000	.000	.106	.290	.275	.660	1.516		

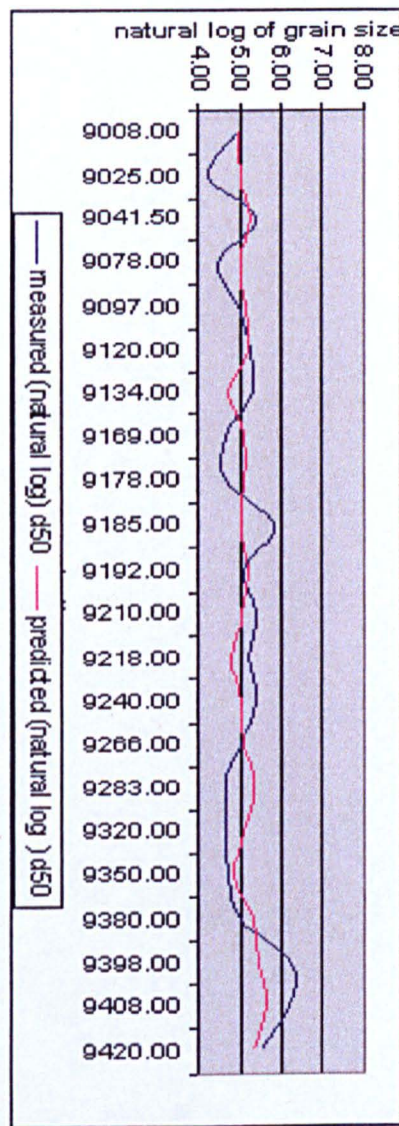


**Figure 6-14 Five-log regression model output compared with measured output.**

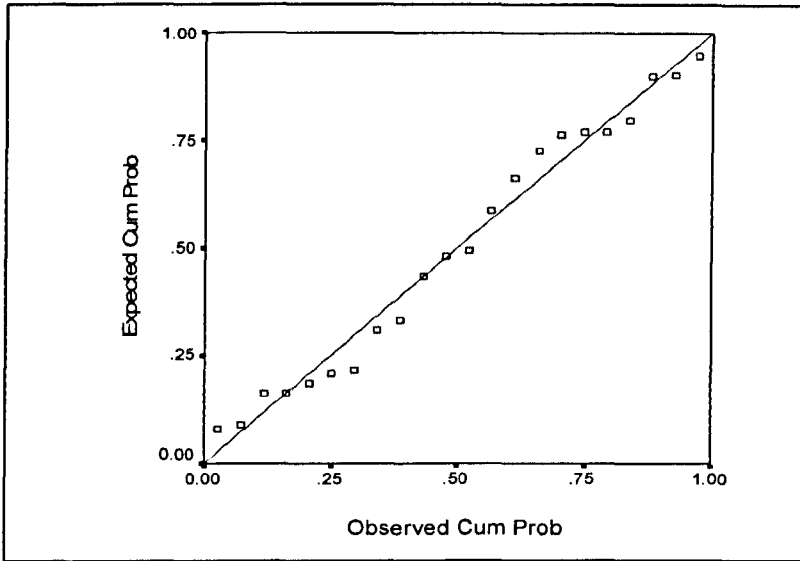


**Figure 6-15 Normal P-P plot of standardized residual  $d_{50}$  (natural log) for the three-log regression model**

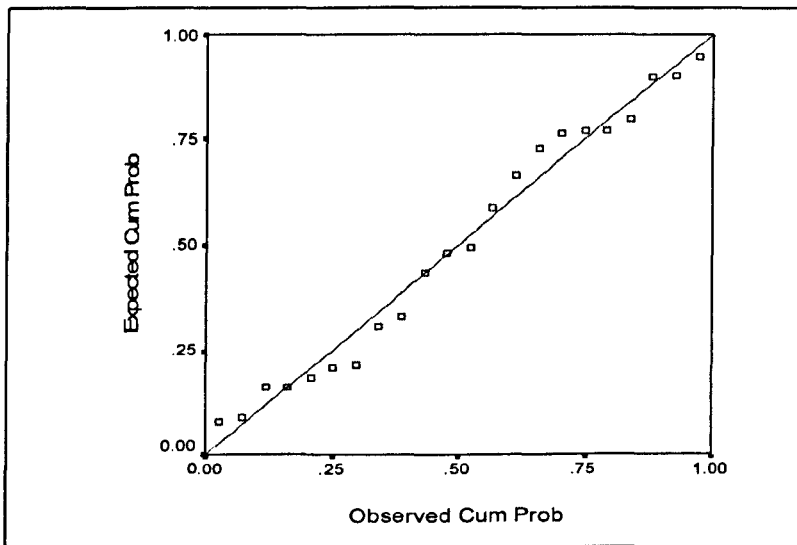


**Figure 6-16 Normal P-P plot of standardized residual  $d_{50}$  (natural log) for the four-log regression model**

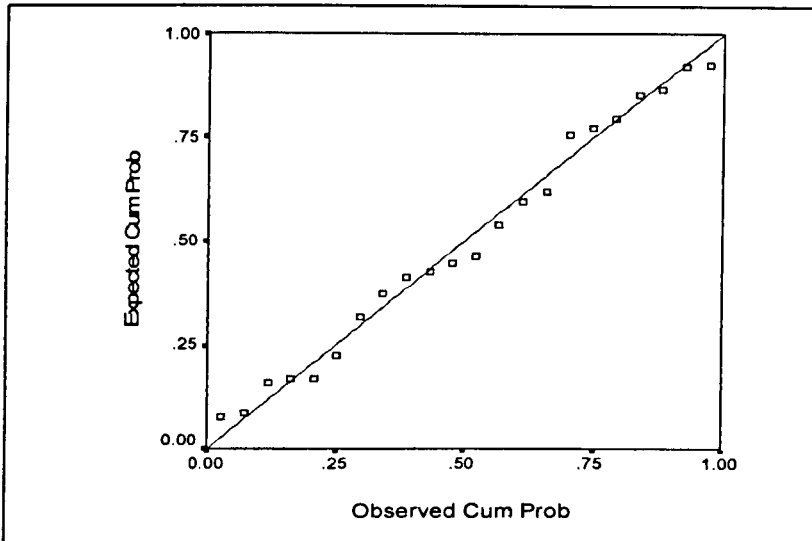


**Figure 6-17 Normal P-P plot of standardized residual  $d_{50}$  (natural log) for the five-log regression model**

## 6.2 Modelling grain size distribution using statistical techniques

### 6.2.1 Variable controlling grain size distribution

The petrophysical and textural parameters that exercise control on the grain size distribution pattern of any sediments are listed in Table 6-13.

<b>Table 6-13 Parameters exercising control on grain size distribution</b>	
<b>Petrophysical parameters</b>	<b>Textural parameters</b>
Porosity	Grain size
Permeability	Grain shape
Water saturation/irreducible water saturation	Sorting
Cementation exponent	Grain packing
	Pore size distribution
	Specific surface area of grain
	Shale volume/content

Grain size distribution can therefore be said to be a function of porosity, permeability, water saturation or irreducible water saturation, cementation exponent, grain size, grain shape, sorting, grain packing, pore size distribution and shale volume or content. The relation can be expressed as:

$$GSD = f(\phi, k, s_{wirr}, m_e, d, g_{sh}, g_s, a_p, P_D, S_A, V_{sh}) \quad 6-1$$

Where

$\phi$  = porosity

$k$  = permeability

$s_{wirr}$  = irreducible water saturation

$m_e$  = cementation factor

$d$  = median grain size

$g_{sh}$  = grain shape

$g_s$  = grain sorting

$a_p$  = grain packing

$P_D$  = pore size distribution

$S_A$  = specific surface area of grain

$V_{sh}$  = volume of shale

### 6.2.2 Interrelationship among variables

Some sort of interrelationship exists among some of the variables listed in section 6.2.1 above. For example grain packing is a function of sorting, which in turn, exercises a great control on porosity. Sorting itself is dependent on the grain size and shape. Packing can therefore be said to be dependent on sorting, grain size and grain shape and can therefore be used to account for these three variables.

In order to assess this interrelationship especially among suspect variables, multivariate and correlation analysis have been performed on four of the variables in which interrelationship is suspected including packing, porosity, pore size distribution, and specific surface area. The four variables have been presented as a sub model of the form expressed in the relation below:

$$d_{50}=f(\phi, a_p, P_D, S_A)$$

6-2

The results of the analysis are shown in Table 6-14. The Variation Inflation Factor (VIF) of 4.9 and 4.7 for porosity and packing respectively suggest there is a strong multicollinearity between the two variables. Though VIF values of 1.2 and 1.1 for specific surface area and pore size distribution respectively suggest some sort of multicollinearity in them, these values can be ignored as they are small enough for the purpose of this work. The case for multicollinearity among the variables is also strengthened by the R-sq (adj) of 0.2%, which is very poor.

**Table 6-14 The statistical parameters used to assess interrelationship between four variables**

Parameter	Coefficient	SE Coefficient	T	P	VIF
Porosity	-0.0337	0.01441	-0.23	0.822	4.9
Packing	-0.02955	0.006380	-0.46	0.657	4.7
Specific surface area	-0.0003632	0.0004248	-0.86	0.421	1.2
Pore size distribution	0.10382	0.07740	1.34	0.222	1.1
R-sq = 36.5%      R-sq(adj) = 0.2%					

In order to evaluate the effects of each of the variables on the overall performance of the model and to be sure where multicollinearity actually exists within the variables, each variable was removed from the sub-

model in turn and the p-value and VIF computed. The results are shown in Tables 6-15 to 6-18.

When porosity and packing were removed in turn, the p values of the three remaining variables dropped drastically while their VIFs fell within the range 1.1 – 1.2 (Tables 6-15 and 6-16). However when the other variables - specific surface area and pore size distribution - were removed in turn, the p-values and the VIFs were still very large (Tables 6-17 and 6-18)

**Table 6-15 The statistical parameters used to assess interrelationship between three variables when porosity is removed**

Parameter	Coefficient	SE Coefficient	T	P	VIF
Packing	-0.004258	0.002931	-1.45	0.184	1.1
Specific surface area	-0.0003411	0.0003889	-0.88	0.406	1.2
Pore size distribution	0.10431	0.07266	1.44	0.189	1.1
R-sq = 36.0%      R-sq(adj) = 12.0%					

**Table 6-16 The statistical parameters used to assess interrelationship between three variables when packing is removed**

Parameter	Coefficient	SE Coefficient	T	P	VIF
Porosity	-0.009193	0.006692	-1.37	0.207	1.2
Specific surface area	-0.0003757	0.0004026	-0.93	0.378	1.2
Pore size distribution	0.10119	0.07330	1.38	0.205	1.1
R-sq = 34.50%      R-sq(adj) = 10.0%					

**Table 6-17 The statistical parameters used to assess interrelationship between three variables when specific surface area is removed**

Parameter	Coefficient	SE Coefficient	T	P	VIF
Porosity	-0.00063	0.01381	-0.05	0.965	4.6
packing	-0.003301	0.006259	-0.53	0.612	4.6
Pore size distribution	0.11761	0.07442	1.58	0.153	1.0
R-sq = 29.8%      R-sq(adj) = 3.5%					

**Table 6-18 The statistical parameters used to assess interrelationship between three variables when pore size distribution is removed**

Parameter	Coefficient	SE Coefficient	T	P	VIF
Porosity	-0.00389	0.01510	-0.26	0.803	4.9
packing	-0.002327	0.006673	-0.35	0.736	4.6
Specific surface area	0.0004819	0.0004357	-1.11	0.301	1.2
R-sq = 20.1%      R-sq(adj) = 0.0%					

Further evaluation was performed using simple linear correlation to examine pairwise relationships between the variables. The table below (Table 6-19) shows the results of the analysis.

The high Pearson correlation coefficient and very low p-value for the correlation between porosity and packing (Table 6-19) confirmed the earlier results that there is strong multicollinearity between packing and porosity

**Table 6-19 Correlation coefficients and p-value for linear correlation evaluation.**

Parameter	Porosity	Specific surface area	Pore size distribution	Packing
Porosity		Pearson correlation = 0.367 P-Value = 0.241	Pearson correlation = 0.159 P-Value = 0.622	Pearson correlation = 0.885 P-Value = 0.000
Specific surface area	Pearson correlation = 0.367 P-Value = 0.241		Pearson correlation = -0.246 P-Value = 0.440	Pearson correlation = -0.303 P-Value = 0.338
Pore size distribution	Pearson correlation = 0.159 P-Value = 0.622	Pearson correlation = -0.246 P-Value = 0.440		Pearson correlation = 0.169 P-Value = 0.599
Packing	Pearson correlation = 0.885 P-Value = 0.000	Pearson correlation = -0.303 P-Value = 0.338	Pearson correlation = 0.169 P-Value = 0.599	

### 6.2.3 Multiple Regression Analysis

Based on the statistical studies in the preceding sections, five petrophysical and textural parameters were used in a multiple regression analysis to obtain a regression model for the prediction of  $d_{50}$ . The five parameters used are porosity ( $\phi$ ), permeability ( $k$ ), irreducible water

saturation ( $s_{w_{irr}}$ ) specific surface area ( $S_A$ ) and cementation factor ( $m_e$ ). The regression equation is presented in equation 6-3.

$$d_{50} = -611 + 189\phi + 2.13k - 13.3S_{w_{irr}} + 396m_e - 32.4S_A \quad 6-3$$

An independent field data has been used to test the regression model presented in equation (6-3). The results of testing (Figure 6-18) show large deviations between the predicted and actual data. This is an indication that the model is not robust enough for use in field prediction and analysis of grain size data.

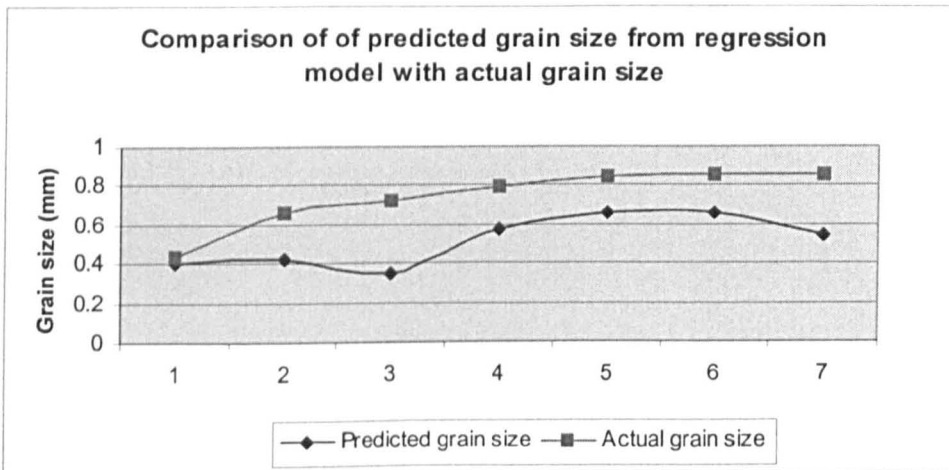


**Fig 6-18 Comparison of the statistical regression model with measured data**

## 6.3 Modelling grain size distribution using analytical technique

### 6.3.1 Rationale for the analytical model

A variety of models exists which relate median grain size ( $d_{50}$ ) to some textural and petrophysical parameters. The major shortcoming though is that many of these models tend to suggest a simple relationship between

$d_{50}$  and a few of these parameters. A need for a composite model, which considers as many parameters as may have control on the  $d_{50}$  or grain size distribution, is therefore recognised in this work.

### 6.3.1.1 Analytical model development

Coates and Denno (1981)<sup>148</sup> provided an empirical relation for estimating permeability from effective porosity and irreducible water saturation as given below in equation 6-4:

$$k^{1/2} = 100\phi_e^2 \left[ \frac{(1 - S_{wirr})}{S_{wirr}} \right] \quad 6-4$$

Where:

$k$  = permeability

$\phi_e$  = effective porosity

$S_{wirr}$  = irreducible water saturation

Revil et. al. (2002)<sup>149</sup> also gave an empirical relation which relates permeability with mean grain size, effective porosity, packing parameter and cementation exponent.

$$k = \frac{d^2 \phi_e^{3m_c}}{4a_p m_e^2} \quad 6-5$$

Where:

$k$  = permeability

$\phi_e$  = effective porosity

$a_p$  = packing parameter

$m_e$  = cementation factor/exponent

If equation (6-4) is divided by equation (6-5), the result will be:

$$k^{-\frac{1}{2}} = \frac{4 * 100 \phi_e^2 [(1 - s_{wirr}) / (s_{wirr})] * a_p * m_e^2}{d^2 \phi_e^{3m_e}} \quad 6-6$$

Re-arrangement of equation (6-4) will give:

$$d^2 = \frac{4 * 100 \phi_e^{(2-3m_e)} * [(1 - s_{wirr}) / (s_{wirr})] * a_p * m_e^2}{k^{-\frac{1}{2}}} \quad 6-7$$

An expression for calculating the coefficient of packing can be derived from Kozeny-Carman<sup>3-4</sup> equation for permeability estimation as modified by Oyeneyin et. al. (1992)<sup>38</sup>

$$a_p = \frac{10^6 \phi^3}{k S_A^2} \quad 6-8$$

Where:

$\phi$  = Absolute porosity

$S_A$  = Specific surface area of grain particle

The use of equation (6-8) is based on the assumption of non-shaliness in the formation of interest and that absolute porosity can be used to approximate effective porosity.

Equation (6-8) can be substituted in equation (6-7) to give

$$d^2 = \frac{4 * 10^8 * \phi_e^{(s-3m_e)} * [(1 - s_{wirr}) / (s_{wirr})] * m_e^2}{k^{\frac{1}{2}} * S_A^2} \quad 6-9$$

Transforming equation (6-9) into a dimensionally homogeneous one, we have:

$$d = \frac{4 * 10^8 * \phi_e^{(s-3m_e)} * [(1 - s_{wirr}) / (s_{wirr})] * m_e^2}{k^{\frac{1}{2}} * S_A^2} \quad 6-10$$

If the constant in equation (6-10) is replaced by  $C_i$ , the resulting equation is given as:

$$d = \frac{C_i \phi_e^{(s-3m_e)} * [(1 - s_{wirr}) / (s_{wirr})] * m_e^2}{k^{\frac{1}{2}} * S_A^2} \quad 6-11$$

$C_i$  in equation (6-11) accounts for grain packing and shape.

A total of 37 data sets have been used in a spreadsheet analysis to obtain a value for the constant in equation (6-11); the value obtained for the constant is 0.29758. This constant will however need to be determined for every field.

The results of the comparison between the analytical model output and measured data are shown in Figure 6-19.

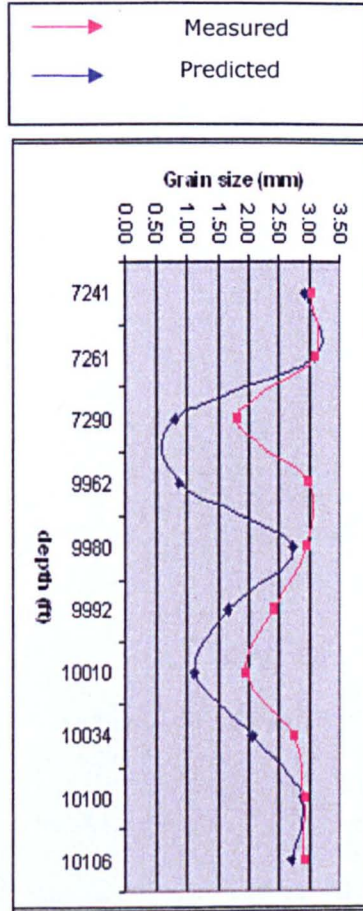


**Figure 6-19 Comparison of analytical model predictions with measured data**

## 6.4 The dimensional analysis Model

The petrophysical and textural parameters that affect the grain size distribution have been listed previously in sections 6.1.2 (Table 6-7).

Expressing these variables using their dimensions, we have

$$\phi = [\text{dimensionless}]$$

$$k = [L^2]$$

$$S_{wirr} = [\text{dimensionless}]$$

$$m_e = [\text{dimensionless}]$$

$$d = [L]$$

$$g_s = [L]$$

$$g_{sh} = [\text{dimensionless}]$$

$$a_p = [\text{dimensionless}]$$

$$D_p = [L]$$

$$S_A = [L^{-1}]$$

$$V_{sh} = [\text{dimensionless}]$$

Using dimensional analysis, the following three relations can be obtained with respect to certain flow and textural properties of a reservoir rock.

$$\Pi_1 = \frac{\sqrt{k/\phi}}{d} \quad 6-12$$

Equation (6-12) describes the unit flow property of the reservoir rock. The term  $\sqrt{k/\phi}$  is the Reservoir Quality Index (RQI) proposed and described by Amaefule et al<sup>150</sup>

$$\Pi_2 = \frac{d * S_A}{D_p} \quad 6-13$$

Equation (6-13) describes the mean grain volume divided by the pore size

$$\Pi_3 = V_{sh} * m * S_{wirr} * a_p * g_s * g_{sh} \quad 6-14$$

Equation (6-14) describes the textural properties of reservoir rocks.

The three equations (6-12, 6-13 and 6-14) can be combined in a multiplication operation to give the median grain size.

$$d_{50} = \left[ \frac{\sqrt{k/\phi}}{d} \right] * \left[ \frac{d * S_A}{D_p} \right] * [V_{sh} * S_{wirr} * m_e * g_s * a_p * g_{sh}] \quad 6-15$$

If the grains are assumed to be well rounded, approximating a sphere; and poorly cemented (unconsolidated), the values of  $g_{sh}$ , the grain shape;  $m_e$ , the cementation factor; and  $a_p$ , the packing coefficient can be approximated by 1.0, 2.15 and 0.62 respectively.

Substituting these values in (6-15), we have:

$$d_{50} = 1.33 * \left[ \sqrt{\frac{k}{\phi}} \right] * \left[ \frac{S}{D_p} \right] * [V_{sh} * S_{wirr} * g_s] \quad 6-16$$

Parameters in equation (6-16) are in SI units. There is therefore a need to convert them to field units. Specific surface area,  $s$  and pore size,  $D_p$  retain their SI units while permeability,  $k$  is converted to field unit to give

$$GSD = 1.33878 * \left[ \sqrt{\frac{k}{\phi}} \right] * \left[ \frac{S}{D_p} \right] * [V_{sh} * S_{wirr} * g_s] \quad 6-17$$

The model has been used to predict grain size ( $d_{50}$ ) from a field data. The results, though were not compared with the actual field grain size data due to unavailability of appropriate data, appeared reasonable as shown in Figure 6-20.

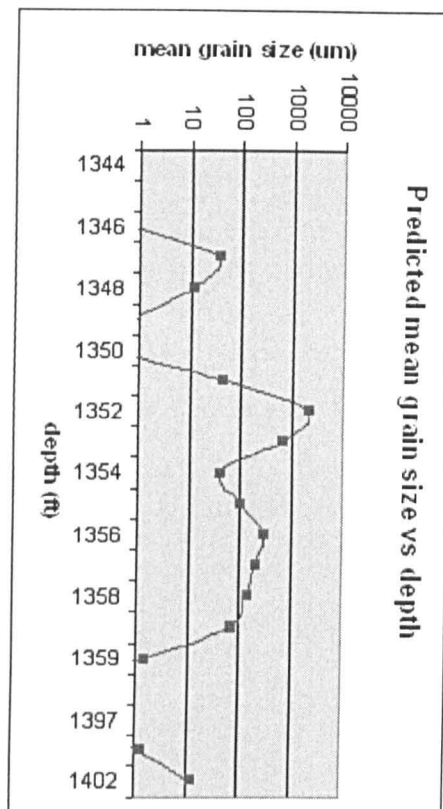


**Figure 6-20 Predictions from the dimensional analysis model**

## 6.5 Modelling grain size distribution using combined neural networks and statistical techniques

### 6.5.1 First neural network implementation

A Neural network with four input nodes, four hidden layer nodes and one output node was built for the first implementation of the neural network modelling. The numbers of input and output nodes were chosen to match the numbers of inputs into and output from the network. However the number of hidden layer nodes was chosen heuristically as there are no rules governing the choice of number of hidden layer nodes. Experiments were performed later to decide on the optimum number of nodes in the hidden layer. The topology of the network used in the initial implementation is shown in Figure 6-21 and summarised in the Table 6-20 below.

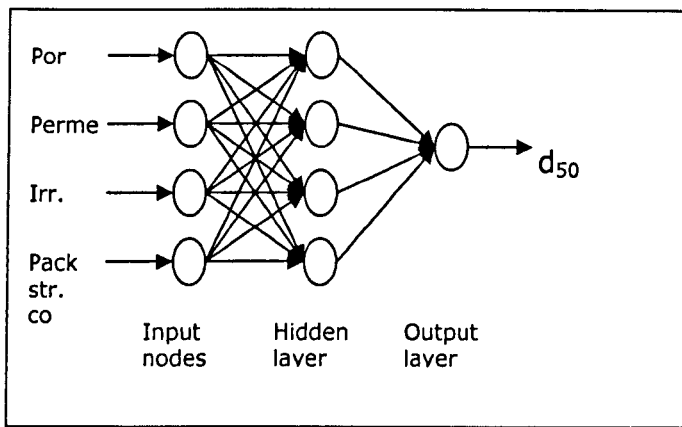


**Figure 6-21 Topology of the NN used for the first implementation**

**Table 6-20 Summaries of the initial neural network topology**

Network parameters	Number/value of parameters used in network
Network layers	1
Input nodes	4
Output nodes	1
Hidden layer nodes	5
Learning rate	0.75
Momentum	0.9

### 6.5.1.1 Input and output data selection

The choice of input data was influenced by the in-depth statistical studies carried out to understand the nature of the relationship between certain log data and grain size; and reported in the previous sections. The data input into the NN were porosity, permeability, irreducible water saturation, and pack structure coefficient. Only four were chosen to reduce network complexity. The data were derived using a combination of various well logs. The desired output data was the median grain size from core analysis.

---

### 6.5.1.2 Data Normalisation and de-normalisation

Input and output data were respectively normalised to lie within a range between 0 and 1 and de-normalised to assume their original values, using the procedures and processes described in chapter 5. Normalisation is necessary because the sigmoid transfer function used within the hidden and the output layers of the neural network where neural computation takes place is capable of returning only values within this range.

### 6.5.1.3 Neural network coding

A multi-perceptron (MLP) neural network model was coded in C++ for the modelling studies. The training algorithms used for the coding was error backpropagation training algorithm, being the typical training algorithm for MLP. The EBP training algorithm is summarised in seven steps as given below:

1. Apply the first pattern.
2. Perform the forward pass.
3. Perform the backward pass.
4. Do 1, 2 & 3 for all the patterns up to the last pattern.
5. Is total summed error for all patterns less than a specified error tolerance? If no, go to 1.
6. Else, go to 7.
7. Stop network training.

Processes taking place in stage three of the learning process are very crucial to the network learning and they include:

- Calculation of the output nodes' errors
- Change of output layer weights
- Calculation of hidden layer errors by back propagating the output layer errors

- Change of hidden layer weight

### 6.5.1.4 The Network training and validation

The network was trained using an error tolerance of 0.01. The low error tolerance was chosen because it was observed that the lowest difference obtainable between any two desired output data points was 0.01. The training was achieved iteratively with the network error decreasing with increasing number of iterations. Figure (6-22) is a plot of network error versus iterations or epoch for the first training implementation. The network error decreased from 0.29 at 1000 epochs to 0.01 at 140,000 epochs.

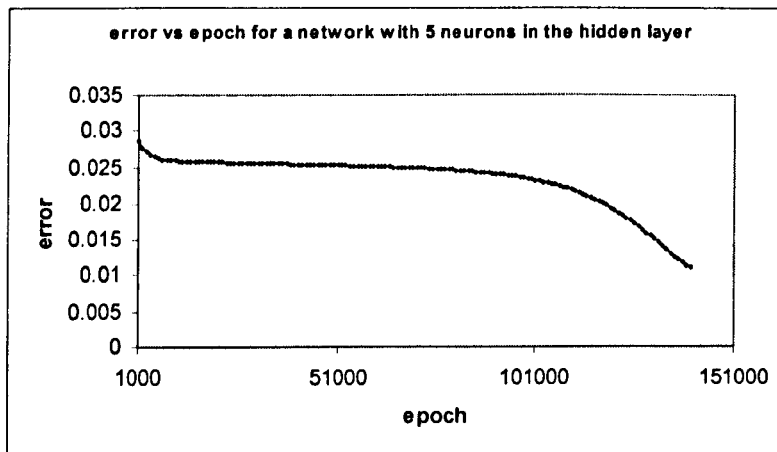


**Figure 6-22 NN error versus epoch for the initial training implementation**

### 6.5.2 Network optimisation

The purpose of network optimisation is to be able to make a decision on the optimum network topology and associated parameters such as learning rates, transfer functions in the hidden and output layers. In

optimising this network, effects of learning rate, number of neurons in the hidden layer and number of layers were investigated. These are discussed in sections 6.4.2.1 to 6.4.2.3.

### 6.5.2.1 Effect of learning rate on network

Five implementations using different learning rates – 0.3, 0.5, 0.75, 0.9 and 1.0 – were carried out to study the effects of learning rate on the network performance with a view to determining the optimum learning rate for the final network implementation.

The network trained very well with the five learning rates as evident from the final network errors, which are below the tolerance for all the learning rates. However the network convergence with the learning rates of 0.3 and 0.5 was very slow, taking too much training time. Although the network converged rapidly with the learning rates of 0.9 and 0.1, the network errors were more than the errors obtained with the lower learning rates of 0.3 and 0.5 by more than 0.02. This suggests that the network may have missed important data structure. With the learning rate of 0.75, the network converged rapidly and still had an error very close to those obtained with the learning rates of 0.3 and 0.5 (See Figure 6-23 below).

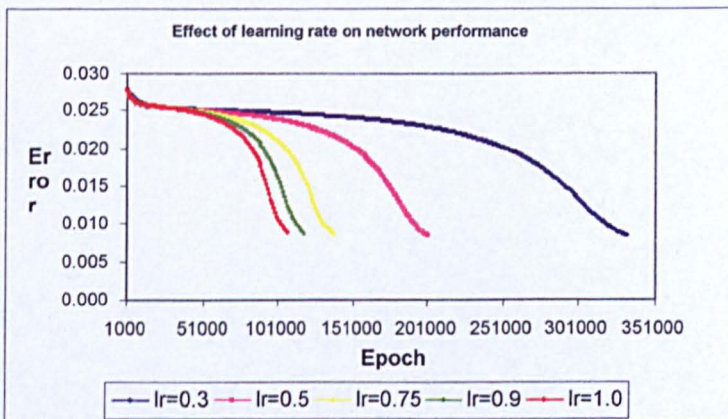


**Figure 6-23 Effect of learning rate on NN performance**

### 6.5.2.2 Effect of number of hidden layers on network performance

Three implementations using different numbers of hidden layers – 1, 2 and 3 – were carried out to study the effect of number of hidden layer on the network performance. Using one hidden layer, the network converged rapidly over 139000 epochs and had a final error of 0.008; using two hidden layers the convergence was achieved over 350000 epochs with the final network error standing at 0.01; while with three hidden layers the network convergence was slow but the network error compared well with the error obtained with one-layer network. Figure 6-24 below shows the effects of number of hidden layers on the network training.

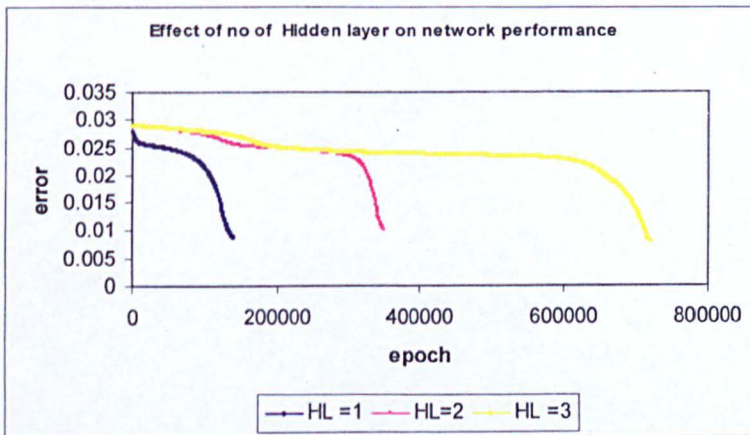


**Figure 6-24 Effect of number of hidden layers on NN performance**

### 6.5.2.3 Effect of number of neurons in the hidden layers

Four implementations using different number of neurons in the hidden layer – 2, 3, 5 and 7 - were carried out to study the effect that the number of neurons in the hidden layer will have on network performance and to be able to determine the exact number of neurons in the hidden layer that would optimise the network performance.

It was observed that three-neuron hidden layer network performed better as evident from its fast convergence and low network error (Figure 6-25).

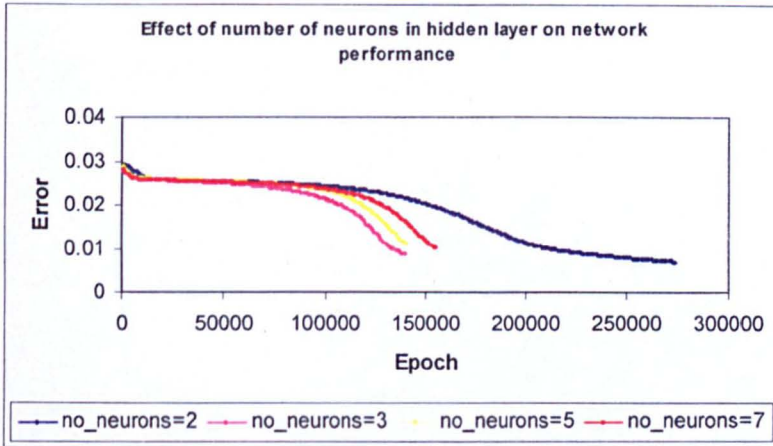


**Figure 6-25 Effect of number of neurons in the hidden layer on NN performance**

### 6.5.3 Optimised network

As stated earlier the results obtained from the optimisation studies have been used as a tool for the determination of the final network topology. The topology of the final optimised network is shown in Figure 6-26 and summarised in Table 6-21 below. The plot of network error versus epoch for the final training implementation is also shown Figure 6-27.

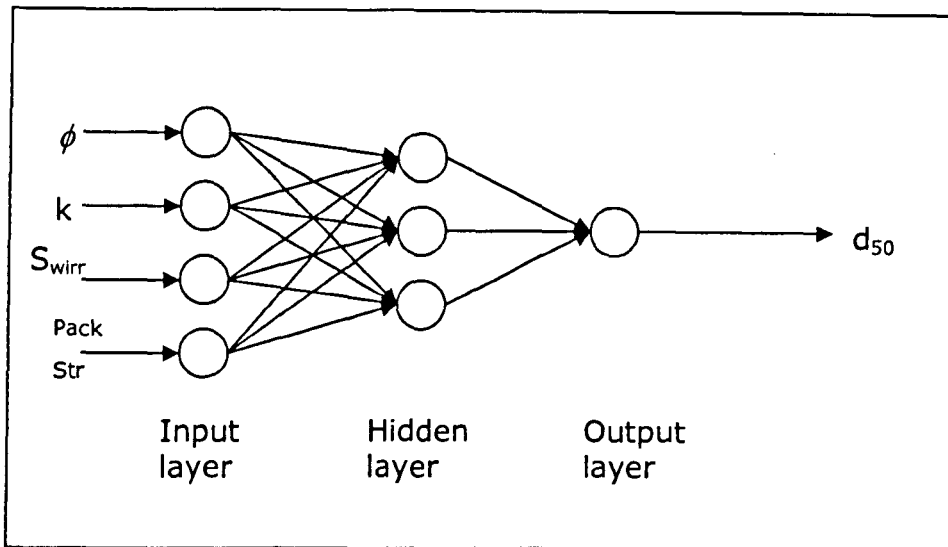


**Figure 6-26 Topology of NN for the final implementation**

**Table 6-21 Summaries of the final neural network topology**

Network parameters	Number/value of parameters used in network
Network layers	1
Input nodes	4
Output nodes	1
Hidden layer nodes	3
Learning rate	0.75
Momentum	0.9

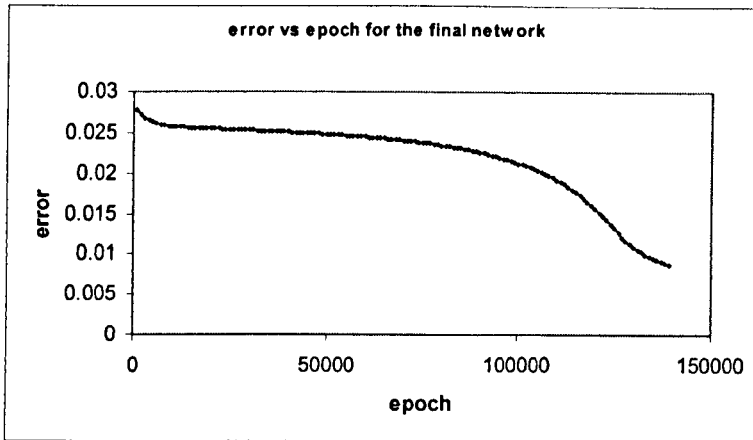


**Figure 6-27 Error versus epoch for the final training implementation**

#### 6.5.4 Neural network testing

In order to ascertain that the neural network had actually learnt and can perform on data it was not presented with during training, part of the data purposefully set aside for testing was then presented to the network without any target output. The results of this are presented in Figure 6-28 and Table 6-22. The results show that the neural network model is able to predict  $d_{50}$  with a low error margin; they also shows that the neural network model performed better than the multivariate, analytical and dimensional analysis model developed and reported in earlier sections in this chapter.

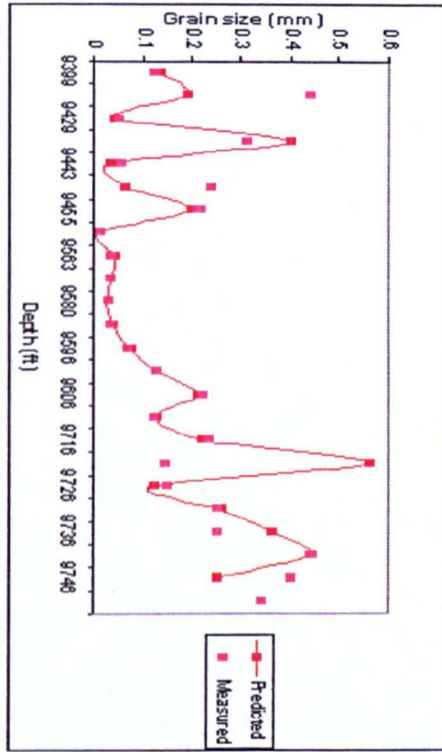


Figure 6-28 Comparison of NN predictions with measured data

**Table 6-22 Error analysis for neural network model**

Depth (ft)	Measured (mm)	Predicted (mm)	Abs_error	% error	Abs_error
9399	0.121	0.132	-0.011	-9.09091	9.090909
9415	0.436	0.19	0.246	56.42202	56.42202
9429	0.048	0.04	0.008	16.66667	16.66667
9439	0.31	0.4	-0.09	-29.0323	29.03226
9443	0.049	0.03	0.019	38.77551	38.77551
9450	0.236	0.06	0.176	74.57627	74.57627
9455	0.213	0.2	0.013	6.103286	6.103286
9558	0.01	0.011	-0.001	-10	10
9563	0.034	0.04	-0.006	-17.6471	17.64706
9574	0.029	0.032	-0.003	-10.3448	10.34483
9580	0.026	0.024	0.002	7.692308	7.692308
9585	0.033	0.035	-0.002	-6.06061	6.060606
9596	0.066	0.073	-0.007	-10.6061	10.60606
9601	0.127	0.125	0.002	1.574803	1.574803
9606	0.219	0.214	0.005	2.283105	2.283105
9711	0.12	0.123	-0.003	-2.5	2.5
9716	0.23	0.22	0.01	4.347826	4.347826
9721	0.14	0.56	-0.42	-300	300
9726	0.15	0.12	0.03	20	20
9731	0.249	0.256	-0.007	-2.81124	2.811245
9736	0.251	0.36	-0.109	-43.4263	43.42629
9741	0.44	0.44	0	0	0
9746	0.4	0.25	0.15	37.5	37.5
9751	0.34	0.24	0.1	29.41176	29.41176
corre co	0.654932462		Mean error	-6.09024	6.090238
			Abs mean error	6.090238	

## 6.5.5 Neural network prediction of orientational median grain size

### 6.5.5.1 Application of permeability anisotropy

As stated in earlier sections section, a plethora of models abounds that suggest an existence of correlation between grain size and a number of textural/petrophysical properties of rock. Some of the most common of these properties are permeability, packing coefficient, porosity, irreducible water saturation, etc. Except permeability that has a directional attribute, all other properties are scalar quantities with no directional attributes.

The directional attribute of permeability is caused by stratigraphic, lithologic, sedimentologic or depositional nature of the reservoir rocks. Permeability anisotropy,  $\lambda_k$ , a dimensionless ratio, is often used to express the directional nature of permeability. It is mathematically represented as

$$\lambda_k = \frac{k_H}{k_V} \quad 6-18$$

where  $k_H$  is horizontal permeability and  $k_V$  is vertical permeability.

Techniques for estimating permeability anisotropy are numerous and well documented in the literature<sup>151-154</sup>.

In this work, the concept of directional permeability was used to predict median grain size of the reservoir sand in both horizontal and vertical orientations. The methodology involved the presentation of directional permeability (horizontal and vertical permeabilities) data to the trained network reported in section 6.4.1. The network was then trained with these data and appropriately optimised using the procedures described earlier in section 6.4.2. Figure 6-29 is an example of orientational grain size predicted by the neural network. The figure shows large differences between horizontal and vertical median grain sizes especially at shallower depths. This confirms that grain size distribution varies with the distribution orientation.

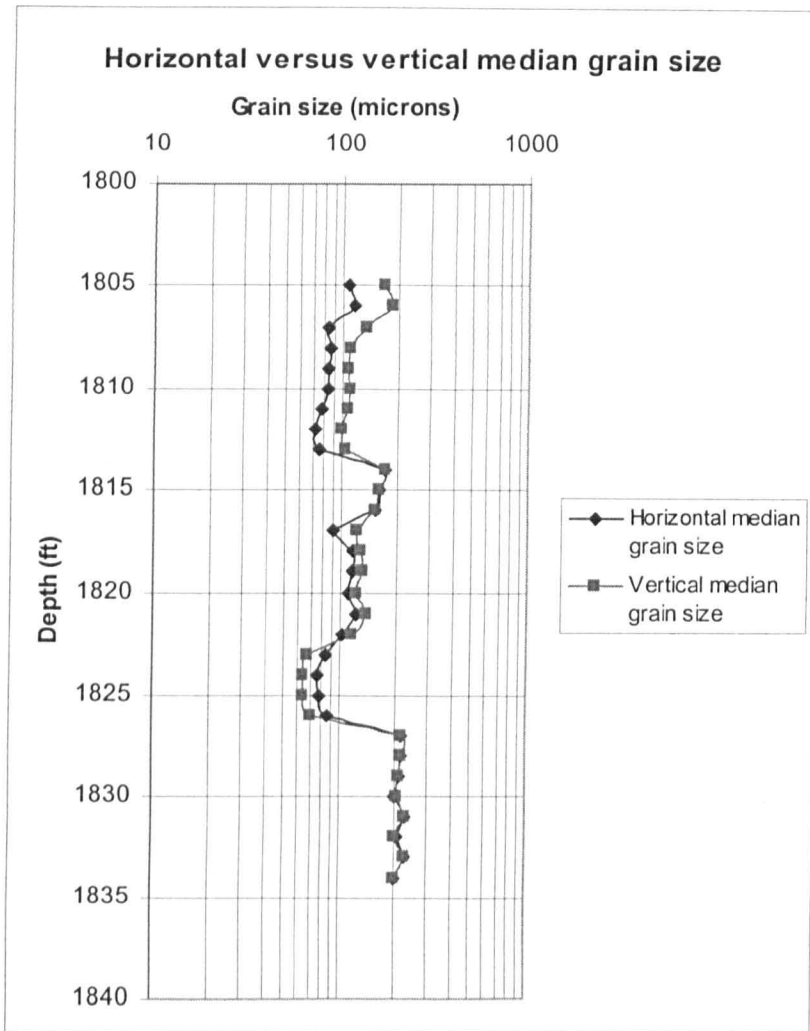


**Figure 6-29** Orientational median grain size predicted from neural network

### 6.5.6 Determination of other percentile sizes

Median grain size is one of the characterising parameters of sandstone formation in formation evaluation and engineering analysis work for oil and gas operations and grain size distribution analysis. Other important characterising parameters are the other percentile sizes and the standard deviation or sorting. The neural network model reported earlier is only capable of predicting median grain size. There is therefore a need to develop procedures for estimating the values of these other percentiles and standard deviation.

### 6.5.6.1 Equation relating percentile sizes with standard deviation

The equation describing a normally distributed grain size is given as<sup>155</sup>:

$$y = \frac{1}{\sigma_{\theta} \sqrt{2\pi}} \exp \left[ -\frac{(d - d_{50})^2}{2\sigma_{\theta}^2} \right] \quad 6-19$$

$d$  is the grain size of interest,  $d_{50}$  is mean;  $y$  is frequency,  $\sigma_{\theta}^2$  is variance and  $\sigma_{\theta}$  is standard deviation.

In a normally distributed grain size, mean grain size =  $d_{50}$  = median grain size.

$$\text{Let } t = \frac{d - d_{50}}{\sigma_{\theta}} \quad 6-20$$

Substituting (6-20) in (6-19) and integrating the result, the resulting standard normal equation in which  $d_{50} = 0$  and  $\sigma_{\theta} = 1$  is given as:

$$\int dy = \frac{1}{\sqrt{2\pi}} \int_{-\infty}^{\infty} \exp \left[ -\frac{t^2}{2} \right] dt \quad 6-21$$

A plot of  $\frac{dy}{dt}$  versus  $t$  gives the normal probability curve. A typical curve for  $-4 < t < 4$  is shown in figure 6-29.

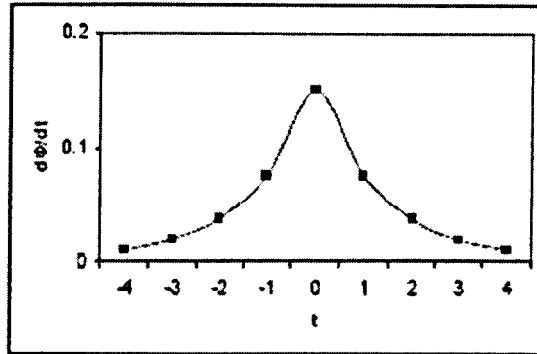


**Figure 6-30 A typical normal probability curve for a range  $-4 < t > 4$**

Equations for calculating the major percentile distribution of grain size can be obtained from the integrals of relative frequency values for ranges of values of  $t$  from transposed equation 6-20.

$$\sigma_{\phi} = \frac{d - d_{50}}{t} \quad 6-22$$

For  $-1 < t > +1$  (one standard deviation from the mean), the integrals (as given in statistic tables) of the relative frequency are approximately 16% and 84% respectively; equation (6-22) can then be written as:

$$d_{50} - d_{16} = \sigma_{\phi} \quad 6-23$$

and

$$d_{84} - d_{50} = \sigma_{\phi} \quad 6-24$$

Similar equations can be written for a number of other percentiles as shown in Table 6-23.

These equations can be used to estimate  $d_1$ ,  $d_2$ ,  $d_{16}$ ,  $d_{84}$ ,  $d_{98}$ ,  $d_{99}$  of any normally distributed grain size once the median or mean grain size and standard deviation or sorting are known. Other percentile size distribution can then be found by interpolation and extrapolation when these values are plotted on either arithmetic or log probability scale.

<b>Table 6-23 Equations for 1,2,98 and 99 percentiles</b>		
<b>t</b>	<b>Integrals</b>	<b>Equation</b>
$-2 < t > +2$	2%  and  98%	$d_{50} - d_2 = 2\sigma_\phi$  and $d_{98} - d_{50} = 2\sigma_\phi$
$-3 < t > +3$	1%  and  99%	$d_{50} - d_1 = 3\sigma_\phi$  and $d_{99} - d_{50} = 3\sigma_\phi$

### 6.5.6.2 Equations for estimating the standard deviation

Krumbein and Monk<sup>95</sup> gave an equation relating permeability to textural parameters of geometric mean grain size and standard deviation, which is a measure of sorting. This equation was developed empirically using very well sorted sediment samples ranging from -0.75 to 1.25phi in mean grain size, and with standard deviations ranging from 0.04 to 0.80phi. The equation is expressed as:

$$k = 760d_g^2 e^{1.31\sigma_\phi}$$

6-25

Where:

$k$  = permeability (Darcy)

$d_g$  = geometric mean grain size (phi)

$\sigma_\phi$  = standard deviation (phi)

If equation (6-24) is transposed, it becomes:

$$\sigma_\phi = \frac{1}{1.3} \log_e \left[ \frac{k}{760 * d_g^2} \right] \quad 6-26$$

The geometric mean grain size used by Krumbein and Monk<sup>95</sup> is equal to the arithmetic median grain size for normally distributed sand sizes<sup>156</sup>. They can therefore be used interchangeably in equation (6-26).

Similarly, Bergs<sup>96</sup> gave an equation relating permeability of sands to the median grain size, porosity and a term he called phi percentile deviation of sand grain size distribution, which equals ( $Phi_{84.1} - Phi_{16.5}$ ). The equation is expressed as:

$$k = 5.1 * 10^{-6} * \phi^{5.1} d_{50}^2 e^{-1.385\sigma_\phi} \quad 6-27$$

Where:

$k$  = permeability (md)

$d_{50}$  = median grain size (mm)

$\phi$  = porosity (percent)

$\sigma_\theta$  = Phi percentile deviation of sand grain size distribution ( $Phi_{84.1} - Phi_{16.5}$ )

The equation has been reported to perform well when used for 30% - 40% porosity sand<sup>97</sup>

If equation (6-27) is transposed, it becomes:

$$\sigma_{\phi} = \frac{1}{-1.385} \log_e \left[ \frac{k}{5.1 * 10^{-6} * \phi^{5.1} * d_{50}^2} \right] \quad 6-28$$

The two transposed equations have been tested and compared using some limited field data. The results are shown in Figures 6-31 to 6-32, and Table 6-18 to 6-19. The comparison of transposed Bergs equation with measured data shows very poor correlation coefficient (0.14) between predicted and measured standard deviation (Table 6-18). The poor performance may have been as a result of the porosity effect on Bergs equation; porosity is not known to have any effect on grain sorting. Output from transposed Krumbein and Monk equation however exhibits some degree of agreement with the measured data. The 31% mean error and the 0.66 correlation coefficient shown in Table 6-19 and Figure 6-31 respectively may be due to the twin factor of extremely poor sorting of the sands whose data was used for the analysis and the error inherent in the data. The sorting of the sand ranges from 3.3phi to 8.6phi; this is outside the range krumbein and Monk<sup>95</sup> employed in their derivation experiment.

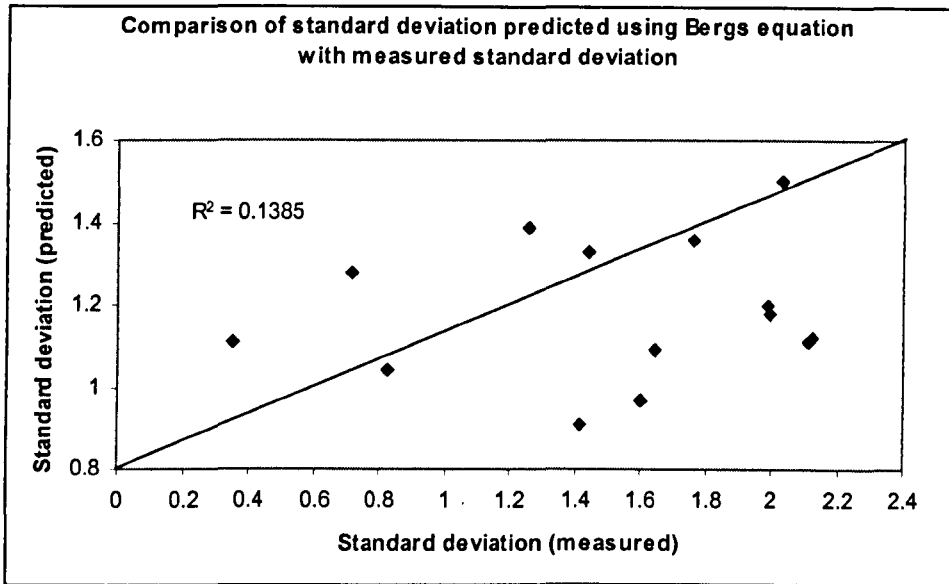


**Figure 6-31 Comparison of standard deviation or sorting predicted using transposed Bergs model with the measured data**

**Table 6-24 Error analysis for Bergs equation**

Std (predicted)	Std (measured)	Abs_error	% error	Abs_value (% error)
0.712248662	1.28	0.56775134	44.35557328	44.35557328
1.25667821	1.39	0.13332179	9.591495683	9.591495683
2.123702145	1.12	-1.0037021	-89.61626295	89.61626295
1.762382751	1.36	-0.4023828	-29.58696699	29.58696699
2.109197931	1.11	-0.9991979	-90.01783162	90.01783162
1.640516372	1.09	-0.5505164	-50.50608917	50.50608917
1.995220797	1.18	-0.8152208	-69.08650822	69.08650822
0.348042163	1.11	0.76195784	68.64485018	68.64485018
1.988620712	1.2	-0.7886207	-65.71839267	65.71839267
1.437216881	1.33	-0.1072169	-8.061419624	8.061419624
1.414323358	0.91	-0.5043234	-55.42014923	55.42014923
0.82177843	1.04	0.21822157	20.98284327	20.98284327
2.029022462	1.5	-0.5290225	-35.26816413	35.26816413
1.59764547	0.97	-0.6276455	-64.70571856	64.70571856
Average error				50.1115904

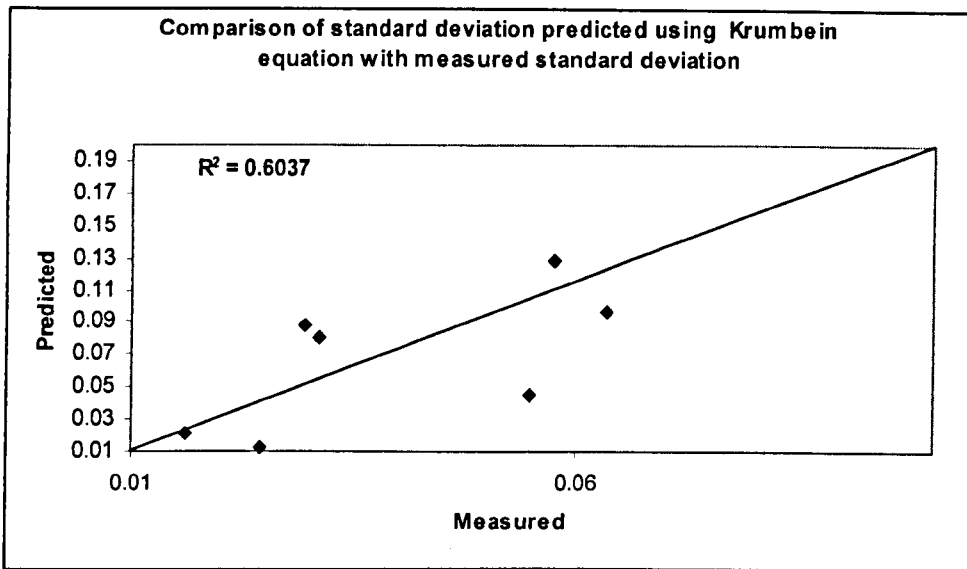


**Figure 6-32 Comparison of standard deviation or sorting predicted using transposed Krumbein and Monk model with the measured data.**

**Table 6-25 Error analysis for krumbein & Monk equation**

Std (predicted)	Std(measured)	Abs_error	% error	Abs value (% error)
6.361990962	5.351074441	-1.0109165	-18.89184186	18.89184186
3.497304584	5.083141235	1.5858367	31.19796554	31.19796554
4.446930847	4.189680297	-0.2572506	-6.140099763	6.140099763
5.56706212	5.956795501	0.3897334	6.542668469	6.542668469
3.285375001	7.097887821	3.8125128	53.71334284	53.71334284
3.367409645	3.979373349	0.6119637	15.37839379	15.37839379
1.522756791	3.319045586	1.7962888	54.12064247	54.12064247
3.638075252	5.006941609	1.3688664	27.33937129	27.33937129
2.95771698	4.122805453	1.1650885	28.25960347	28.25960347
2.975818362	5.680382066	2.7045637	47.61235552	47.61235552
2.207096245	4.658355759	2.4512595	52.62070226	52.62070226
6.434116729	6.200249538	-0.2338672	-3.771899656	3.771899656
5.061777468	5.117787378	0.0560099	1.09441651	1.09441651
3.909863101	5.844768884	1.9349058	33.10491521	33.10491521
2.499619277	4.556393349	2.0567741	45.14039756	45.14039756
2.298394037	6.168771307	3.8703773	62.74146143	62.74146143
1.283183273	5.51292532	4.229742	76.72409477	76.72409477
5.330594363	4.997693533	-0.3329008	-6.661089317	6.661089317
6.097719649	8.64385619	2.5461365	29.45602617	29.45602617
Average error				31.60585726

### 6.5.6.3 Orientational grain size distribution prediction

An excel-based tool has been packaged based on all the models reported in the previous sections of this chapter, for predicting grain size distributions in both horizontal and vertical orientations. The models on which the tool is based are:

- The neural network model for predicting horizontal and vertical median grain size based on horizontal and vertical permeability
- The two models for predicting standard deviation or sorting
- The models for estimating percentile sizes

Figures 6-33 and 6-34 are example plots of horizontal and vertical grain size distribution at depths of 1805ft and 1825ft (the same data sets used in the neural network modelling was used) respectively from the tool.

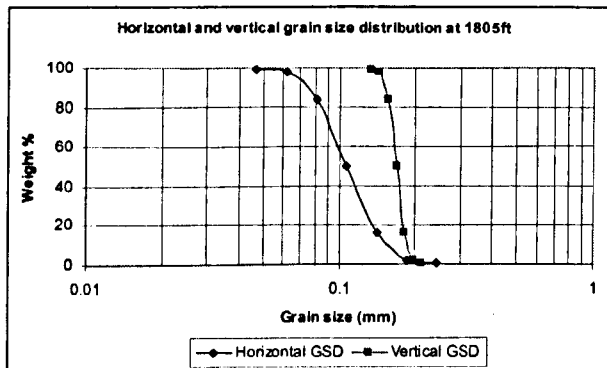


**Figure 6-33 Example of orientational grain size distribution at 1805ft (predicted using the tool)**

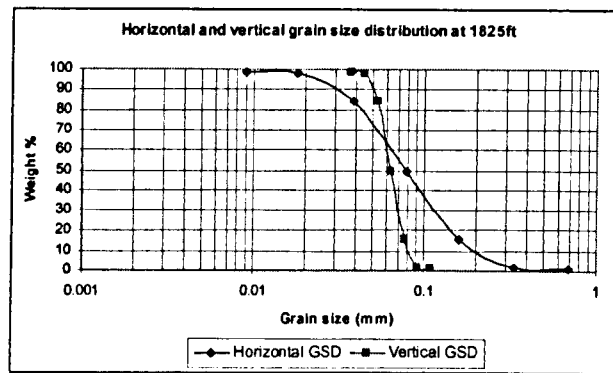


**Figure 6-34 Example of orientational grain size distribution at 1825ft (predicted using the tool)**

## 6.6 Validation of NN/analytical grain size distribution model

A Middle East gas field data from different wells taken from various depths has been used to validate the grain size distribution model. The data was selected from four different wells at various depths in such a way that the final validation accounted for the two sand sequences in the field. Data on Petrophysical parameters such as porosity, permeability etc. for the field and for each well was not available on depth by depth basis; only average values for these parameters were available for the whole field. Assumptions therefore had to be made to use this data for the validation exercise. Figures 6-35 to 6-38 show the results obtained during the validation.

Even though the data was limited and assumptions had to be made on most petrophysical parameters of the sand sequences, it is still evident from Figures 6-35 to 6-38 that the model generally performed very well for all the well data chosen except for well CK-1A, sand sequence I-25 at depth 3962.33ft, where a large deviation was observed from  $d_{30}$  (30<sup>th</sup> percentile sizes) and below (Figure 6-36); and well CK-2, sand sequence I-20 at depth 4112ft, where the deviation, even though not unacceptable, was pervasive throughout the grain size distribution curve ( $d_1$  to  $d_{100}$ ) (Figure 6-38). The rather poor performance of the model on these well data could be attributed to the assumptions made.

Unavailability of directional permeability data or directional resistivity log for the field and wells also made it impossible for the orientational grain size distribution functionality of this model to be validated.

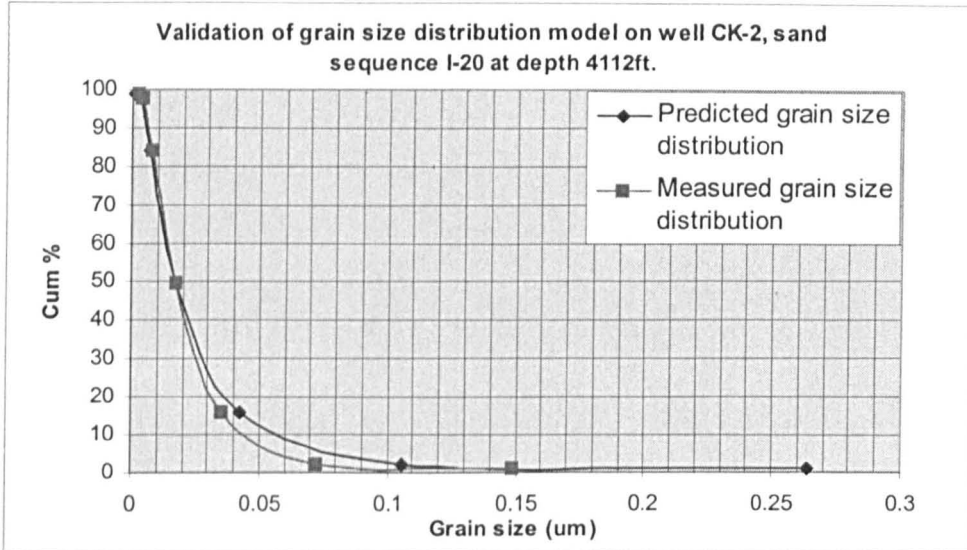


**Figure 6-35 Validation of grain size distribution model on well CK-2, sand sequence I-20 at depth 4112ft.**

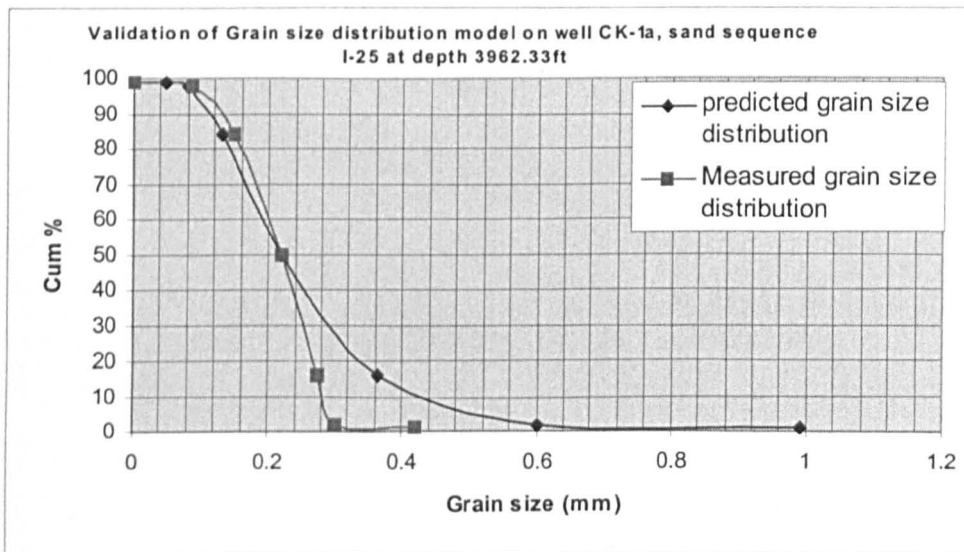


**Figure 6-36 Validation of grain size distribution model on well CK-1A, sand sequence I-25 at depth 3962.33ft.**

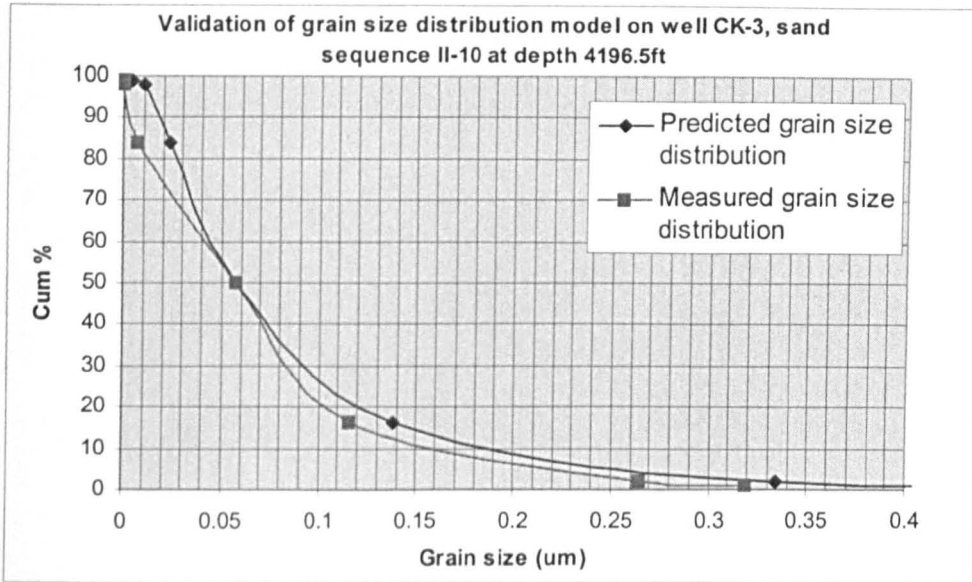


**Figure 6-37 Validation of grain size distribution model on well CK-3, sand sequence I-10 at depth 4196.5ft.**

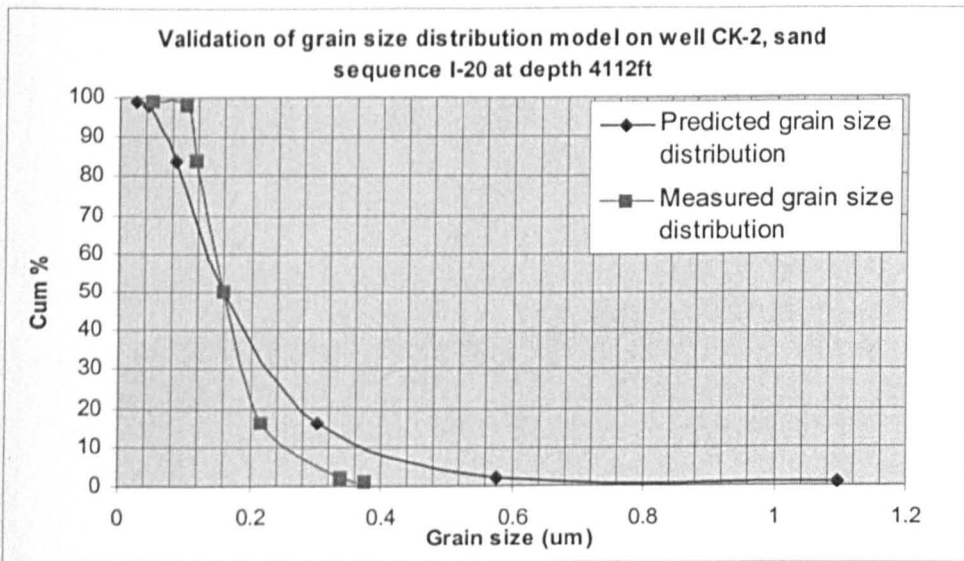


**Figure 6-38 Validation of grain size distribution model on well CK-2, sand sequence I-20 at depth 4112ft.**

---

## 6.7 Summary

The following are the summaries drawn for the studies reported in this chapter:

- Neural network modelling technique through series of comparative studies has been confirmed to perform better than other modelling techniques such as statistical multivariate analysis, dimensional analysis and analytical techniques in resolving the complex relationship between grain size and log/petrophysical parameters.
- A neural network model has been developed to predict median grain size
- Equations have been developed to estimate other percentile sizes such as  $d_1$ ,  $d_2$ ,  $d_{16}$ ,  $d_{84}$ ,  $d_{98}$ , and  $d_{99}$ . Also existing equations have been adopted and modified to predict standard deviation or sorting.
- Both Bergs and Krumbein and Monk permeability equations have been mathematically transposed for the estimation of sorting or standard deviation.
- Impact of porosity effect on Berg's permeability model may increase error margin in sorting estimation.
- An excel based tool has been developed to predict grain size distributions
- The models have been extensively validated on well data from a Middle East gas field. The results of the validation show that the model performs well even on incomplete data.

---

## Chapter 7

# UCS modelling

In this chapter the results of UCS modelling are presented. Two different modelling techniques – dimensional analysis and neural network - have been utilised for the UCS modelling for comparison purposes. As part of the studies, the existing UCS models have also been reviewed and ranked prior to the modelling work. This is with a view to ascertaining the controlling parameters of reservoir rock strength. The results of the review studies have been instrumental to the proposal of a new UCS model.

The proposed UCS model is premised on the hypothesis that change in grain size distribution, as parametised by median grain size and sorting, during oil and gas production from any sand producing reservoirs, will cause a change in the UCS of such reservoirs' rocks. UCS of the reservoir rock can therefore be predicted continuously in real time for sanding potential analysis.

### 7.1 Existing UCS models review and ranking

Porosity and many other petrophysical and textural parameters such as grain size, sorting etc., have been known to correlate very well with unconfined compressive strength (UCS) of rock<sup>3, 106, 157, .</sup> However the nature and type of the relationship between UCS and these parameters is somehow still not well understood due to the varied relationship types being widely reported between them in the literature (for example, linear, exponential and logarithmic relationships have been widely reported in literatures)<sup>2-4,106,157-158,</sup>. This is obviously as a result of the complex nature of this relationship.

In order to understand some of the models being currently used for UCS estimation in the industry (see table 7-1) with a view to bringing out their

---

weaknesses and strengths for the purpose of evaluating their applicability, they have been reviewed and ranked based on their constitutive parameters. The procedures for review and ranking of the models are detailed under the headings below:

Table 7-1 models for UCS prediction

References	Model/Equations	Review/Comments
Gavito 1996	$C_o = E(0.008V_{sh} + 0.00045(1 - V_{sh}))$ $E = a((2\rho_b)/(1 + \nu))(1/\Delta t_s^2), \quad \nu = (0.5K^2 - 1)/(K^2 - 1)$ $K = \Delta t_s / \Delta t_c$ <p>where <math>a</math> is a conversion factor</p>	The model expresses UCS as being dependent on Young's modulus and volume of shale. Young's modulus can be computed from bulk density, Poisson ratio and interval transit time, all of which can be got directly from density and sonic log. It is also possible to estimate porosity and overburden stress from this equation as they are also a function of sonic travel time and bulk density respectively.
Hin & Disseault... 2002	$(a) \sigma_{ucs} = 2\sigma_T \frac{\sin \phi}{1 - \sin \phi}$ <p>where <math>\phi</math> is the angle of internal friction and <math>\sigma_T</math> is rock tensile strength</p> <p><math>\sigma_T</math> can be computed from the particulate mechanics relation:</p> $(b) \sigma_T = \frac{1 - \phi F_c}{\phi d^2}$	This model relates UCS with tensile strength and internal friction angle. Tensile strength can be computed from model (b) from the petrophysical parameters of porosity and grain size and cohesive strength due to capillary force. Variable $F_c$ changes with water saturation expressing the effect of water saturation.
Tokle et. al. 1986	$\sigma_{ucs} = aGR' + bDT' + cRHOB' + dNPHI' + eCAL + fROK' +$ <p>where a, b, c... are regression coefficients.</p>	This model gives a correlation by regression analysis of core UCS with normalised log parameters (gamma ray, acoustic travel time, bulk density, neutron porosity, calliper and rock number). The rock unit number (ROK) introduces the lithological effect. This could enable prediction of strength for different lithologies.
Tiab and Donaldson 1996	$(a) \sigma_{ucs} = \left( \frac{2 \cos \phi}{1 - \sin \phi} \right) \sigma_{ii}$ $(b) \sigma_{ii} = 2.6 * 10^{-8} \frac{E}{c_b} (0.0035V_{sh} + 0.0045)$	The model is based on Mohr-Coulomb theory and expresses UCS as being dependent on internal friction angle and the initial tensile strength. Another equation is provided to compute the initial tensile strength from Young's modulus, bulk compressibility and volume of shale.
Sarda et. al. 1993	$(a) \sigma_{ucs} = f \left( \left( \phi * \left( \frac{\rho_b^2}{\Delta t_s^2} \right) * \left( \frac{\Delta t_c^2 - 4\Delta t_s^2}{3} \right) * g(V_{sh}) \right) \right)$	This equation expresses UCS as function of bulk density, interval transit times and volume of shale. It is possible to compute the Young's modulus, shear modulus and Poisson ratio from the independent parameters in this equation. However, the equation only expresses UCS as function of these parameters a

Table 7-1 Existing UCS models (cont'd)

References	Model/Equations	Review/Comments
Sein 1985	$G = 90\sigma_{ucs} + 165.47$ where $G$ is Shear Modulus (MPa) and $\sigma_{ucs}$ is uniaxial compressive strength (MPa)	This model provides a linear expression between shear modulus and the uniaxial compressive strength. The relationship between UCS and petrophysical and mechanical properties is complex and complicated. A linear model such as this may not adequately capture this complex relationship.
Pikryl 2001	$Y = a \log(X) + b$ where $Y$ is strength (UCS), $X$ the mean grain diameter and $a < 0 < b$	This model represents the general form of series of correlations between UCS and mean grain size. The model was based on a study carried out on granitic rocks, which ordinarily exhibit low porosity and high degree of cementation. The tendency is for the model to over-estimate the strength of rock if used for sediments with even slightly higher porosities and lesser degree of cementation.
Holt et. al. 1987	$\sigma_{ucs} = b_1 EK_b (0.008V_{sh} + 0.0045(1 - V_{sh}))$ where $b_1$ is a calibration factor	This model expresses UCS as being dependent on Young's modulus, bulk modulus and volume of shale.

### 7.1.1 Parameters exercising control on rock strength

Based on the extensive review of literature and field practice, the parameters, which exercise control on the UCS of a reservoir rock, were identified and grouped into three major categories. The parameters and the categories into which they fall are shown in table 7-2. The rationale for their consideration and their weighting is also discussed further.

<b>Table 7-2: Variables impacting rock formation strength (UCS)</b>		
No	Parameters	Categories
1	Porosity	Petrophysical/textural parameters
2	Median grain size	
3	Standard deviation from mean grain size	
4	Overburden stress	Mechanical parameters
5	Horizontal stress	
6	Pore pressure	
7	Bulk Modulus	
8	Viscosity of oil	Failure inducing/flow parameters
9	Viscosity of displacing fluid (water)	
10	Density of oil	
11	Density of displacing fluid (water)	
12	Velocity of oil	
13	Velocity of displacing fluid	
14	Interfacial tension between water and oil	

### **7.1.1.1 Mechanical property parameters**

These parameters are considered the most important for UCS estimation in any sanding potential evaluation work. The reason being that they are the inherent properties of rocks, which determine whether or not they will yield when subjected to external failure-inducing forces. Based on this, these parameters were given a weighting of 50 out of a possible 100.

### **7.1.1.2 Failure-inducing parameters**

Most of these parameters are due to operational factors and inherent fluid properties, which can be managed much more easily than mechanical property parameters. They tend to induce failure in rocks especially during drilling and production operations by either increasing the magnitude of stress acting on the rocks, distorting rock stress equilibrium, or reducing the inherent formation strength, affecting its ability to withstand its stress environment. These parameters are therefore considered second in order of importance, to UCS evaluation. Consequently, they were given a weighting of 30 out of a possible 100.

### **7.1.1.3 Petrophysical parameters**

These are petrophysical properties of rocks, which have some level of control on the mechanical strength of rocks. They tend to increase or lower the strength of rocks and their ability to withstand stress. For example, porosity and permeability are known to affect formation strength adversely while volume of shale tends to contribute significantly well to formation strength. These parameters were given a weighting of 20 out of a possible 100.

---

### 7.1.2 Ranking Criteria and Procedure

Each group of parameters was given a weighting that was proportional to the magnitude of control it has on the strength of reservoir formation based on the extensive review of previous work. The basis for this was the frequency of use of these parameters by previous workers in the development of various existing models for predicting UCS. This group weighting was subsequently applied to every parameter in each group. The weighting for each parameter was then normalised to one by dividing it with the total combined weighting of all the parameters.

Each model was then considered based on the numbers of parameters listed in table 7-2, that it accommodates and the total cumulative weight of these parameters. A cut-off point of 0.5 was set and the total cumulative point of each model was compared with this cut-off point. Any model whose TCP was lower than the cut-off was considered not robust enough for UCS estimation.

### 7.1.3 Results of Ranking

The results of the ranking as shown in figure 7-1 (see appendix C-1 for the ranking spreadsheet) reveal that majority of the model of the models have a ranking of less than 0.3. Only three of the models – Gavito (1996)<sup>157</sup>, Sarda et. al. (1993)<sup>84</sup> and Tokle et. al. (1986)<sup>106</sup>– have a ranking (0.4) close to the cut-off. Based on this ranking it was concluded that the models do not consider very important parameters which might impact the strength of reservoir rock and might therefore not predict or estimate UCS or strength of rock satisfactorily for the purpose of sanding potential prediction. Apart from this, all the models are also not capable of real time prediction of UCS. This was an indication of the need to develop a new model, which would incorporate more parameters and have capabilities for real time prediction.

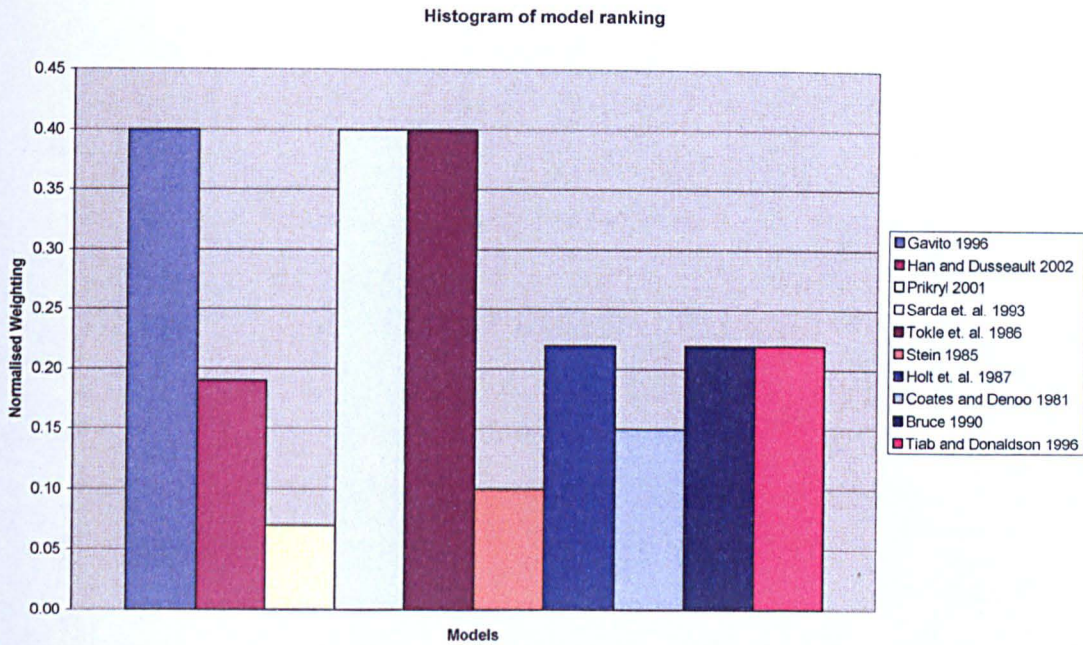


**Figure 7-1 Histogram of Model ranking**

### 7.1.4 Further evaluation of some existing models.

In order to justify the results of the ranking, two of the three models – Gavito (1996)<sup>157</sup> and Sarda et al.(1993)<sup>84</sup> - with ranking close to the cut-off point were further evaluated using some field data. To evaluate Sarda et al (1993) model, a variant of their equation which explicitly relates UCS to porosity was used, the rationale being that the original equation only implicitly relates UCS to porosity; expressing it as a function of some porosity-related parameters (see Table 7-1). Figures 7-2 and 7-3 show the results of the evaluation whilst Table 7-3 shows the mathematical calculations carried out. Sarda et al. (1993)<sup>84</sup> model was found to grossly overestimate UCS by a factor of 5 while Gavito (1996)<sup>157</sup> model was found to grossly overestimate it by as much a factor of 10. As shown in Table 7-3, the data used in the calculations is from a high porosity formation. That perhaps explains why the model grossly overestimated the formation UCS as porosity based UCS models tend to perform better on data from low porosity formation. The third model – Tokle et al (1986)<sup>106</sup> - could not be evaluated further due to non-publication of the model constants.

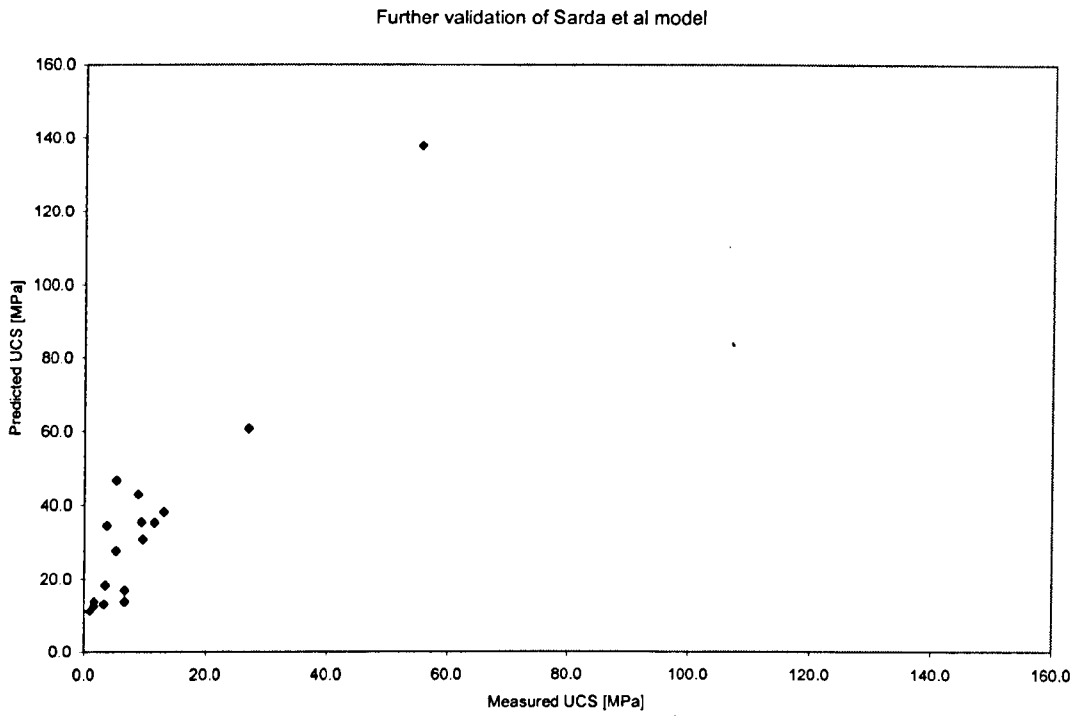


**Figure 7-2 Further evaluation of Sarda et al<sup>84</sup> Model**

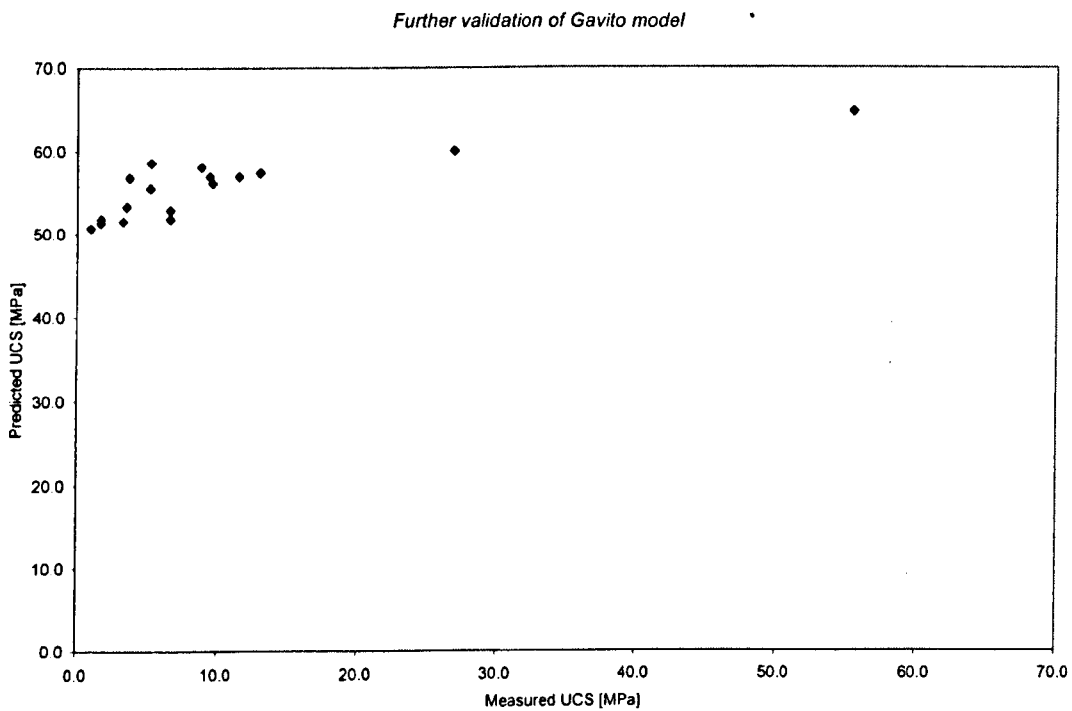


**Figure 7-3 Further evaluation of Gavito<sup>157</sup> Model**

Depth [m]	Porosity	Sarda UCS [Mpa]	Gavito UCS [Mpa]	Measured UCS [Mpa]
891.4	32.5	13.9	51.8	1.7
892	7.0	137.8	64.8	55.5
892.4	33.1	13.2	51.5	3.3
895.7	32.5	13.9	51.8	6.6
896.3	24.9	27.7	55.6	5.2
896.5	30.4	16.9	52.9	6.6
897.1	19.0	46.8	58.6	5.2
897.5	22.1	35.4	57.0	11.5
897.7	23.7	30.8	56.2	9.6
898.5	22.1	35.5	57.0	9.4
904.1	20.0	43.0	58.1	8.8
904.5	16.1	60.7	60.1	26.9
904.9	21.3	38.2	57.4	13.0
914.9	22.4	34.6	56.9	3.7
915.1	29.5	18.3	53.3	3.5
915.7	33.6	12.6	51.3	1.6
916.5	34.8	11.3	50.7	1.0

## 7.2 UCS modelling using dimensional analysis

### 7.2.1 Variable controlling rock strength

The comprehensive sets of variables that are considered to impact the strength of any rock formation are listed in table 7-2. The mechanical and petrophysical properties cannot be controlled in field operation whilst the failure inducing properties can be controlled. The mechanical and petrophysical properties are therefore considered in this study. If parameters are chosen to represent each of the two parameter categories, Uniaxial Compressive Strength (UCS) can be said to be a function of porosity, overburden stress, horizontal stress, grain size, pore pressure, total cohesive forces and bulk compressibility. The relation can be expressed in a functional form as:

$$UCS = f(\phi, \sigma_{ov}, \sigma_H, d, P_p, S_{ic}, C_b)$$

7-1

Equation (7-1) can be expressed mathematically as

$$g = (UCS, \phi, \sigma_{ov}, \sigma_H, d, P_p, S_{tc}, C_b) \quad 7-2$$

Where UCS = uniaxial compressive strength

$\phi$  = porosity

$\sigma_{ov}$  = overburden stress

$\sigma_H$  = horizontal stress

d = grain size

$P_p$  = Pore pressure

$S_{tc}$  = Total cohesive strength

$C_b$  = Bulk compressibility

Expressing these variables using their dimensions, we have:

$$UCS = [ML^{-1}T^{-2}]$$

$$\phi = [\text{dimensionless}]$$

$$\sigma_{ov} = [ML^{-1}T^{-2}]$$

$$\sigma_H = [ML^{-1}T^{-2}]$$

$$d = [L]$$

$$P_p = [ML^{-1}T^{-2}]$$

$$S_{tc} = [MLT^{-2}]$$

$$C_b = [M^{-1}LT^2]$$

## 7.2.2 Application of Buckingham Pi Theorem

Using Buckingham pi theorem, the parameters in equation (7-2) can be written in four independent dimensionless  $\Pi$  groups (i.e. the number of physical parameters or variables listed (seven in this case) less the number of independent physical units (three in this case)):

$$\Pi_1 = \left[ \frac{\sigma_{ov}}{\sigma_H} \right] \quad 7-3$$

$$\Pi_2 = [P_p * C_b] \quad 7-4$$

$$\Pi_3 = \left[ \frac{UCS * d^2}{S_{tc}} \right] \quad 7-5$$

$$\Pi_4 = \left[ \frac{1}{\phi} \right] \quad 7-6$$

$\Pi_1$  describes the inverse of stress path;  $\Pi_2$ , the product of reservoir pore pressure and the bulk compressibility;  $\Pi_3$ , the ratio of the product of uniaxial compressive strength and the grain size to the total cohesive strength;  $\Pi_4$ , the inverse of porosity.

The dimensionless groups (equation (7-3) through (7-6)) can be expressed in a functional form:

$$F(\Pi_1, \Pi_2, \Pi_3, \Pi_4) = 0 \quad 7-7$$

Thus we have

$$F\left[\left[\frac{\sigma_{ov}}{\sigma_H}\right], \left[\frac{P_p * C_b}{1}\right], \left[\frac{UCS * d^2}{S_{tc}}\right], \left[\frac{1}{\phi}\right]\right] = 0 \quad 7-8$$

Re-writing equation (7-8), we have:

$$\left[\frac{UCS * d^2}{S_{tc}}\right] = G\left[\left[\frac{\sigma_{ov}}{\sigma_H}\right], \left[\frac{P_p * C_b}{1}\right], \left[\frac{1}{\phi}\right]\right] \quad 7-9$$

Solving equation (7-9), we can be obtained as given below

$$UCS = G_i \left[ \frac{\sigma_{ov} * S_{tc} * P_p * C_b}{\sigma_H * d^2 * \phi} \right] \quad 7-10$$

$G_i$  is a constant; its value was statistically derived.

### 7.2.3 Validation of Dimensional Analysis model for UCS

Field data from UK North Sea has been used to test and validate the Dimensional Analysis model. Figure 7-4 compares the UCS predictions from the dimensional analysis model with the measured UCS. It is evident from the figure that the model either over-predicts or under-predicts UCS. The average percent deviation of the predicted UCS from the measured data is between 50% and 60%.

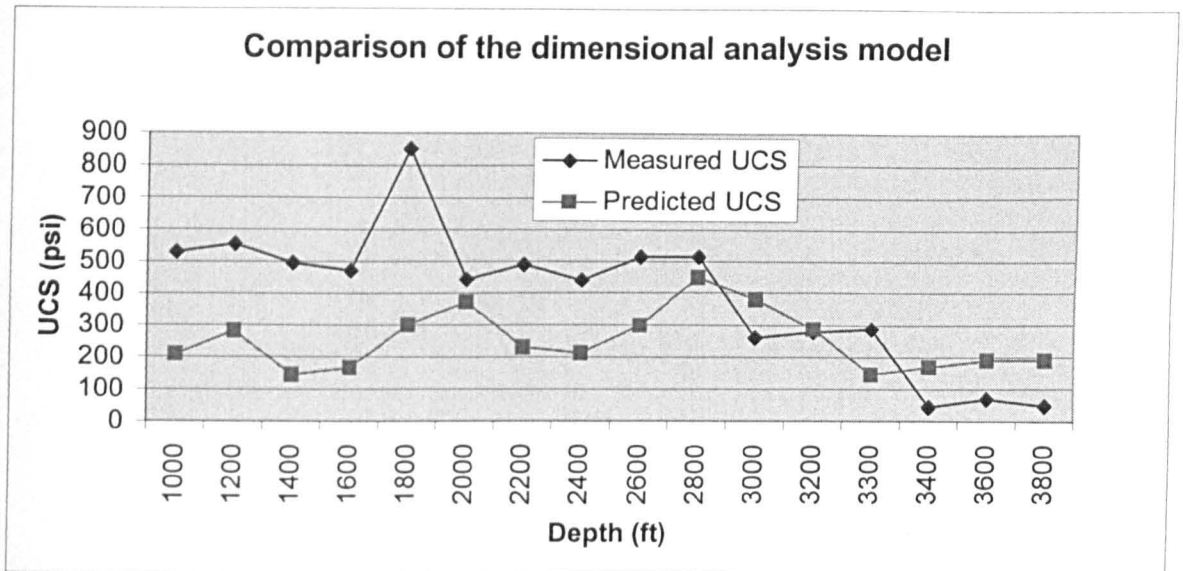


**Figure 7.4 Comparison of the dimensional analysis model predictions with measured UCS**

## 7.3 Neural network modelling

The neural network reported in chapter six has been adapted for this study. The adaptation procedure involved restructuring the input and hidden layers' neurons. The modelling process and procedure, including results are detailed in the following sections.

### 7.3.1 Input and output data selection

Five parameters, median grain size, sorting, stress path, bulk compressibility and porosity, were selected as inputs to the neural network based on the parameter ranking earlier carried out in which all the parameters that have been confirmed to affect UCS were grouped into three major categories - mechanical, failure-inducing and petrophysical/textural (see Table 7-2). The five parameters were selected to represent each of the major groups and to achieve the aim of this work, which is to use grain size distribution information to predict UCS in

real time (see Table 7-4 the group affiliation of each input parameter). UCS was the target output parameter.

The selected (input and output) data were normalised to lie within a range between 0 and 1. Normalisation is necessary because the sigmoid transfer functions used within the hidden and the output layers of the neural network are capable of returning only values that lie within these ranges. The procedure used for normalisation has been described in detail in chapter five.

**Table 7-4: Affiliation of input parameters**

<b>Parameters</b>	<b>Group affiliation</b>
Bulk Compressibility	Mechanical property
Stress path	Failure inducing property
Porosity	Petrophysical/textural property
Median grain size	Petrophysical/textural
Sorting	Petrophysical textural

### 7.3.2 Building the network

A two-layer network was built during the first implementation of the neural network modelling. The topology of the network is summarised in table 7-5.

**Table 7-5: Summaries of the neural network topology for UCS modelling**

<b>Network parameters</b>	<b>Parameter values</b>
Network layers	2
Input nodes	5
Output nodes	1
Hidden layer nodes	5
Learning rate	0.75
Momentum	0.9

The numbers of input and output nodes were determined by the numbers of input and output elements respectively. The number of neurons in the hidden layer, the learning rate and the transfer functions in both the hidden and output layers were however chosen by experimental "trial and error" method because of the overriding need to optimise them. Sensitivity analysis was performed later to study the effect of these parameters on the performance of the network and determine the right number and/or the right types of the parameters to use in the final neural network topology. The sensitivity analysis studies and their results are described in sections 7.3.5.

### 7.3.3 Network training

The network was trained using error tolerance of 0.3. This error tolerance was chosen to allow the network generalise well even when a corrupted or imperfect pattern (data) was presented to it. The network error decreased steeply from 0.64 to 0.40 over 4000 epochs and then decreased gently over 40000 epochs to 0.39, from where it gently decreased and stabilised at 0.27 over 20000 epochs. The training was achieved over a total of about 64000 epochs (see Figure 7-5).

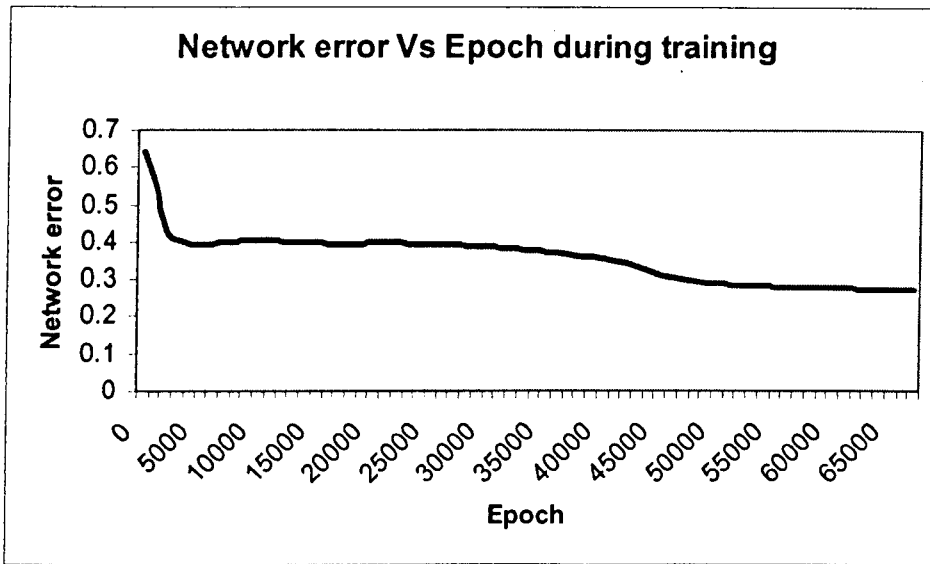


**Figure 7-5 Network error vs. epoch during training**

### 7.3.4 Network cross-validation

The purpose of network cross-validation was to monitor the training and determine whether or not the network was actually training. The cross-validation was done using a part of training data set purposely set aside. The final network error stabilised at 0.1 over about 8000 epochs during cross-validation (see Figure 7-6).

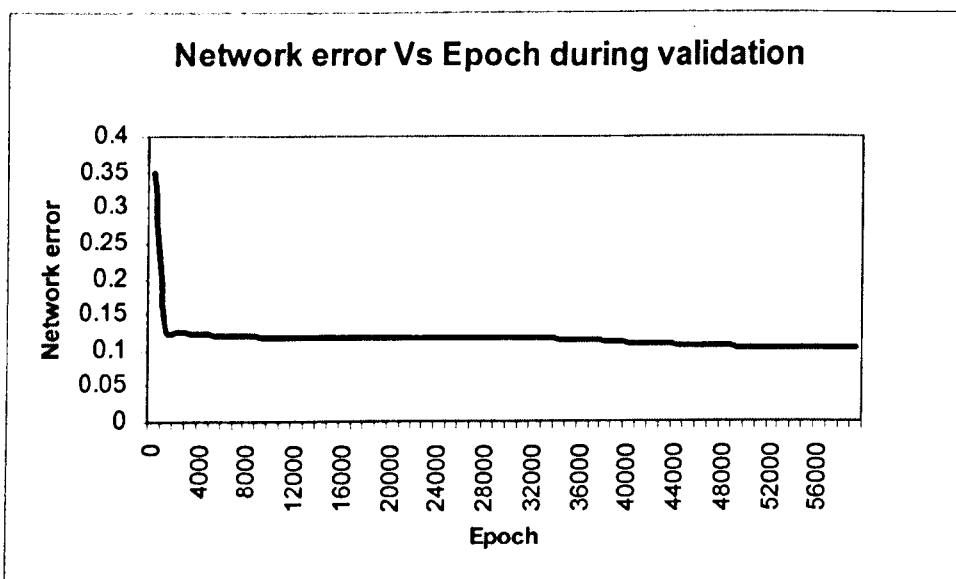


**Figure 7-6 Network error vs. epoch during validation**

---

### **7.3.5 Sensitivity analysis studies**

Sensitivity analysis studies entailed the evaluation of the effects of key network parameters on network training and capability to generalise rather than memorise when new data it has not seen before is presented to it. Parameters such the learning rate, number of hidden layers, and number of neurons in hidden layer were used in the sensitivity studies.

#### **7.3.5.1 Effect of learning rate on network**

Four implementations of neural network were carried out using varying learning rates – 0.3, 0.5, 0.75 and 0.9 – on both the training and validation sets to study the effect of learning rate on the network performance with a view to determining the optimum learning rate for the final network topology.

It was found that the network performed better both on training and validation sets when the learning rate was 0.75 as evident in the lowest network error at this learning rate (see Figures 7-7 & 7-8). The network was found to converge into a number of local minima on the training set when the learning rate was 0.9.

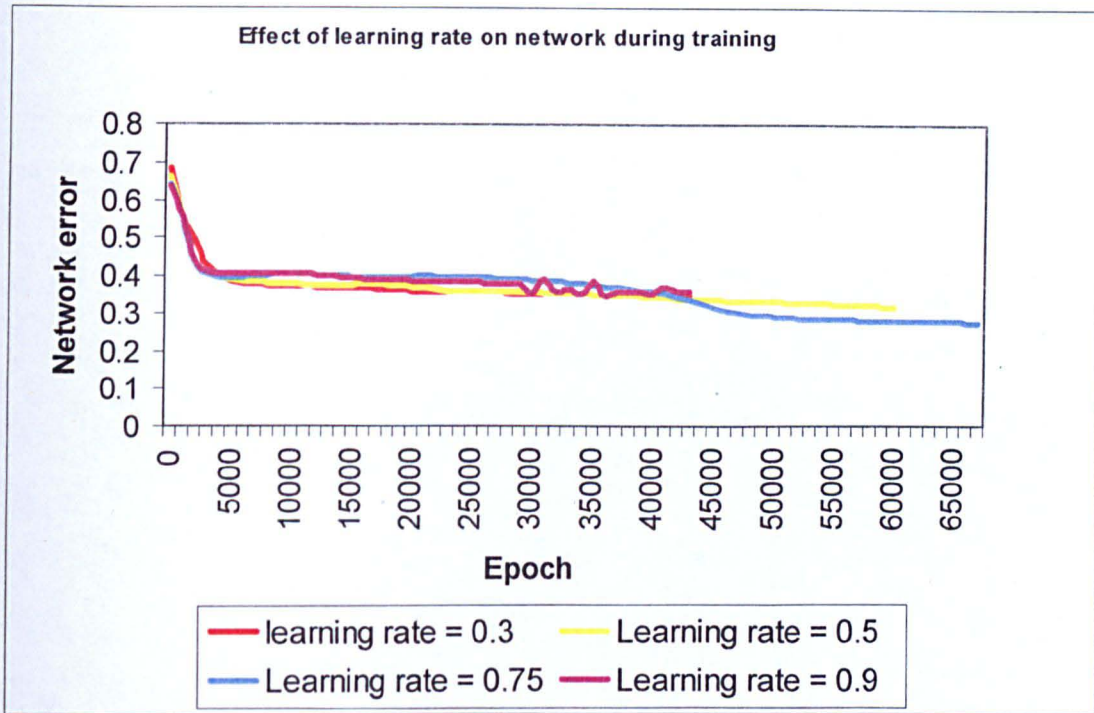


Figure 7-7 Effect of learning rate on network during training

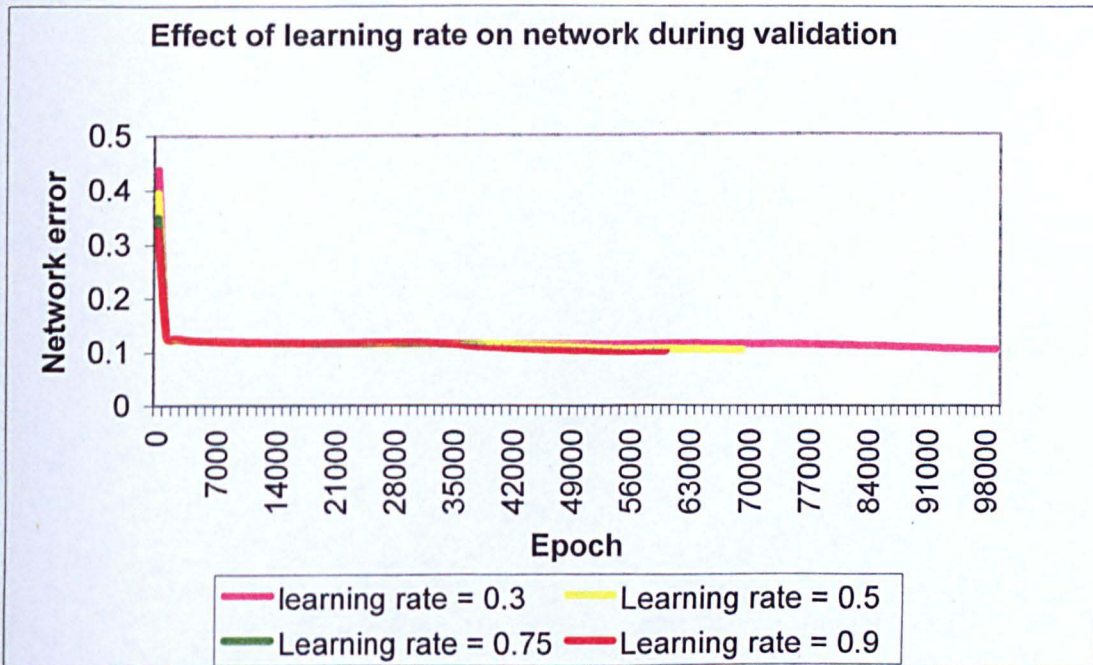


Figure 7-8 Effect of learning rate on network during validation

### 7.3.5.2 Effect of number of hidden layer

Five implementations of neural network using varying number of hidden layers - 1, 2, 3, 4 & 5 - were carried out on both training and validation sets to study the effect of hidden layer number on the network performance. It was found that increasing number of hidden layers increases the network complexity, impacting negatively on its performance. Networks with one and two hidden layers performed better. However the performance of network with 1 hidden layer was best as evident in the lowest network error (see Figures 7-9 & 7-10).

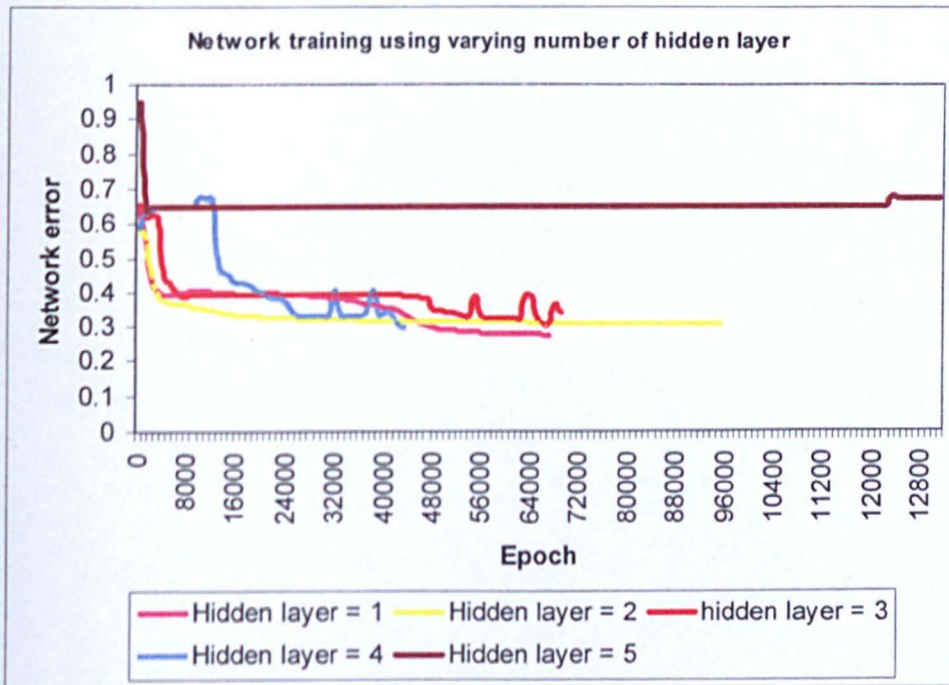
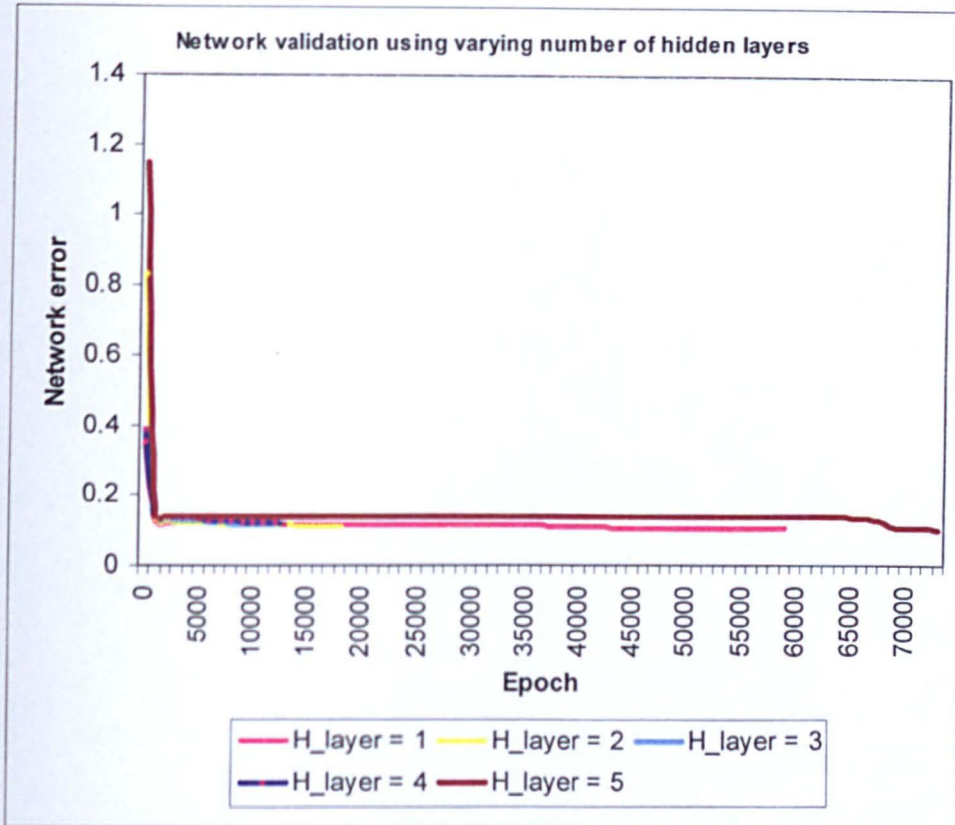


Figure 7-9 Network training using varying no of hidden layers



**Figure 7-10 Network validation using varying no of hidden layers**

### 7.3.5.3 Effect of number of neurons in the hidden layer

Five implementations of neural network using varying number of neurons in hidden layers – 3, 4, 5, 6 & 7 - were carried out on both training and validation sets to study the effect of number of neurons in the hidden layer on the network performance and to be able to determine the exact number of neurons in the hidden layer that would optimise the network performance. It was found that four – and five-neuron hidden layer performed better, with five-neuron hidden layer having the best performance. (see Figure 7-11 and 7-12).

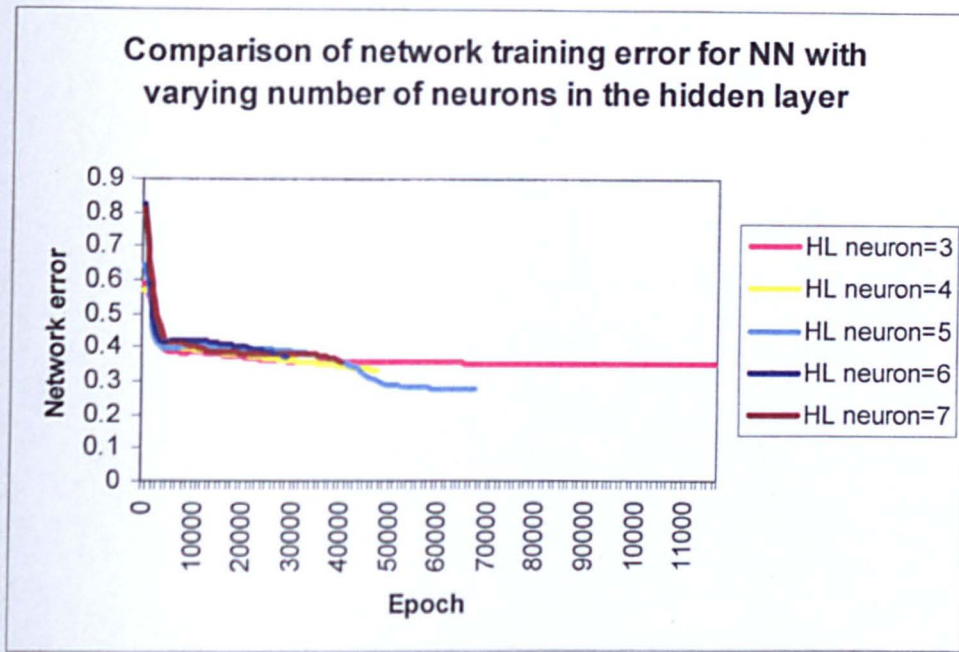


**Figure 7-11 Comparison of network training error for NN with varying no of neurons in the hidden layer**

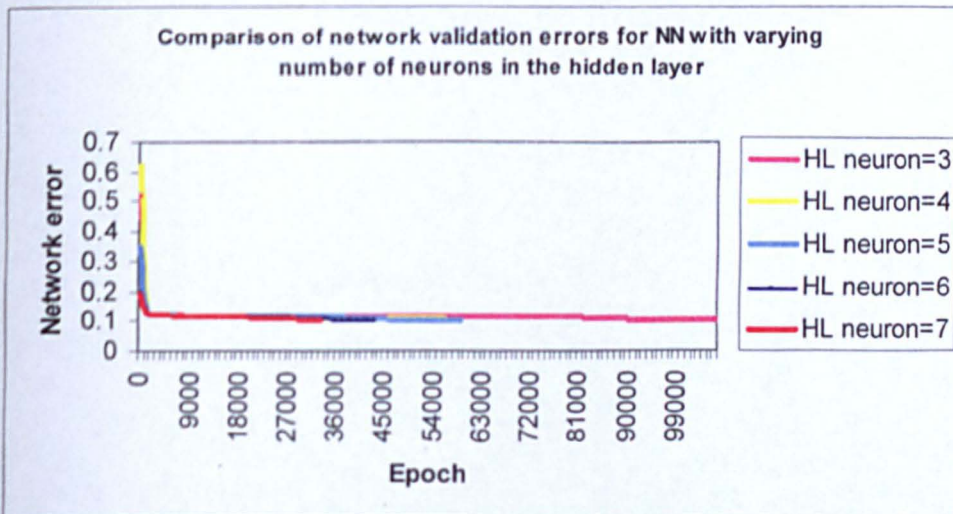


**Figure 7-12 Comparison of network validation error for NN with varying no of neurons in the hidden layer**

### 7.3.6 Final network implementation

The final network implementation was based on the results of the sensitivity studies carried out in the previous section. The final network topology used is summarised in Table 7-6.

**Table 7-6: Summaries of the final neural network topology for UCS modelling**

<b>Network parameters</b>	<b>Parameter value</b>
Network layers	3
Input nodes	4
Output nodes	1
Hidden layer nodes	5
Learning rate	0.75
Momentum	0.9

### 7.3.7 Neural network model testing.

Part of the data purposely set aside and not presented to neural network during training and cross validation was used to test the performance of the neural network model. The neural network was found to have learned the data structure very well (see Figures 7-13 and 7-14). In figure 7-13, the predicted data closely match the measured data whilst Figure 7-14 shows a high correlation coefficient of approximately 0.93 between the predicted and the measured UCS.

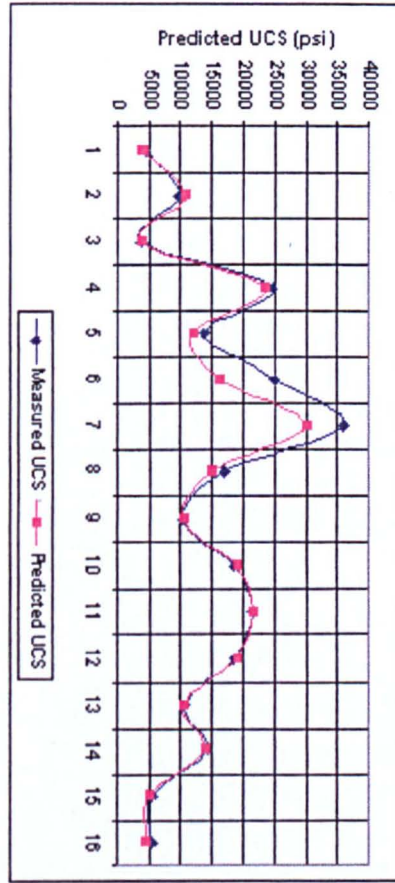


Figure 7-13 Neural network testing for UCS prediction

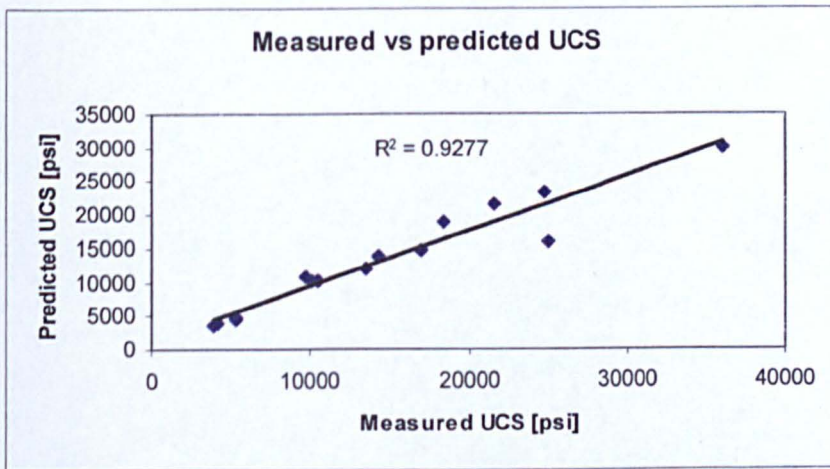


Figure 7-14 Measured versus predicted UCS from the NN

---

## **7-4 Validation of neural network model for predicting UCS**

Limited laboratory data from a Middle East field was used to validate the neural network model. This data is totally different from the data used in the neural network training, cross-validation and testing. Most of the petrophysical and geomechanical data required as inputs into the NN model to generate UCS were not available for the various sand sequences; only average values of these data were available for the entire field. Assumptions were therefore made to generate these data across the various sand sequences for which UCS was predicted.

Figure 7-15 shows the results of the UCS model validation for the various sand sequences at different depths. From the figure it is obvious that for a number of sand sequences, the model predictions do not match the measured data well. This may be attributed to the limited nature of the data and assumptions made to generate input data across the sand sequences. Another factor that may have contributed to the large deviations in some of the model predictions is the limitation of the data used in the training of the neural network. This, no doubt, underlines the importance of using large data assemblages for the training of neural network to equip it with experiential knowledge for excellent predictive ability rather than data memorisation. However, close observation reveals that the model generally performed better on data from sand sequence II-10, irrespective of their depth of occurrence. This may be as a result of the quality of the petrophysical and geomechanical data from this sequence.

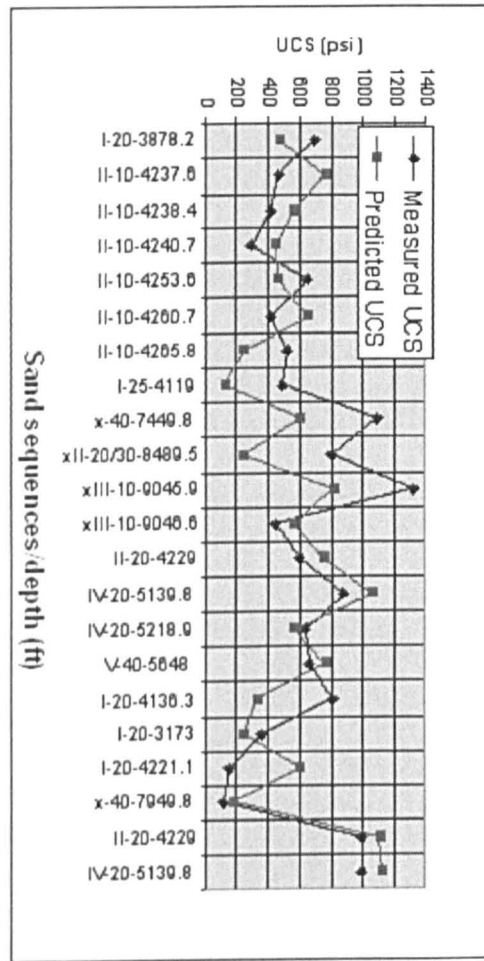


**Figure 7-15 Validation of UCS NN model on laboratory data obtained from a Middle East field.**

### 7.5 Summary

The summary of the studies the studies reported in this chapter are:

- The parameters or factors, which affect the Uniaxial Compressive Strength (UCS) have been identified and grouped accordingly. The identified factors have also been ranked.
- A ranking procedure has been developed for UCS models. This has been applied to a number of existing UCS models. The results of the ranking have shown that these models are deficient and cannot be relied upon for UCS prediction. The results of the ranking have

---

been justified by further evaluation of two of the three ranked best using a field data.

- Two modelling techniques – dimensional analysis and neural network – have been used for UCS prediction for the purpose of comparison.
- A neural network model has been developed for UCS prediction. The model has been tested and validated with limited laboratory data obtained from a Middle East field sand sequences.

## Chapter 8

### Real time sanding potential prediction

In this chapter, the real time sanding potential prediction model developed in this work is reported. The model is an integrated one and includes sub-models such as the Critical Drawdown (CDD) model, the Yield Flow Rate (YFR) model, the Critical Particle Velocity ( $V_{cp}$ ) model and the Sand Volume/Rate model. The sanding potential model, through these sub-models, is coupled to the grain size distribution (GSD) and Uniaxial Compressive Strength (UCS) models reported in chapters six and seven respectively.

Also reported in this chapter are the methodologies and the assumptions made in formulating these models; and the results of testing and validation.

#### 8.1 Onset of sanding model.

Recalling the Hoek-Brown<sup>132</sup> failure criterion given in chapter four (in equation 4-37) and replicated below (as equation 8-1):

$$\sigma_1 = \sigma_3 + \sqrt{m\sigma_{ucs}\sigma_3 + s\sigma_{ucs}^2} \quad 8-1$$

At the borehole wall the effective principal stresses  $\sigma_1'$  and  $\sigma_3'$  in equation 8-1 can be represented by the effective tangential,  $\sigma_\theta'$  and radial,  $\sigma_r'$  stresses. The methodology and rationale for this are discussed in chapter four. Equations for estimating both the tangential and radial stresses are also given in chapter four (see equations 4-25 to 4-27).

The Hoek-Brown failure criterion can therefore now be expressed in terms of the radial and tangential stress (equation 8-2):

$$\sigma_{\theta} = \sigma_r + \sqrt{m\sigma_{ucs}\sigma_r + s\sigma_{ucs}^2} \quad 8-2$$

Substituting equations 4-26 and 4-24 (given in chapter four) for estimating tangential and radial stresses respectively in equation (8-2), we have:

$$3\sigma_H' - \sigma_h' - P_w + P_r = (P_w - \alpha P_r) + \sqrt{m\sigma_{ucs}(P_w - \alpha P_r) + s\sigma_{ucs}^2} \quad 8-3$$

Note that the sign (') stand for the effective variant of the parameters.

Equation (8-3) can be re-arranged to give:

$$3\sigma_H' - \sigma_h' + 2\alpha P_r - 2P_w = \sqrt{m\sigma_{ucs}(P_w - \alpha P_r) + s\sigma_{ucs}^2} \quad 8-4$$

Further rearrangement of equation (8-4) gives:

$$3\sigma_H' - \sigma_h' + 2(\alpha P_r - P_w) = \sqrt{m\sigma_{ucs}(P_w - \alpha P_r) + s\sigma_{ucs}^2} \quad 8-5$$

$\alpha$ , a scaling factor, which measures the effectiveness of the formation pore/fluid pressure response to its stress environment, ranges from zero to one<sup>123</sup>. In formation where the response is 100% effective in counterbalancing the stress environment,  $\alpha$  is usually one. If it is assumed that the reservoir pore/fluid pressure exhibits maximum effectiveness in counterbalancing its stress environment, then  $\alpha = 1$

So if  $\alpha = 1$ ; and  $y = CDD_i = (P_r - P_w)$

Substituting for  $y$  in equation (8-5), we have:

$$3\sigma_H - \sigma_h + 2y = \sqrt{m\sigma_{ucs}(P_w - P_r) + s\sigma_{ucs}^2} \quad 8-6$$

Taking the square of both sides of equation (8-6), it becomes:

$$\left((3\sigma_H' - \sigma_h') + (2y)\right)^2 = m\sigma_{ucs}(P_w - P_r) + s\sigma_{ucs}^2 \quad 8-7$$

Expanding the left hand side of equation (8-7), we have:

$$(3\sigma_H' - \sigma_h')^2 - 2(3\sigma_H' - \sigma_h')2y + 4y^2 = m\sigma_{ucs}(P_w - P_r) + s\sigma_{ucs}^2 \quad 8-8$$

Rearranging, equation (8-8) it becomes:

$$4y^2 + 4(3\sigma_H' - \sigma_h')y + (3\sigma_H' - \sigma_h')^2 = m\sigma_{ucs}(P_w - P_r) + s\sigma_{ucs}^2 \quad 8-9$$

Let  $A = (3\sigma_H' - \sigma_h')$ ; substituting for  $A$  in equation (8-9), it becomes:

$$4y^2 + 4Ay + A^2 = m\sigma_{ucs}(P_w - P_r) + s\sigma_{ucs}^2 \quad 8-10$$

Re-arranging equation (8-10) and opening the bracket, it becomes:

$$4y^2 + 4Ay + A^2 - m\sigma_{ucs}P_w - m\sigma_{ucs}P_r - s\sigma_{ucs}^2 = 0 \quad 8-11$$

Rearranging equation (8-11) further, we have:

$$4y^2 + 4Ay + A^2 + m\sigma_{ucs}(P_r - P_w) - s\sigma_{ucs}^2 = 0 \quad 8-12$$

Recall that  $(P_r - P_w) = y$ ; substituting for  $y$  in equation (8-12) and rearranging, it becomes:

$$4y^2 + (4A + m\sigma_{ucs})y + (A^2 - s\sigma_{ucs}^2) = 0 \quad 8-13$$

Equation (8-13) is a quadratic equation and can be solved using the solutions of a quadratic equation. The equation can therefore be written in the form of the general quadratic equation (equation 8-14).

$$ay^2 + by + c = 0 \quad 8-14$$

The solution of the quadratic equation of this form can be written as:

$$y = \frac{-b \pm \sqrt{b^2 - 4ac}}{2a} \quad 8-15$$

Comparing equation (8-13) with equation 8-14,

$$a = 4; b = (4A + m\sigma_{ucs}); \text{ and } c = (A^2 - s\sigma_{ucs}^2)$$

Substituting for  $a$ ,  $b$  and  $c$  in equation (8-15) and recalling that  $y = (P_r - P_w) = CDD_i$ , it then becomes:

$$CDD_i = \frac{(4A + m\sigma_{UCS}) \pm \sqrt{(4A + m\sigma_{UCS})^2 - 16(A^2 - s\sigma_{UCS}^2)}}{8} \quad 8-16$$

This model predicts the critical drawdown pressure at which failure will occur (onset of sand production) for any reservoir rock at the initial reservoir pressure condition. Onset of sand production may however not coincide with the onset of failure in majority of sand production cases. These cases are addressed in the later sections of this chapter. The strength parameter (UCS) input to the model is dependent on the grain size distribution. As the grain size distribution changes during the post-failure production period, the strength of the formation also changes. This may further extend the boundary of the failure envelope. This is perfectly captured by the model and reflected in its predictions as shown in section 8.1.2.

### 8.1.1 Hoek and Brown (1988)<sup>160</sup> estimates of model parameters

Hoek and Brown (1988)<sup>160</sup> developed, based on series of experimental work, estimates of  $m$  and  $s$ , the constants in the model, for a wide range of rocks under a wide range of conditions that can be encountered in the petroleum formation. The estimated values of these parameters reflected the level of disturbance undergone by the rock formation they used in their experiment. The estimates as given by Hoek and Brown (1988)<sup>160</sup> are given in table 8-1. These estimates can be used for the constant terms  $m$  and  $s$  in the developed model to predict failure in petroleum formations provided information about their lithological make up and level of disturbance is available.

**Table 8-1 Hoek and Brown (1988)<sup>160</sup> estimates of m and s**

	Carbonate rocks e.g. Limestone	Lithified argillaceous rocks e.g. Shale	Arenaceous rocks e.g. sandstone	Fine grained igneous rock e.g. Rhyolite	Coarse grained igneous rock e.g. Granite
Intact rock	m = 7 s = 1	m = 10 s = 1	m = 15 s = 1	m = 17 s = 1	m = 25 s = 1
Undisturbed rock	m = 4.10 s = 0.189	m = 5.85 s = 0.189	m = 8.78 s = 0.189	m = 9.95 s = 0.189	m = 14.63 s = 0.189
Moderately weathered rock	m = 0.9-2.0 s = 0.00198-0.0205	m = 1.35-2.86 s = 0.00198-0.0205	m = 2.03-4.298 s = 0.00198-0.0205	m = 2.301-4.871 s = 0.00198-0.0205	m = 3.383-7.163 s = 0.00198-0.0205
Heavily weathered rock	m = 0.219 s = 0.00002	m = 0.313 s = 0.00002	m = 0.469 s = 0.00002	m = 0.532 s = 0.00002	m = 0.782 s = 0.00002

### 8.1.2 Preliminary analysis and testing of model

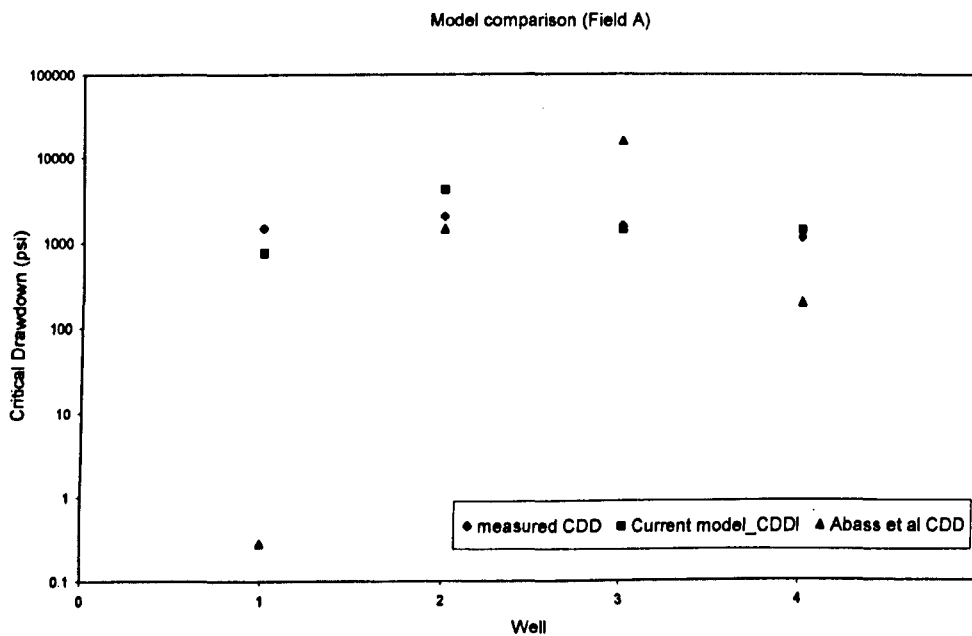
Two sets of North Sea field data, obtained from Field A and B were used to analyse, test and compare the CDD model with another onset of sand prediction model and measured data. The results are shown in Figures (8-1) to (8-4); and Tables (8-2) and (8-3).

Figure 8-1 shows the results obtained when data from Field A was utilised for comparison of the performance of the current model with Abass et al model in terms of accurate predictions of Critical Drawdown for Field A. The results, as shown in the Figure, indicate that the current model march the measured CDD better than Abass et al model. The degree of closeness (correlation coefficient) between the predicted CDD by the two models and measured data is shown in Figure 8-2. The current model predictions

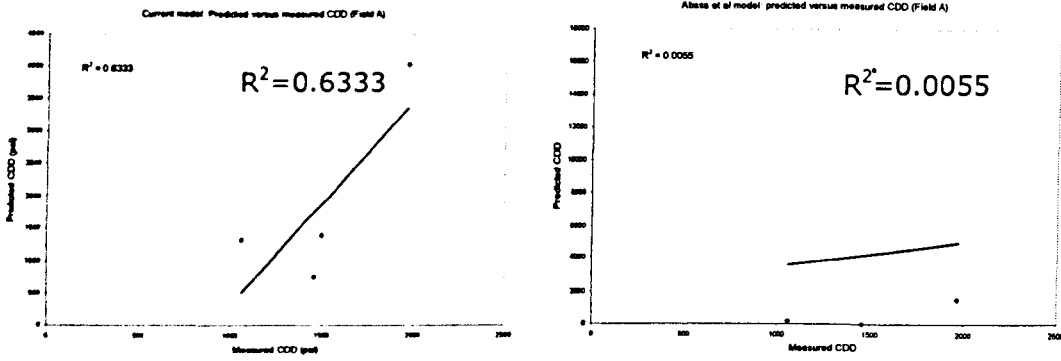
have a correlation coefficient of 0.6333 whilst for Abass et al predictions, the correlation coefficient is 0.0055. This is a very low insignificant correlation coefficient

Figure 8-2 shows the results obtained from the use of Field B data. The results also indicate that the current model predictions march the measured data better than Abass et al model. Determination of the correlation coefficients for two model predictions shown in Figure 8-4 shows that the current model predictions have a correlation coefficient of 0.9123 whilst Abass et al predictions have a correlation coefficient of 0.6259.

In general the results indicate that the current CDD model outperformed Abass et al (2003)<sup>49</sup> Critical Drawdown (CDD) model and match better the measured CDD for both Fields A and B.



**Figure 8-1 Comparison of CDD model with Abass et al CDD model using a North Sea field data (Field A).**



**Figure 8-2 Correlation coefficients of predicted versus measured CDD for the current model and Abass et al model ( Field A)**

**Table 8-2 Results of analysis and testing of preliminary CDDi model with data from Field A**

	Measured CDD <sub>i</sub> [MPa]	Predicted CDD <sub>i</sub> <sup>1</sup> [MPa]	Predicted CDD <sub>i</sub> <sup>2</sup> [MPa]
1	1457	1164.2	13691.89
2	1966	2417.7	6024.6
3	1498	1152.1	45373.9
4	1060	971.5	8959.0

1 First solution of a quadratic equation  
2 Second solution of a quadratic equation

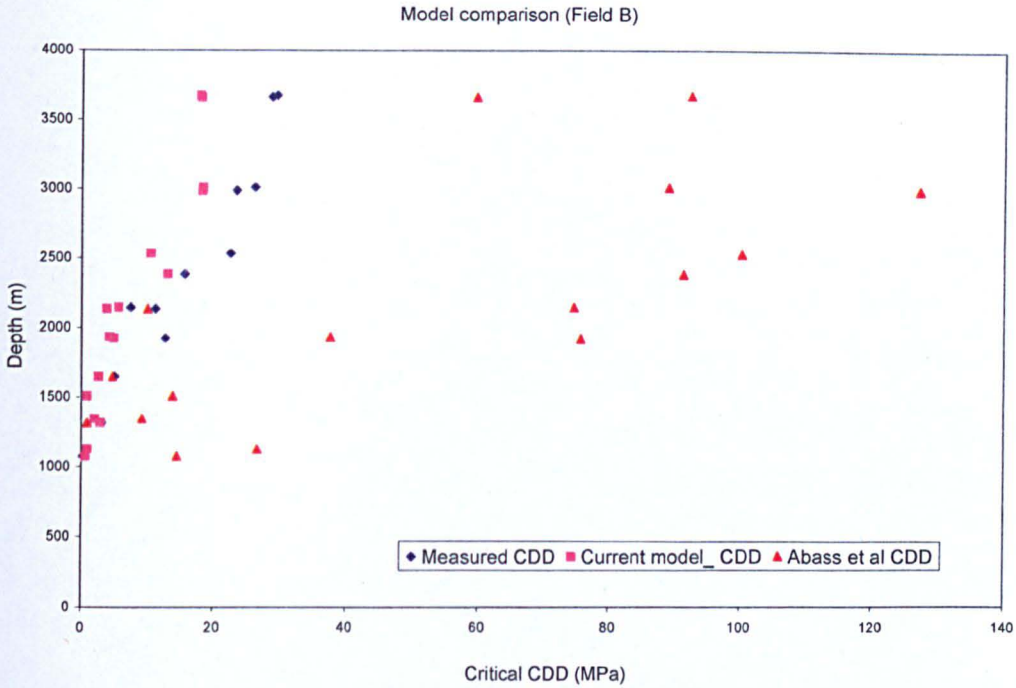


**Figure 8-3 Comparison of CDD models with Abass et al CDD models using a North Sea field data (Field B)**

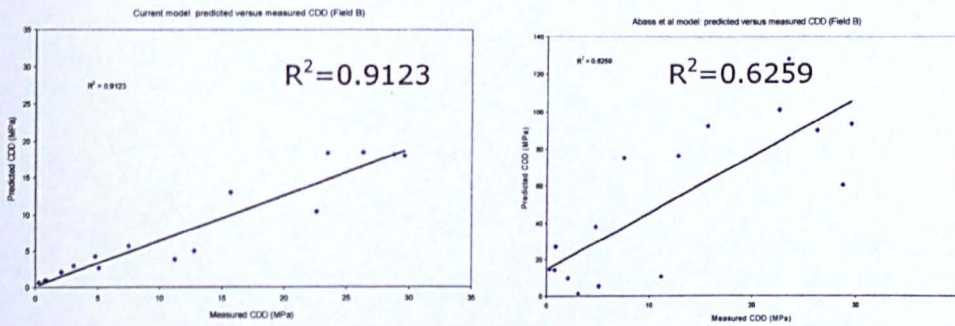


**Figure 8-4 Correlation coefficients of predicted versus measured CDD for the current model and Abass et al model (field B)**

**Table.8-3 Results of analysis and testing of preliminary CDD<sub>i</sub> model with data from Field B**

	Measured CDD <sub>i</sub> [MPa]	Predicted CDD <sub>i</sub> <sup>1</sup> [MPa]	Predicted CDD <sub>i</sub> <sup>2</sup> [MPa]
1	3.1	2.7	127.3
2	0.3	0.5	118.0
3	15.7	11.8	157.7
4	0.9	1.0	104.8
5	0.8	0.9	182.6
6	2.1	1.8	104.1
7	23.5	17.8	176.0
8	26.3	19.0	167.5
9	4.8	5.0	135.7
10	7.5	6.0	139.7
11	5.1	3.4	72.7
12	29.6	20.2	127.3
13	28.8	19.5	128.0
14	11.2	8.3	31.7
15	22.6	11.9	46.5
16	12.8	6.4	28.5

1 First solution of a quadratic equation

2 Second solution of a quadratic equation

## 8.2 Coupling CDD model with time

The current CDD<sub>i</sub> model only predicts the critical drawdown pressure at which failure will occur in reservoir formation rocks for initial reservoir pressure conditions when the reservoir is either yet to be put on production or is producing but yet to experience any serious depletion due to production. The critical drawdown may however change over time as the reservoir experiences more and more depletion.

Hettema et al. (2006)<sup>161</sup> presented an empirical model for estimating the sand production critical drawdown pressure at initial reservoir pressure based on extensive sand production data from a North Sea field straddling

the Norwegian and UK sectors. The model was a product of fitting models into the large sand production data they obtained from the field (Figure 8-5).

The model relates critical drawdown pressure at initial reservoir pressure ( $CDD_i$ ) with the critical drawdown pressure at the current reservoir pressure ( $CDD_c$ ), the initial reservoir pressure  $P_{ri}$  and the current reservoir pressure,  $P_{rc}$ . It is expressed mathematically as.

$$CDD_i = CDD_c + n(P_{ri} - P_{rc}) \quad 8-17$$

$CDD_c$  is critical drawdown pressure at the current reservoir pressure due to continual reservoir depletion;  $P_{ri}$  is the initial reservoir pressure;  $P_{rc}$  is the current reservoir pressure; and  $n$  is a dimensionless parameter, which represents the ratio of change in critical drawdown pressure with reservoir depletion.

Hettema et al. (2006)<sup>161</sup> suggests that  $n = 1$  when drawdown and depletion are equally important for sand production.

The validity of Hettema et al (2006)<sup>161</sup> model may be explained by the concept of effective stress, which establishes that reservoir pressure counterbalances other stresses such as overburden and horizontal stresses that act on the reservoir formation. The balance of these stresses termed "effective" increases with decrease in reservoir pressure over its production period.

If equation (8-17) is re-arranged and  $CDD_i$  is substituted for, we simply obtain a model for predicting Critical Drawdown ( $CDD$ ) as a function of depletion in real time.

$$CDD_c = \left[ \frac{(4A + m\sigma_{UCS}) \pm \sqrt{(4A + m\sigma_{UCS})^2 - 16(A^2 - s\sigma_{UCS}^2)}}{8} \right] - \left[ n \frac{(P_{ri} - P_{rc})}{1} \right] \quad 8-18$$

Figures 8-6 to 8-9 show examples of CDD predictions against depletion (time) by the model at various depths using the same data utilised for the model testing and validation in section 8.1.2.

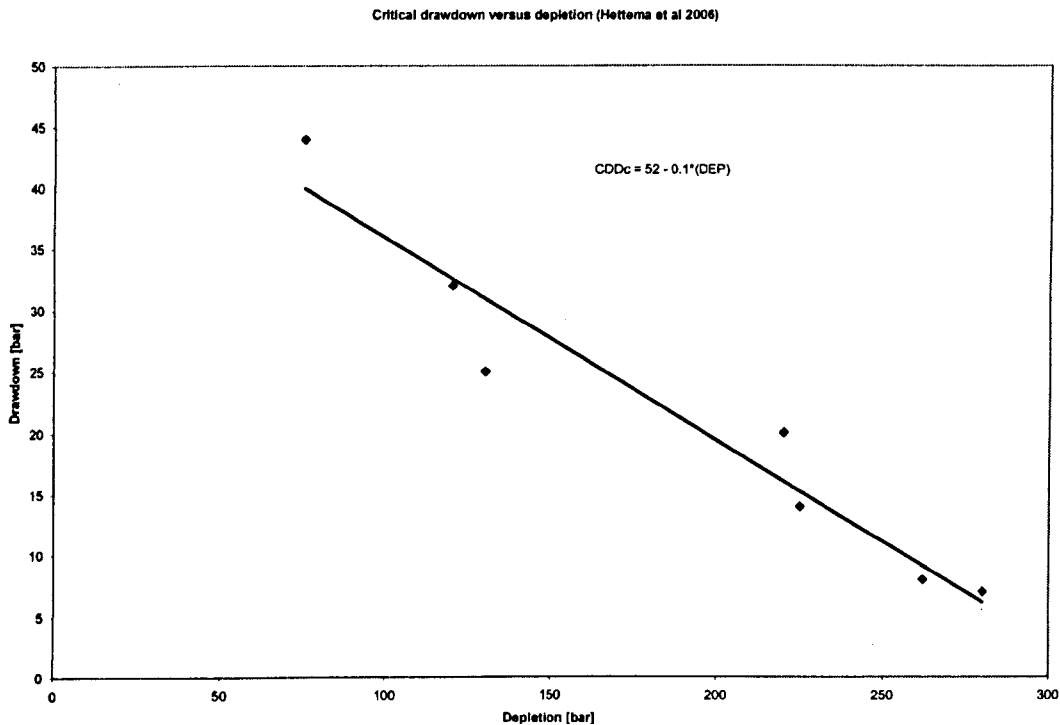
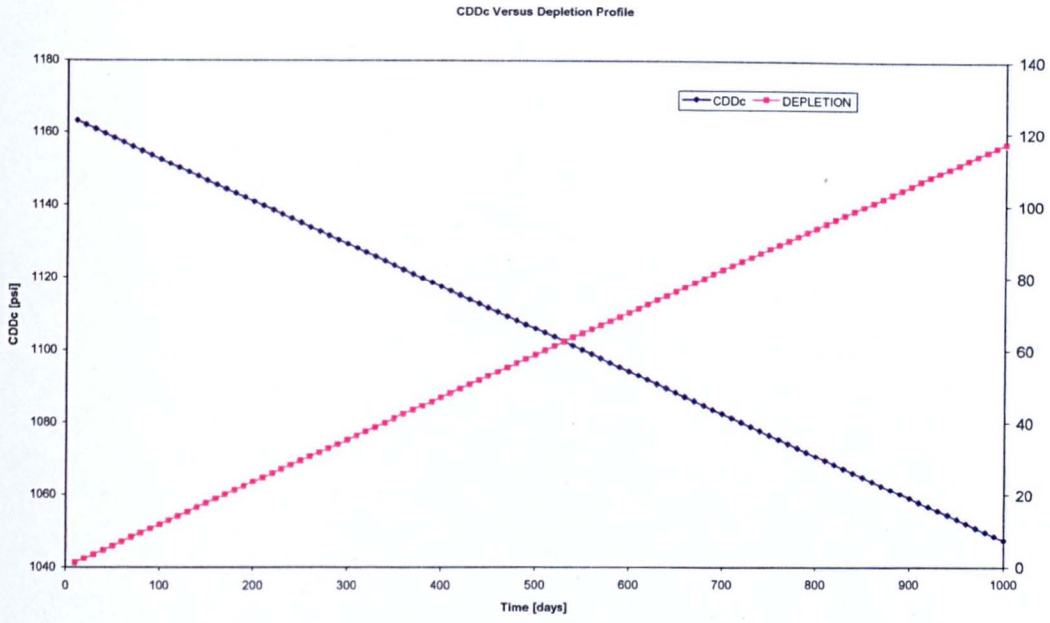
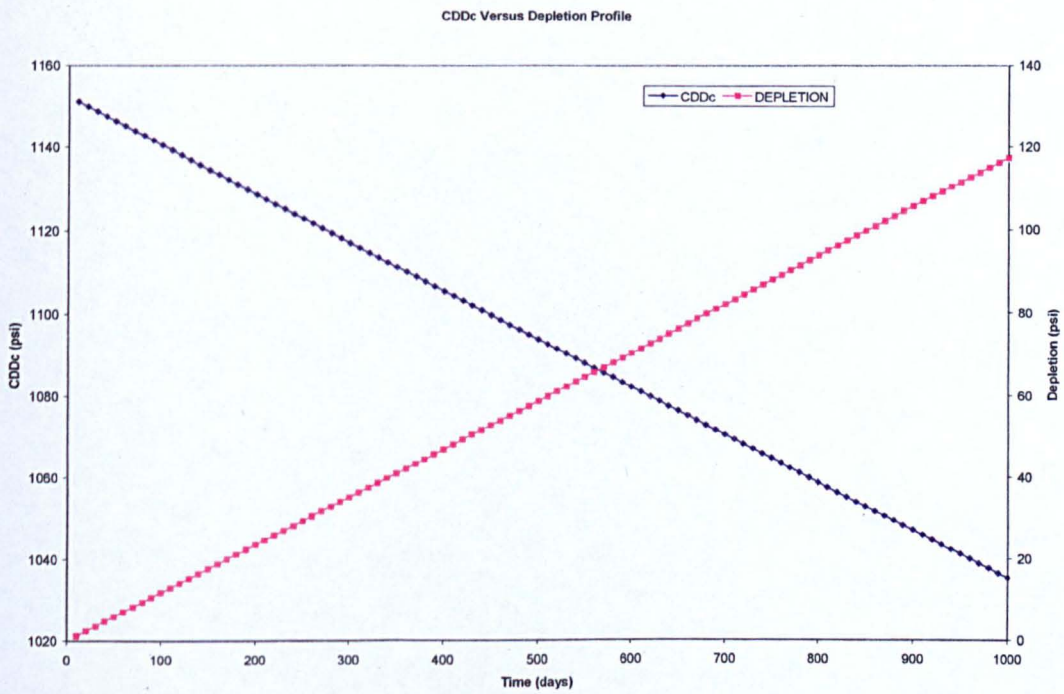


Figure 8-5 A linear fit into Hettema et al (2006) data.



**Figure 8-6 CDD<sub>c</sub> versus depletion at 4675ft**



**Figure 8-7 CDD<sub>c</sub> versus depletion at 6412ft**

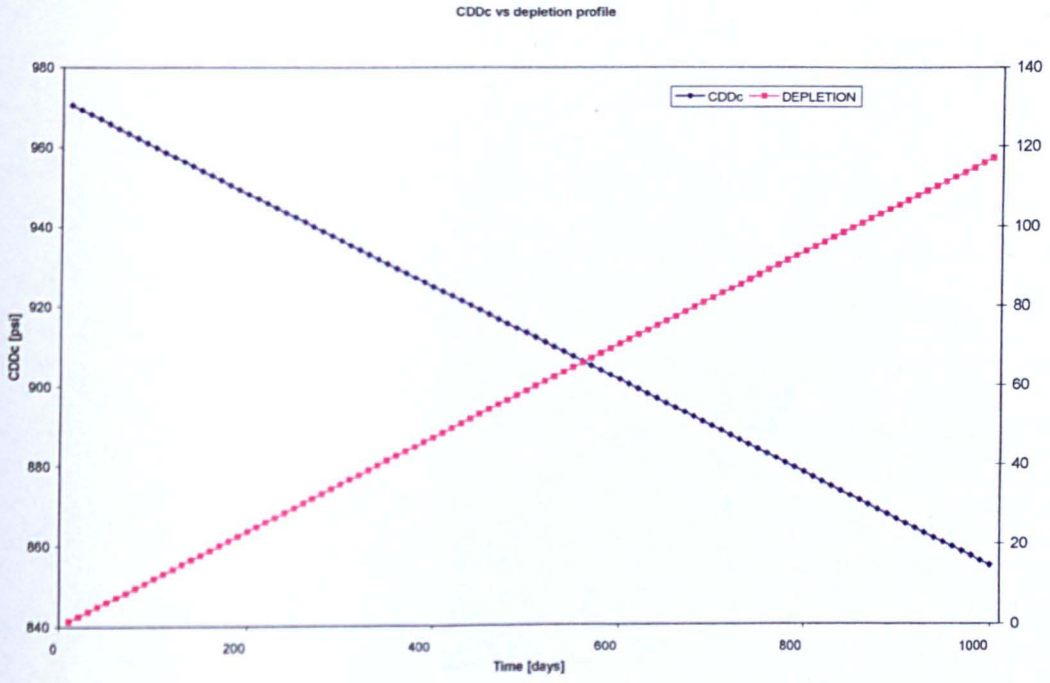


Figure 8-8 CDD<sub>c</sub> versus depletion at 4675ft

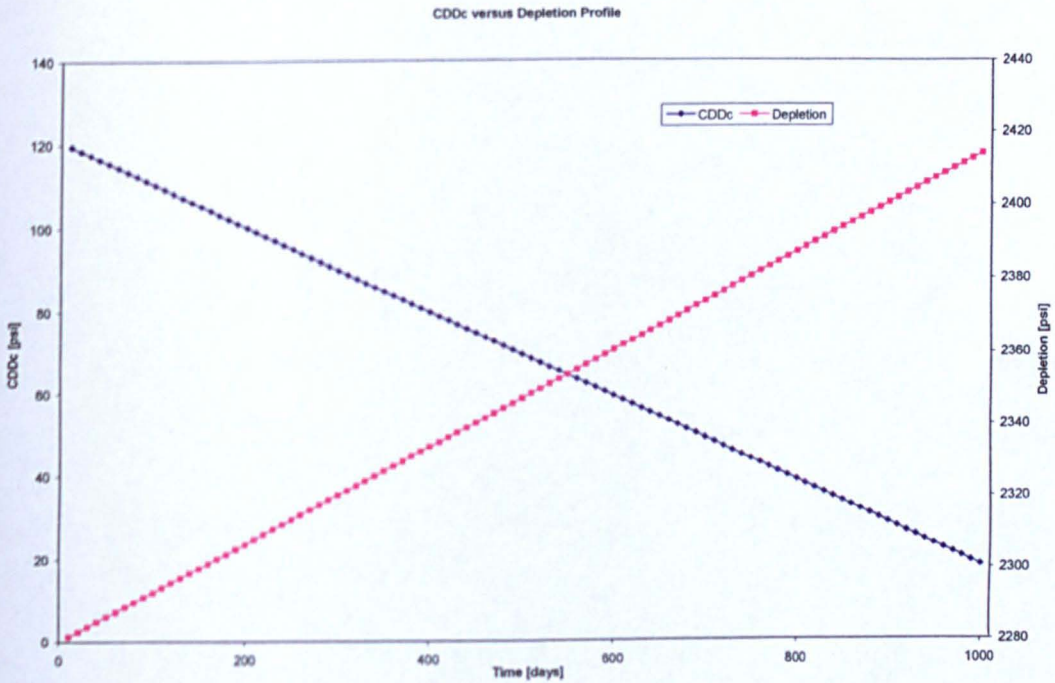


Figure 8-9 CDD<sub>c</sub> versus depletion at 17000ft

### 8.2.1 Case studies: example calculations

Example calculations were carried out in two case studies of a Middle East field to illustrate and demonstrate the field application of the Critical Drawdown (CDD) model. The field data used as input to the Critical Drawdown model are given for case studies 1 and 2 respectively in Tables 8-4 and 8-5.

The initial CDD predicted in case study 1 at initial reservoir conditions is 522psi. The change in CDD over a 4.5-year production period at a reservoir depletion rate of 0.11psi/day was predicted; the profile obtained is shown in Figure 8-10. This prediction shows that over a 4.5-year period, the CDD will decrease steadily from its peak value of 552psi to 372psi.

For the second case study, the predicted CDD at initial reservoir conditions is 582psi. The change in CDD over the same 4.5-year production period, but at a reservoir depletion rate of 0.22psi/day, was also predicted; the profile of which is shown in Figure 8-11. In this case the CDD will decrease steadily from a peak value of 582psi to 221psi.

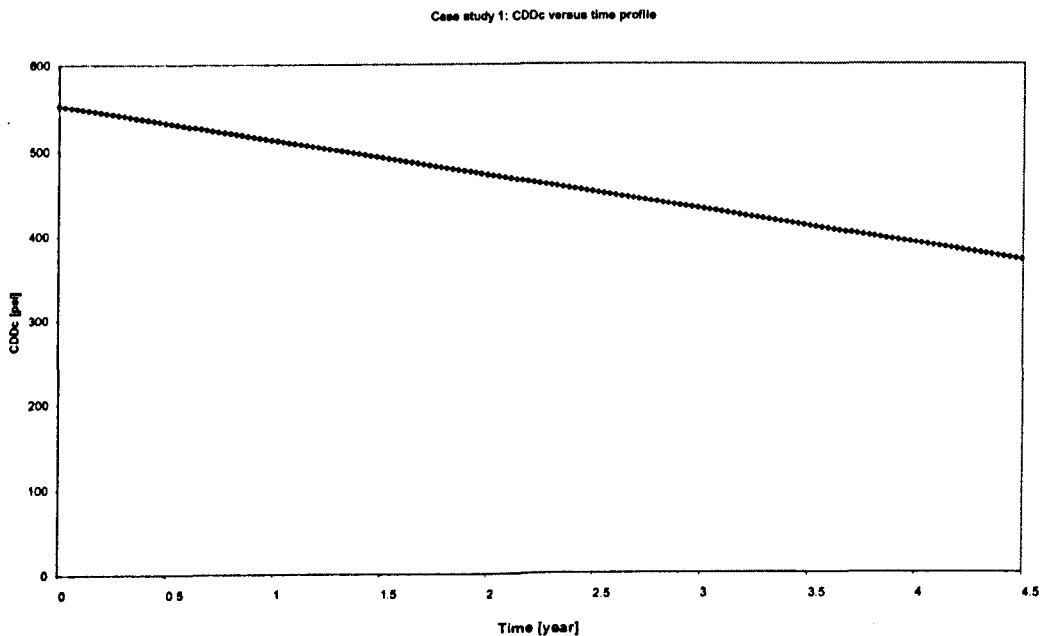


Figure 8-10 Case study 1: Change in CDD with time

Table 8-4 Case study 1 well data		
Well data		Unit
Top reservoir depth	5779	ft
Base reservoir depth	5809	ft
Reservoir thickness	30	ft
Unconfined Compressive Strength	1926	psi
	3411	psi
Vertical stress	2650	psi
Minimum horizontal stress	2730	psi
Maximum horizontal stress	1797	psi
Reservoir pressures	0.11	psi/day
Well depletion rate	15	
m	1	
s	552	psi
Calculated CDD		

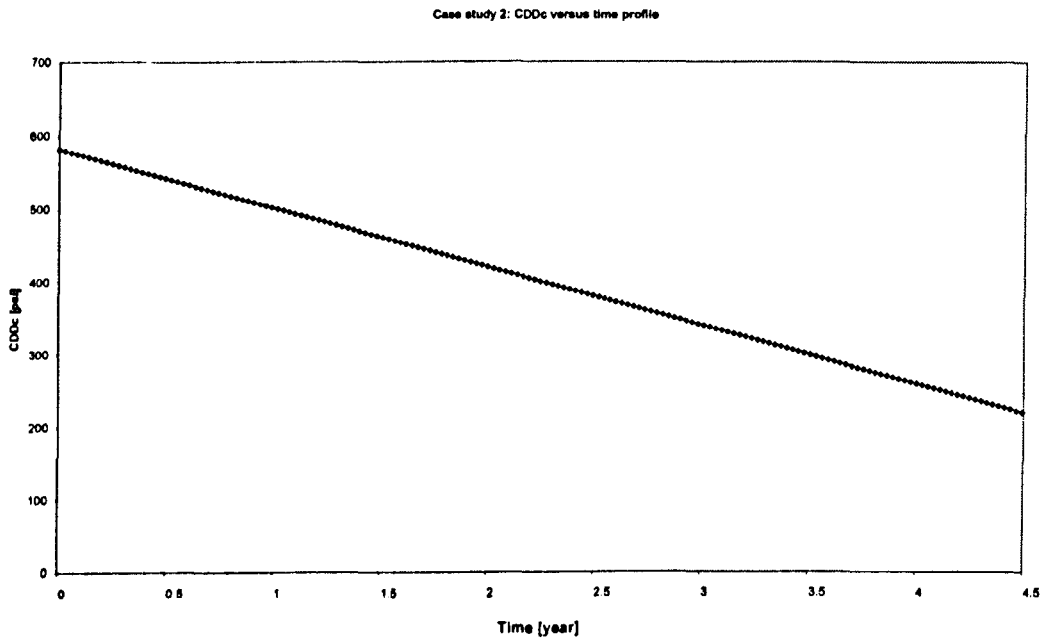


Figure 8-11 Case study 2: Change in CDD with time

**Table 8-5 Case study 2 well data**

Well data		Unit
Top reservoir depth	5430	ft
Base reservoir depth	5500	ft
Reservoir thickness	70	ft
Unconfined Compressive Strength	1926	psi
Vertical stress	3561	psi
Minimum horizontal stress	2725	psi
Maximum horizontal stress	2807	psi
Reservoir pressures	1775	psi
Well depletion rate	0.21	psi/day
m	15	
s	1	
Calculated CDD	582	psi

## 8.3 Effect of water breakthrough on sand failure

### 8.3.1 Theoretical background

Strength derived from capillary pressure effect is one of the unconsolidated sand stabilising factors<sup>162</sup>. Others as reported in open literatures are the strength due to cementitious materials and mechanical attributes of sand<sup>3,162-163</sup>. Of all the factors contributing to the strength of unconsolidated reservoir sand, capillary strength and strength due to cementitious materials, especially if they are chemically reactive calcium carbonate cements, are most affected by water breakthrough<sup>3</sup>. The quantitative evaluation of the effect of water breakthrough on the strength due to cementitious materials is however extremely difficult<sup>162</sup>.

The capillary pressure is the pressure difference between the non-wetting and wetting phase fluid pressure within the reservoir<sup>167</sup>. It is generally

considered to be a function of the interfacial tension between the two fluid phases, the contact angle made by the usually curved interface between the two fluids and the pore throat diameter<sup>3,167</sup>.

$$\Delta P_c = \frac{2\sigma_{\text{int}} \cos \theta_c}{d_{\text{pore}}} \quad 8-19$$

$\Delta P_c$  is the capillary pressure;  $\sigma_{\text{int}}$  is the interfacial tension;  $\theta_c$  is the contact angle; and  $d_{\text{pore}}$  is the pore throat diameter.

The interfacial tension between the two fluid phases in a porous medium furnishes a cohesive strength, which helps to keep the sand grains together even when they have already failed<sup>3</sup>. However at high water (wetting phase) saturations, the interface between the two fluid phases may break down leading to drastic reduction in or even zero interfacial tension<sup>167</sup>. From equation (8-19), interfacial tension and capillary pressure have a direct relationship. It is therefore expected that the capillary pressure and hence the capillary cohesive strength will reduce during significant water breakthrough.

Water breakthrough has two major impacts on sand production; These are:

(1) Contributes to sand failure through a variety of mechanisms such as

- Reduction of apparent rock cohesion due to reduced capillary bonding<sup>5</sup>.
- Chemical reaction between water and the rock materials such as carbonate dissolution, quartz hydrolysis, ferruginous deposits and clay swelling leading to reduced mechanical strength<sup>3,164</sup>.
- Fluid flow erosion of the grain matrix due to increased fluid drag during two-phase flow<sup>7</sup>.

- Plugging of parts of the pay zone due to relative permeability effects resulting in concentration of fluid inflow at permeable intervals leading to hydrodynamically induced instability<sup>164</sup>

(2) Transports already failed sand from the failure site to the wellbore

The occurrence of the first will essentially lead to sand failure but may not necessarily signal the onset of sand production. The occurrence of the second will however most likely coincide with the onset of sand production.

### **8.3.2 Field evidence supporting the roles of water in sand production**

Onset of sand production is often reported to coincide with the onset of water breakthrough<sup>3,162-165</sup>. There is however no consensus of opinions among the operators about the exact roles of water in sand failure and production.

However detailed analysis of sand production data from a North Sea reservoir operated by Statoil, though did not provide a systematic relation between the onset of sand production and water breakthrough<sup>164</sup> has given some preliminary evidence that water indeed has some effect on sand failure/sand production as shown in Figure 8-12.

Figure 8-12 is a plot of average sand production rates before and during water breakthrough for several wells in a North Sea field where sand production was experienced. A careful analysis of the figure shows that majority of the analysed wells (more than 90%) have higher sand production rate during water breakthrough than before water breakthrough. This is clearly an evidence that water breakthrough plays a major role in sand production.

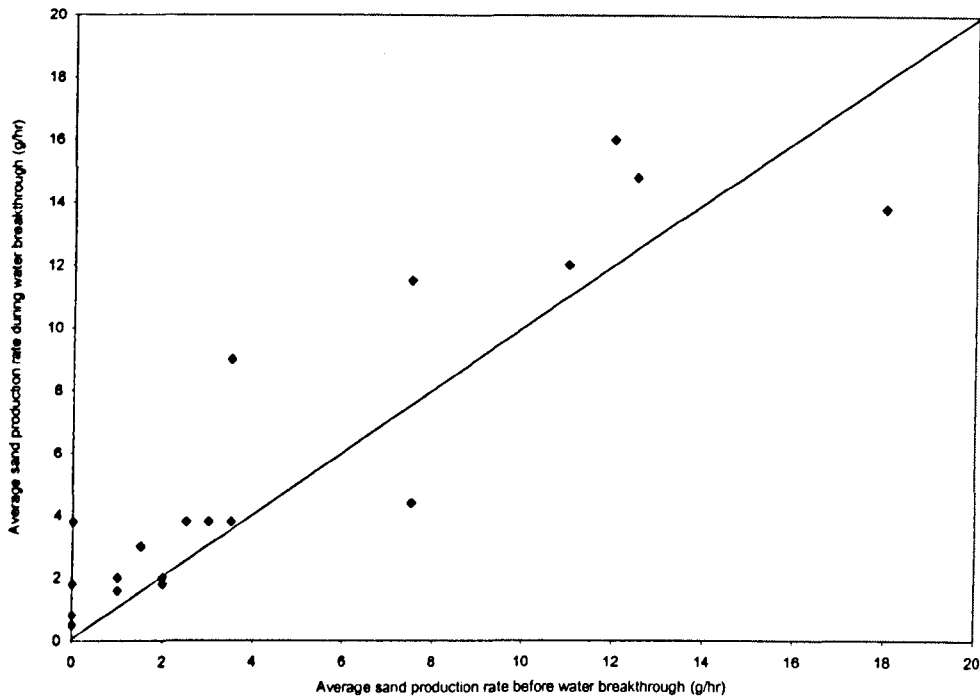


**Figure 8-12 Comparison of sand production during and before water breakthrough for several North Sea field wells<sup>164</sup>.**

### 8.3.3 Experimental evidence supporting the roles of water in sand production

Sand arches formation, growth and stabilisation are crucial to unconsolidated reservoir sand stabilisation<sup>165-166</sup> especially in the sand areas opposite the perforation zones within the reservoir sand. The destabilisation of the sand arches may lead to sand production.

This phenomenon was investigated by Hall and Harrisberger (1970)<sup>165</sup> in their sand arch experiment in which they used water as a wetting phase and kerosene as a non-wetting phase. Their results concluded that kerosene-water interfacial tension provided enough cohesion to stabilise the arch. This conclusion came from the observation that the arch was stable to outward flow of the non-wetting phase (Kerosene) at residual saturation of the wetting phase (water); while the outward flow of the wetting phase destroyed the arch. Cleary et al (1979)<sup>166</sup>, in addition to showing the major roles of interfacial tension in sand arch stabilisation,

also underlined the effect of fluid production rate. They showed that high fluid flow rate would also cause arch instability. Tippie and Kohlhaas (1973)<sup>168</sup> however showed through series of experimental studies that a higher flow rate in itself does not cause arch instability but sudden increase rather than gradual increase of fluid flow rate. This argument seems logical if sudden change in flow rate is considered in the light of the expected backpressure on the sand and the pressure drop within the sand.

### 8.3.4 Modelling the effect of water breakthrough on sanding potential

Before water breakthrough, the reservoir pore space is assumed to be only oil saturated; it is therefore logical to also assume that the oil phase only is responsible for the pressure within the reservoir the reservoir pressure  $P_r$ . After water breakthrough, when the interfacial tension between oil and water has broken down (according to equation 8-19) and the reservoir becomes saturated with both oil and water, it can also be assumed that both oil and water are now responsible for or contribute to the reservoir pressure.

Assuming a steady state flow of fluid within the reservoir, the pressure due to water and oil can be estimated respectively as:

$$P_w = P_f - \frac{q_w \mu_w}{2\pi k k_{rw} h} \ln \frac{r_e}{r_w} \quad 8-20$$

and

$$P_o = P_f - \frac{q_o \mu_w}{2\pi k k_{ro} h} \ln \frac{r_e}{r_w} \quad 8-21$$

$p_w$  and  $p_o$  are pressures due to water and oil respectively;  $p_f$  is the far field reservoir pressure;  $q_w$  and  $q_o$  are the water and oil volumetric flow rate respectively;  $\mu_w$  and  $\mu_o$  are the water and oil kinematic viscosity respectively;  $k_{rw}$  and  $k_{ro}$  are the water and oil relative permeabilities respectively;  $k$  is the absolute reservoir permeability;  $h$  is the reservoir thickness;  $r_e$  is the reservoir drainage radius; and  $r_w$  is the well radius

The difference between the pressures of water and oil occupying the pore spaces of a reservoir rock is known as capillary pressure, which can be represented mathematically as<sup>167</sup>:

$$\Delta P_c = P_o - P_w \quad 8-22$$

If capillary pressure is taken essentially as a function of phase saturation, equation (8-23) can be written as:

$$\Delta P_c = P_o s_o - P_w s_w \quad 8-23$$

$s_o$  and  $s_w$  are oil and water saturation respectively.

The total phase saturation (assuming a saturated reservoir) in the reservoir is given by:

$$s_w + s_o = 1 \quad 8-24$$

The oil phase saturation is therefore given as:

$$s_o = 1 - s_w \quad 8-25$$

Substituting equation (8-25) for  $s_o$  in equation (8-23), we have:

$$\Delta P_c = P_o(1 - s_w) - P_w s_w \quad 8-26$$

Equations 8-20 and 8-21 for water and oil pressures can be put in equation (8-26).

$$\Delta P_c = \left[ P_f - \left( \frac{q_o \mu_o}{2\pi k k_{ro} h} \ln \frac{r_e}{r_w} \right) \right] \left[ \frac{1 - s_w}{1} \right] - \left[ P_f - \left( \frac{q_w \mu_w}{2\pi k k_{rw} h} \ln \frac{r_e}{r_w} \right) \right] \left[ \frac{s_w}{1} \right] \quad 8-27$$

Re-arrangement of equation (8-27) gives:

$$\Delta P_c = \frac{1}{2\pi k h} \ln \frac{r_e}{r_w} \left[ \frac{q_w \mu_w s_w}{k_{rw}} - \frac{q_o \mu_o (1 - s_w)}{k_{ro}} \right] \quad 8-28$$

The total fluid flow from the reservoir is given as

$$q_T = q_w + q_o \quad 8-29$$

Where  $q_T$  is the total fluid flow rate from the reservoir,  $q_w$  is the flow rate of water and  $q_o$  is the flow rate of oil.

Re-arranging equation (8-29), we have:

$$q_w = q_T - q_o \quad 8-30$$

The fraction of the total flow  $f_w$  from a reservoir, which is water, is defined by equation (8-31)<sup>169</sup>:

$$f_w = \frac{q_w}{q_o + q_w} = \frac{q_w}{q_T} \quad 8-31$$

Re-arrangement of equation (8-31) gives:

$$q_w = f_w q_T \quad 8-32$$

If equations (8-30) and (8-32) are equated, we have

$$q_o = q_T (1 - f_w) \quad 8-33$$

If equations (8-32) and (8-33) are put in equation (8-28) we have:

$$\Delta P_c = \frac{1}{2\pi kh} \ln \frac{r_c}{r_w} \left[ \frac{q_T f_w \mu_w s_w}{k_{rw}} - \frac{(q_T (1 - f_w)) \mu_o (1 - s_w)}{k_{ro}} \right] \quad 8-34$$

The equation for computing fractional flow of water  $f_w$  in a horizontal reservoir is given by equation(8-35)<sup>169</sup>:

$$f_w = \frac{1}{1 + \frac{\mu_w}{k_{rw}} \cdot \frac{k_{ro}}{\mu_o}} \quad 8-35$$

A new CDD equation, which accounts for water breakthrough in terms of the level of interfacial tension and capillary pressure between the water and oil phase can therefore be written.

$$CDD_c = (CDD_i - \Delta P_c) - (P_{ri} - P_{rc}) \quad 8-36$$

---

Where  $\Delta P_c$  is the capillary pressure.

### 8.3.4.1 Validation of effect of water breakthrough

Three different data sets have been used to model the effect of water breakthrough on the capillary pressure. The data sets are shown in Tables 8-6 to 8-8. Water and oil relative permeabilities for the three cases were computed using the empirical relations by Juanes and Patzek (2003)<sup>170</sup> which simply treat relative permeability as a function of water saturation.

However the water saturation range for the data was assumed for the computation. Figure (8-13) shows the plots of water saturation against oil and water relative permeabilities and fractional flow for the three cases considered.

Figure 8-14 shows the plots of water breakthrough versus the capillary pressure for the three cases considered in the validation exercise. The plots for the three cases confirm the theoretical basis which explains the effect of water on the critical drawdown model. The negative values returned by the model indicate that the impact of water breakthrough on critical drawdown (CDD) is negative. In effect, as suggested by equation 8-36, the value of critical drawdown (CDD) will be reduced especially at high water breakthrough. At low water breakthroughs of up to 0.6, the change in the capillary pressure is relatively low whilst at water breakthrough of more than 0.6; there is an appreciable change in the predicted capillary pressure.

<b>Table 8-6 Reservoir/well data: case 1</b>		
Property	Value	Unit
CDD	1479	psi
Reservoir thickness	21	ft
Well radius	0.35	ft
Reservoir drainage radius	210	ft
Absolute permeability	20	mD
Oil viscosity	2	cP
water viscosity	1	cP
Total fluid production rate	540	bbl/d

<b>Table 8-7 Reservoir/well data: case 2</b>		
Property	Value	Unit
CDD	1885	psi
Reservoir thickness	31.5	ft
Well radius	0.35	ft
Reservoir drainage radius	203	ft
Absolute permeability	10	mD
Oil viscosity	2	cP
water viscosity	1	cP
Total fluid production rate	810	bbl/d

<b>Table 8-8 Reservoir/well data: case 3</b>		
Property	Value	Unit
CDD	1957.5	psi
Reservoir thickness	19.88	ft
Well radius	0.35	ft
Reservoir drainage radius	218.5	ft
Absolute permeability	15	mD
Oil viscosity	2	cP
water viscosity	1	cP
Total fluid production rate	486	bbl/d

Effect of water saturation on oil relative permeability, water relative permeability and fractional flow of water (case 1, 2 & 3)

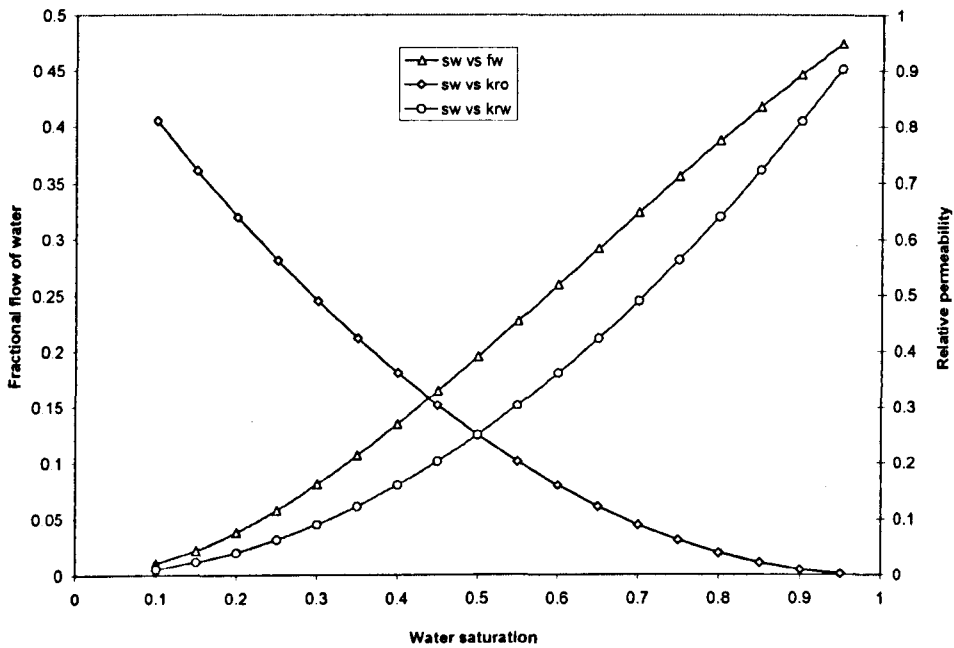


Figure 8-13 Effect of water saturation on oil relative permeability, water relative permeability and fractional flow of water for cases 1, 2 and 3

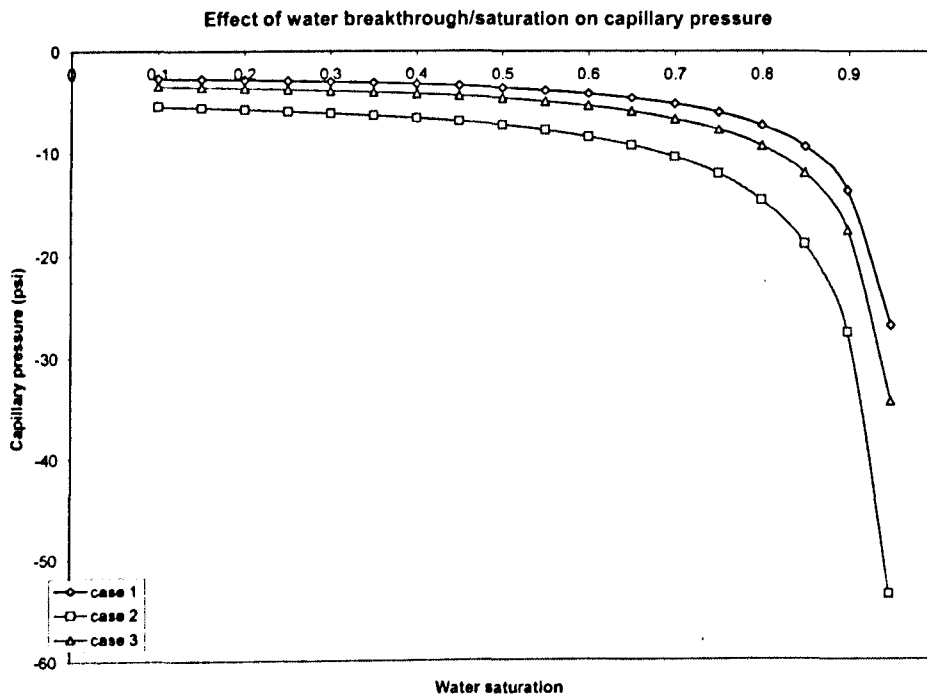


Figure 8-14 effect of water breakthrough on capillary pressure

## 8.4 Effects of completion types on CDD

### 8.4.1 Perforated completion

In perforated completion, casing strings are run through the pay or reservoir zone and cemented in place; small holes are then shot into the sides of the casings at pay zone level to allow for unhindered flow of fluid into the wellbore and provide support to the wellbore.

Perforated completion especially partial perforation of the casing string across the reservoir will cause additional pressure drop<sup>167</sup> due to convergence of fluid flow on the perforations<sup>171-172</sup>. This additional pressure drop will impact the original prediction of Critical Drawdown Pressure from the CDD model.

Samsuri et al (2003)<sup>173</sup> divided the perforation into two sections (fig. 8-15); the first is the perforation in the formation outside the casing represented by B, and the second is the tunnel across the casing and the cement represented by A. They assumed a linear flow regime in the casing-cement section of the perforation and approximated the pressure drop in this section using Saucier (1974)<sup>174</sup> equation:

$$\Delta P_A = 0.888 \frac{L_p \mu q B}{A_p} + 9.1 \cdot 10^{-13} \beta_{nv} L_p \rho_f \left( \frac{qB}{A_p} \right)^2 \quad 8-37$$

where:

$L_p$  = length of perforation (inch)

$\mu$  = dynamic viscosity (cP)

$\rho_f$  = fluid density (g/cm<sup>3</sup>)

$q$  = production or flow rate (cm<sup>3</sup>/s)

$k$  = permeability (Darcy)

$A_p$  = Flow area of perforation tunnel (inch<sup>2</sup>)

$\beta_{hv}$  = high velocity coefficient

B = formation volume factor

The first term on the right of equation 8-37 represents the pressure drop due to Darcy flow and the second term represents the additional pressure drop due to high velocity flow<sup>173</sup>.

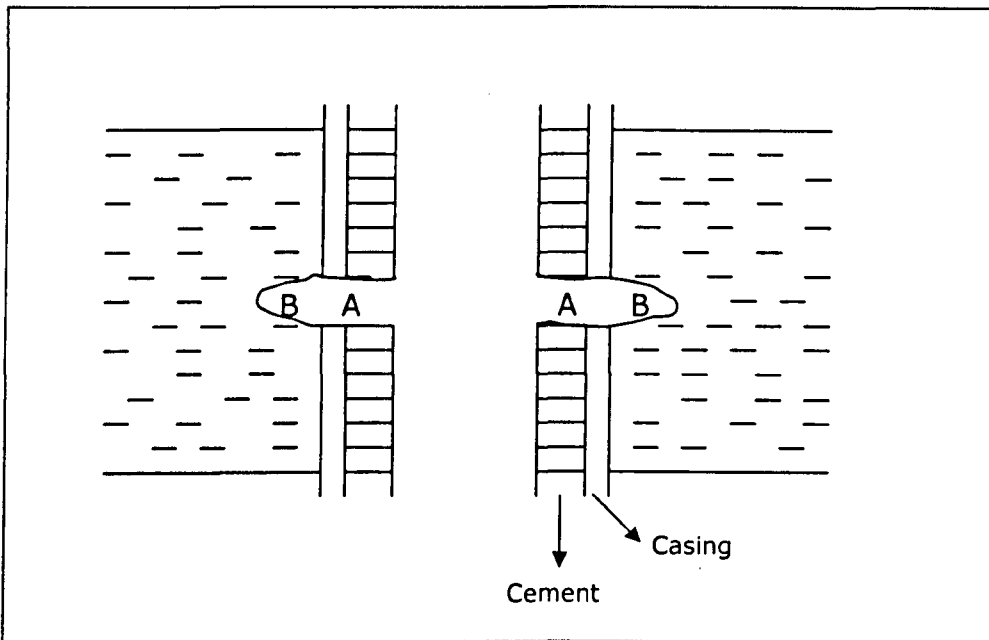


**Figure 8-15 Perforation completion schematic (after Samsuri et al 2003<sup>16</sup>)**

The high velocity coefficient  $\beta_{hv}$  can be estimated from Brown (1984)<sup>175</sup> correlation, which gives it as a function of permeability:

$$\beta_{hv} = \frac{1.47 \cdot 10^7}{k^{0.55}} \quad 8-38$$

Where permeability  $k$  is in md unit.

The pressure drop in the perforation section within the reservoir (point B) is the most critical and has the greatest impact on the predictions of

critical drawdown pressure from the CDD model. The effect of the pressure drawdown within the casing-cement section (point A) may be assumed to impact the casing and cement stability only and not propagated to the reservoir region.

If it is assumed that the flow from B to A within the perforation is linear and that there is negligible or no pressure loss as the fluid flows from B to A, then the fluid flow pressures in the two areas are equal. Equation 8-37 can therefore be modified to consider number of perforation shots per foot (SPF) and used to estimate the pressure drop in the area around point B. Figure 8-16 shows the effect of both perforation length and area on the pressure drop around perforation.

$$\Delta p_B = \left[ 0.888 \frac{L_p \mu q B}{kA} + 9.1 \cdot 10^{-13} \beta_{nv} L_p \rho \left( \frac{qB}{A} \right)^2 \right] * \frac{1}{SPF} \quad 8-39$$

Where SPF is the number of perforation shots per foot.

The corrected critical pressure drawdown at failure for a perforated completion can therefore be given as

$$CDD_c = (CDD_i - \Delta P_B) - (P_{ri} - P_{rc}) \quad 8-40$$

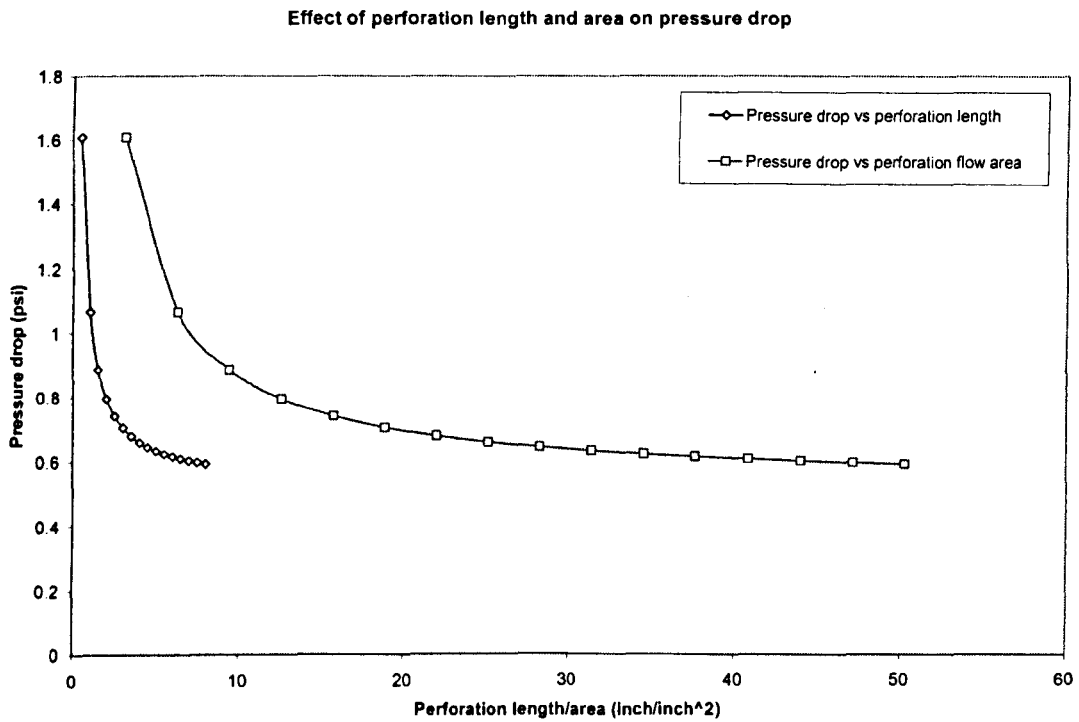


**Figure 8-16 Effect of perforation length and area on pressure drop**

### 8.4.2 Open-Hole Completion

In open-hole completion the pay zone is left bare with no casing strings across it; the casing shoes are set on top of the pay zone. Open-hole completion is commonly used for much consolidated reservoir rock, which has little or no risk of sand production<sup>167</sup>.

Assuming there is no damage skin around the bare open hole, which may cause additional pressure drop near wellbore, the predicted critical pressure drop from the CDD model is not expected to change. The critical drawdown pressure at failure for open hole can therefore be written as:

$$CDD_c = (CDD_i - \Delta P_{OH}) - (P_{ri} - P_{rc}) \quad 8-41$$

where  $\Delta P_{OH} = 0$

### 8.4.3 Gravel Pack Completion

Gravel packs are a sand control method used to prevent the flow of sand into the wellbore during production and yet allows rapid unhindered flow of hydrocarbon into it. Gravel packs consist of either screens or slotted/perforated liners placed in the wellbore region opposite the pay zones; and specially designed high permeability gravel sizes mixed in a carrier fluid placed in the annulus between the screens or slotted/perforated liners and the formation sands (figure 8-17).

In gravel packs, pressure drops are expected to occur within the gravel pack bodies and in the screens or slotted or perforated liners as the production fluids move towards the wellbore. These pressure drops are represented by  $\Delta P_g$  and  $\Delta P_s$ , respectively.

The pressure drop within the gravel pack bodies can be estimated using Forchheimer's equation. This equation has a track record of success in its application for the prediction of pressure drops in granular porous media<sup>176-179</sup>. It is expressed mathematically as:

$$\Delta P_g = \frac{L_g \mu q}{k_1 A_g} + \frac{L_g \rho_f}{k_2} \left( \frac{q}{A_g} \right)^2 \quad 8-42$$

Where:

$L_g$  = length or thickness of gravel pack (ft)

$\mu$  = dynamic viscosity of fluid (cP)

$\rho_f$  = density of fluid (g/cm<sup>3</sup>)

$q$  = production or flow rate (cm<sup>3</sup>/s)

$k_1$  &  $k_2$  = Darcy and non Darcy permeabilities

$A_g$  = Flow area of gravel pack (ft<sup>2</sup>)

Darcy and non-Darcy permeabilities can be estimated from porosity and mean or median particle size<sup>176-179</sup>.

$$k_1 = \frac{\phi_r^3 * d_r^2}{150(1 - \phi_r)^2} \quad 8-43$$

$$k_2 = \frac{\phi_r^3 * d_r}{1.75(1 - \phi_r)} \quad 8-44$$

Where  $\phi_r$  is gravel porosity and  $d_g$ , the gravel mean or median particle size.

The pressure drop across the screen openings, assuming they are circular, can be approximated with the pressure drop in a fluid flowing through a straight cylindrical pipe. The pressure drop through a straight cylindrical pipe can be estimated using Darcy-Weisbach equation<sup>177-178</sup>. Applying this to the pressure drop scenario during flow through the screen slot openings, the equation can be written as

$$\Delta P_s = f \frac{\rho_f}{2d_s} * \left( \frac{q}{A_s} \right)^2 \quad 8-45$$

Where  $f$  frictional factor;  $\rho_f$ , the fluid density;  $d_s$ , the internal diameter of screen slot opening;  $q$ , the flow rate and  $A_s$  the area of screen opening.

The frictional factor for both laminar and turbulent flows are given respectively<sup>180</sup> as:

$$f = \frac{Re}{64} \quad 8-46$$

and

$$\frac{1}{\sqrt{f}} = -1.8 \times \log \left[ \left( \frac{6.9}{\text{Re}} \right) + \left( \frac{K_{rd}}{3.7} \right)^{1.11} \right] \quad 8-47$$

Where Re is Reynold's number;  $K_{rd}$  is the ratio of screen opening inner roughness to screen slot opening inner diameter and is given by equation 8-48. Table (8-9)<sup>181</sup> gives the typical average roughness of commercial pipes of different materials.

$$K_{rd} = \frac{\varepsilon_s}{d_s} \quad 8-48$$

Where  $\varepsilon_s$  is the screen opening inner roughness and  $d_s$  the screen opening inner diameter.

Renold's number is a dimensionless factor given by

$$\text{Re} = \frac{\rho v d_s}{\mu} \quad 8-49$$

Assuming n number of same-size screen openings, the total pressure drop through the entire screen openings will be indirectly proportional to the number of slot openings per unit length of the screen, referred to as density of openings,  $d_o$  (1/cm) and is given by:

$$\Delta P_s = \left[ f \frac{\rho_f}{2d_s} \left( \frac{q}{A_s} \right)^2 \right] \frac{1}{d_o} \quad 8-50$$

Where  $d_o$  is the density of slot openings or number of slot openings per unit length of the screen

The total pressure drop through the gravel pack completions can therefore be approximated by:

$$\Delta p_{gc} = \Delta p_g + \Delta p_s \quad 8-51$$

Figure 8-18 shows the pressure drop versus area of screen slot openings in a typical gravel pack completion.

Incorporating this into the CDD model to account for the effect of gravel pack completions, a new equation can be written.

$$CDD_c = (CDD_i - \Delta P_{gc}) - (P_{ri} - P_{rc}) \quad 8-52$$

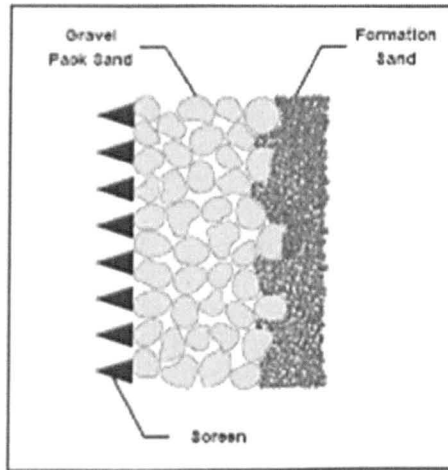


**Figure 8-17 A cross section of gravel pack completion (The Robert Gordon University, 2003<sup>181</sup>)**

<b>Table 8-9<sup>181</sup> Average inner roughness of commercial pipe</b>		
No	Pipe material	Average inner roughness
1	Steel tube	0.0460
2	Copper	0.0015
3	Glass tubing	0.0001
4	Polythene	0.0010
5	Flexible P.V.C	0.2000
6	Rigid P.V.C	0.0050
7	Cast iron tube	0.2600

Pressure drop versus area of screen slot openings

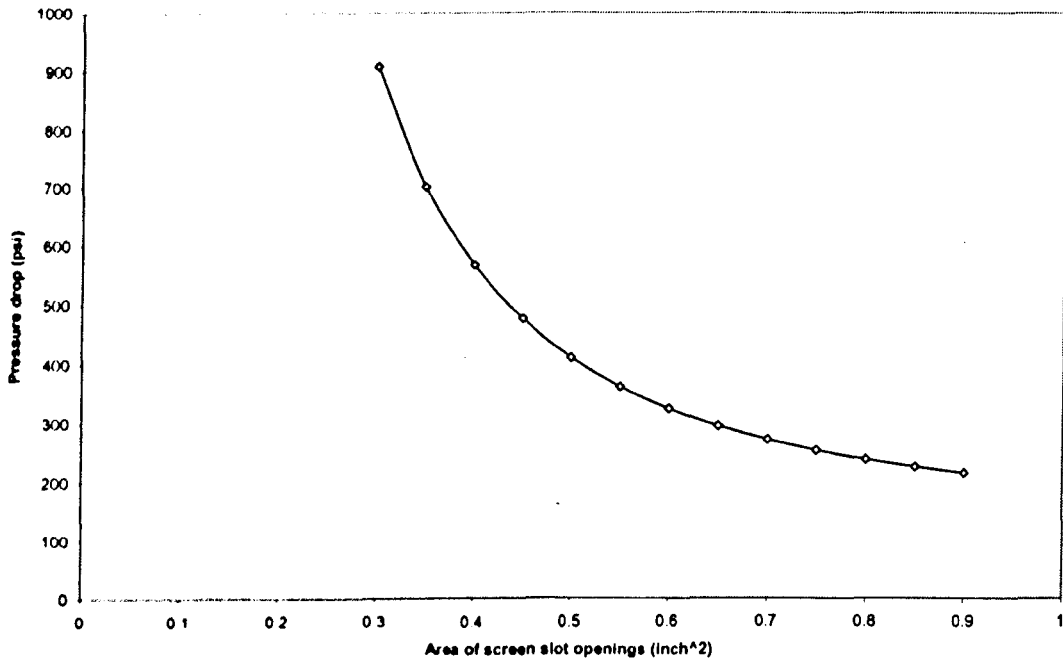


Figure 8-18 Pressure drop versus area of screen slot openings

---

## 8.5 Further validation of Critical Drawdown (CDD) model

Limited data sets from a Middle East field taken from different sand sequences at varying depth from ten different wells have been used to validate the CDD models (see Table 8-10 for details of the well data). The data sets represent geomechanical information on different sand sequences encountered in different wells. For the sand sequences encountered in multiple wells such as I\_25, II\_20 and II\_30, their geomechanical data and depth of occurrence are very close in all the wells in which they are encountered as shown in Table 8-10. It is therefore assumed that the petrophysical properties for each of the sand sequences in different wells will be the same. In addition they are expected to exhibit similar behaviours under the same drawdown regime.

The validation was done in such a way to account for all the sand sequences occurring in the field. Sand sequences such as II\_20, II\_30 and I\_25 that are encountered in multiples wells were randomly selected from only one well. The results of the validation for all the sand sequences are shown in Table 8-11. The results show that the models predictions for sand sequences I\_25, II\_20 and II\_30 are in agreement with the field measured maximum critical drawdown whilst the predictions for sand sequence I\_20 is of the order of 3 less than the field measured maximum drawdown. Real time predictions of Critical Drawdown (CDD) for a nine-year period have also been carried out for sand sequences I\_25, II\_20 and II\_30 as shown in Figures 8-19 to 8-21. A depletion rate of 72psi per year was assumed for all the wells

**Table 8-10 Well Data for CDD model validation**

Well ID	Top Depth (ft)	Base Depth (ft)	Reservoir Thickness (ft)	Sand Sequence	Vertical Stress (psi)	Min Horizontal Stress	Max Horizontal Stress	Initial Reservoir Pressure (psi)	Current Reservoir Pressure (psi)	UCS (psi)	Max CDD (psi)
Cak-A8	5779	5809	30	I_25	3411	2650	2730	1797	1593	1926	145
Cak-A4	5565	5595	30	II_20	3593	2767	2851	1828	1618	1926	364
Cak-A13	5788	5818	30	II_20	3618	2774	2858	1811	1668	1926	151
Cak-B1	5430	5500	70	II_20	3561	2725	2807	1775	1723	1926	448
Cak-B2	6888	6908	20	II_30	3565	2731	2813	1783	1712	1926	505
Cak-B3	6078	6140	62	I_20	3327	2587	2664	1762	1643	1926	718
Cak-B4	4451	4478	27	II_30	3564	2729	2811	1779	1710	1926	287
Cak-B5	5186	5218	32	I_25	3304	2571	2648	1756	1579	1926	932
Cak-A7	5424	5454	30	I_25	3421	2658	2737	1800	1460	1926	360
Cak-A12	5690	5728	38	I_25	3425	2658	2738	1797	1472	1926	647
Cak-A8	5779	5809	30	I_25	3411	2650	2730	1797	1593	1926	145

**Table 8-11 Predicted CDD versus measured CDD for a Middle East field**

Well ID	Sand sequence	Predicted CDD (psi)	Originally predicted CDD (psi)
Cak-A8	I_25	144	145
Cak-B1	II_20	448	478
Cak-B2	II_30	443	505
Cak-B3	I_20	288	718

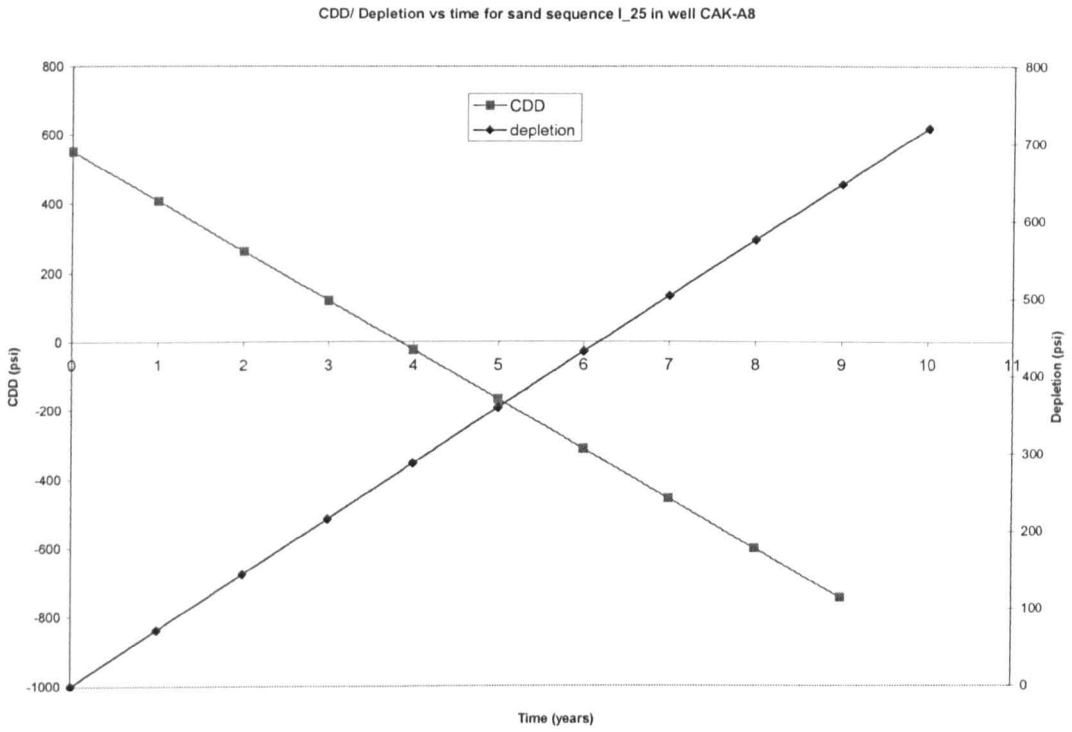


**Figure 8-19 CDD/Depletion vs time for sand sequence I\_25 in well CAK-A8**

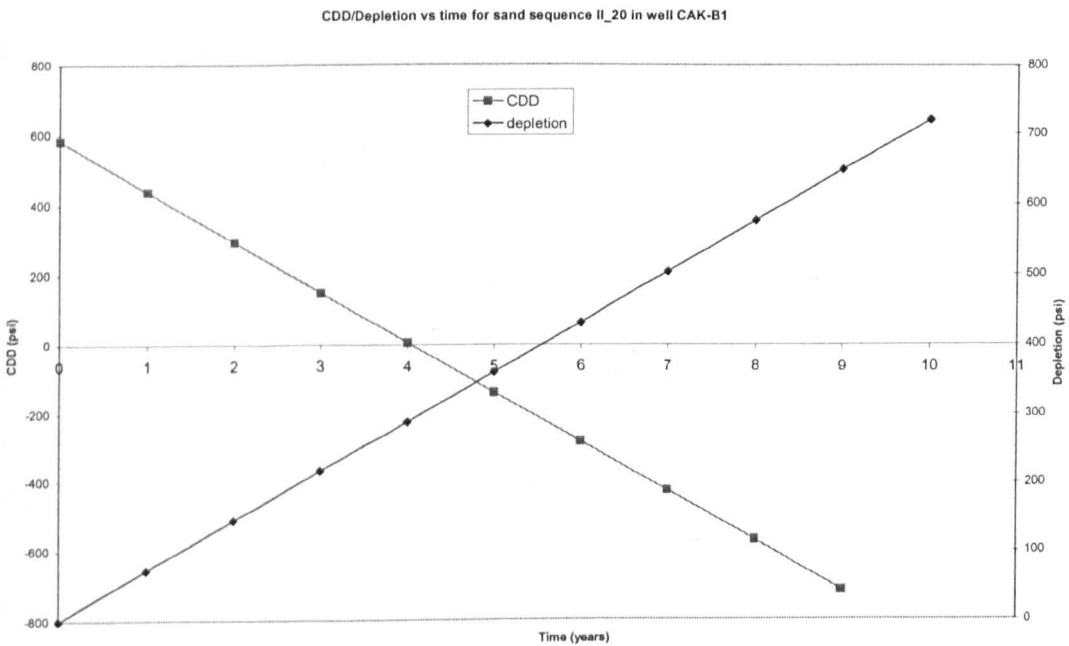


**Figure 8-20 CDD/Depletion vs time for sand sequence II\_20 in well CAK-B1**

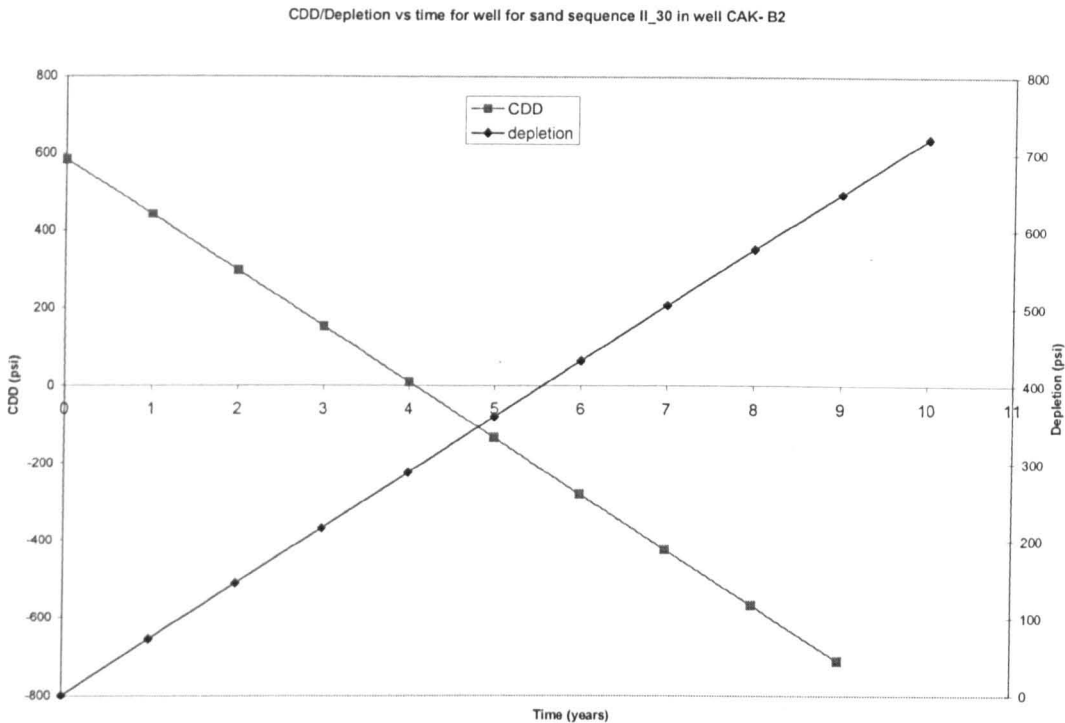


**Figure 8-21 CDD/Depletion vs time for sand sequence II\_30 in well CAK-B2**

### 8.6 Real time sand volume and rate quantification

Sand is deemed to have failed when the critical drawdown predicted by the CDD model is exceeded. For sand to be produced, the failed sand must be fluidized and transported through the sandface to the wellbore. At fluidisation, the failed sands are detached from the formation and begin to move; the fluid velocity then helps to drag them towards the wellbore. The flow rate at which the sands become detached and begin to move is referred to as the yield flow rate whilst the fluid velocity at which the drag is enough to move them towards the wellbore is referred to as the critical flow velocity. However the quantity of sand produced from a reservoir formation is largely dependent on the two parameters described above and of course the formation grain volume.

The approach to sand volume and rate quantification used in this work assumes that all the processes described above contribute to the volume

of produced sand. All the processes are therefore fully described mathematically in the following sections and fully integrated into the sand quantification model.

### 8.6.1 Equation for yield flow rate and fluid velocity

The solution of Darcy equation for radial flow from the reservoir into the well in terms of pressure is given as<sup>169</sup>:

$$P_r - P_{wr} = \frac{q\mu * \left( \ln \frac{r_e}{r_w} \right)}{2\pi hk} \quad 8-53$$

Where  $p_r$  is the reservoir pressure in psi;  $p_{wr}$  the wellbore flowing pressure in psi;  $q$  is the flow rate in  $\text{cm}^3/\text{s}$ ,  $\mu$  is the viscosity in cP;  $k$  is the permeability in Darcy; and  $h$  is the reservoir thickness in cm;  $r_e$  is the drainage radius in cm and  $r_w$  the wellbore radius in cm.

The term  $(p_r - p_{wr})$  is assumed to be the sand free pressure drawdown ( $P_{DD}$ ) at which the well is flowing to be able to produce oil at no risk of failure or sand production. This equation can therefore be re-written as:

$$P_{DD} = \frac{q\mu * \left( \ln \frac{r_e}{r_w} \right)}{2\pi hk} \quad 8-54$$

If the sand free drawdown is increased to produce more oil to a point where the reservoir pressure cannot tolerate any further drawdown and bottom hole flowing pressure,  $p_{wr}$  reaches the critical value called the critical well flowing pressure, then the term  $(p_r - p_{wr})$  changes to  $(p_r - p_{cwr})$ , where subscript  $c_{wr}$  represents critical well flowing pressure. This new drawdown is equivalent to the the Critical Drawdown pressure (CDD). Equation (8-54) may therefore be written as:

$$CDD = \frac{q_y \mu * \left( \ln \frac{r_e}{r_d} \right)}{2\pi h k} \quad 8-55$$

Where  $q_y$  is the sand yield flow rate. In this drawdown pressure condition, the failed sand grains within the reservoir may become mobilised in the flowing fluid ready to come to the surface.

From equation (8-55), we obtain an equation for the yield flow rate as

$$q_y = \frac{2\pi h k * CDD}{\mu * \left( \ln \frac{r_e}{r_w} \right)} \quad 8-56$$

The critical velocity within the wellbore at which the sand begins to move to the surface can be obtained as:

$$V_{cp} = \frac{q_v}{A_{pore}} \quad 8-57$$

Where  $A_{pore}$  is the area of pore and is estimated by  $(\pi d_{por}^2 / 4)$ .

The Blake-Kozeny equation (equation 8-58) can be used to estimate  $d_{pore}$ .

$$d_{pore} = \frac{d_{s0} \phi}{3(1 - \phi)} \quad 8-58$$

Where  $d_{50}$  is median grain size, and  $\phi$  is porosity.

### 8.6.1.1 Sensitivity of yield flow rate to permeability and viscosity

Sensitivity studies have been conducted to investigate the sensitivity of the yield flow rate to permeability and viscosity. Figure 8-22 is a plot of yield flow rate versus permeability. The plot suggests a direct linear relationship between permeability and yield flow rate. These results in essence suggest that yield flow rate will increase with increase in permeability. This is not unexpected in porous systems where low permeability may lead to a large restriction to flow and hence a large pressure gradient across the flow system. This phenomenon has a potential to aggravate the sand failure process leading to sand mobilisation and production. However the relationship shown in Figure 8-23 between yield flow rate and viscosity shows a totally different pattern. At low viscosity ( $< 1$ ), the yield flow rate is highly sensitive to viscosity whilst at high viscosity ( $> 1$ ), the yield flow rate shows little or no sensitivity to viscosity.

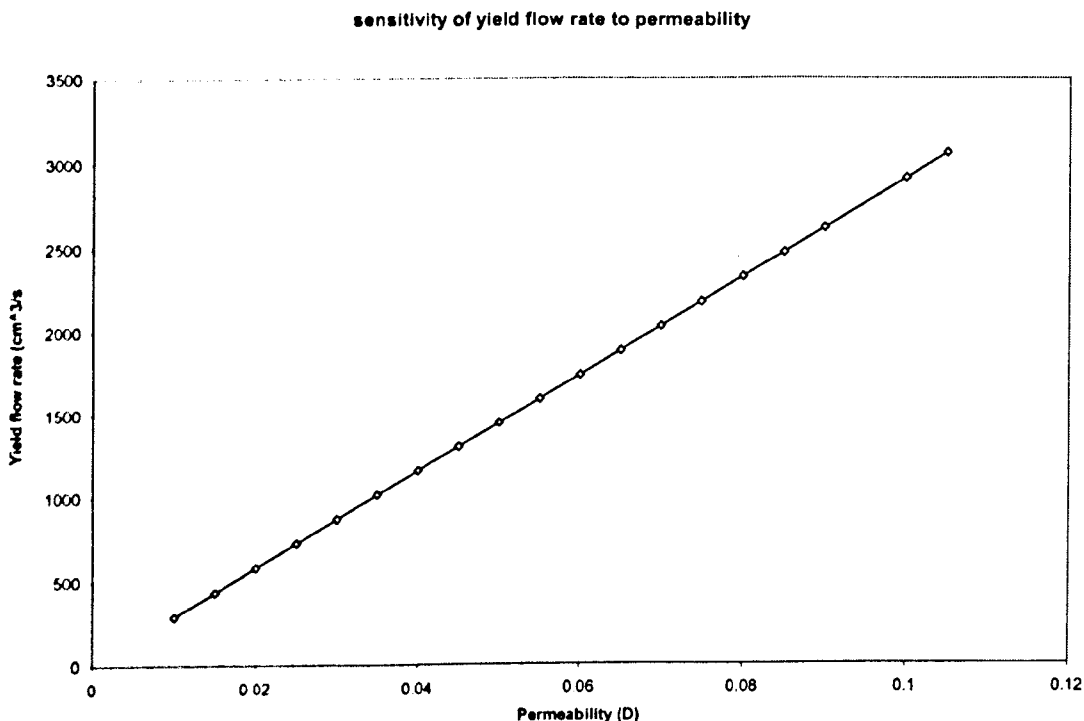


**Figure 8-22 Sensitivity of yield flow rate to permeability**

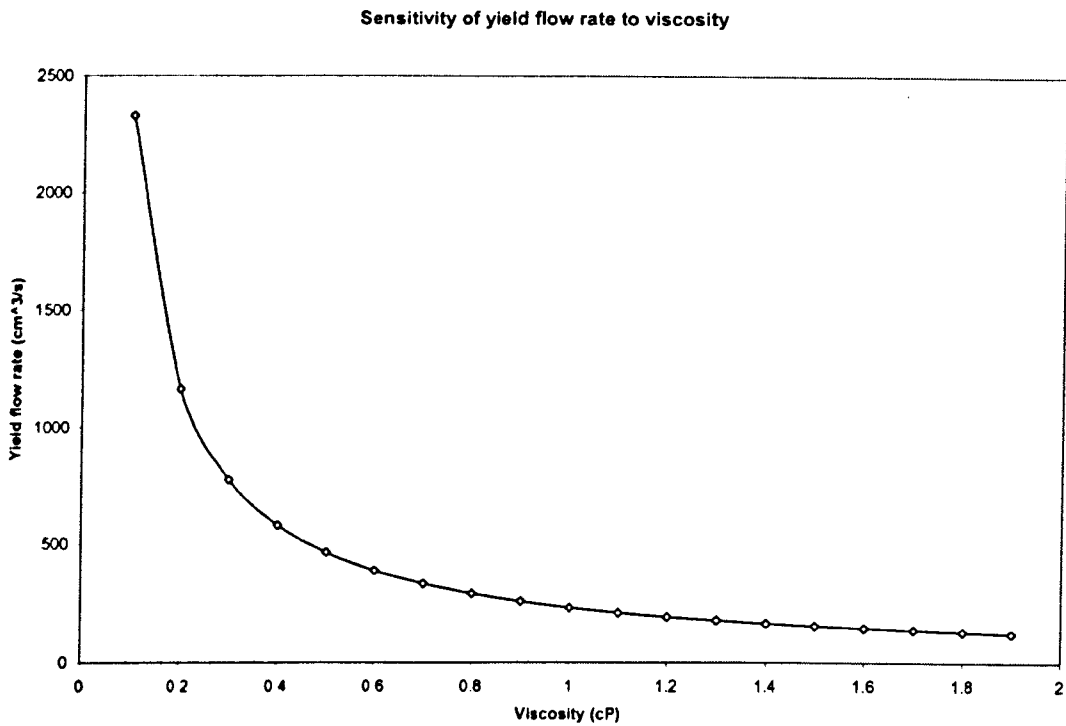


**Figure 8-23 Sensitivity of yield flow rate to viscosity of flowing fluid**

### 8.6.1.2 Validation of yield flow rate

Data from four wells in a North Sea field have been used to validate the yield flow rate model. The model has been used to estimate the yield flow rates from the four wells. The results obtained as shown in Table 8-12 compare very well with the actual flow rates to sand production in all the three wells.

To further validate the model, the sensitivity of the yield flow rate to critical drawdown (CDD) has been investigated. The data from three wells (well 1, 2 and 3) have been used for this purpose. For each well, an assumed range of critical drawdown (20atm to 200atm) was used and corresponding yield flow rate calculated. Figure 8-24 shows the response pattern of yield flow rate to critical drawdown (CDD) for well 1, 2 and 3.

From the figure, change in well 3 yield flow rate at varying CDD is more noticeable whilst well 1 yield flow rate shows the least sensitivity.

In general, the response pattern shown in Figure 8-24 suggests that at higher CDD, the yield flow rate is also high. This is consistent with expectation as rock formations which exhibit higher CDD would be expected to support high sand free production rate in comparison to formations with lower CDD.

Property	Well 1	Well 2	Well 3	Well 4	Unit
Reservoir thickness	600	700	800	1000	cm
Well radius	10	10	10	10	cm
Reservoir drainage radius	8000	7000	6500	6000	cm
Absolute permeability	0.01	0.02	0.015	0.01	D
Oil viscosity	2	2	2	2	cP
CDD	102	120	145	275	atm
Flow rate at sand production	678	1000	988	1300	cm <sup>3</sup> /s
Yield flow rate (predicted)	287.6	805.6	843.9	1350.5	cm <sup>3</sup> /s

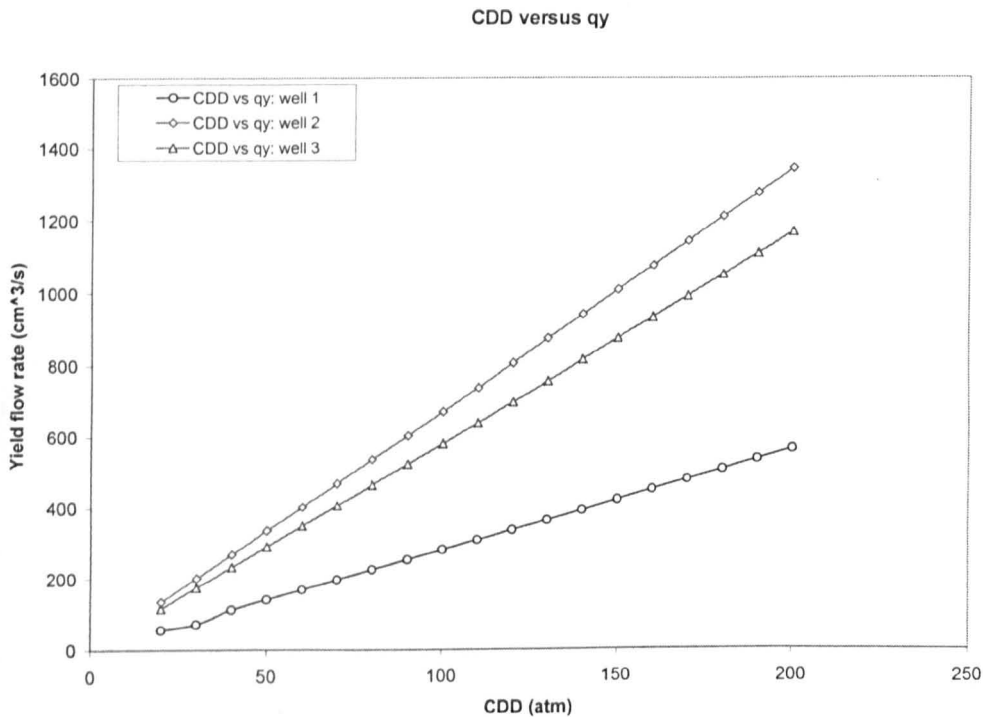


**Figure 8-24 Comparison of change in yield flow rate at varying critical drawdown (CDD)**

### 8.6.2 Estimation of detached/produced sand volume

The standard equation for calculating porosity in the oil and gas industry is given as:

$$\phi = \frac{V_b - V_p}{V_b} \quad 8-59$$

Where  $V_b$  is the reservoir formation bulk volume and  $V_p$  is grain particle volume

If equation (8-59) is transposed, it can be used to compute the volume of grain in the reservoir formation. An equation for the initial grain particle volume at times  $t=0$  when no sand production has taken place within the reservoir can therefore be written as:

$$V_{pi} = V_b [1 - \phi_i] \quad 8-60$$

Where  $V_{pi}$  is the initial volume of grain particle and  $\phi_i$  is initial porosity at time  $t=0$ .

A similar equation for the final grain particle volume at time  $t > 0$  when the reservoir is already producing sand can also be written.

$$V_{pf} = V_b [1 - \phi_f] \quad 8-61$$

Where  $V_{pf}$  is the final volume of grain particle and  $\phi_f$  is the final porosity at time  $t > 0$ .

The volume of sand producible from any reservoir at any time  $t=n$  is the volume differential between the final and initial grain particle volumes; this is written as:

$$V_{pp} = V_{pi} - V_{pf} \quad 8-62$$

Substituting equations 8-60 and 8-61 in equation 8-62, we have:

$$V_{pp} = [V_b(1 - \phi_i) - V_b(1 - \phi_f)] \quad 8-63$$

Solution of equation (8-63) will yield

$$V_{pp} = [V_b(\phi_f - \phi_i)] \quad 8-64$$

However, the reservoir is in a constant state of stress, which changes with time throughout its production life; this stress is expected to affect both the reservoir matrix and pore volumes, and by extension, porosity. Assuming however that the rock matrix is incompressible, the effect of stress on the pore volume or porosity can be captured by pore volume compressibility<sup>182-183</sup>. The initial and final porosities can therefore be written to account for this.

$$\phi_i = \phi_i * C_{pi} \quad 8-65$$

$$\phi_f = \phi_f * C_{pf} \quad 8-66$$

Where  $C_{pi}$  and  $C_{pf}$  are the initial and final rock pore volume compressibility.

Substitution of equations (8-65) and (8-66) in equation 8-64 will give:

$$V_{pp} = [V_b (\phi_f C_{pf} - \phi_i C_{pi})]$$

8-67

### 8.6.3 Sand volume and rate prediction models

#### 8.6.3.1 Sand volume prediction model

The methodology for sand volume prediction model involved acquisition of field and experimental sand production data from the major petroleum provinces of the world and plotting their scatter plots. Linear models were then fitted into all the data to obtain linear models of the form given in equation 8-70.

Figures 8-25 to 8-28 are the scatter plots obtained for the sand production data used in this study. The correlation coefficients obtained for all the plots are approximately 100%.

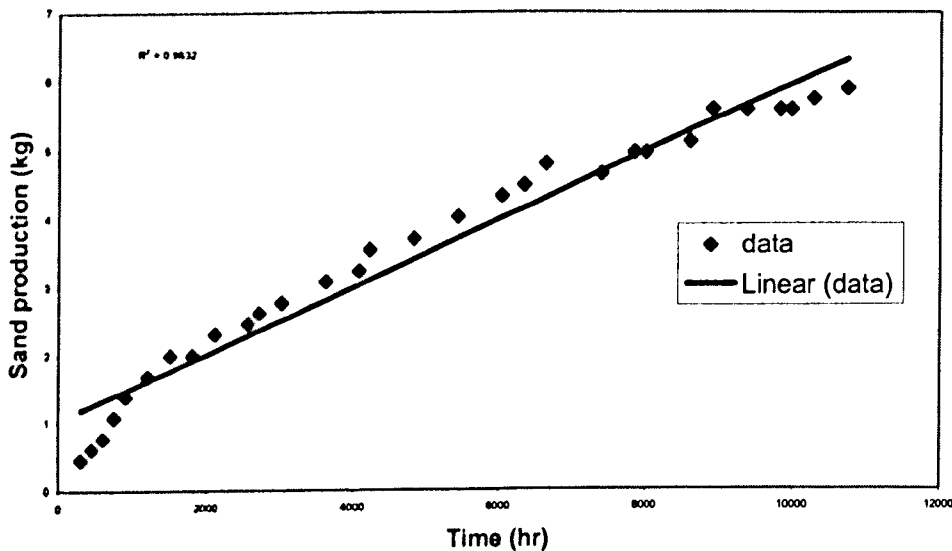


Figure 8-25 Plot of sand production versus time (North Sea data)

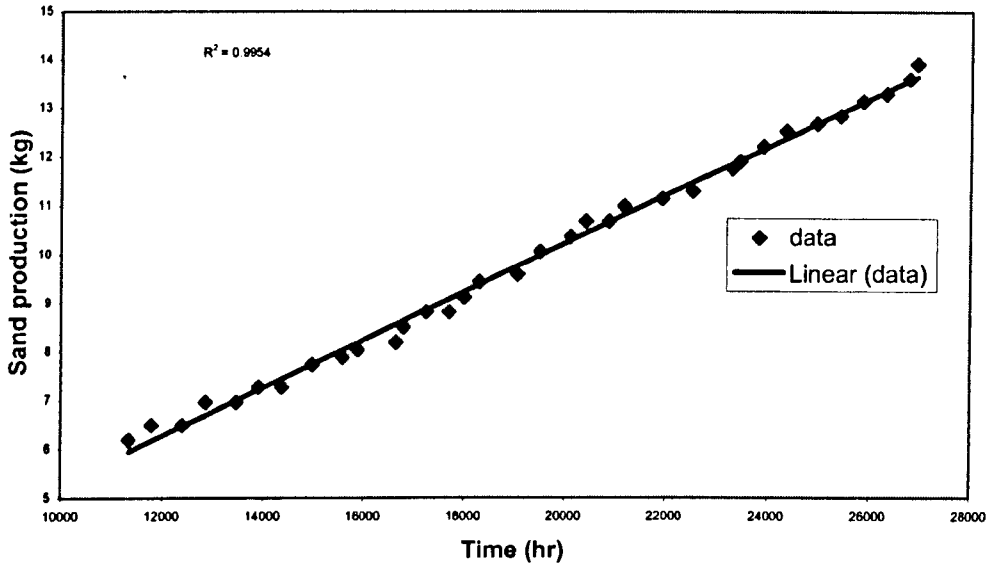


Figure 8-26 Plot of sand production versus time (Niger Delta data)

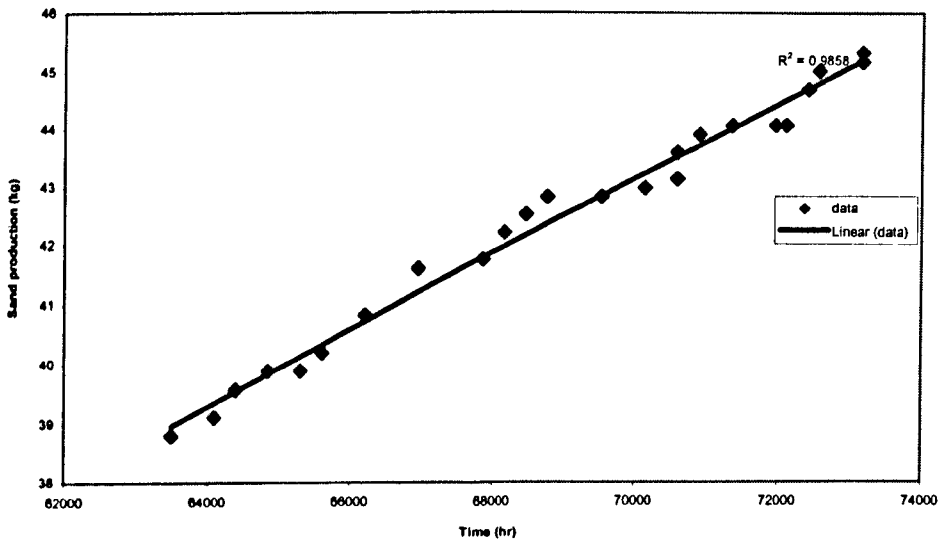
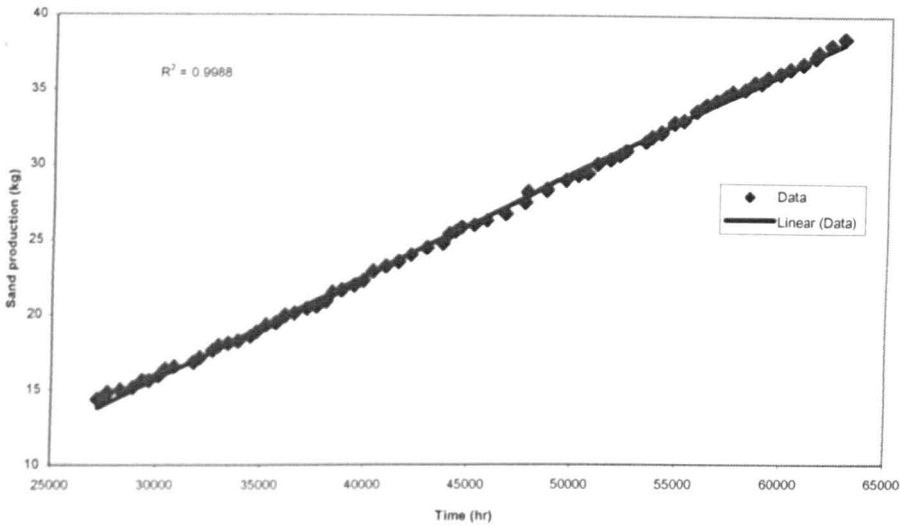


Figure 8-27 Plot of sand production versus time (Gulf of Mexico)



**Figure 8-28 Plot of sand production versus time (experimental data)**

If it is assumed that the data plotted in Figures 8-25 – 8-28 generally replicate the relationship between volume of sand production and time, then the volume of sand produced from any reservoir with time can be approximated by the linear model obtained from the data:

$$V_s = m_s t + c \quad 8-68$$

Where  $V_s$  is the volume produced from the reservoir;  $m_s$  is a constant and is dependent on the critical fluid velocity, the producible/detached reservoir sand grain volume and the producing interval;  $c$  is also a constant and is the initial volume of produced sand as a result of opening the choke for production for the first time.

Assuming there is no initial sand production when the chokes are opened for production, then  $c = 0$ ; equation. (8-68) can be re-written to take account of this:

$$V_s = m_s t \quad 8-69$$

Since  $m_s$  is a function of the critical fluid velocity, the producible/detached reservoir sand grain volume and the producing interval, equation (8-69) can be written to account for all these parameters.

$$V_s = \frac{[(V_b(\phi_f C_{pf} - \phi_i C_{pi})) \times V_{cp} \times t]}{L} \quad 8-70$$

Where L is length of production interval; other model parameters have been given in Sections 8.6.1 and 8.6.2.  $V_{cp}$  is the critical flow velocity at which failed and detached grain particles begin to move towards the wellbore. The equation for estimating it has been derived and presented in equation 8-57. It is also linked to the neural network predicted median grain size by the Blake-Kozeny equation (equation 8-58).

### 8.6.3.2 Rate of sand production model

The rate of sand production is the amount or volume of sand produced per unit time. This is expressed mathematically as:

$$R_s = \frac{V_s}{t} \quad 8-71$$

If equation (8-71) is differentiated with respect to t, we obtain a rate equation:

$$\frac{dV_s}{dt} = \frac{[(V_b(\phi_f C_{pf} - \phi_i C_{pi})) \times V_{cp}]}{L} \quad 8-72$$

The rate of sand production is therefore given as:

$$R_s = \frac{dV_s}{dt} = \frac{[(V_b(\phi_f C_{pf} - \phi_i C_{pi})) \times V_{cp}]}{L} \quad 8-73$$

## 8.7 Sand volume and rate model testing

A North Sea field data taken from two wells (Table 8-13) with different reservoir properties have been used to test the sand volume and rate model. The following assumptions were made in order to use the data:

- (a) Porosity was assumed to increase for the two reservoirs at a rate of 1% per sand production year
- (b) The critical particle velocities for the two reservoirs were assumed

Figures 8-29 and 8-30 show the results of the testing. The actual field sand production data from the fields were not available so it was not possible to compare the predictions with the field sand production data. However predictions from the model as shown in Figures 8-16 and 8-17 seem realistic.

Table 8-13 North Sea well data		
Reservoir property	Well I	Well I
Reservoir volume (ft <sup>3</sup> )	62831	60318
Pore volume compressibility (psi <sup>-1</sup> )	10 <sup>-6</sup>	10 <sup>-6</sup>
Reservoir thickness (ft)	20	15
Porosity	0.3	0.3

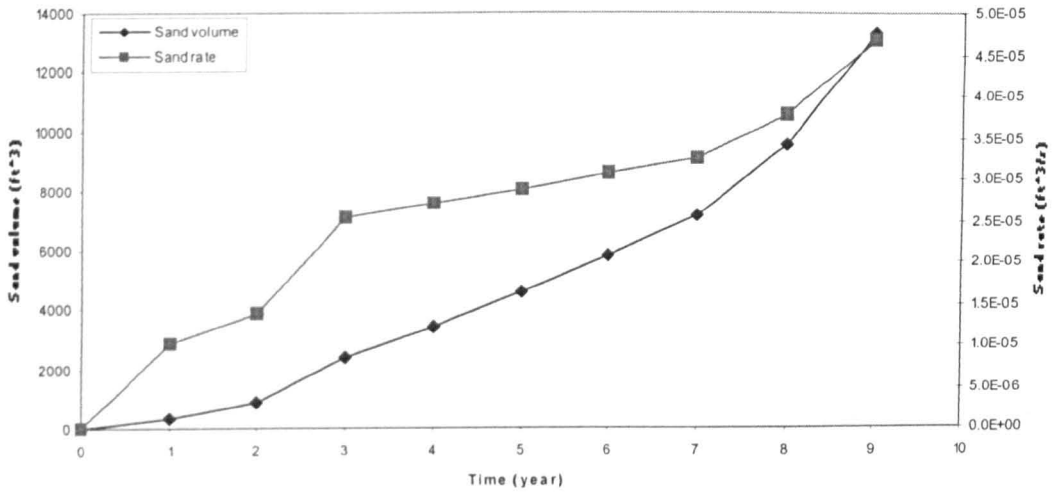


Figure 8-29 sand volume and rate predictions from well I.

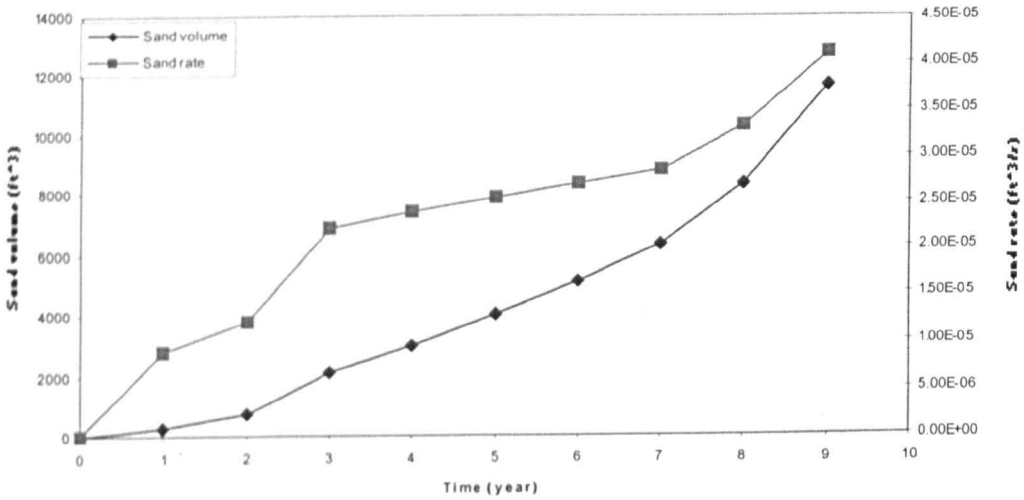


Figure 8-30 sand volume and rate predictions from well II

## 8.8 Summary

In this chapter the following deliverables have been achieved:

- Real time sanding potential prediction model has been developed. The model is an amalgamation of several sub-models such as the Critical Drawdown (CDD) model, for predicting the onset of sand failure or sand production; the yield flow rate model, for predicting the critical flow rate that causes sand detachment from the parent reservoir sand after failure; the critical particle velocity model, for predicting the flow velocity at which sands begin to move towards the well-bore; and sand volume and rate model, for predicting the amount of sand that will be produced at any given time during the well/reservoir life cycle. The Critical Drawdown (CDD) model is however the key model and the starting point of the sanding potential prediction model. These sub-models have been tested and validated individually and collectively as a single sanding potential prediction model.
- Hoek and Brown failure criterion has been adopted and used to develop the Critical Drawdown (CDD) model based on well-defined and widely tested criteria of its non-linearity and ability to model both failed and intact rocks as opposed to other failure criteria in use in the oil and gas industry.
- Simple mathematical and analytical methods have been used in developing the models developed and reported in this work; this makes them simple to use as opposed to complex numerical models. Solution of quadratic equation has been used specifically for the formulation of the Critical Drawdown model.
- The sanding potential prediction model considers the effect of water breakthrough and completion type on the sand failure and production. The Critical Drawdown (CCD) model, a sub-model of the sand prediction model, can be used for both oil and gas field/reservoir.

## Chapter 9

### Field analysis package

The models developed in this work have been packaged into field analysis tools to be used for analysing sand production related problems in the field. The field analysis package reported in this chapter are the Grain Size Distribution (GSD) package, which predicts the grain size distribution of reservoir formation; and the Critical Drawdown (CDD) package, which predicts the critical drawdown at which failure will occur and the yield flow rate that will trigger sand production. The GSD is based on the neural network and analytical models reported in chapter six whilst the CDD package is based on the neural network model for UCS and the Critical Drawdown model. The two packages are built using Microsoft Excel platform.

#### 9.1 Critical Drawdown (CDD) package

The critical drawdown package is based on the CDD model and can be used to predict the Critical Drawdown (CDD) which would trigger formation failure, the Yield Flow Rate at which the failed sands become fluidised and begin to move towards the wellbore and the critical particle velocity at which the failed mobile sands are travelling.

The critical drawdown package is divided into three modules. The three modules are listed thus:

- The Input module
- The Gravel pack completion results module
- The perforation completion results module

##### 9.1.1 The Input module

The Input module consists of two sections, one each for the gravel pack and the perforation completions (Figure (9-1)). It also allows the user to

input identity information about the field or well. The input data to the predictor may be obtained from conventional log, LWD/MWD, PLT and or field correlations. The symbols used for the input parameters in the Input module are given in Table 9-1.

**Table 9-1 Input parameters' symbol in CDD package**

Parameters	Gravel Completion
$\sigma_H$	Maximum horizontal stress
$\sigma_h$	Minimum horizontal stress
$P_{ri}$	Initial reservoir pressure
$P_{rc}$	Current reservoir pressure
n	Hettema constant
UCS	Unconfined Compressive Strength
m	Hoek-Brown constant
s	Hoek-brown constant
DD	Pressure drawdown
k	Permeability
h	Reservoir thickness
$\mu$	Fluid viscosity
$r_e$	Reservoir drainage radius
$r_w$	Wellbore radius
$\rho_f$	Fluid density
$d_s$	Diameter of screen opening
$d_o$	Density of screen opening
$A_s$	Area of screen opening
q	Flow rate
$L_g$	Length of gravel pack
$A_g$	Area of gravel pack
$d_g$	Gravel median grain size
$\phi_g$	Gravel porosity
$\phi$	Formation porosity
$d_{50}$	Formation median grain size
$A_p$	Area of perforation
B	Formation volume factor
$L_p$	Length of perforation
SPF	Shot Per Foot

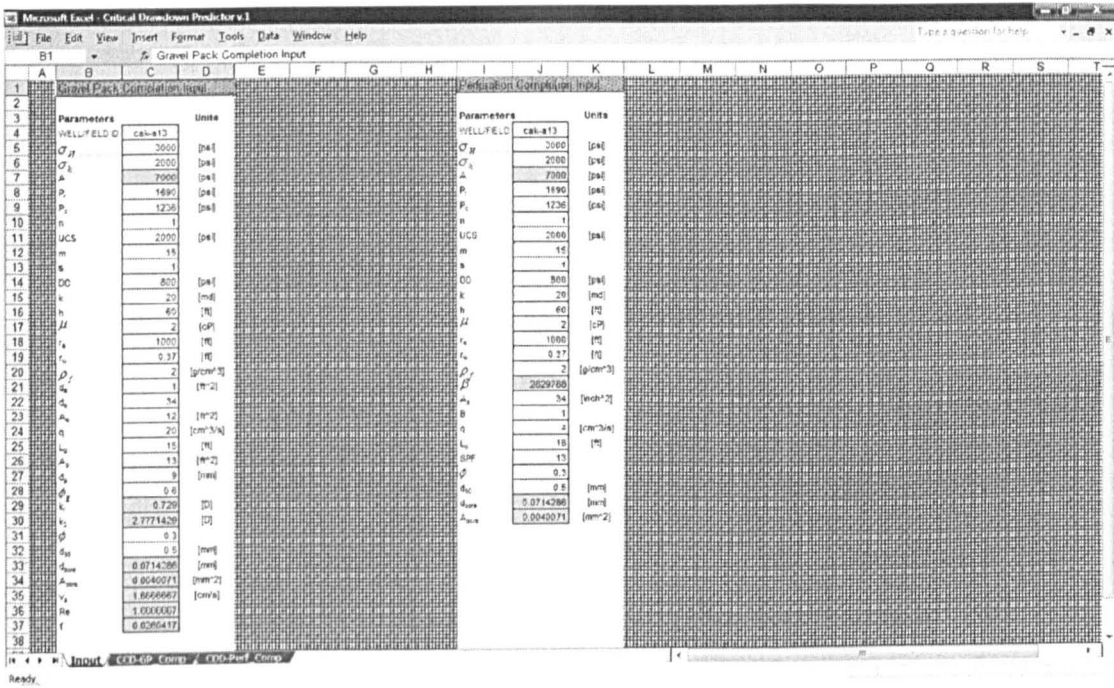


Figure 9-1 Screen shot of CDD input module

### 9.1.2 The gravel pack completion results module (GP\_Comp)

This module allows the display of the Critical Drawdown results for a gravel pack completion. The results for three important sanding production parameters – the Critical Drawdown (CDD), the Yield Flow Rate ( $q_y$ ) the Critical Particle Velocity - are displayed. The results of CDD are displayed in two cells; but only one of the results is correct as the CDD model on which this is based has the solution of a quadratic equation. The correct solution will have to be determined by intuition.

	A	B	C	D	E	F	G	H	I	J	K	L	M	N	O	P	Q	R	S	T
1			Root 1	Root 2	Unit															
2		CDD	328.132	13183.1																
3																				
4		qv	6289425		[cm <sup>3</sup> /s]															
5																				
6		Vs	1.6E+09		[cm/s]															
7																				
8																				
9																				
10																				
11																				
12																				
13																				
14																				
15																				
16																				
17																				
18																				
19																				
20																				
21																				
22																				
23																				
24																				
25																				
26																				
27																				
28																				
29																				
30																				
31																				
32																				
33																				
34																				
35																				
36																				
37																				
38																				

**Figure 9-2** Screen shot of gravel pack completion results module

### 9.1.3 The perforation completion results module (Perf\_Comp)

This module allows the display of the Critical Drawdown results for a perforation completion. It also displays the results for the three important sand production parameters; and displays the results of CDD in the same manner the gravel pack completion module does. Figure 9-3 is a screen shot of this module.

	A	B	C	D	E	F	G	H	I	J	K	L	M	N	O	P	Q	R	S	T
1			Rock 1	Rock 2	Units															
2		CDD	328.132	13221	[psi]															
3																				
4		q <sub>v</sub>	6307527		[cm <sup>3</sup> /s]															
5																				
6		V <sub>s</sub>	1.6E+09		[cm/s]															
7																				
8																				
9																				
10																				
11																				
12																				
13																				
14																				
15																				
16																				
17																				
18																				
19																				
20																				
21																				
22																				
23																				
24																				
25																				
26																				
27																				
28																				
29																				
30																				
31																				
32																				
33																				
34																				
35																				
36																				
37																				
38																				

**Figure 9-3** Screen shot of perforation completion results module

### 9.1.4 Using the CDD package

This package requires a PC with a Windows Operating System with Microsoft Excel Installed.

To use the CDD package, the Unconfined Compressive Strength (UCS) of formation will have to be obtained from the stand alone neural network model developed for this purpose. Other input parameters may be obtained as described in section 9.1.1. These parameters are entered appropriately in the cells with white background. No data should be entered in cells with blue background as entries to these cells get calculated automatically. Once input data are entered, the results for both gravel pack and perforation completions can be obtained from CDD-GP\_Comp and CDD-P\_Comp modules respectively. This allows comparison of the two completions in terms of their failure potential and the choice of appropriate completion taking into account the field development philosophy. The results should be saved as a separate workbook and/or printed off using Microsoft Excel print menu.

## 9.2 Grain size distribution package

The grain size distribution package is used for predicting the grain size distribution of the formation in real time prior to and during sand production. It is based on the neural network model presented in chapter six for prediction of median grain size of formation based on petrophysical properties.

The grain size distribution package is divided into four modules, namely

- Input module
- Standard deviation module
- The GSD chart module
- The GSD table module

### 9.2.1 Input module

This allows user to input the required data into the package. It also allows for the input of field/well information such as ID and depth. The input data to the predictor may be obtained from conventional logs, LWD/MWD, PLT and correlations. The symbols used in the package for the input parameters are give in Table 9-2 whilst Figure 9-4 is a screen shot of the input module.

**Table 9-2 Input parameters' symbols in GSD package**

Symbol	Definition
k	Permeability
$\phi$	Porosity
d <sub>50</sub>	Median grain size

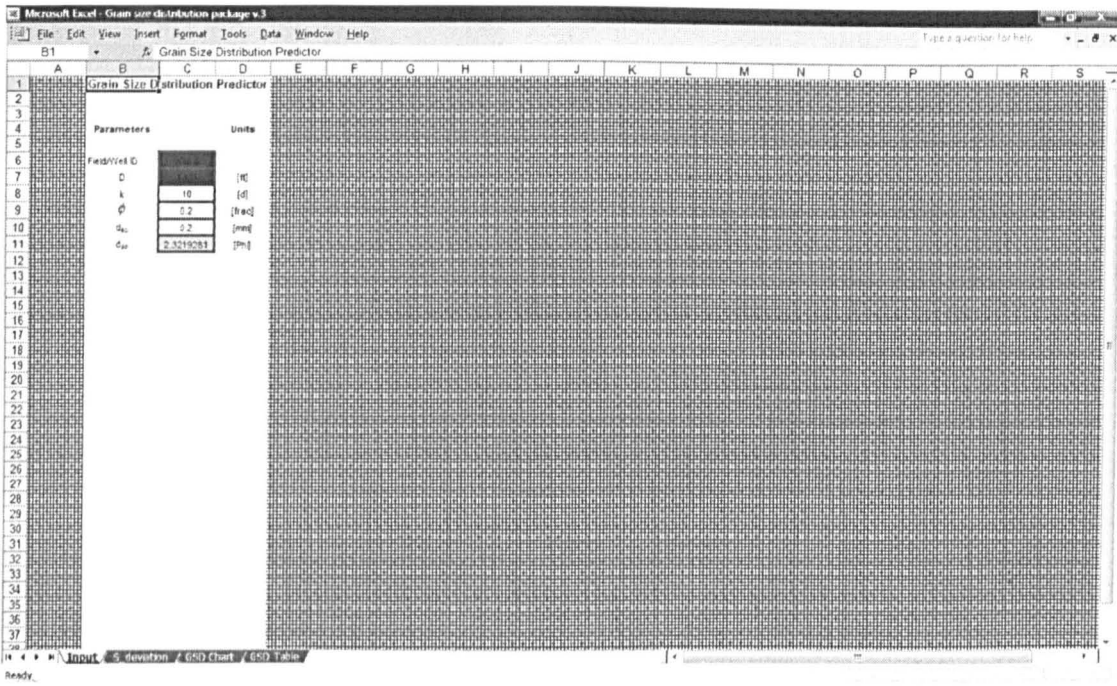


**Figure 9-4** Screen shot of GSD input module

### 9.2.2 Standard deviation module

This module allows the display of the standard deviation or sorting results. The standard deviation scale of Folk (1974)<sup>74</sup> is used in the package. The screen shot of this module is shown in Figure 9-5.

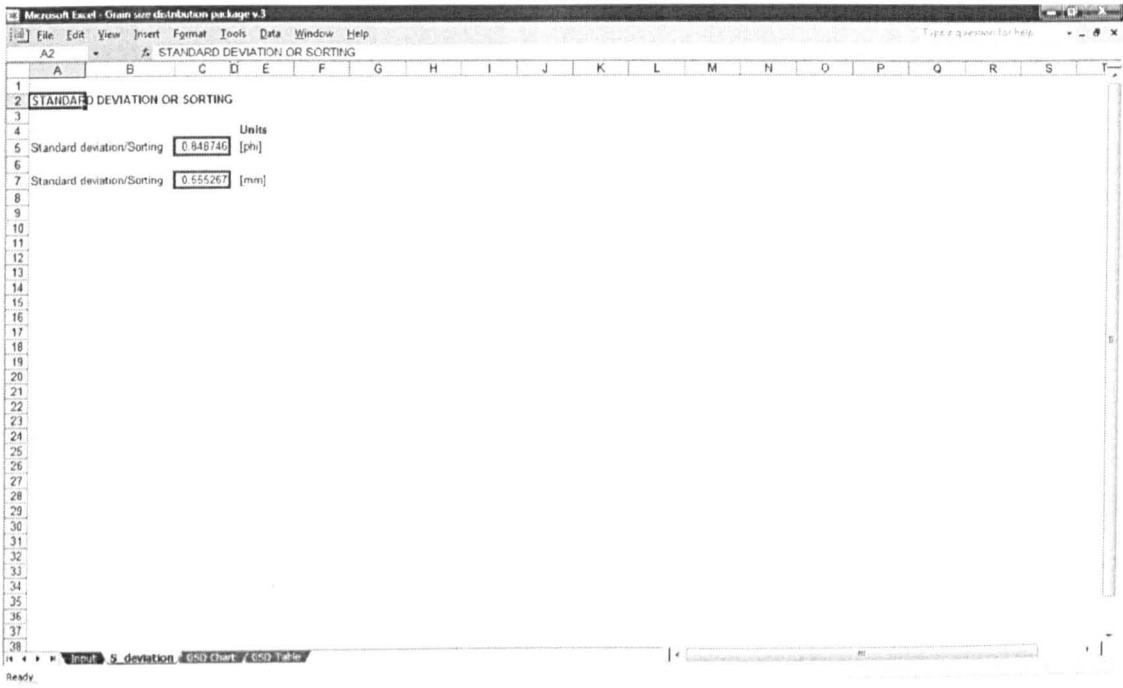


**Figure 9-5 Screen shot of GSD S\_deviation module**

### 9.2.3 GSD chart module

This module displays the grain size distribution results in a chart. The screen shot of this module is shown in Figure 9-6

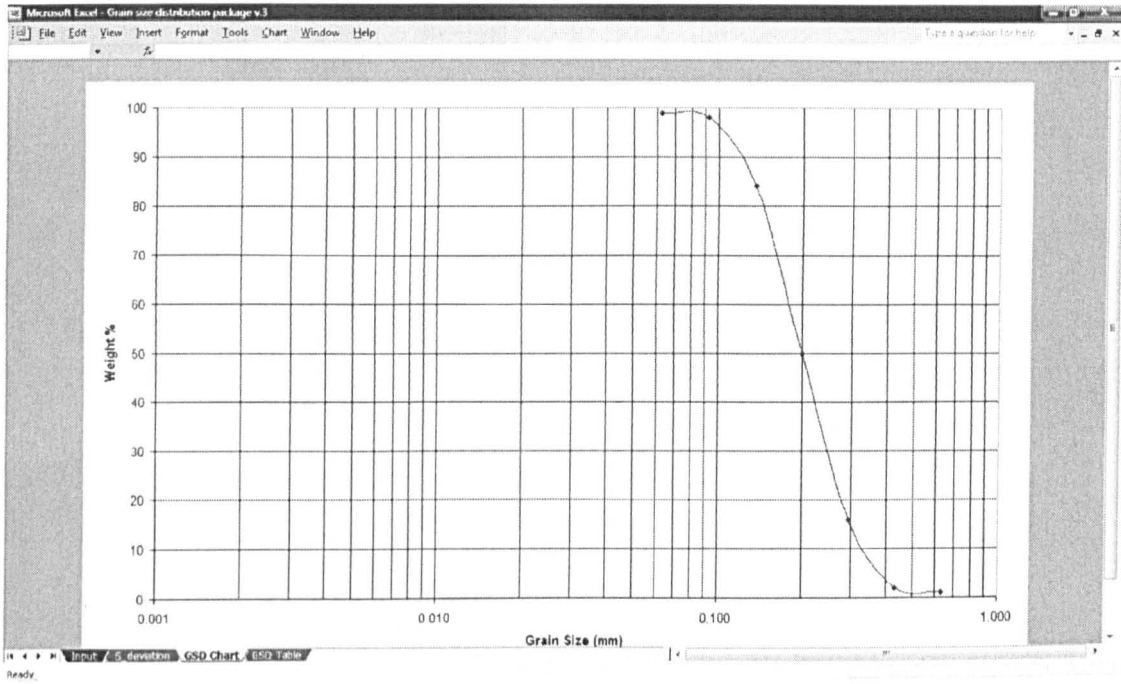


Figure 9-6 Screen shot of GSD chart module

### 9.2.4 The GSD results module

This module displays the results of the GSD in form of a table. The screen shot of this module is given in Figure 9-7.

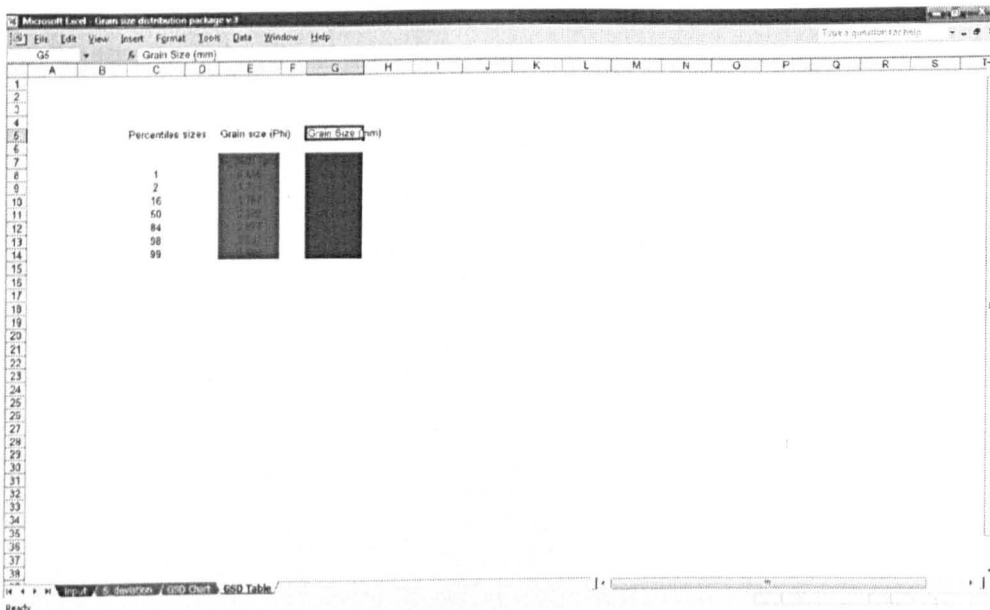


Figure 9-7 Screen shot of GSD table module

### **9.2.5 Using the GSD package**

This package requires a PC with a Windows Operating System with Microsoft Excel installed.

To use the GSD package, the median grain size of the formation will have to be obtained from the stand alone neural network model developed for this purpose. Other input parameters may be obtained as described in section 9.2.1. These parameters are entered appropriately in the cells with white background. No data should be entered in cells with blue background as the inputs to these cells get calculated automatically. Once input data are entered, the results can be obtained from the chart and table modules. The results should be saved as a separate workbook and/or printed off using Microsoft Excel print menu.

# Chapter 10

## Conclusions

This chapter presents the conclusions drawn for the entire work in this thesis vis-à-vis the aim and objectives declared in chapter one.

### 10.1 Conclusion

The following conclusions have been drawn for the work reported in this thesis:

- Extensive review of previous work in sanding potential prediction have revealed that all the existing current models for predicting sand failure and production from reservoirs are not robust enough and lack the functionality for real time sanding potential prediction.
- The strong correlation between grain size distribution and sanding potential in reservoir rocks has been established. This relationship has been utilised in this work to predict the Uniaxial Compressive Strength (UCS) of reservoir rocks in real time as a function of change in grain size distribution during production operations.
- This work has built upon the previous work, which introduced the application of neural network to grain size distribution prediction and extended it to sanding potential prediction via the prediction of Uniaxial Compressive Strength.
- A combined neural network and statistical techniques have been used to develop a unique procedure for predicting grain size distribution in real time.
- A review and ranking of some existing Uniaxial Compressive Strength (UCS) models being used in the oil and gas industry have been carried out. The review and ranking showed that all the ranked existing models performed poorly on the ranking criteria used.

- 
- A new neural network based model incorporating change in grain size distribution has been developed for predicting the Uniaxial Compressive Strength (UCS).
  - A new Critical Drawdown (CDD) model based on Hoek and Brown failure criterion has been developed for predicting the onset of sand failure and sand production. The model has been coupled to time via depletion profile to enable it predict failure in real time. The model also takes into account the effect of water breakthrough and different completion types.
  - A yield flow rate model, particle velocity and sand volume and rate models have been developed.

# **Chapter 11**

## **Review and recommendations for further studies**

In this chapter, the entire work and results reported in this thesis are reviewed. The aim of this review is to match results obtained with the declared objectives in chapter one to identify areas that can be improved in future studies. Following the review are the recommendations for further studies; these recommendations are given to broaden the scope for future studies, improve areas identified in the review and address some of the issues relating to the validation and robustness of some of the models developed.

### **11.1 Review of work**

In this work, the strong relationship between grain size distribution parameters and strength parameters of formation rock has been utilised to develop strength and failure models for sand failure analysis and sand production prediction. In addition, a grain size distribution model has been developed to predict grain size distribution in real time to generate inputs parameters for the strength and failure models.

In developing the grain size distribution models, various modelling techniques such as multivariate methods, multiple regression analysis and neural network methods were used for the purposes of comparing their predictive capability. The results obtained shows that neural network based models have better predictive capability. This informed the eventual use of neural network modelling technique for the grain size distribution prediction model developed in this work. However, the unavailability of required volume and type of data meant that the model was developed with limited data.

Neural network technique was also used for the Unconfined Compressive Strength (model) developed based on the comparison of modelling techniques carried out in the development of the grain size distribution.

The failure analysis and sand production prediction model was developed using mathematical and analytical methods. The model is based on Hoek-Brown failure criterion. This model has been well validated on oil well data but not on gas well data due to difficulty in sourcing data.

The three major models have been integrated into a field analysis package for analysing sand failure and predicting sanding potential of reservoir formation including sand rate and volume. The field analysis package has been tested and validated on limited field data with results generally within reasonable error limits. However, the Microsoft Excel platform on which the package is based may limit its performance on complex field data.

In summary, with the developments of the models discussed, all of the declared objectives of these studies have been achieved. However, difficulty in sourcing data has not made it possible for extensive testing and validation of the developed models. Recommendations for further work have been given in section 11.2 to address some of these issues.

## **11.2 Recommendations for further work**

The following are the recommendations for further work:

- Limited data were used in this work in training, validating and testing the neural networks used in grain size distribution and Uniaxial Compressive Strength (UCS) modelling due to difficulty in sourcing the right amount of data. The negative impact of this on the predictive capability of the resulting neural network models is obvious. Future studies should consider assembling larger data sets and using the same to re-train, re-validate and re-test the neural networks.

- 
- The onset of sand and sand volume/rate prediction models should be more extensively validated to identify their limitations. Specifically large data sets from the major petroleum provinces of the world from both oil and gas well/field should be used to ascertain the capability of the model and its applicability in oil and gas reservoirs.
  - The sanding potential prediction model only considers a two phase-flow of water and oil after water breakthrough but do no consider gas flow either in a two-phase flow or three-phase flow situations within the reservoir. Future studies should therefore incorporate the effect of gas flow in these flow conditions to be able to appropriately quantify the effect of gas breakthrough.
  - The present study considers the effect of just three completion types namely open hole, perforated completion and gravel packs. Future developments of this work and the resulting sanding potential prediction models should incorporate more completion types if not all completion types to make the models more versatile, robust and adaptable.
  - All the models, especially the analytical/mathematical model should be validated further with data from different petroleum provinces and with diverse reservoir conditions and fluid flow scenarios. Specifically, the validation of the grain size distribution model did not include validation of orientational grain size distribution prediction capability due to lack of data.
  - The present studies assume that well are either wholly vertical or horizontal. In wholly vertical well, where the well penetrates the formation at right angle, the additional shear stress acting on the formation is considered negligible; also in wholly horizontal well, where the well lies parallel to the formation, the additional shear stress on the formation is very small. However the additional shear stress on formation may become increasingly high with increasingly obtuse well angle, leading to reduced CDD as a result of loss of strength. Further studies should therefore consider the effect of well

angle on the Critical Drawdown model and volume of sand production.

- The excel-based Critical Drawdown (CDD) and Grain Size Distribution (GDS) predictors can be made more robust and efficient with capability for better automation. Specifically, a code can be developed for it and continually improved using a more robust platform in future studies.

---

## References

1. Oyeneyin M. B. 2003, "Challenges of Underbalanced Drilling in West Africa," SPE 85662; Nigeria Annual Inter. Conf. & Exh., 4-6, Aug., Abuja, Nigeria.
2. Prikryl, R. 2001, "Some Structural Aspects of Strength Variation in Rocks". Int. J. Rock Mech. & Min. Sc. 38(2001) 671-682.
3. Han, G. and Dusseault, M. B. 2002, "Quantitative Analysis of Mechanism for Water-Related Sand Production". SPE 73737
4. Tiab, D. and Donaldson, E. C., 1996, Petrophysics – Theory and Practice of Measuring Reservoir Rock and Fluid Transport Properties, Gulf Publishing, Houston , Texas.
5. Oyeneyin, M. B. & Faga, A. T. 1999, "Formation-Grain-Size Prediction Whilst Drilling: A key Factor in Intelligent Sand Control Completions". SPE 56626, 1999 SPE Annual Tech. Conf. and Exhibition, Houston, Texas, 3-6 Oct 1999
6. Fjaer E., et al., 2006. Petroleum Related Rock Mechanics, Development in Petroleum Science (33), Elsevier, Amsterdam, Netherlands
7. Nouri, A. et al., 2003, "A Comprehensive Approach to Modelling Sanding During Oil Production," SPE 81032, Presented at the SPE Latin American and Caribbean Petroleum Engineering Conference held in Port-of-Spain, Trinidad , West Indies, 27 – 30 April 2003.
8. Dusseault M. B. & El-Sayed S., 2000, "Heavy-Oil Production Enhancement by Encouraging Sand Production, SPE 59276, Presented at the 2000 SPE/DOE Improved Oil Recovery Symposium held in Tulsa, Oklahoma, USA, 3 – 5 April. 2000.
9. Tronvoll J. et al., 2001, "Tool of Sand Management," SPE 71673, Presented at the 2001 SPE Annual Technical Conference and Exhibition held in New Orleans, Louisiana, USA, 30 Sep – 3 Oct. 2001.

- 
10. Wang, Y. & Chen, C. C., 1999, "Improved Production and sand (Cold) Production in Conventional and Heavy Oil Reservoirs – A Field Case and Simulation," SPE 57290, SPE Asia Pacific Improved Oil Recovery Conference, Kuala Lumpur, Malaysia, 1999.
  11. Smith, G. E., "Fluid Flow and Sand Production in Heavy Oil Reservoirs Under Solution Gas Drive", SPE 15094, Presented at the SPE California Regional Meeting, Oakland, California, 1986.
  12. Mathis S. P., 2003, "Sand Management: A Review of Approaches and Concerns," SPE 82240, Presented at the SPE European Formation Damage Conference held in The Hague, The Netherlands, 13 – 14 May 2003.
  13. Papamichos E., 2002, "Sand Mass Prediction in North Sea Reservoir," SPE/ISRM 78166, Presented at the SPE/ISRM Rock Mechanics Conference held in Irving, Texas, USA, 20 – 23 Oct. 2002.
  14. Oluyemi G. et al, 2006(a), "Prediction of Directional Grain Size Distribution: An Integrated Approach," SPE 105989, presented at the 30<sup>th</sup> SPE Annual International Conf. & Exh., Abuja, Nigeria, July 31 – Aug. 2, 2006
  15. Oluyemi G., et al, 2006(b), "Real Time Continuous Reservoir Strength Prediction from Grain Size Distribution Information Using Neural Network", SPE 105960, presented at the 30<sup>th</sup> SPE Annual International Conf. & Exh., Abuja, Nigeria, July 31 – Aug. 2, 2006
  16. Veeken, C. A. M. et al., 1991, "Sand Production Prediction Review: Developing an Integrated Approach." SPE 22792.
  17. Kanj, M. Y. & Abousleiman, Y. 1999, "Realistic Sanding Predictions: A Neural Approach". SPE 56631, SPE Ann. Techn. Conf. & Exhibition, Houston, Texas, 3-6 Oct 1999.
  18. Stein, N. and Hilchie, D. W. 1972, "Estimating the Maximum Production Rate Possible from Friable Sandstones Without Using Sand Control," JPT (Sept 1972) 1157-1160.

- 
19. Stein, N. et al. 1974, "Estimating the Maximum Sand-Free Production Rates from Friable Sand for Different Well Completion Geometries," JPT (Oct. 1974) 1156-1158.
  20. Hall, C. D. and Harrisberger, W. H. 1970, "Stability of Sand Arches: A key to Sand Control," JPT (July 1970) 821-829.
  21. Vriezen, P. B. et al, 1975, "Erosion of Perforation Tunnels in Gas Wells." SPE 5661.
  22. Addis, M. A. et al. 1998, "The Influence of the Reservoir Stress-Depletion Response on the Lifetime Considerations of Well Completion Design". SPE/ISRM 47289, SPE/ISRM Eurock '98, Trondheim, Norway, 8-10 July 1998.
  23. Antheunis, D. et al. 1976, "Perforation Collapse: Failure of Perforated Friable sandstones". SPE 5750, SPE-European Spring Meeting, Amsterdam, The Netherlands, 8-9 April 1976.
  24. Coates, D. R. and Denoo, S. A. 1981, "mechanical Properties Program Using Borehole Analysis and Mohr's Circle," Proceedings SPWLA 22<sup>nd</sup> Annual Logging Symp., June 23-26, 1981.
  25. Geertsma, J. 1985, "Some Rock-mechanical Aspects of Oil and Gas Well Completions," SPE J. (Dec 1985) 848-856.
  26. Morita, N. et al. 1989, "A quick Method to Determine Subsidence, Reservoir Compaction, and In-Situ Stress Induced by Reservoir Depletion". SPE 17150, Journal Petrol. Tech. 1989.
  27. Risnes, R. & Bratli, R. K. 1981, "Sand Stresses Around a Wellbore". SPE 9650, Middle E. Oil Techn. Conf., Manama, Bahrain, 9-12 March 1981.
  28. Bratli, R. K. & Risnes, R. 1979, "Stability and Failure of Sand Arches". SPE 8427, SPE-AIME 54<sup>th</sup> Ann. Techn. Conf. & Exhibition, Las Vegas, Nevada, 23-26 Sept. 1979.
  29. Van den Hoek, P. J. et al. 2000, "A New Concept of Sand Production Prediction: Theory and Laboratory Experiments". SPE 65756.

- 
30. Cole, R. C. & Ross, C. 1998, Sand Stabilization and Exclusion, In: Petroleum Well Construction, ed. Economides, M. J., Larry, T. W. & Dun-Norman, S; John Wiley and Sons Ltd., West Sussex, England.
  31. Himmatramka, A. K., 1981, "Analysis of Productivity Reduction Due to Non-Darcy Flow and True Skin in Gravel-Packed Wells", SPE 10084, Presented at the 56<sup>th</sup> SPE/AIME Annual Fall Technical Conference and Exhibition, San Antonio, Texas, Oct 5 - 7, 1981
  32. Coberly, C. J. & Wagner, E. M., 1938, "Some Considerations in the Selection and Installation of Gravel Packs for Oil Wells, "Pet Tech. (August 1938) pp 1-20.
  33. Hill, K. E., 1941, "Factors Affecting the Use of Gravel in Oil Wells, "Oil Weekly (May 1941), pp 13-20
  34. Schwartz, D. H., 1968, "Successful Sand Control Design for High Rate Oil and Water Wells," J. Pet Tech (Sept 1968), pp 1193-1198
  35. Britt, L. K., 2000, "Optimum Formation Control Through the Development of Effective Proppant and Gravel Sizing Criteria," Project Proposal, NSI Technologies Inc.
  36. Saucier, R. J., 1974, " Considerations in Gravel Pack Design," JPT (Feb 1974), pp 205-212
  37. Salahudin et al, 2006, "Controlling High Fines Production in High Volume Gas Wells," World Oil, Vol 227, No 8; August 2006
  38. Oyeneyin, M. B. et al, 1992, "Optimum Gravel Sizing for Effective Sand Control", SPE 24801, presented at the SPE Annual Tech. Conf. & Exh., 4-7, Oct, 1992, Washington DC
  39. Tronvoll, J, & SØnstebØ, E. F. , 1997, "Productivity Effects of Drawdown and Depletion in Open Hole Completions: Do Screens Plug?" SPE 38191, presented at the 1997 SPE European Formation Damage conf., The Hague, The Netherlands, 2-3 June 1997
  40. Constien, V. G. & Skidmore, V., 2006, "Standalone Screens Selection Using Performance Mastercurves", SPE 98363, presented at the 2006 SPE International Symp. And Exhib. On Formation Damage Control, Lafayette, LA, 15-17 feb. 2006

- 
41. Innes G., et al 2006, "Next Generation Expandable Completion Systems," SPE 106342, presented at the 2006 SPE Technical Symposium of Saudi Arabia Section, Dhahran, Saudi Arabia, 21-23 May 2006
  42. Metcalfe P. & Whitelaw, C., 1999, "The Development of the First Expandable Sand Screen," Paper OTC 11032, presented at the 1999 Offshore Technology Conf., Houston, 3-6 Oct, 1999.
  43. Metcalfe, P. D., Urselmann, R., & Saeby, J. 2001 "The Global Impact of Expandable Sand Screens on Reservoir Drilling and Completion," SPE 67726, presented at the 2001 SPE/IADC Drilling Conference, Amsterdam, 27 Feb – 1 Mar, 2001.
  44. Lau, H. C., et al., 2004, "Openhole Expandable-Sand-Screen Completions in Brunei," SPE Drilling and Completion, March 2004.
  45. Weekse A., Grant S., & Urselmann, R., 2002, "Expandable Sand Screen: Three New World Records in the Brigantine Field," IADC/SPE 74549, presented at the IADC/SPE Drilling Conference, Dallas, Texas, 26-28 Feb. 2002
  46. Al-Lamki, A, Twycross, J & Clarke, G., 2004, "Maximising Productivity in the Scoter Gas Condensate Field, UKCS: A Multidisciplinary Approach to Expandable Sand Screen Design and Subsea Installation", SPE 91004, presented at the SPE Annual Tech. Conf. and Exhib., Houston, Sept 2004
  47. Wang, J. L. et al, 2003, "An Alternative Wellbore Stabilisation and Sand Control System in Multi-Lateral Wells", SPE 80445, presented at the SPE Asia Pacific Oil and Gas Conf. & Exhib., Jakarta, April 2003
  48. Jones, C. et al, 2005, "Expandable Sand Screens Selection, performance, Reliability: A Review of the First 340 Installations," SPE/IADC 97282, SPE/IADC Middle East Drilling Technology Conference & Exhibition, Dubai, UAE, 12-14 Sept 2005.
  49. Abass H. H et al, 2003, "Sand Control During Drilling, Perforation, Completion and Production," SPE 81492

- 
50. Parlar M. et al. 1998, "New Chemistry and Improved Placement Practices Enhance Resin Consolidation: Case Histories from the Gulf of Mexico," SPE 39435, Inter. Symp. On Formation Damage Control, Lafayette, Louisiana; Feb. 18-19, 1998.
51. Sadrpanah H., et al., 2005, "Designing Effective Sand Control Systems to Overcome Problems in Water Injection Wells," SPE 93564.
52. Nisbet, W. J. R & Dria, D. E. 2003, "Implementation of a Robust Deepwater Sand Monitoring Strategy", SPE 84494, presented at the SPE Annual Tech. Conf. & Exh., Denver, Colorado, USA, 5 -8 Oct. 2003
53. ClampOn, 1999, "Meeting the Sand Control Challenge", Asia Exploration & Production Business Magazine, May/June 1999
54. Porder T., 2006, "Tore: A New Tool for Sand Management", 1<sup>st</sup> SPE/SMN European Sand Management Forum, 3 - 4, March, 2006, Aberdeen.
55. McPhee, C. A. & Enzendorfer, C. K., 2004, "Sand Management Solutions for High-Rate Gas Wells, Sawan Field, Pakistan", SPE 86535, presented at the SPE Int. Symp. & Exh. on Formation Damage, Lafayette, Louisiana, USA, 18-20 Feb, 2004
56. McPhee, C. A., et al, 2000 "Sand Management in Bongkot Field, Gulf of Thailand: an Integrated Approach", SPE 64467, presented at the 2000 SPE Asia Pacific Oil and Gas Conf. & Exh, Brisbane, Australia
57. Willson, S. M. et al, "New Model for Predicting the Rate of Sand Production", SPE/ISRM 78168, presented at the SPE/ISRM Rock Mechanics Conference, Irving, Texas, 20-23 Oct 2002
58. Vaziri H., Xiao, Y. & Palmer I., 2002, "Assessment of Several Sand Prediction Models with Particular Reference to HPHT Wells", SPE 78235, presented at the SPE/ISRM Rock Mechanics Conference, Irving, Texas, 20-23 Oct 2002

- 
59. Palmer, I., et al, 2003, "Predicting and Managing Sand Production: a New Strategy", SPE 84499, presented at SPE Annual Tech. Conf. & Exh., Denver, Colorado, USA, 5-8 2003.
60. Wang Y. & Lu, B. 2001, "A coupled Reservoir-Geomechanics Model and Applications to Wellbore Stability and Sand Prediction", SPE 69718, presented at the 2001 SPE Int. Thermal Operations & Heavy Oil Sym., Margarita, Venezuela, March 12-14, 2001
61. Morita, N. et al. 1989, "A quick Method to Determine Subsidence, Reservoir Compaction, and In-Situ Stress Induced by Reservoir Depletion". SPE 17150, Journal Petrol. Tech. 1989.
62. Wu, b. & Tan, C. P., 2002, "Sand Production Prediction of Gas Field – Methodology and Field Application", SPE/ISRM 78234, presented at the SPE/ISRM Rock Mechanics Conf., Irving, Texas, 20-23 Oct. 2002
63. Wang Z., Peden, J. M. & Damasena, E. S. H., 1991, "The Prediction of Operating Conditions to Constrain Sand Production from Gas Well," SPE 21681, Production Operation Symposium, April 7-9, 1991
64. Faga , A T 2000, Prediction of Grain-Size Distribution in Clastic Reservoirs for Gravel Pack Design, Unpublished PhD Thesis, Mechanical and Offshore Engineering Department, The Robert Gordon University, Aberdeen.
65. Blott S J and Pye K., 2001, "GRADISTAT: A Grain Size Distribution and Statistics Package for the Analysis of Unconsolidated Sediments," Technical Communication: Earth Surface Processes and Landforms 26, 1237-1248 (2001)
66. Udden, J A. 1914, "Mechanical Composition of Clastic Sediments," Bulletin of the Geological Society of America; 25 : 655-744
67. Wentworth, C. K. 1922, "A Scale of Grade and Class Terms for Clastic Sediments," Journal of Geology 30 : 377-392
68. Krumbein, W C 1934, "Size Frequency Distribution of Sedimentary Rocks," J. Sed. Petrol., 4, 65-77, 1934

- 
69. Hugman R H H & Friedman M, 1979, "Effects of Texture and Composition on Mechanical Behaviour of Experimentally Deformed Carbonate Rocks. *Am. Assoc. Pet. Geol. Bull.*, 1979, 63, 1478-1489
  70. Olsson W A, 1974 "Grain Size Dependence of Yield Stress in Marble," *J. Geophys. Res.*, 1974, 79, 4859-4862
  71. Palchik, V 1999, "Influence of Porosity and Elastic Modulus on Uniaxial Compressive Strength in Soft Brittle Porous Sandstone," *Rock Mech. & Rock Eng.*, 32-4 (1999), 303-309
  72. Selley R C 1982, *An Introduction to Sedimentology*. Academy Press., London,
  73. Gutierrez M A et al. 2002, "Grain Sorting Effect on Seismic Velocities: Rock Physics Models for Reservoir Quality Prediction," AAPG Annual Meeting, March 10-13, 2002
  74. Folk R, 1974, *Petrology of Sedimentary Rocks*, Hemphill Publishing Company
  75. Kageson-Loe N, 2005, "Selection of Most Appropriate Sandface Completion: Overcoming the Conflict between Sand Retention and Productivity," IQPC Sand Control and Management, Aberdeen, 29-30 Nov, 2005.
  76. Moriwawon B., Oluyemi, G and Oyenyin, M B, 2005, "Real Time Sanding Potential Prediction: Ensure You Are Equipped for Sand," IQPC Sand Control and Management, Aberdeen, 29-30 Nov, 2005.
  77. Folk, R. L. 1955, "Student Operator Error in Determination of Roundness, Sphericity, and Grain Size," *J. Sedimentary Petrology*, 25(4), 297-301
  78. Barrett, P. J. 1980, "The Shape of Rock Particles, A Critical Review," *Sedimentology*, 27, 291-303
  79. Meloy, T. P. 1977, "Fast Fourier Transforms Applied to Shape Analysis of Particle Silhouettes to Obtain Morphological Data," *Powder Technology*, 17, 27-35

- 
80. Clark, N. N. 1987, "A New Scheme for Particle Shape Characterisation Based on Fractal Harmonics and Fractal Dimensions," *Powder Technology*, 51, 243-249
  81. Hyslip, J. P. and Vallejo, L. E. 1997, "Fractal Analysis of the Roughness and Size Distribution of Granular Materials," *Engineering Geology*, 48, 231-244.
  82. Bowman, E. T, Soga, K and Drummond, W, 2001, "Particle Shape Characterisation Using Fourier Descriptor Analysis," *Geotechnique*, 51(6), 545-554
  83. Sukumaran, B and Ashmawy, A. K. 2001, "Quantitative Characterisation of the Geometry of Discrete Particles," *Geotechnique*, 51(7), 171-179
  84. Sarda et al, 1993, "Use of Porosity As a Strength Indicator for Sand Production Evaluation", SPE 26454, presented at the 68th SPE Annual Tech. Conf. & Exhibition, Houston, Texas, 3-6, Oct. 1993
  85. Eldmann K. et al., 1998, "Predicting Rock Mechanical Properties from Wireline Porosities," SPE/ISRM 47344
  86. Hayton, S., et al, 2001, "Effect of Mica on Particle-Size Analyses Using the Laser Diffraction Technique", *Journal of Sedimentary Research*; May 2001; Vol. 71, no 3, p. 507-509
  87. Trentesaux, A., et al, 2001, "Carbonate Grain-Size Distribution in Hemipelagic Sediments from a Laser Particle Sizer", *Journal of Sedimentary Research*; Sept. 2001; Vol. 71, no 5, p. 858-862
  88. Kenkkila, J. 2005, "The Laser Diffraction Grain Size Analysis of Late Miocene Flood-Plain Sediments from Lantian, in Shaanxi Province, Northern China", MSc Thesis, Department of Geology, University of Helsinki.
  89. Malvern , 2005, *Mastersizer 2000 Manual*.
  90. Eshel, G. et al, 2004, "Critical Evaluation of the Use of Laser Diffraction for Particle -Size distribution Analysis", *Soil Sc. Soc. of America Journal (SSSAJ)*, 68:736-743 (2004)

- 
91. Oyno, L. et al, 1998, "Prediction of Petrophysical Parameters Based on Digital Video Core Images". SPE Reservoir Evaluation and Engineering, Feb., 1998.
  92. Slichter, S. C. 1899, "Theoretical Investigation of the Motion of Groundwater." US Geol. Surv., NTIS, Springfield, VA, 19th Annual Report, 1989, pp 295-384
  93. Kozeny, J. 1927, "Über Kapillare Leitung Des Wassers Im Bodem (Aufstieg Ver Sikeung Und Anwendung Auf Die Bemasserung)." Sitzungsber Akad., Wiss, Wein, Math-Naturwiss, KL, Vol 136 (IIa) 1927.
  94. Carman, P. C., 1937, "Fluid Flow through Granular Beds" Trans Inst. Chem. Eng., 1937, Vol. 15, pp. 150-166
  95. Krumbien, W. C. and Monk, C. D. 1942, "Permeability as a Function of the Size Parameters of Unconsolidated Sand." Trans. AIME, Vol. 151, pp 153-162
  96. Bergs, R. R., 1970, "Method for Determining Permeability from Reservoir Rock Properties," Trans Gulf Coast Ass. Geol. Soc.; Vol. XX; pp 303-317
  97. Sparling, D. D. 1974, "Sand and Gravel – A study of Their Permeabilities", SPE 4772, presented at the SPE of AIME Symposium on Formation Damage Control, New Orleans, La, Feb., 7-8, 1974
  98. Ciccotti M. and Mulargia F., 2004, "Differences between Static and Dynamic Elastic Moduli of a Typical Seismogenic Rock", Geophysical Journal International, Vol. 157, Issue 1, pp 474, April 2004
  99. Holt R. M. et. al. 1987, "Rock Mechanical Analysis of North Sea Reservoir Formations," SPE 16796, presented at the 62nd Annual Technical Conference and Exhibition of the Society of Petroleum Engineers held in Dallas TX Sept. 27-30. 1987
  100. Jones M. E., Leddra, M. J., Goldsmith, A. S. and Edwards, D, 1992, The Geomechanical Characteristics of Reservoirs and

- 
- Reservoir Rocks, Health and Safety Executive - Offshore Technology Report, HMSO Books London
101. Hosking J. R. 1955, "A comparison of Tensile Strength, Crushing Strength and Elastic Properties of Road-making Rocks," *Quarry Man. J.*, Vol. 39, 1955, pp. 200 - 212
  102. Ringstad, C. et al., 1998, "Prediction of Rock Parameters from Micro-Indentation Measurements: The Effect of Sample Size," SPE/ISRM 47313, presented at SPE/ISRM Eurock '98, Trondheim, Norway, 8 - 10 July 1998
  103. Katz, O., Reches, Z. & Roegiers, J-C., 2000, "Evaluation of Mechanical Rock Properties Using a Schmidt Hammer," *Int. J. of Rock Mech. and Mining Sci.* 37 (2000) 723-728
  104. Richard, T. et al., 1998, "The Scratch Test As a means to Measure Strength of Sedimentary Rocks," presented at SPE/ISRM Eurock '98, Trondheim, Norway, 8 - 10 July 1998
  105. Schei, G. et al., 2000, "The Scratch Test: An Attractive Technique for Determining Strength and Elastic Properties of Sedimentary Rocks," presented at the 2000 SPE Annual Technical Conf. & Exhibition, Dallas, Texas, 1 - 4 Oct. 2000
  106. Tokle et al, 1986, K. et al. 1986, "Predicting Uniaxial Compressive Strength from Log Parameters." SPE 15645.
  107. Meulenkamp F. and Grima M. A., 1999, "Application of Neural networks for the Prediction of the Unconfined Compressive Strength (UCS) from Equotip hardness," *Int. J. of Rock Mech. and Mining Sci.* 36 (1999) 29-39
  108. Singh, V. K., Singh, D. & Singh, T. N.; 2001, "Prediction of Strength Properties of some Schistose Rocks from Petrographic Properties Using Artificial Neural Networks," *Int. J. of Rock Mech. & Min. Sci.* 38 (2001) 269-284
  109. Xue T. et al. , 2004, "Numerical Method to Determine Mechanical Parameters of Engineering Design in Rock Masses," *Journal of Zhejiang University SCI.* 2004 5(7): 884-889

- 
110. Knudsen, F. P., 1959, "Dependence of Mechanical strength of Brittle Polycrystalline Specimens on Porosity and Grain Size," J. American Ceramic Soc. (1959), 42, pp. 376-387
  111. Palchik, V. 2006, "Application of Mohr-Coulomb Failure Theory to Very Porous Sandy Shales," Inter. J. of Rock Mech. & Mining Sc. 43(2006), pp.1153-1162
  112. <http://www.liv.ac.uk/seismic/links/info.html>
  113. Madland, M. V. et al., 2002, "Temperature Effects in Brazillian, Uniaxial and Triaxial Compression Tests with High Porosity Chalk," SPE 77761, presented at the SPE Annual Tech. Conf. & Exh., San Antonio, Texas, 29 Sept. - 2 Oct. 2002.
  114. Capes, C. E., 1980, Particle Size Enlargement; In: Handbook of Powder Technology; Vol. 1; Amsterdam, Elsevier; 1980; pp. 23-26
  115. Schuber H., 1984, Capillary Forces - Modelling and Application in Particulate Technology, Powder Technology; 47:105-16
  116. Colliins, P. M, 2002, "Geomechanics and Wellbore Stability Design of an Offshore Well, North Sea," SPE/PS-CIM/CHOA 78975, presented at SPE Inter. Thermal Operations and Heavy Oil Sym. And Inter. Horizontal Well technology Conf, Calgary, Alberta, Canada, 4-7 November 2002.
  117. <http://courses.washington.edu/me354a/Thick%20Walled%20Cylinders.pdf>
  118. <http://www.fractech.co.uk/flash/pea135.html#twc>
  119. Janbu, N., 1985, "Soil Models in Offshore Engineering, 25<sup>th</sup> Ranking Lecture, Geotechnique, Vol. 35; pp. 241-281
  120. Terzaghi, K. 1936, "The Shearing Resistance of Saturated Soils and the Angle Between the Planes of Shear," Proceeding of the Inter. Conf. on Soil Mechanics and Foundation Engineering, Vol. 1; Cambridge, Massachusetts, USA. Pp 54-56
  121. Terzaghi, K. 1943, Theoretical Soil Mechanics, New York Wiley

- 
122. Hans, G. 2003, Rock Stability under Different Fluid Flow Conditions; PhD thesis, Chemical Engineering, University of Waterloo, Ontario Canada.
  123. Brandt, H. 1955, "A study of the Speed of Sound in Porous Granular Media," *Trans ASME*, vol. 77, 1955, pp.479
  124. Malvern, L. E., 1969, *Introduction to the Mechanics of a Continuous Medium*, Prentice-Hall
  125. Abass H. and Neda. J., 1998, *Rock Mechanics in Wellbore Construction*; In : *Petroleum Well Construction* (Ed. M. J. Economides, L. T. Watters and S. Dun-Norman); John Wiley & Sons Ltd, Chichester England
  126. Lowrey J. P. & Ottesen, S. 1995, "An Assessment of the Mechanical Stability of Wells Offshore Nigeria", *SPE Drilling & Completions*, March 1995
  127. Sinha B. K. et al., 2006, "Horizontal Stress Magnitude Estimation Using the Three Shear Moduli – A Norwegian Sea Case Study," *SPE 103079*, presented at the 2006 SPE Annual Tech Conf. and Exh., San Antonio, Texas, USA, 24-27, Sept 2006.
  128. Kry, P. R. and Gronseth, J. M., 1983, "In Situ Stresses and Hydraulic Fracturing in the Deep Basin," *Journal of Canadian Petroleum Technology*; Nov. – Dec. 1983 Issue, p. 31-36
  129. Bell J. S., 2003, "Practical methods for Estimating In-situ Stresses for Borehole Stability Applications in Sedimentary Basins," *J. Petrol. Sc. & Eng.* 38 (2003), pp 111-
  130. Khan M. & Teufel L. W. 2000, "The effect of Geological and Geomechanical Parameters on Reservoir Stress Path and Its Importance in Studying Permeability Anisotropy," *SPE Reservoir Eval. & Eng.* 3(5), Oct. 2000
  131. Edelbro, C. 2004, *Evaluation of Rock Mass Strength Criteria*; Licentiate Thesis, Division of Rock Mechanics, Department of Civil and Environmental Engineering, Lulea University of Tech.,

- 
132. Hoek, E. and Brown, E. T., 1980, *Underground Excavations in Rock*. London: Institution of Mining and Metallurgy; p. 527
  133. ACook A. et al 2004, "Practical Approaches to Sand Management," *Oilfield Review*; Spring 2004.
  134. Morita, N., Whitfill, D. L., fedde, O. P and Lovik, T. H., 1987, "Parametric Study of Sand Production Prediction: Analytical Approach," SPE 16990, presented at the 62nd Annual Tech. Conf. and Exh., Dallas, TX, Sept. 27-30, p.561-575)
  135. Engelbrecht, A. P. 2002, *Computational Intelligence , An Introduction*; John Wiley & Sons Ltd, Chichester England
  136. Master, T. 1993, *Practical Neural network Recipe in C++*; Academic Press Inc. San Diego.
  137. Macleod Chris, 2004, Personal Communication
  138. Wasserman P. D, 1989, *Neural Computing: Theory and Practice*; Van Nostrand Reinhold, new York
  139. Braunschweig, B & Days, R., 1995, *An Overview of AI Techniques and of Their Use in the Petroleum Industry*; In: *Artificial Intelligence in the Petroleum Industry – Symbolic and Computation Applications* (ed. B. Braunschweig and R. Day); Series on Artificial Intelligence in the Petroleum Industry, Editions Technip, Paris.
  140. Zhou, C., & Wu, X., 1993, "Neural Network-Based Formation Parameters Logs in Quantitative Log Analysis: A Comparative Study," SPE 25359, SPE Asia Pacific Oil & Gas Conf. & Exh., Singapore, 8-10 Feb. 1993
  141. Chawathe, A, 1994, "The application of Kohonen Type Self Organisation Algorithm to Formation Evaluation," SPE 29179, Eastern Regional Conf. & Exh., Charleston, WV, USA, 8-10 Nov. 1994
  142. Mohaghegh, S. et al, 1995, "Design and Development of an Artificial Neural Network for Estimation of Formation Permeability," SPE Computer Application, Dec. 1995

- 
143. Soto, R. B. et al, 1997, "Use of Neural Networks to Predict the Permeability and Porosity of Zone "C" of the Cantagallo Field in Colombia," SPE 38134, Petroleum Computer Conference, Dallas, TX, USA, 8-11 June 1997
  144. Liu, Y. & Sacchi, M. D., 2003, "Propagation of Borehole Derived Properties Via a Support Vector Machine(SVM); 54 CSEE Recorder, Dec. 2003
  145. Uden, R. C., Smith, M. & Hubert, L., 2003, "Neural Network Training for Reservoir Characterisation of Litho Facies," EAGE 65th Conf. & Exh. , Stavanger, Norway, 2-5 June 2003.
  146. Yu, W., Rubio J. J. & Morales A., 2004, "Optimisation of Crude Oil Blending with Neural Networks," 43rd IEEE Conference on Decision and Control; Dec 14-17, Atlantis Paradise Island, Bahamas
  147. Yu, L., Wang, S. & Lai, K. K., 2006, "An Integrated Data Preparation Scheme for Neural Network Data Analysis," IEEE Transactions on Knowledge and Data Engineering, Vol. 18, No. 2, Feb. 2006
  148. Coates, G. R. & Denoo, S., 1981, "The Producibility Answer Product," The Technical Review, Schlumberger, Houston (June) 29 (2), 55-63
  149. Revil et al., 2002, "A New Permeability Model from NMR data" unpublished
  150. Amaefule et al., 1993, "Enhanced Reservoir Description: Using Core and Log Data to Identify Hydraulic Flow Units and Predict Permeability in Uncored Intervals/Wells," SPE 26436, Annual Tech. Conf. And Exhibition, Houston, Texas, Oct. 3-6, 1993
  151. Schon, J. H. 2003 et al., "Imparting Directional Dependence on Log-Derived Permeability," SPE Reservoir Evaluation & Engineering 2003
  152. You-Sheng, X & Xian-Zhi, X. 2001, "A New Numerical Method For the Analysis of the Permeability Anisotropy Ratio," Chin. Phys. Soc., Vol 11, No 6, June 2002.

- 
153. Lock, P. A. et al. 2001, "Estimating the Directional Permeability of Reservoir Sandstones Using Image Analysis," Proceedings of the 6th Nomadic Symposium on Petrophysics, 15-16 May 2001, Trondheim, Norway.
  154. Angeles, R. et al., 2005, "Efficient and Accurate Estimation of Permeability and Permeability Anisotropy from Straddle-Packer Formation Tester Measurements Using the Physics of Two-Phase Immiscible Flow and Invasion," SPE 95897, presented at the 2005 SPE Technical Conference and Exhibition held in Dallas, Texas, USA, 9-12 Oct., 2005.
  155. Washington, C., 1992, Particle Size Analysis in Pharmaceuticals and Other Industries - Theory and Practice, Ellis Horwood Ltd. Chichester, 1992
  156. Stockham, J. D., 1977 "What is Particle Size: The Relationship Among Statistical Diameters," In Particle Size Analysis 1977, Ann Arbor Sci Pub, Ann Arbor, Michigan (Ed. John D. Stockham & Edward G. Fochtman)
  157. Gavito, D. G. 1996, "A New Rock Strength Model and Its Practical Applications." SPE 35322
  158. Stein, N. 1985, "Strength of Cementation is Estimated from Well logs", Oil and Gas Journal (15 July 1985), 132-33.
  159. Bruce J., 1990, "Uniaxial Compressive Strength Estimation of Clastic Sedimentary Rocks" Chin. Geom. Soc. Vol. 2, No 9, Feb., 1990.
  160. Hoek, E. and Brown, E. T. 1988, "The Hoek-Brown Failure Criterion - A 1988 Update", 15<sup>th</sup> Canadian Rock Mechanics Symposium, p.31-38
  161. Hettema, M.H. et al. 2006, "The Relative Importance of Drawdown and Depletion in Sanding Wells: Predictive Model Compared with Data from the Statfjord Field," SPE 97794, Int. Sym. & Exh. On Formation Damage Control, 15-17 Feb. Lafayette, Louisiana, USA.

- 
162. Han G et al. 2002, "Quantifying Rock Capillary Strength Behaviour in Unconsolidated Sandstones," SPE/ISRM 78170, SPE/ISRM Rock Mechanics Conference, Irving, Texas, 20-23 Oct. 2002.
  163. Papamichos E., Brignoli M and Santarelli F J, 1997, "An experimental and Theoretical Study of a Partially Saturated Collapsible Rocks," *Mechanics of Cohesive-Frictional Materials*, 2, 1-28, 1997
  164. Skjaerstein A, Tronvoll J, Santarelli F J and Joranson H, 1997, "Effect of water Breakthrough on Sand Production: Experimental and Field Evidence," SPE 38806
  165. Hall C D and Harrisberger W H, 1970 "Stability of Sand Arches: A Key to Sand Control," *J. Pet Tech.*
  166. Cleary M P, Melvan J J and Kohlhaas C A 1979, "The Effect of Confining Stress and Fluid Properties on Arch Stability in Unconsolidated Sand" SPE 8426
  167. Jahn F., Cook M & Graham N, 1998, *Hydrocarbon Exploration and Production - Development in Petroleum Science 46*, Elsevier Science BV, Amsterdam, The Netherlands, pp. 216 - 217
  168. Tippie D B and Kohlhaas C A., 1973, "Effect of Flow Rate on Stability of Unconsolidated Producing Sands," SPE 4533, 48<sup>th</sup> Annual Fall Meeting of SPE-AIME, Las Vegas, Nevada, 30 Sep. - 3 Oct., 1973.
  169. Dake, L. P., 1978, *Fundamental of Reservoir Engineering*, 19<sup>th</sup> Impression 2002, Elsevier Science B.V., Amsterdam, The Netherlands
  170. Juanes, R. and Patzek, T. W., 2003 "multiscale Numerical Modelling of Three Phase Flow," SPE 84369, 2003 SPE Annual Tech. Conf. & Exhibition, Denver Colorado, USA, 5 - 8 Oct.
  171. Pucknell J. K. and Mason J. N. E., 1992; "Predicting The Pressure Drop in a Cased-Hole Gravel Pack Completion," SPE 24984,

- 
- Presented at the European Petroleum Conference held in Cannes, France, 16-18 November 1902
172. McLeod H. O., 1983, "The Effect of Perforating Conditions on Well Performance," SPE 10649
173. Samsuri A. et al, 2003, "An Integrated Sand Control Method Evaluation," SPE 80444, Presented at the SPE Asia Pacific Oil and Gas Conference and Exhibition held in Jakarta, Indonesia, 15-17 April 2003
174. Saucier, R. J. (1974), "Considerations in Gravel-Pack Design." Journal of Petroleum Technology; Society of Petroleum Engineers.
175. Brown, K. E. 1984, The Technology of Artificial Lift Methods, Penn Well Books, Tulsa.
176. Macdonald, F, et al., "Flow Through Porous Media – the Ergun Equation Revisited", Ind. Eng. Chem. Fundam., v.18, n.3, p. 199, 1979 (Murilo D. M. 1999).
177. Liu, S. et al., "Steady Incompressible Laminar Flow in Porous Media", Chem. Eng. Science, v.49, n.21, p.3565, 1994 (Murilo D. M. 1999).
178. Du Plessis, J. P. & Masliyah, J. H., "Flow Through Isotropic Granular Porous Media" Transport in Porous Media, v.6, p.207, 1991 (in Murilo D.M. 1999)
179. Murilo, D. M. et al., "Prediction of Ceramic Foams Permeability Using Ergun's Equation", Material Research, vol. 2, n.4, Sao Carlos Oct. 1999.
180. [www.pipeflow.co.uk/public/control.php?\\_path](http://www.pipeflow.co.uk/public/control.php?_path)
181. <https://campus.rgu.ac.uk/campus/myoffice/mymodules/wellengineeringd.cfm?m=XCjMcuDXa8x8&CFID=9354454&CFTOKEN=49570570>
182. diabira L., et al., 2001, Porosity and Permeability Evolution Accompanying Hot Fluid Injection into Diatomite, SUPRI TR-123,

prepared for US department of Energy, Contract No DE.FC26-00BC15311

183. Khatchikian Alberto, 1995, "Determining Reservoir Pore Volume Compressibility from Well logs," SPE 26963

**Appendices**

---

**Appendix A-1 Derivation of tangential stress at  $\theta_a = 0^\circ$  and  $\theta_a = 90^\circ$** 

$$\text{Given } \sigma'_\theta = \sigma'_H + \sigma'_h - 2(\sigma'_H - \sigma'_h)\cos 2\theta_a - (p_w - p_p) \quad \text{A1}$$

$$\text{When } \theta_a = 0^\circ, \cos 2\theta_a = 1$$

Therefore:

$$\sigma'_\theta = \sigma'_H + \sigma'_h - 2(\sigma'_H - \sigma'_h)1 - (p_w - p_p) \quad \text{A2}$$

Opening up the brackets, equation A2 becomes:

$$\sigma'_\theta = \sigma'_H + \sigma'_h - 2\sigma'_H + 2\sigma'_h - p_w + p_p \quad \text{A3}$$

Rearranging equation (A3), it becomes

$$\sigma'_{\theta=0} = 3\sigma'_h - \sigma'_H - p_w + \alpha p_p \quad \text{A4}$$

$$\text{Similarly, when } \theta_a = 90^\circ, \cos 2\theta_a = -1$$

Therefore:

$$\sigma'_\theta = \sigma'_H + \sigma'_h - 2(\sigma'_H - \sigma'_h)(-1) - (p_w - p_p) \quad \text{A5}$$

Opening up the brackets, equation A5 becomes

$$\sigma'_\theta = \sigma'_H + \sigma'_h + 2\sigma'_H - 2\sigma'_h - p_w + p_p \quad \text{A6}$$

Rearranging equation A6, it becomes

$$\sigma'_{\theta=90} = 3\sigma'_H - \sigma'_h - p_w + \alpha p_p \quad \text{A7}$$

**Appendix B-1 Grain size for wells C4, C6 and C7**

Median grain size data from sieve analysis							
Percentile	95	84	75	50	25	16	5
<b>Depth (ft)</b>	<b>Well C4</b>						
8608.2	120	178	235	387	517	564	913
8610.0	110	150	180	250	375	420	850
8612.7	30	125	142	180	202	210	420
8616.6	60	120	140	145	193	210	420
8634.9	2	30	50	85	111	120	300
8637.0	25	40	80	95	128	140	300
	<b>Well C6</b>						
9921.2	109	166	230	353	402	420	600
9924.3	40	140	190	280	376	410	410
9925.7	55	140	175	230	374	426	426
9934.3	48	199	190	250	324	350	420
9936.0	40	130	160	300	359	380	420
9941.7	40	120	150	200	281	310	600
9946.2	50	125	145	190	264	290	420
9948.0	75	130	150	180	202	210	420
9951.6	80	130	170	250	360	400	420
9957.9	40	115	150	250	324	350	420
9972.4	45	115	132	190	264	290	420
9986.5	60	90	130	210	280	305	850
9991.6	95	120	155	180	202	210	300
10002.4	105	125	160	180	202	210	300
10012.7	9	19	40	85	133	150	300
10015.0	6	18	35	70	91	98	150
10019.4	4	15	40	66	91	100	210
10031.4	22	48	75	155	195	210	850
10034.4	60	80	110	140	169	180	210
10036.5	35	65	88	120	135	140	210
10037.8	35	60	85	120	138	145	150
	<b>Well C7</b>						
9670.0	100	170	190	250	330	350	500
9673.0	63	100	120	180	230	260	600
9714.0	45	70	95	135	195	235	450
9722.0	55	63	70	100	150	190	350
9756.0	51	63	75	110	150	170	300
9758.0	45	55	68	110	200	290	700
9810.0	45	55	68	110	150	200	355
9814.8	60	68	79	130	195	240	480
9826.9	40	55	68	110	175	225	490
9846.0	52	63	74	105	145	150	200

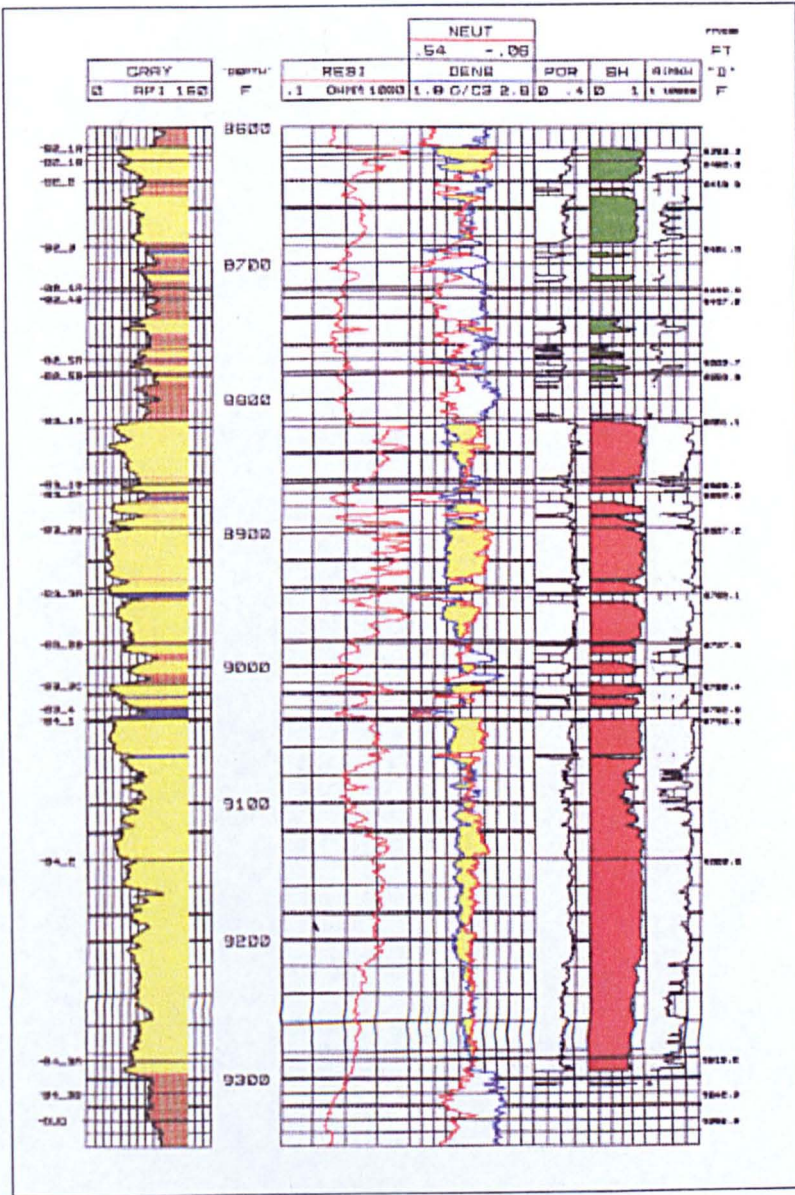
**Appendix B-2 Grain size for wells C5 and C8**

Median grain size data from sieve analysis							
Percentile	95	84	75	50	25	16	5
<b>Depth (ft)</b>	<b>Well C5</b>						
9598.5	22	55	60	90	119	130	210
9599.0	14	45	69	85	117	130	210
9648.5	20	50	70	85	99	105	210
9650.5	32	60	82	90	115	125	150
9651.5	20	50	77	95	106	110	420
9655.5	21	48	75	80	99	106	300
9657.0	15	40	68	75	100	110	300
9659.5	22	55	65	90	101	105	300
9663.5	13	36	65	68	102	115	211
9665.5	15	43	65	50	93	110	211
9670.0	8	17	57	66	108	125	300
9672.0	17	49	80	120	127	130	420
9680.5	13	23	85	134	169	183	420
9684.0	9	21	80	132	176	194	420
	<b>Well C8</b>						
9008.0	64	70	91	136	188	254	425
9025.0	56	144	177	231	306	343	450
9041.5	42	45	48	68	214	308	450
9078.0	62	157	173	220	293	332	450
9097.0	64	68	73	88	279	341	475
9120.0	38	75	100	143	202	264	400
9134.0	87	122	151	188	222	237	325
9169.0	125	155	168	203	242	272	375
9178.0	1	5	52	99	156	176	250
9185.0	24	51	77	100	138	153	250
9192.0	90	244	268	329	417	457	500
9210.0	81	105	129	162	216	275	425
9218.0	90	158	173	221	292	322	400
9240.0	62	139	155	184	233	270	375
9266.0	62	151	170	218	295	347	600
9283.0	50	76	96	147	219	302	600
9320.0	5	37	69	101	148	190	375
9350.0	5	36	73	110	161	207	375
9380.0	27	56	85	114	177	230	425
9398.0	1	8	78	148	232	297	450
9408.0	30	100	184	515	605	641	700
9420.0	10	103	220	482	593	634	700
9427.0	2	15	50	250	540	595	665

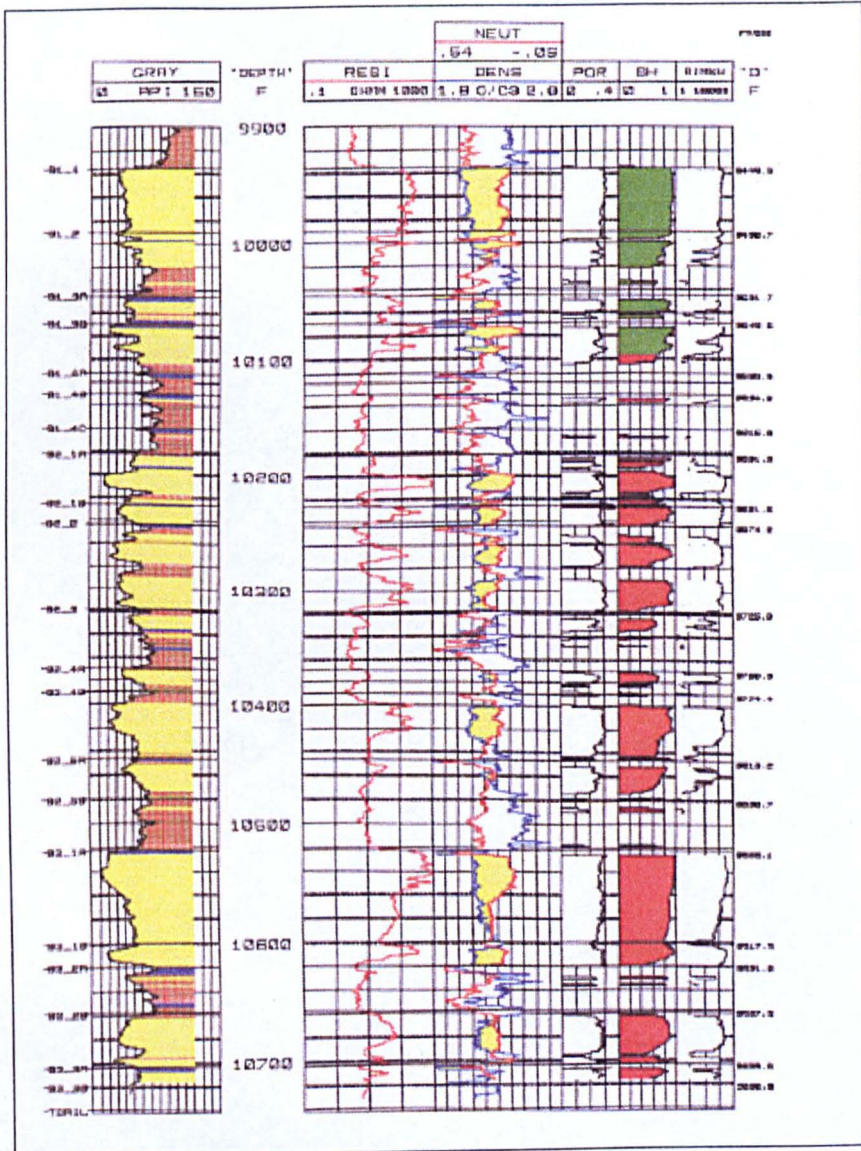
**Appendix B-3 Grain size for well C10**

Median grain size data from sieve analysis							
Percentile	95	84	75	50	25	16	5
Depth (ft)	Well C10						
9403.9	30	115	280	375	430	460	600
9417.0	225	290	360	440	510	560	700
9430.6	10	100	270	350	440	480	600
9439.3	160	240	320	420	550	630	900
9444.4	10	54	181	310	375	410	540
9450.7	100	163	250	360	460	530	680
9456.5	50	153	265	350	460	520	690
9558.1	5	15	63	230	290	315	370
9564.1	10	45	90	250	355	370	430
9573.1	5	20	95	410	570	640	920
9583.7	5	55	132	355	520	560	695
9588.4	37	47	58	90	148	163	186
9597.7	105	115	125	163	230	250	290
9605.5	105	120	135	186	270	295	350
9622.0	20	148	310	520	760	820	990
9640.0	5	50	167	400	580	680	1000
9661.8	8	20	38	90	181	250	340
9694.1	5	52	200	400	490	620	840
9700.8	20	80	148	360	560	660	940
9728.0	20	26	32	53	90	115	163
9747.0	20	60	115	275	380	450	800
9760.2	38	43	48	66	99	122	148
9761.3	2	11	23	59	131	148	167
9769.1	2	60	210	420	580	650	900
9805.6	50	163	300	530	780	920	1700
9834.7			5	60	167	185	215
9847.3	7	45	80	255	350	390	510
9857.6	90	110	132	200	315	360	490
9889.4	70	128	185	390	540	600	800
9896.3	5	30	54	210	300	360	620
9906.5	70	133	200	430	530	570	670
9927.6	2	14	35	115	230	255	290
10020.5	80	140	200	400	555	620	900
10034.8	30	45	60	113	200	220	270
10043.9	2	20	60	230	300	325	385
10054.3	25	100	148	380	550	620	800
10057.2	154	175	195	270	390	435	550

Appendix B-4 Well logs - well C4



Appendix B-5 Well logs - well C6

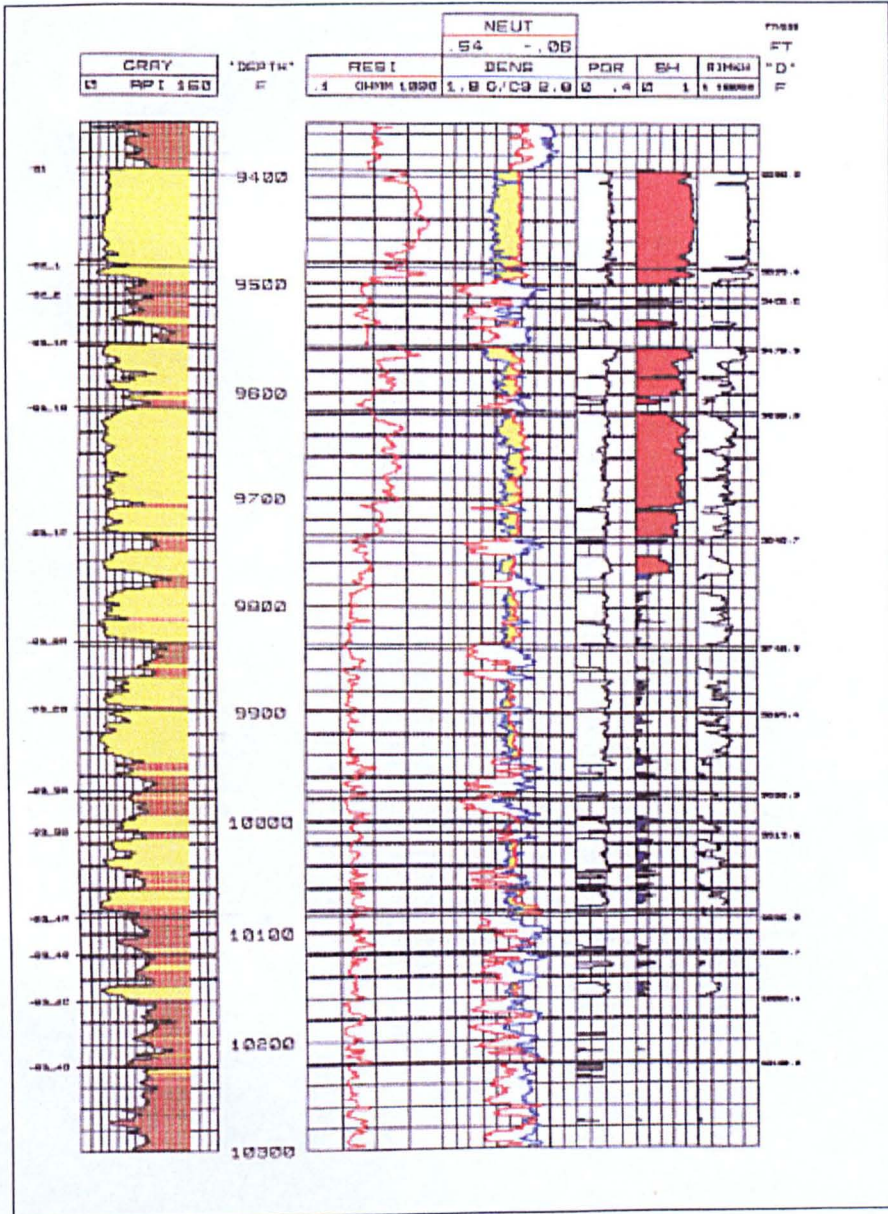








Appendix B-9 Well logs - well C10



### Appendix C-1 Existing UCS models ranking spreadsheet

PARAMETERS	WEIGHTING	NORMALISED WEIGHTING	Gavito 1996	Hon & Dusseault 2002	Prikryl 2001	Sarda et al. 1993	Tokle et al 1986	Stein 1995	Prabhakar 1997	Coates & Denoo 1981	Bruce 1990	Tiab & Donaldson 1996
<b>Mechanical strength parameters</b>												
Bulk compressibility	50	0.05	0.05			0.05	0.05		0.05	0.05	0.05	
Matrix compressibility	50	0.05										
Pore compressibility	50	0.05										
Shear modulus	50	0.05	0.05			0.05	0.05	0.05				
Young modulus	50	0.05	0.05				0.05		0.05		0.05	0.05
Bulk modulus	50	0.05	0.05			0.05	0.05		0.05	0.05	0.05	0.05
Poisson ratio	50	0.05	0.05			0.05	0.05					
Angle of internal friction	50	0.05		0.05		0.05						0.05
Capillary bond force	50	0.05		0.05								
Formation strength	50	0.05	0.05	0.05	0.05	0.05	0.05	0.05	0.05	0.05	0.05	0.05
Cementation/cohesion	50	0.05										
<b>Failure-inducing parameters</b>												
		0.00										
Overburden stress	30	0.03	0.03			0.03	0.03					
Effective stress	30	0.03										
Drawdown	30	0.03										
Production rate	30	0.03										
Depletion	30	0.03										
Fluid pressure gradient	30	0.03										
Wettability & Water breakthrough	30	0.03										
Compaction	30	0.03	0.03			0.03	0.03					
Pore pressure	30	0.03										
<b>Petrophysical properties</b>												
		0.00										
Porosity	20	0.02	0.02	0.02		0.02	0.02					
Permeability	20	0.02										
Grain size	20	0.02		0.02	0.02							
Grain size distribution	20	0.02										
Volume of shale	20	0.02	0.02			0.02	0.02		0.02		0.02	0.02
	<b>920</b>	<b>1.00</b>	<b>0.40</b>	<b>0.19</b>	<b>0.07</b>	<b>0.40</b>	<b>0.40</b>	<b>0.10</b>	<b>0.22</b>	<b>0.15</b>	<b>0.22</b>	<b>0.22</b>